

On Aspects of Mixed Continuum-Atomistic Material Modelling

Vom Fachbereich Maschinenbau und Verfahrenstechnik
der Technischen Universität Kaiserslautern
zur Verleihung des akademischen Grades
Doktor-Ingenieur (Dr.-Ing.)
genehmigte Dissertation

von Dipl.-Ing. Rudolf Sunyk
aus Kiew

Hauptreferent:	Prof. Dr.-Ing. P. Steinmann
Korreferenten:	Prof. Dr. H. Gao Prof. Dr. G. Friesecke
Vorsitzender:	Prof. Dr.-Ing. D. Eifler
Dekan:	Prof. Dr.-Ing. P. Steinmann

Tag der Einreichung:	21. Oktober 2003
Tag der mündlichen Prüfung:	14. Juli 2004

Kaiserslautern, Juli 2004
D 386

Vorwort

Diese Arbeit entstand in der Periode zwischen dem Februar 1999 und dem Mai 2003 am Lehrstuhl für Technische Mechanik der Technischen Universität Kaiserslautern. Dem Lehrstuhlinhaber Professor Paul Steinmann bin ich unendlich dankbar für die Anregung zu dieser Arbeit, für ständige konstruktive Diskussionen und kaum zu unterschätzende Empfehlungen, für ein besonderes Gefühl des aktuellen Trends in Mechanik, dem die Geburt dieses überdisziplinäres Werks zu verdanken ist. Vor allem bin ich Herrn Professor Steinmann aber dafür dankbar, dass er mich überzeugt hat, meinen jetzigen Weg zu gehen, als ich 1998 an einer Verzweigung stand.

Herrn Professor Huajian Gao und Herrn Professor Gero Friesecke danke ich für die Übernahme des Korreferates, für wichtige Anmerkungen und weiterführende Gespräche, die mir sicherlich geholfen haben, einige Aspekte dieser Arbeit besser zu verstehen und auch potentielle Entwicklungswege vorstellen zu können.

Herrn Dr.-Ing. Stefan Hartmann danke ich für die umfassende und kompetente Unterstützung bei meinen ersten Schritten in Mechanik an der Gesamthochschule-Universität Kassel, die mich letztendlich nach Kaiserslautern führten.

Ich danke Herrn Dipl.-Ing. (FH) Thorsten Dietz für eine kleine, aber wesentliche experimentelle Unterstützung.

Ich danke allen meinen Kollegen für die sehr warme und freundliche Atmosphäre, die all diese Jahre am Lehrstuhl herrschte. Ich danke dem guten Schicksal, das mir eines Tages als Büronachbar den Dipl.-Ing. Ralf Denzer geschickt hat, dessen höchste Kompetenz, ständige Hilfsbereitschaft und nicht zuletzt guter Humor bei Lösung von vielen mit der Arbeit verbundenen Problemen so ausgezeichnet geholfen haben.

Ich danke meiner Familie und insbesondere meiner Frau Natalia für permanente Unterstützung und unendliche Toleranz.

Karlsruhe, Juli 2004

Rudolf Sunyk.

Abstract

key words: non-linear mechanics, interatomic potentials, Cauchy-Born rule, strain localization, infinitesimal rank-one convexity, higher-order continuum, path-change procedure, microstructures

In the present work, various aspects of the mixed continuum-atomistic modelling of materials are studied, most of which are related to the problems arising due to a development of microstructures during the transition from an elastic to plastic description within the framework of continuum-atomistics.

By virtue of the so-called Cauchy-Born hypothesis, which is an essential part of the continuum-atomistics, a localization criterion has been derived in terms of the loss of infinitesimal rank-one convexity of the strain energy density. According to this criterion, a numerical yield condition has been computed for two different interatomic energy functions. Therewith, the range of the Cauchy-Born rule validity has been defined, since the strain energy density remains quasiconvex only within the computed yield surface.

To provide a possibility to continue the simulation of material response after the loss of quasiconvexity, a relaxation procedure proposed by Tadmor et al. [89] leading necessarily to the development of microstructures has been used. Thereby, various notions of convexity have been overviewed in details.

Alternatively to above mentioned criterion, a stability criterion has been applied to detect the critical deformation. For the study in the postcritical region, the path-change procedure proposed by Wagner and Wriggers [94] has been adapted for the continuum-atomistic and modified.

To capture the deformation inhomogeneity arising due to the relaxation, the Cauchy-Born hypothesis has been extended by assumption that it represents only the 1st term in the Taylor's series expansion of the deformation map. The introduction of the 2nd, quadratic term results in the higher-order materials theory. Based on a simple computational example, the relevance of this theory in the postcritical region has been shown.

For all simulations including the finite element examples, the development tool MATLAB 6.5 has been used.

Nomenclature

Atomistic features

\mathcal{C}_0	Material lattice configuration
\mathcal{C}_t	Spatial lattice configuration
\mathbf{R}_i	Site vector of the atom i in \mathcal{B}_0
\mathbf{r}_i	Site vector of the atom i in \mathcal{B}_t
E_i	Contribution of the atom i to the total internal energy E^{int}
\mathbf{f}_i	Force acting on the atom i due to all other atoms
\mathbf{k}_{ij}	Atomic level stiffness
V_i	Volume of the Voronoi cell in the material configuration

Continuum features

\mathcal{B}_0	Material body configuration
\mathcal{B}_t	Spatial body configuration
\mathbf{X}	Site vector in \mathcal{C}_0
\mathbf{x}	Site vector in \mathcal{C}_t
\mathbf{F}	Material deformation gradient
$\bar{\mathbf{F}}$	Homogenized material deformation gradient
W_0	Strain energy density
\mathbf{P}	1 st Piola-Kirchhoff stress tensor
$\bar{\mathbf{P}}$	Homogenized 1 st Piola-Kirchhoff stress tensor
\mathbf{S}	2 nd Piola-Kirchhoff stress tensor
$\boldsymbol{\tau}$	Kirchhoff stress tensor
$\boldsymbol{\sigma}$	Cauchy stress tensor
\mathbb{L}	4 th -order two-point tangent operator (linearization of \mathbf{P})
\mathbb{C}_1	4 th -order material tangent operator (pull-back of \mathbb{L})
\mathbb{C}	4 th -order material tangent operator (linearization of \mathbf{S})
\mathbb{E}_1	4 th -order spatial tangent operator (push-forward of \mathbb{L})
\mathbb{E}_2	4 th -order spatial tangent operator (linearization of $\boldsymbol{\tau}$)

2nd-order theory

\mathbf{G}	2^{nd} -order deformation gradient, a rank-3 tensor
\mathbf{Q}	2^{nd} -order stress, a rank-3 tensor
K	Main curvature of $\partial\mathcal{B}_0$
\mathbf{t}_0^Q	2^{nd} -order stress traction on $\partial\mathcal{B}_0$
\mathbf{t}_0^P	Surface traction on $\partial\mathcal{B}_0$
\mathbb{M}_{GG}	6^{th} -order two-point tangent operator needed for linearization of \mathbf{Q}
$\mathbb{M}_{GF}, \mathbb{M}_{FG}$	5^{th} -order two-point tangent operators needed for linearization of \mathbf{Q}
ε	Deformation inhomogeneity measure

Finite Element features

\mathcal{B}^h	Approximated body configuration (material or spatial)
\mathbf{u}^h	Approximated global displacement vector
$(\bullet)_e$	Values related to the element e
ξ	Local coordinates
\mathbf{J}_e	Jacobi matrix of the transformation from local to global material element coordinates
\mathbf{j}_e	Jacobi matrix of the transformation from local to global spatial element coordinates
$N_I(\xi)$	Shape function at the node I
\mathbf{F}_I^{int}	Internal force vector at the node I
\mathbf{F}_e^{int}	Internal element force vector
\mathbf{a}_e	Incidence matrix of the element e
$\mathbf{R}(\mathbf{x})$	Residual force
\mathbf{K}_T	Global stiffness matrix
K_T^e	Element stiffness matrix
K_{TIJ}^e	Contribution of the nodes I and J to K_T^e

Material parameters

ε, σ	Parameters of the Lennard-Jones pair potential
$\varepsilon, r_0, \alpha,$	Parameters of the EAM potential
$\beta^{(0)}, Z, A$	

Convexity and localization features

$I(\varphi)$	Non-linear functional
\mathbb{R}^m	m -Dimensional vector space
$\mathbb{R}^{n \times m}$	Space of $n \times m$ matrices
$L^p(\mathcal{B})$	Space of p times integrable functions
$W^{1,p}(\mathcal{B}, \mathbb{R}^m)$	Sobolev space
$CW PW$	Convex, polyconvex,
$QW RW$	quasiconvex and rank-one convex envelopes of W
\mathcal{B}_L	Material configuration with characteristic length L
$\nabla'_X(\bullet)$	Generalized gradient
$\det'(\bullet)$	Generalized determinant

$[[\bullet]]$	Jump of a field quantity
\mathbf{m}	Spatial polarization vector
\mathbf{N}	Material normal to the localization surface
\mathbf{q}	Acoustic tensor
\mathbf{A}_i	Additional inner displacement of the atom i
$\tilde{\mathbf{W}}_0$	Relaxed strain energy density
$\mathbf{b}_{ij}, \mathbf{b}_{ii}$	2^{nd} -order tensors needed for linearization of the equation system in the relaxation problem
$\mathbb{B}_{ij}, \mathbb{B}_{ii}$	3^{rd} -order tensors introduced as temporary values
λ_j, φ_j	Eigenvalues and eigenvectors of the global tangential stiffness matrix \mathbf{K}_t
ξ_j	Scaling factors

Contents

Abstract	i
Nomenclature	iii
Introduction	1
1 Interatomic Interactions in Crystalline Solids	7
1.1 Interactions in the Nature	7
1.1.1 Hierarchy of the Elementary Particles	8
1.1.2 The four Kinds of Interactions	8
1.2 Types and Nature of the Interatomic Interactions	10
1.2.1 Heteropolar (Ionic) Bonding	11
1.2.2 Homopolar (Covalent) Bonding	12
1.2.3 Van der Waals Bonding	13
1.2.4 Metallic Bonding	15
1.2.5 Nature of Repulsion	20
1.3 Modelling of Various Chemical Bonds	22
1.3.1 The full Hamiltonian and its Series Expansion	22
1.3.2 Pair Potentials	23
1.3.3 Many-Body Potentials for Modelling of Covalent Bonds	26
1.3.4 Many-Body Potentials for Modelling of Metals	28
2 Continuum-Atomistic Constitutive Modelling	33
2.1 Atomistic Constitutive Modelling	33
2.2 1 st - Order Hyperelastic Continua	35
2.3 1 st - Order Cauchy-Born Rule	39
2.4 Scale Transition: Continuation and Homogenisation	47
2.4.1 Continuous homogenisation	47
2.4.2 Continuation	49
2.4.3 Discrete homogenisation	51
2.5 Finite Element Implementation	53
2.5.1 Continuum-Atomistic Constitutive Law	53
2.5.2 The Structure of the Simulation Code	56
2.6 Examples	58
2.6.1 Indentation Test	58

2.6.2	Horizontal Shearing	66
3	Microstructures and Energy Minimisation	69
3.1	Definitions and Statements	71
3.1.1	Weak Convergence and Sequential Weak Lower Semicontinuity	71
3.1.2	Notions of Convexity	73
3.1.3	Different Envelopes of a Function	78
3.1.4	Existence of minimiser; Relaxation	79
3.2	Application to a Discrete Lattice System	80
4	Transition to Plasticity in Continuum-Atomistics	85
4.1	Loss of Infinitesimal Rank-1 Convexity	85
4.1.1	Localisation Analysis in Continuum Mechanics	85
4.1.2	Derivation of the Localisation Criterion for Continuum-Atomistic Modelling	87
4.1.3	Examples	87
4.1.4	Computation of Failure Surface	90
4.2	Finite Element Implementation	93
4.2.1	Indentation Test	94
4.2.2	Horizontal Shearing	98
4.3	Relaxation	101
4.3.1	Derivation of Equilibrium Conditions	101
4.3.2	Implementation at the Micro Scale	103
4.3.3	Stability Criterion and Path-Change Procedure	110
5	Higher – Order Gradients in Continuum-Atomistics	121
5.1	2^{nd} – Order Hyperelastic Continua	122
5.2	2^{nd} – Order Cauchy-Born Rule	123
5.3	Examples	125
5.3.1	Geometric Characterisation of a Prototype Deformation	125
5.3.2	Detailed Investigations	127
5.3.3	Simple Deformation Inhomogeneity Measure	129
6	Discussion	135
A	Investigation of $\sum_{j \neq i} \mathbf{R}_{ij} \otimes \mathbf{R}_{ij}$	139
B	On the Discrete Homogenisation	143
C	The Non-Linear Finite Element Method	149
D	The Frame Indifference of $W(\mathbf{F})$	159
E	Derivation of the Higher-Order Equilibrium and Boundary Conditions	161
	Bibliography	163

Introduction

“Modern material science is based on the fundamental experience that the properties of materials are not unalterably determined by their average chemical composition but they are to a large extent influenced by their microstructure... Thus, modern “materials research” is often used as a synonym for “microstructure research.”

Dierk Raabe, “Computational Materials Science”

Multiscale simulation methods in computational material science have matured considerably during the last decade. Among a large number of various approaches, the techniques using semi-empirical energy potential functions stemming directly from lattice statics or dynamics, see e.g. Kohlhoff et al. [45], Phillips [73], Shenoy et al. [78], Gao et al. [34], Klein et al. [43], Arroyo and Belytschko [2] and Nakane et al. [64], could be highlighted. Thereby, the continuum quantities such as the stress tensor or the tangent operator can be represented in terms of the derivatives of these potentials and depend consequently on the atomistic forces and stiffnesses.

The present work is based on such mixed method known as quasicontinuum. The quasicontinuum framework advocated by Tadmor [88] consists of two different approaches. Thereby, in particular, the local or continuum-atomistic (in the terminology used here) approach is only valid as long as the deformation field remains sufficiently homogeneous. If the deformation becomes non-homogeneous, the non-local or the atomistic-continuum (in the terminology used here) approach is more appropriate. This approach lies close to a pure atomistic simulation.

A significant ingredient of the former, i.e. the continuum-atomistic approach is the Cauchy-Born rule (CBR) originally stemming from Cauchy [17, 16, 19, 18] and generalized by Born [13, 14]. This rule states essentially that all atoms of a single crystal volume follow the prescribed displacement of its boundary, see Milstein [58], Ericksen [27], Zanzotto [96]. The validity of the CBR is studied e.g. by Friesecke and Theil [33], whereby it turns out that the CBR fails for sufficiently large deformations.

The aim of the present work is not to improve the existing quasicontinuum model but to propose an alternative solution strategy that extends the accepted Cauchy-Born rule and allows to stay within the frame of a continuum setting throughout the entire simulation.

The failure of the CBR at the elastic limit is so to say a bifurcation point for the quasicontinuum method and for the method proposed here. Whereas the quasicontinuum method switches to a pure atomistics as soon as the deformation field becomes sufficiently inhomogeneous, the frame of the continuum mechanics is used here even in the plastic region. To capture the plasticity phenomena,

the relaxation method used e.g. by Tadmor et al. [89] is applied. Such a relaxation procedure has been also used by Klein and Gao [44] to remedy the CBR applied to covalently bonded materials like silicon. On the other hand, the CBR is not able to capture an inhomogeneous deformation of the crystal lattice. It is a reason to switch to the non-local limit within the quasicontinuum method. Another proposal is made here, namely a kinematical method allowing to take the inhomogeneity into account: the extension of the CBR by using the higher-order theory like the Toupin-Mindlin theory, see e.g. Fleck and Hutchinson [30].

Thus, according to the citation from the book of D. Raabe [76] at the beginning of introduction, most aspects of the continuum-atomistic modelling studied here are related to the capturing of the problems arising due to the development of microstructures during the transition from elasticity to plasticity.

The dissertation is structured as follows. In the 1st chapter, the nature of different interatomic interactions is discussed and a detailed overview of main pair as well as many-body energetic functions providing a more or less realistic description of interactions in solids is given.

The 2nd chapter contains a brief review of both atomistic and continuum formulations. Then, based on these classical conceptions, a formulation of the mixed continuum-atomistic approach is introduced through substitution of a phenomenological strain energy density by an atomistic energy function stemming from ab-initio methods. A transition from a discrete lattice system to a continuous medium at the micro scale (continuation) as well as from a continuous system at the micro scale to a continuous system at the macro scale (homogenisation) is handled in this chapter. Finally, the finite element implementation of the continuum-atomistic principle is discussed in detail.

In the 3rd chapter, a mathematical foundation of the non-convex mechanical problems for continuous as well as for discontinuous systems is reviewed. Thereby, the failure of continuum-atomistics is handled.

A transition to plasticity is then discussed in chapter 4. A localisation condition in the form of vanishing determinant of the localisation tensor is thereby derived and the explicit format of this tensor for the continuum-atomistic approach is obtained. It is emphasised that within this mixed approach, macroscopic field values such as the stress tensor, the fourth order tangent operator and the localisation tensor are determined by discrete atomic level forces and stiffnesses. Moreover, several planar homogeneous deformations such as simple shear and uniaxial extension are applied to the (111)–plane of *fcc*–type crystals and the corresponding localisation criterion is investigated. Finally, the derived localisation condition determined by the properties at the atomistic scale is applied to compute a failure condition for single crystals at the continuum scale, see also Sunyk and Steinmann [85, 86]. In the 2nd part of this chapter, the application of the relaxation principle to the continuum-atomistic model is handled.

The 5th and last chapter, contains the extension of the continuum-atomistic framework by introduction of the 2nd order Cauchy-Born rule based on the higher-order theories. The proposition to apply the higher-order gradient formulation to capture the inhomogeneous deformation at the atomic scale¹ is supported by several computational examples, see also Sunyk and Steinmann [87].

A discussion completes this work. All additional considerations, which have no influence on the understanding of the main ideas as well as more or less complicated derivations are placed in the appendix.

¹besides an additional motivation to guarantee the lower size bound for microstructures, which arise due to the relaxation after the loss of infinitesimal rank-one convexity

Einleitung

“Modern material science is based on the fundamental experience that the properties of materials are not unalterably determined by their average chemical composition but they are to a large extent influenced by their microstructure... Thus, modern “materials research” is often used as a synonym for “microstructure research.”

Dierk Raabe, “Computational Materials Science”

Die Methoden der Materialmodellierung gleichzeitig auf verschiedenen Längeskalen haben sich stark binnen der letzten zehn Jahren durchgesetzt. Die Methoden, die semi-empirische energetische Potentialfunktionen verwenden, welche direkt aus der Gitterstatik oder Dynamik abstammen, können unter der grossen Zahl verschiedener Vorgehensweisen ausgezeichnet werden, s. z.B. Kohlhoff et al. [45], Phillips [73], Shenoy et al. [78], Gao et al. [34], Klein et al. [43], Arroyo und Belytschko [2] und Nakane et al. [64]. Solche kontinuumsmechanischen Grössen wie Spannungstensor oder Tangentenoperator können dabei als Ableitungen dieser Potentiale dargestellt werden und hängen folglich von den atomistischen Kräften und Steifigkeiten ab.

Vorliegende Arbeit basiert auf einer solchen gemischten Methoden, die als Quasikontinuum bekannt ist. Diese Methode wurde vom Tadmor [88] entwickelt und besteht aus zwei verschiedenen Vorgehensweisen. Die erste, lokale oder, in der hier verwendeten Terminologie, Kontinuum-Atomistische Methode gilt solange das Verzerrungsfeld ausreichend homogen bleibt. Wenn die Deformation inhomogen wird, eine nichtlokale oder, in der hier verwendeten Terminologie, Atomistisch-Kontinuum-Methode, die sich im Wesentlichen einer rein atomistischen Simulation ähnelt, wird relevant.

Ein wichtiger Bestandteil der ersten, Kontinuum-Atomistischen Methode ist die ursprünglich von Cauchy [17, 16, 19, 18] stammende und vom Born [13, 14] verallgemeinerte Cauchy-Born Regel (CBR). Die Regel behauptet, dass alle Atome aus dem Volumen eines Einkristalls der vorgegebenen Verschiebung an seiner Grenze folgen, s. Milstein [58], Ericksen [27], Zanzotto [96]. Die Gültigkeit der CBR wurde z.B. von Friesecke und Theil [33] studiert. Dabei wurde es u.a. festgestellt, dass die CBR bei grossen Deformationen versagt.

Das Ziel dieser Arbeit besteht nicht darin, die existierende Quasikontinuumsmethode zu verbessern, sondern eine alternative Lösungsstrategie vorzuschlagen, die die akzeptierte CBR erweitert und erlaubt im Rahmen der Kontinuumsmechanik während der ganzen Simulation bleiben.

Das Versagen der CBR an der Grenze der Elastizität ist sozusagen ein Verzweigungspunkt für Quasikontinuum und für die hier vorgeschlagene Methode. Während die Quasikontinuumsmethode zur reinen Atomistik umschaltet, sobald die Deformation ausreichend inhomogen wird, die Kontinuumsmechanische Formulierung wird hier sogar im plastischen Bereich verwendet. Um die Plastizität zu erfassen, wird eine Relaxationsmethode eingesetzt, die von z.B. Tadmor et al. [89] verwendet wurde. Eine solche Relaxationsprozedur wurde auch von Klein und Gao [44] gebraucht, um die CBR für kovalente Materialien wie Silizium verwenden zu können. Auf der anderen Seite ist die CBR nicht fähig, eine inhomogene Deformation des Kristallgitters zu erfassen, was eigentlich die Ursache der Wechsels zur nichtlokalen Methode beim Quasikontinuum ist. Hier ist eine andere, kinematische Vorgehensweise vorgeschlagen: die Erweiterung der CBR durch Verwendung einer Theorie höherer Ordnung, die der Toupin-Mindlin-Theorie ähnlich ist, s. z.B. Fleck und Hutchinson [30].

Also, in voller Zusammenstimmung mit dem oben angegebenen Zitat aus dem Buch von D. Raabe [76], beziehen sich die meisten der hier diskutierten Aspekte der Kontinuum-Atomistik auf die Erfassung der Probleme, die wegen der Entstehung der Mikrostrukturen während des Übergangs zur Plastizität zustande kommen.

Die Dissertation ist folgendermassen strukturiert. Der 1. Kapitel verschafft einen Überblick der Natur verschiedener zwischenatomaren Wechselwirkungen sowie gibt eine detaillierte Beschreibung wichtigen Zwei- und Vielteilchenenergiefunktionen, die für eine mehr realistische Beschreibung der Wechselwirkungen in Festkörpern sorgen.

Der 2. Kapitel enthält eine kurze Beschreibung der atomistischen und kontinuumsmechanischen Formulierungen. Dann, basierend auf diesen beiden klassischen Methoden, ist die gemischte kontinuum-atomistische Formulierung eingeführt, indem die phänomenologische Deformationsenergiedichte durch eine von ab-initio Methoden stammende Energiefunktion ersetzt wird. Ein Übergang von einem diskreten Gitter zu einem kontinuierlichen Medium auf der Mikroskala (Kontinuuisierung), sowie von einem kontinuierlichen System auf der Mikroskala zu einem kontinuierlichen System auf der Makroskala (Homogenisierung) ist in diesem Kapitel behandelt. Ausserdem beinhaltet dieses Kapitel eine ausführliche Diskussion der Finite-Elemente-Implementierung der kontinuum-atomistischen Formulierung.

Im 3. Kapitel ist die mathematische Begründung der nichtkonvexen mechanischen Probleme der kontinuierlichen, sowie diskreten Systeme zusammengefasst. Unter anderem sind die Gründe des Versagens der Kontinuum-Atomistik diskutiert.

Der nächste, 4. Kapitel ist der Übergang zur Plastizität gewidmet. Dabei sind die Lokalisierungsbedingung in Form der verschwindenden Determinante des Lokalisierungstensors und das explizite Format dieses Tensors für die kontinuum-atomistische Formulierung hergeleitet. Die Besonderheit dabei ist, dass solche makroskopischen Feldgrössen wie der Spannungstensor, der 4-stufige Tangentenoperator, sowie der Lokalisierungstensor durch diskrete atomistische Kräfte und Steifigkeiten ausgedrückt sind. Ausserdem sind mehrere ebene homogene Deformationen wie einfache Scherung und einaxialer Zug auf die (111)-Ebene eines fcc -Kristalls angelegt und das entsprechende Lokalisierungskriterium untersucht. Letztendlich ist die hergeleitete Lokalisierungsbedingung, die durch die Eigenschaften auf der atomistischen Skala definiert ist, dazu verwendet, eine Fliessbedingung für Einkristalle auf der Macroskala zu berechnen, s. auch Sunyk and Steinmann [85, 86] Im 2. Teil dieses Kapitels ist die Anwendung der Relaxationskonzepte auf das kontinuum-atomistische Modell behandelt.

Der letzte, 5. Kapitel enthält eine Erweiterung des kontinuum-atomistischen Modells durch Einführung

der Cauchy-Born-Regel 2. Ordnung, die auf den Theorien höherer Ordnung basiert. Der Vorschlag, die die Gradienten höherer Ordnung enthaltene Formulierung zu verwenden, um die Deformation-sinhomogenitäten auf der atomistischen Skala zu erfassen, ist mit mehreren Rechenbeispielen unterstützt², s. auch Sunyk and Steinmann [87].

Eine Diskussion beendet diese Arbeit. Zusätzliche Überlegungen, die auf das Verständnis der Hauptideen keinen Einfluss haben, sowie mehr oder weniger komplizierte Herleitungen sind im Anhang platziert.

²Ausser einer zusätzlichen Motivation der unteren Begrenzung der Dimensionen der Mikrostrukturen, die sich whrend der Relaxation nach dem Verlust der Rang-eins-Konvexität entwickeln.

Chapter 1

Interatomic Interactions in Crystalline Solids

“Whether our description of structure is made at the level of the crystal lattice or the defect arrangements that populate the material or even at the level of continuum deformation fields, a crucial prerequisite which precedes the connection of structure and properties is the ability to describe the total energy of the system of interest.”

Rob Phillips, “Crystals, Defects and Microstructures”

The first problem, which should be solved for any kind of material modelling is the choice of the energy function describing the system of interest. The material model proposed in this work contains energy functions stemming directly from the interatomic energetics. For this reason, I find it purposeful in this chapter, to overview the question of what kind of forces holds collection of single atoms together and drives them to form the well-known crystalline structures. Furthermore, some important interatomic energy functions are reviewed in this chapter. Two of them (Lennard-Jones pair potential and Embedded-Atom potential) are used in the proposed model. Most data is based on the materials from the already cited book of Rob Phillips [73] as well as two further books of Israelachvili [41] and Allen & Tildesley [1]. As the information source, the materials of Particle Data Group [71] have been used in the 1st section.

1.1 Interactions in the Nature

Four fundamental interactions, which explain almost all observed physical processes excepted the particle masses, are presently known: weak, strong, electromagnetic and gravitational. Any attempt to describe these four different interactions leads to an introduction of numerous elementary particles. For this reason, a short overview of the particle hierarchy is given.

1.1.1 Hierarchy of the Elementary Particles

In 1898, Joseph Thompson measures the electron and proposes his "plum-pudding" model of the atom which describe an atom as a slightly positive sphere with small, raisin-like negative electrons inside. Then in 1919, Ernest Rutherford finds the first evidence of a proton and in 1931, James Chadwick discovers the neutron. So by the mid 1930s, the understanding of the fundamental structure of matter seemed to be complete. Protons, neutrons, and electrons provided the building blocks of all matter.

In 1948, the Berkeley synchro-cyclotron produces the first artificial particles and in 1953, the so called "particle explosion" begins: a lot of new particles have been discovered up to now. Finally, after eighteen years of searching at many accelerators, the top quark with an unexpectedly large mass of 175 GeV^1 is discovered at Fermilab.

Today, the following hierarchy of the elementary particles is accepted. New discoveries have shown that there are six types of quarks. Each quark type is called a flavour. The six flavours of quarks are up, down, strange, charm, bottom, top, in increasing order of mass. An electrical charge of quarks is a fraction of the proton charge. For instance, the charm-quark is charged with $+2/3 e$. The quark's fractional electric charges have not been observed for the simple reason that quarks are never found separately, but only inside composite particles called hadrons. There are two classes of hadrons: baryons, which contain three quarks, and mesons, which contain one quark and one antiquark. The well-known baryons are neutrons and protons consisting of the down-down-up and down-up-up quarks respectively.

There are also six types of particles, called leptons. In contrast to the quarks, any of the six leptons may be found by itself. The electron is the best known lepton. Two other charged leptons, the muon, (discovered in 1936) and the tau (discovered in 1975) differ from the electron by their larger mass. The other three leptons are called neutrinos, have no electric charge and have very little, if any, mass. There is one type of neutrino corresponding to each type of electrically charged lepton. For each of the six leptons, there is an antilepton with equal mass and opposite charge.

Both the leptons and quarks as well as protons and neutrons belong to fermions, the particle with fractional spin². The particles with a whole spin are called bosons. An example of bosons are photons and gluons.

1.1.2 The four Kinds of Interactions

Fundamental weak and strong interactions are related to the processes involving elementary particles. The weak interactions occur for all fundamental particles except for gluons and photons³. Weak interactions are the only processes, in which a quark can change to another type of quark, or a lepton to another lepton. They are responsible for the fact that more massive quarks and leptons decay to produce lighter quarks and leptons. That is why surrounding stable matter contains only electrons and the two lightest quark types (up and down). Beta decay of nuclei was the first observed weak process. Weak forces are very short-ranged. In ordinary matter, their effects are negligible except in cases where they allow an effect that is otherwise forbidden. There are a number of conservation laws

¹ $1\text{eV} = 1.6021892 \cdot 10^{-19}\text{J}$

²Spin is the intrinsic angular momentum of particles.

³In particle processes, the forces are described as due to the exchange of particles; for each type of force, there is an associated carrier particle. Gluons are carrier particles for strong interactions (colour force fields), photons are carrier particles of electromagnetic interactions; the carrier particles of weak interactions are W and Z bosons

that are valid for strong and electromagnetic interactions, but violated by weak processes.

Fundamental strong interactions occur between any two particles that have colour charge⁴, that is, quarks, antiquarks, and gluons. The strong force holds quarks together to form hadrons; its carrier particles are called gluons because they so successfully "glue" the quarks together. The binding of colour-neutral protons and neutrons to form nuclei is a residual strong interaction effect due to their strongly-interacting quark and gluon constituents and is similar to the residual electrical interaction, which leads to the binding of electrical-neutral atoms to form molecules. The strong forces have a short range similar to the weak forces.

Gravitational interactions occur between any two objects that have energy. Mass is just one possible form of this energy (photons are massless, but they experience gravitational forces). Gravitational interactions between fundamental particles are extremely weak, at least thirty orders of magnitude smaller than the weak interaction. Hence, gravitational effects can be ignored in particle physics processes involving small numbers of particles. The only reason why gravity is an important force is that there is no such thing as negative energy and, thus, the gravitational effects of all objects are summed - there is never any cancellation. The earth exerts a much stronger gravitational pull on any object than its electric pull. The electric charges in the earth are all balanced out (the positive charges of atomic nuclei screened by the negative charges of the electrons), but the masses of all the atoms in the earth add together to give a large gravitational effect on objects on the surface of the earth. The carrier particle for gravitational interactions has been named the graviton. However, no fully satisfactory quantum theory of gravitational interactions via graviton exchange has been identified.

The fourth, electromagnetic fundamental interactions are of highest importance for our application. These interactions occur between any two particles that have electric charge. On the one hand, only electromagnetic interactions are responsible for the binding force that causes negatively charged electrons to combine with positively charged nuclei to form atoms. On the other hand, residual electromagnetic interactions between electrically neutral atoms are responsible for the binding of atoms to form molecules and most of the forces (apart from gravity) that we experience in everyday life. This chapter is actually dedicated to description of these interactions.

Creation of a unified theory of all interactions could modify the relativistic quantum mechanics radically and would possibly lead to a new understanding of our world. The role of such a universal approach could play the so called String Theory⁵ which predicts the existence of force-carrying particles, such as photons and gluons - and gravitons - with the correct force laws. It also implies some more bizarre predictions, for example, the existence of seven extra space dimensions. But any revision of this theory lies outside the present work.

The main properties of the four fundamental interactions described above are listed in table 1.1.

⁴colour charge is the charge associated with strong interaction. "colour" is an attribute of quarks and gluons that cannot be seen and have nothing to do with the colours of visible light. Each quark carries one of the three types colour charge and there are eight possible types of colour charge for gluons. Similar to electrically-charged particles interacting by exchanging photons, colour-charged particles interact by exchanging gluons. All observed particles such as leptons, photons, hadrons, W and Z bosons have no strong interaction and hence no colour charge.

⁵The String Theory supposes that elementary particles are not point like but rather are small lines or loops of energy, "strings". It is very difficult to formulate a theory in which elementary particles have nonzero size which is consistent with relativity and with quantum mechanics.

Table 1.1: Summary of the four fundamental interactions

Interactions	Gravitational	Weak	Electromagnetic	Strong	
		(Electroweak)		Fundamental	Residual
Acts on:	Energy Mass	-	Flavour	Electrical Charge	colour Charge
Particles Experiencing:	All	Quarks, Leptons	Electrical Charged	Quarks Gluons	Hadrons
Carrier:	Gravitons	W & Z Bozons	Photons	Gluons	Mesons

1.2 Types and Nature of the Interatomic Interactions

As mentioned above, electromagnetic interactions are essentially responsible for any interatomic and intermolecular bonding. This statement became first possible in the 1920s after the great success of quantum theory and in particular, the understanding of the electronic structure of atoms. Moreover, the Hellman-Feynman theorem states: “Once the spatial distribution of the electron clouds has been determined by solving the Schrödinger equation, the intermolecular forces may be calculated on the basis of straightforward classical electrostatics.”⁶ Thereby, the only problem is to find the exact



Figure 1.1: From left to right: P. Ehrenfest, W. Heitler, F. London, L. Pauling

⁶The Hellman-Feynman theorem was originally proven by P. Ehrenfest [24] and later discussed by Hellman (1937) and independently rediscovered by Feynman (1939)

solution of the Schrödinger equation, which could only be realised for the simplest systems such as a hydrogen atom or a hydrogen-like electron-hole pair (an exciton). For this reason, the hamiltonian of the system of interest should be represented as a series expansion and the consideration of each ensuing term in this expansion leads to a new type of interaction.

This section contains a description of main bonding types. There are hetero- and homopolar, van der Waals and metallic bonds and each of them should be further individually characterised. A description of phenomena like hydrophobic interaction, hydrogen bonding or solvation forces lies outside this work.

1.2.1 Heteropolar (Ionic) Bonding

The main point in the theory of interatomic interactions is the huge difference between the masses of atoms and electrons. Because of this difference, the nuclei have lower velocities compared to electrons and can be viewed as fixed. Thereby, the problem reduces to studying the electrons motion in the electrostatic field of fixed nuclei. The total pair interaction energy includes both the electrons part and the electrostatic energy of the nuclei.

As shown by Heitler and London [36], an ability of atoms to form a bond is related to their spin which must be mutually compensated. As a quantitative measure of this ability, the double spin of the atom of interest can be used. This number is equal to the chemical valence of the corresponding element. For example, all elements in the 3rd group of the periodic table have the electronic configuration $s^2 p$ with the spin $S = 1/2$ in the normal (not excited) state. But by a relatively small excitation of an electron from the filled s -hull, a transition to the $s p^2$ -state with the spin $S = 3/2$ results. For this reason, the elements of the 3rd group show valence 1 as well as 3. Thereby, the 1st elements such as aluminium Al or boron B are 3-valent only.

The filled electron hulls are almost not influenced by bond formation. On the contrary, the distribution of the electron density in the outer, non-filled hulls can be dramatically changed. In the extreme case of so called heteropolar bonding, all valent electrons change from an atom to another one so that the molecule consists of two ions charged according to their valence in units of the electron charge e .

This bonding is almost isotropic and can be characterised by relatively high coordination numbers ⁷. The ionic bond is caused by the Coulomb interaction which decreases with the distance r as $1/r$ and is consequently long ranged. An interaction of two charges Q_1 and Q_2 separated by the distance r is given by

$$\Phi^{Coulomb}(r) = \frac{Q_1 Q_2}{4 \pi \varepsilon_0 \varepsilon r} \quad (1.1)$$

where ε is the dielectric constant of the medium. Depending on the sign of charges, the resulting forces can be attractive or repulsive. Admittedly in the lattice an electrostatic interaction is screened and decays at large distances as $\exp(-r)$. This screening is caused by the fact that positive-charged ions have negative-charged ions in their vicinity.

Heteropolar bonded crystals tend to form structures with the highest density. The majority of dielectrics belongs to ionic crystals. This is related to the fact that contrary to metals where the charge carriers are electrons the charge carriers in such crystals are ions. Because of this, the electric conductivity in ionic crystals is connected to the mass transfer phenomena and is strongly dependent on temperature. A prototype example for an ionic crystal is $NaCl$.

⁷The number of nearest neighbours of an atom or ion.

1.2.2 Homopolar (Covalent) Bonding

Another extreme bonding type is the so-called homopolar or covalent bond. The constituting atoms remain averaged neutral in this case. In contrast to the heteropolar molecules, the homopolar molecules show no sufficient dipole moment. The interaction problem of two electrically neutral atoms should be solved to find how the homopolar bond decreases with an increase in distance. This energy consists of two parts: the coulomb interaction energy between the nuclei (1.1) and an unknown electron interaction energy. At large distances, the electron part is a sum of known electron energies E_0 of two separated atoms corresponding to 0th order of perturbation theory. This means that the unknown energy can be given by the following expression

$$\Phi^{el}(r) = 2 E_0 + \Delta E(r) \quad (1.2)$$

with a perturbation⁸ $\Delta E(r)$ of the free electron energy $2 E_0$ at small distances. The 1st-order perturbation theory yields symmetric and antisymmetric solutions for $\Delta E(r)$, see e.g. Blochinzew [12]⁹:

$$\begin{aligned} \Delta E_a &= \frac{K - A}{1 - S^2} \\ \Delta E_s &= \frac{K + A}{1 + S^2} \end{aligned} \quad (1.3)$$

Here, K denotes an averaged electrostatic interaction energy of atoms without the interaction energy of nuclei accounted by Coulomb potential. A is the so-called exchange energy, the energy of exchange interaction. This interaction is a pure quantum mechanical effect and occurs because of the equivalence of all electrons¹⁰. The condition $0 \leq S \leq 1$ takes the non-orthogonality of the electronic wave functions into account. The total interaction energy of two atoms can thus be expressed as follows

$$\begin{aligned} \Phi_a &= 2 E_0 + \frac{Z^2}{r} + \frac{K - A}{1 - S^2} \\ \Phi_s &= 2 E_0 + \frac{Z^2}{r} + \frac{K + A}{1 + S^2} \end{aligned} \quad (1.4)$$

whereby Z is the nucleus charge. The computation of integrals¹¹ representing K and A shows an exponential decrease of both with an increase in distance, so that $K \sim \exp(-r)$ and the same for A . Both integrals are non-zero as long as the electronic hulls of two atoms are shared. Moreover, only the symmetric solution has a minimum and leads to a formation of a molecule, whereas the antisymmetric solution yields only repulsion. Thus, a formation of the homopolar molecule is defined by exchange

⁸ $\Delta E(r)$ can be viewed as perturbation as long as it remains essentially less than the difference between the main state E_0 and the next excited state E_1 :

$$\Delta E(r) \ll |E_1 - E_0|$$

⁹The derivation relates to a hydrogen molecule

¹⁰This interaction is not caused by some new fundamental interaction and occurs due to the same coulomb interaction of the electrons

¹¹For computation of these integrals for hydrogen see e.g. Slater [80]

interaction only.

The covalent bonding is strongly anisotropic; all bonds are oriented at well-known angles to each other. Such anisotropy of the covalent bond causes e.g. the tetrahedral diamond structure of silicon *Si*. The covalent bonds are short ranged and act at separations of about 0.1 nm . A low coordination numbers, strong temperature dependence of the forbidden zone width, high melting point and hardness belong to typical characteristics of covalent-bonded structures. The covalent bond is a typical attribute of semiconductors such as silicon *Si* and germanium *Ge*. All covalent crystals follow the $8 - N$ rule: each atom is connected with $8 - N$ next neighbours, whereby N is a group number in the table of elements, which belongs the covalent crystal. So silicon and germanium belong to the 4th group and due to this, they form diamond-type lattice with four next neighbours.

There is no principal difference between the hetero- and homopolar bondings. This difference is of quantitative nature: atoms with equal electronegativity¹² tend to form the covalent bond and if the electronegativities differ highly then the appearing bond is ionic. Hetero- and homopolar bondings are two extreme cases of the same phenomena and all transition cases between them are possible. The polar covalent bonding thereby arises e.g. in water H_2O . Quantitative expression of this classification can be summarised in the following rules:

- Electronegativity difference less than 0.5 leads to a non-polar covalent bond.
- Electronegativity difference between 0.5 and 1.6 leads to a polar covalent bond.
- Electronegativity difference between 1.6 and 2.0 leads to
 - an ionic bond, if a metal is involved;
 - a polar covalent bond, if only nonmetals are involved as e.g. in HF .
- Electronegativity difference greater than 2.0 leads to an ionic bond.

1.2.3 Van der Waals Bonding

Van der Waals forces act between atoms and molecules in addition to the already treated forces. The objects can thereby be electrically neutral and do not exhibit any electrical moment (dipole, quadrupole etc.) as is the case by e.g. spherically symmetric helium *He*. These forces are always present and their nature again relates to quantum mechanics. This interaction becomes important at relatively large separations when the 2nd-order perturbation theory is necessary. This fact is caused by exponential dependence of covalent bonding energy (1st-order theory) on separation, whereas the energy perturbation accounted in the 2nd-order theory shows the $1/r^6$ dependence and decreases slower as the 1st-order perturbation, see fig. 1.2. The van der Waals bonding is caused by dynamical deformation of electron hulls and can be explained as follows: even if the time average of all electrical moments of a non-polar atom vanishes, the instantaneous e.g. dipole moment (for 2nd-order perturbation theory the dipole moments are sufficient) is non-zero. This instantaneous moment induces the dipole moments in the neighbour non-polar atoms and an attraction between the atoms occurs. Simple derivation of this $1/r^6$ -rule is based on the representation of interacting atoms as quantum

¹²“The power of an atom in a molecule to attract electrons to itself”, see Pauling [72], p. 88. The modern definition of electronegativity has been introduced in 1932 by Linus Pauling, see fig. 1.1. He also developed a numerical scale of electronegativity.

oscillators. Then, a quantum mechanical calculation shows¹³ that the energy of two interacting oscillators is smaller than the energy of two separated ones exactly by attraction term depending on distance as $1/r^6$. In 1937, F. London [52] derived a van der Waals interaction energy in the form

$$\Phi^{vdW}(r) = -\frac{3}{4} \frac{\alpha_0^2 I}{(4\pi\epsilon_0)^2} \frac{1}{r^6} \quad (1.5)$$

with the first ionization potential I and the electronic polarizability α . Another name for van der Waals forces is dispersion forces due to their influence on visible and UV light dispersion. As mentioned

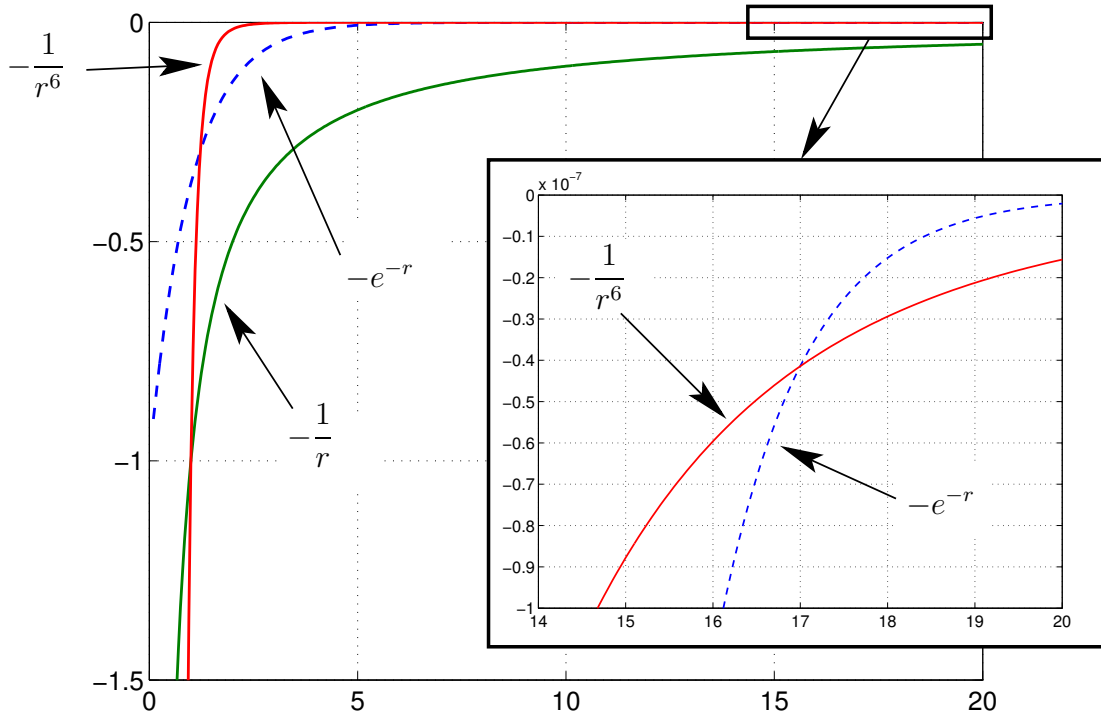


Figure 1.2: Comparison of covalent (e^{-r}), ionic ($1/r$) and van der Waals ($1/r^6$) interaction potentials. At large distances r the van der Waals interaction is stronger as the covalent one. The Coulomb interaction dominates at all separations.

above, the dispersion forces are long ranged and act between distances of 0.2 nm and 10 nm . This bonding is typical for electric-neutral molecular crystals with low melting points and low latent heats of melting. The solid phase of inert gases (e.g. neon Ne , argon Ar), oxygen crystals O_2 , hydrogen H_2 , hydrogen chloride HCl , methane CH_4 as well as organic crystals are accounted for among materials with this type of bond.

Two remarks should be made at this place. Firstly, an important property of the van der Waals forces is their pairwise non-additivity: the interaction energy of two atoms or molecules in a medium is affected by their neighbours. Thereby, the deviation in energy can be positive or negative and reach about 20%. In practice, the non-additivity becomes relevant at small (but not for atomic spacing!) characteristic lengths such as for thin films or bodies separated by a small gap. And finally, at very

¹³see e.g. Blochinzew [12]

large separations, the retardation effect occurs and the distance dependency on the dispersion forces changes to $1/r^7$.

1.2.4 Metallic Bonding

The interaction of outer electron shells in metals is so strong that it is impossible to separate the energy of an atom and the energy levels of collective states of all electrons in the body of interest. The inner electron shells are almost not shared and the metals can be viewed as a positively-charged ionic host bathed in the negatively-charged electronic sea of generalised outer or valence electrons. Such generalisation of electrons leads to high binding energy of metals and causes the specific properties of metals such as good electric and thermal conductivity. Furthermore, metals are characterised by e.g. highest coordination numbers and small compressibility.

An example of an appropriate energetic function is given in one of the following sections. Here, the energetics of electronic liquid in solids should be briefly reviewed.



Figure 1.3: From left to right: E. Schrödinger, F. Bloch, E. Fermi

Energetics of Electrons in Solids

The energy of electrons plays a crucial role in the energetics of metals and hence should be accounted in the total energy computation, whereby the interaction energy of electrons has the same order as their kinetic energy. The theory of such complicated system staying in good agreement with experiment is possible due to the following considerations:

- the behaviour of strong interacting electrons (or electron liquid) is analogous to the behaviour of the collection of free particles (i.e. electron gas) in some external field, which is an averaged field of all ions and other electrons;
- this field reflects the lattice symmetry and, in particular, the periodicity .

Because of these considerations, the problem of the electron motion in a periodic field has a special importance in the description of the metals energetics and should be briefly discussed here. Consider an electron moving in an external field with the following property

$$\Phi(\mathbf{r} + \mathbf{a}_n) = \Phi(\mathbf{r}) \quad (1.6)$$

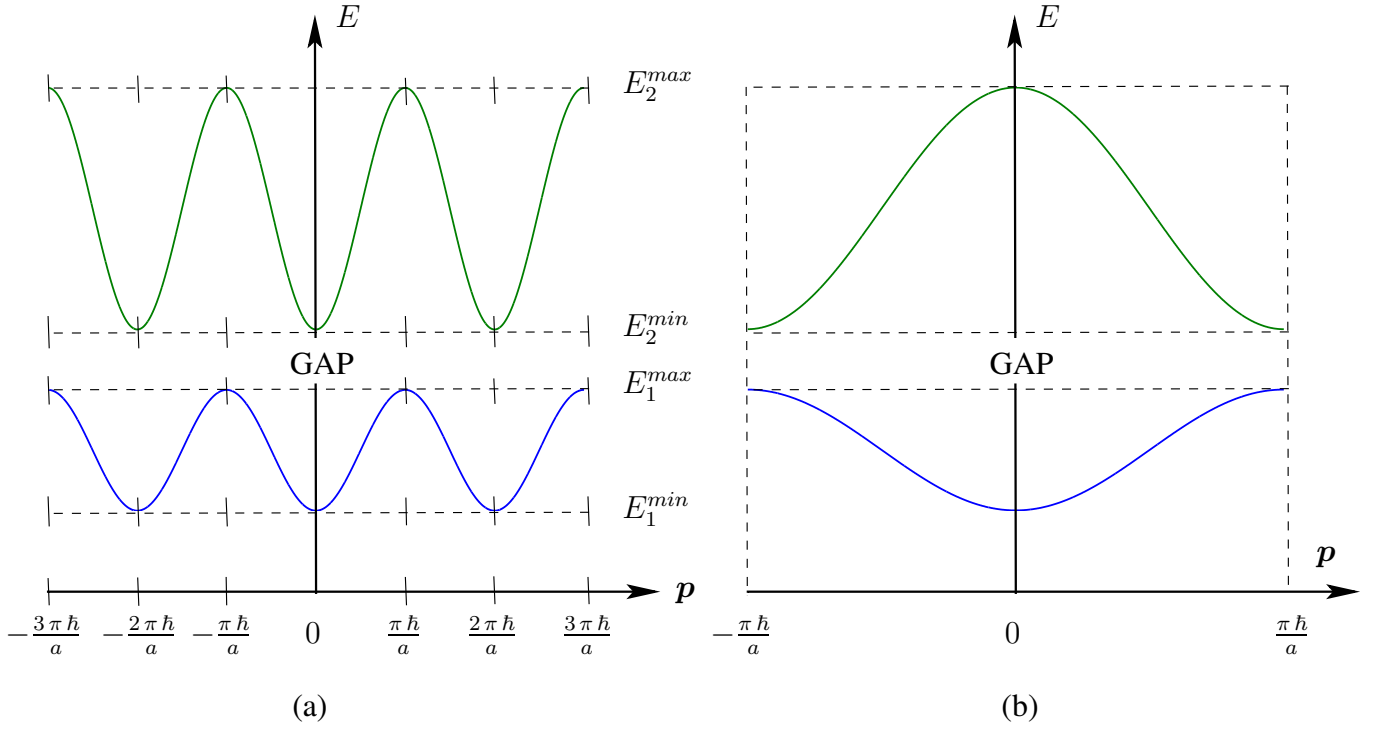


Figure 1.4: The energy of an electron in a periodic field for 1D lattice with the atomic spacing a . (a) The first two energetic zones separated by a gap. (b) Two energetic zones within the 1st Brillouin's unit cell of the length $2\pi\hbar/a$.

whereby \mathbf{a}_n is an arbitrary lattice vector. The time-independent Schrödinger equation describing the behaviour of an electron in such a field is

$$\left[\frac{\hat{\mathbf{p}}}{2m} + \Phi(\mathbf{r}) \right] \psi(\mathbf{r}) = E \psi(\mathbf{r}) \quad (1.7)$$

where $\psi(\mathbf{r})$ is the unknown wave function of electron¹⁴, $\hat{\mathbf{p}} \doteq -i\hbar\nabla$ is the operator of momentum, m is the electron mass and E is the desired electron energy. The solution of this equation is given by well-known Bloch functions, see Bloch [11]

$$\psi(\mathbf{r}) = e^{i\mathbf{p}\cdot\mathbf{r}/\hbar} u(\mathbf{r}) \quad (1.8)$$

with the periodic function $u(\mathbf{r}) = u(\mathbf{r} + \mathbf{a}_n)$ and the quasi momentum \mathbf{p} ¹⁵. Thus, the wave function of an electron in a periodic external field is similar to a planar wave describing a free particle with a periodical modulation.

The energies $E = E_l(\mathbf{p})$, $l = 1, 2, 3 \dots$ are solutions of the eigenvalue problem (1.7) and

¹⁴ $|\psi(\mathbf{r})|^2 d\mathbf{v}$ is the probability of finding the particle described by wave function $\psi(\mathbf{r})$ in the space element $d\mathbf{v}$

¹⁵Because of the periodicity of the Bloch functions, \mathbf{p} should also be periodical so that vectors \mathbf{p} and $\mathbf{p} + \hbar\mathbf{K}$ are equivalent. Here $\mathbf{K} \doteq q_i \mathbf{K}_i$ is a vector of the reciprocal lattice with the basis \mathbf{K}_i connected with the spatial basis \mathbf{a}_i by

$$\mathbf{K}_1 = \frac{2\pi\mathbf{a}_2 \times \mathbf{a}_3}{\mathbf{a}_1 \cdot [\mathbf{a}_2 \times \mathbf{a}_3]} \quad \mathbf{K}_2 = \frac{2\pi\mathbf{a}_3 \times \mathbf{a}_1}{\mathbf{a}_1 \cdot [\mathbf{a}_2 \times \mathbf{a}_3]} \quad \mathbf{K}_3 = \frac{2\pi\mathbf{a}_1 \times \mathbf{a}_2}{\mathbf{a}_1 \cdot [\mathbf{a}_2 \times \mathbf{a}_3]}$$

and q_i are integer. The quasi momentum is thereby uniquely defined in one unit cell of the reciprocal space.

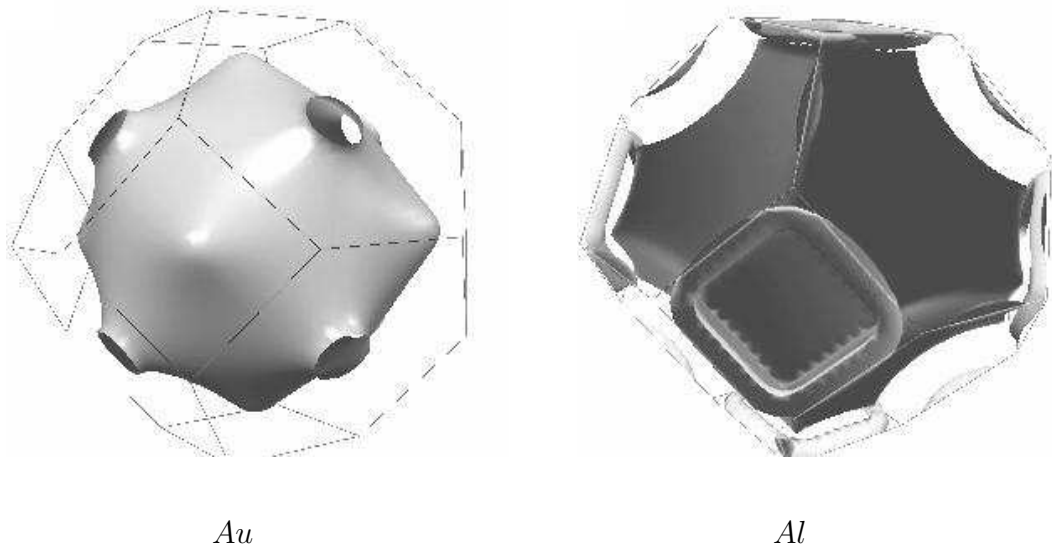


Figure 1.5: Fermi surfaces within the first Brillouin's zones for *Au* (on the left) and for *Al*.

describe the permitted energies of an electron in a periodic field. They form the so-called energetic zones possibly separated by gaps with forbidden energy values. These energies are periodic in the reciprocal space and are usually only considered within one unit cell in this space¹⁶, see fig. 1.4.

Each energetic zone contains exactly $2N$ electrons and no more due to the fact that electrons are fermions¹⁷. Here, N is the number of unit cells in a sample; the number of zones is of course unlimited. The highest energy value is called the Fermi energy. Only electrons with energy close to Fermi energy take part in conductivity and are termed as the valence electrons. The Fermi level is given by the condition $E(\mathbf{p}) = E_F$ and forms the so-called Fermi surface in the space of quasi momentum. This surface can be of a rather complicated shape. Fig. 1.5 shows two well-known examples of these surfaces for gold and aluminium.

All crystals are divided into conductors, semiconductors and insulators depending on how the Fermi energy lies relative to the edge of an energetic zone. Here, there are two possibilities:

- the Fermi energy coincides with a top edge of a zone so that some zones are filled completely while others are empty;
- the Fermi energy lies within an energetic zone called conductive zone in this case.

In the 1st case, weak applied field cannot create an electrical current because of the gap between the energetic zones. The materials with such Fermi energy are insulators and semiconductors, whereby

¹⁶The so called Brillouin's zones are usually used as unit cells of the reciprocal space corresponding to Voronoi polyhedrons in the \mathbf{r} -space. The Brillouin's zone can be constructed by the next procedure:

- connect a node of the reciprocal lattice with all its neighbours;
- construct planes which are perpendicular to each of these connections and divide them into two equal parts.

These planes form the Brillouin's unit cell. It could be shown (is well-known, see any handbook of solid state physics) that for 1D case, the length of the Brillouin's zone is $2\pi\hbar/a$ where a is the atomic spacing in 1D lattice.

¹⁷The zone occupation in metals exhibits a slight dependence on the temperature below the melting point.

the difference is of the quantitative character and depends on the gap width. So the gap of diamond is 6 to 7 eV whereas the gaps of silicon and germanium are 1.11 eV and 0.72 eV respectively. At $T = 0$, all the crystals are insulators. At room temperature, the diamond is again an insulator while silicon and germanium have some electrons in the conductivity zone.

In the 2nd case, any infinitesimally small field causes an electrical current. It is because the energy levels within an energetic zone can be continuously filled and the valence electrons can absorb any small energy portion. The crystals with a non-filled energetic zone are metals. All solids with odd electrons per unit cell such as gold, aluminium, copper, silver are classified as metals. If the energy zones are shared and the Fermi energy lies in this region, the solids with even number of electrons could be metals. Examples of such metals are lead, arsenic and bismuth.

Three Types of metallic-typical Crystal Lattices

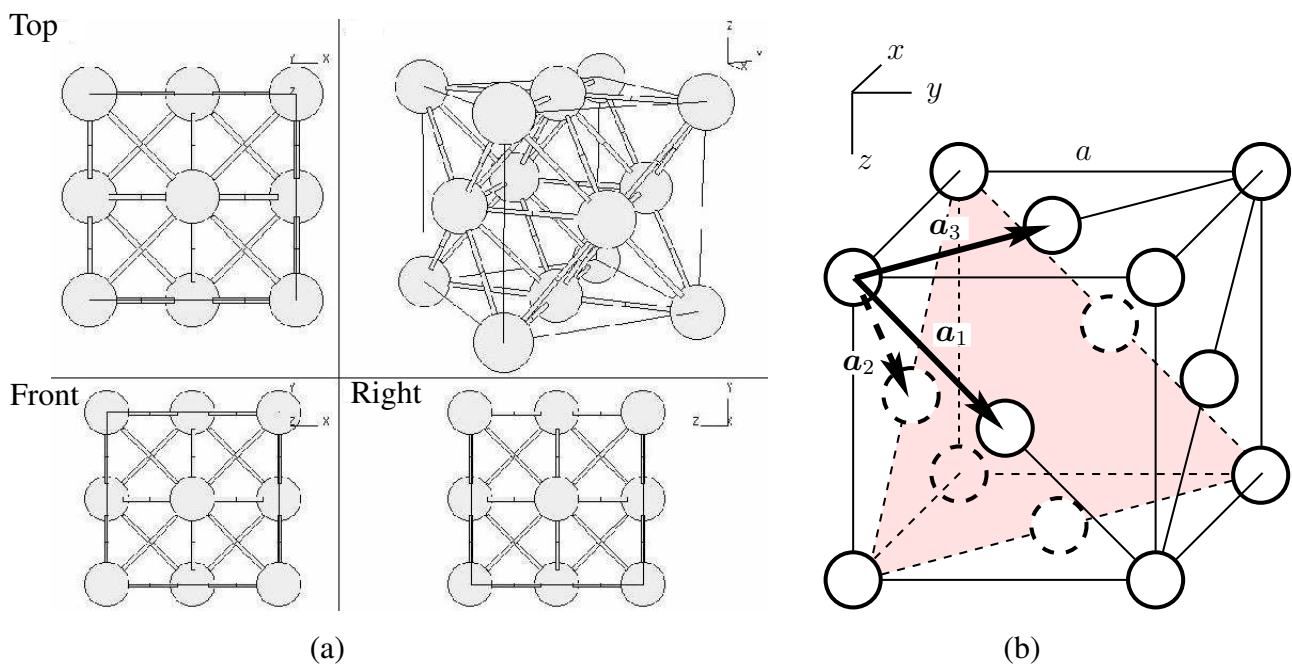


Figure 1.6: The Face-Centered Cubic (A_1) crystal structure; (a) 3D view with top, front and right projections; (b) unit cell with primitive vectors

Most metals form the copper (Cu) structure (close-packed fcc for face-centered cubic), the tungsten (W) structure (bcc for body-centered cubic) and the magnesium (Mg) structure (close-packed hexagonal).

A lot of metals such as aluminium Al , nickel Ni , gold Au , silver Ag , α -cobalt Co , lead Pb and others have the structural type of copper. Furthermore, there are intermetallic alloys with this structure e.g. Au_2Pb or Cu_2Mg . Fig. 1.6¹⁸ depicts the copper structure. The unit cell of this structure is face-centered cubic (fcc) and consists of 4 atoms. Each atom has 12 next neighbours that points at the close-packed structure. The slip system is characterized by close-packed planes $\{111\}$ and directions $\langle 110 \rangle$ in these planes. The lattice parameter is labeled here as a . The primitive vectors \mathbf{a}_1 , \mathbf{a}_2 and

¹⁸This figure and fig. 1.7 contain figures from the website of Naval Research Laboratory [65].

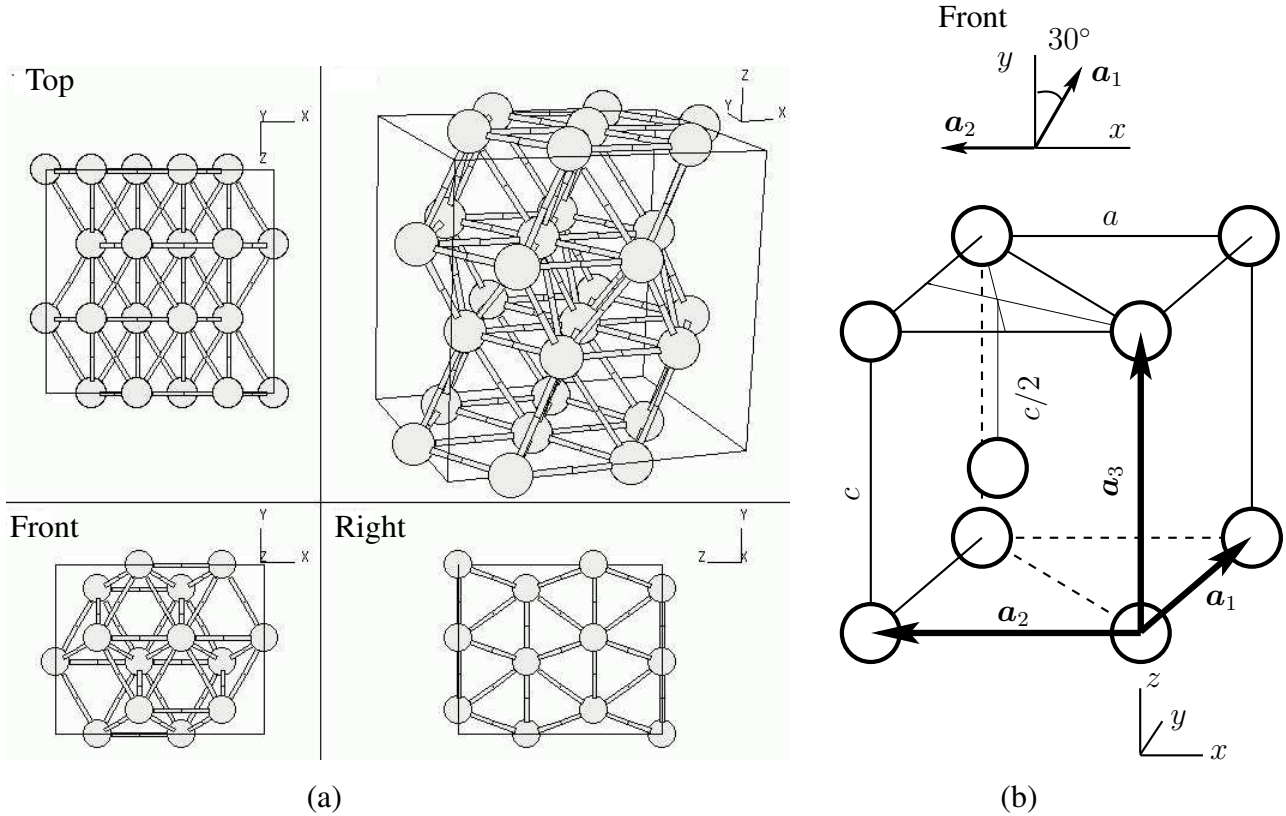


Figure 1.7: The Hexagonal Close-Packed (A_3) crystal structure; (a) 3D view with top, front and right projections; (b) unit cell with primitive vectors

\mathbf{a}_3 then depend on a in the following manner:

$$\begin{aligned} \mathbf{a}_1 &= \frac{a}{2} \mathbf{e}_y + \frac{a}{2} \mathbf{e}_z \\ \mathbf{a}_2 &= \frac{a}{2} \mathbf{e}_x + \frac{a}{2} \mathbf{e}_z \\ \mathbf{a}_3 &= \frac{a}{2} \mathbf{e}_x + \frac{a}{2} \mathbf{e}_y \end{aligned} \quad (1.9)$$

Such metals as cadmium Cd , Be , titanium Ti , cobalt Co , zinc Zn and a number of other metals as well as an intermetallic alloys such as $AgCd$, $AuCd$, $NiMo$ and so on have the magnesium-type lattice. The hexagonal close-packed (HCP) structure is shown in fig. 1.7. The unit cell of HCP is based on three translations, two of them lie in the close-packed layer and the third is perpendicular to this layer. The angle between the first two primitive vectors is 120° . The indicated primitive translations can be represented as follows:

$$\begin{aligned} \mathbf{a}_1 &= \frac{a}{2} \mathbf{e}_x + \frac{a\sqrt{3}}{2} \mathbf{e}_y \\ \mathbf{a}_2 &= -a \mathbf{e}_x \\ \mathbf{a}_3 &= c \mathbf{e}_z \end{aligned} \quad (1.10)$$

Here, a and c denote two lattice parameters. The unit cell can be divided into two trigonal prisms whereby, one of them contains an atom in its center. Such type of unit cell contains two atoms per

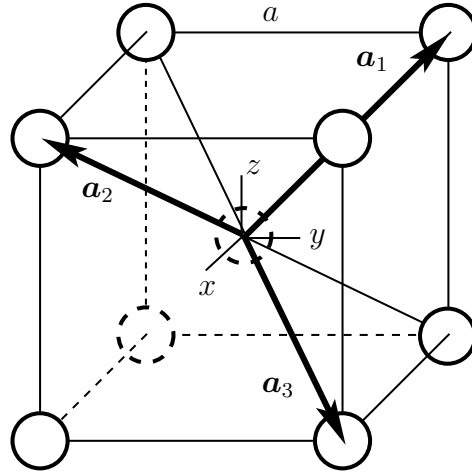


Figure 1.8: The Body-Centered Cubic (A_2) crystal structure: unit cell with primitive vectors

cell. Each atom in HCP-structured metals has 12 next neighbours: 6 in the close-packed layer, three in the upper and three in the lower layers. Plastic deformation in such crystals takes place in the planes $\{0001\}$ and in directions $\langle 11\bar{2}0 \rangle$.

The tungsten-type structure (A_2) is not related to a close-packed lattice. This type of lattice is typical for metals with a high melting point such as Cr , Wd , Mo , Nb , $\alpha - Fe$ and a number of intermetallic alloys, such as $AgZn$ and $CoAl$. Each unit cell has 2 atoms; the coordination number for tungsten-type crystals is 8. The highest packed $\{111\}$ -planes and directions $\langle 111 \rangle$ in these planes define a slip system of bcc crystals. The bcc unit cell is depicted in the fig. 1.8. The primitive vectors are

$$\begin{aligned}
 \mathbf{a}_1 &= -\frac{a}{2} \mathbf{e}_x + \frac{a}{2} \mathbf{e}_y + \frac{a}{2} \mathbf{e}_z \\
 \mathbf{a}_2 &= \frac{a}{2} \mathbf{e}_x - \frac{a}{2} \mathbf{e}_y + \frac{a}{2} \mathbf{e}_z \\
 \mathbf{a}_3 &= \frac{a}{2} \mathbf{e}_x + \frac{a}{2} \mathbf{e}_y - \frac{a}{2} \mathbf{e}_z,
 \end{aligned} \tag{1.11}$$

whereby a is again the lattice parameter.

1.2.5 Nature of Repulsion

At very small separations, the short-ranged repulsive forces arising due to the overlapping of electron hulls should be taken into account. These forces can be divided into groups related to exchange repulsion, hard core repulsion, steric repulsion and Born repulsion (for ions). There is no general equation describing the distance dependence of repulsion but the three most useful potentials are known: the hard sphere potential, the inverse power law potential and the exponential potential.

The hard sphere model mirrors the steeply rising repulsion at small separations obtained from experiments and can be successfully applied in many cases, see e.g. Israelachvili [41], chapter 7. The hard sphere repulsion is given by

$$\Phi_{rep}^{hs}(r) = + \left[\frac{\sigma}{r} \right]^n, \quad n \longrightarrow \infty \tag{1.12}$$

Two other potentials are given by (1.13) (inverse power law) and (1.14) (exponential Born-Meyer repulsion). Whereas the inverse power law has a little theoretical motivation, the exponential law describes the exchange nature of repulsion similar to covalent bonding.

$$\Phi_{rep}^{invpl}(r) = + \left[\frac{\sigma}{r} \right]^n, \quad n \in [9, 16] \quad (1.13)$$

$$\Phi_{rep}^{exp}(r) = +A e^{-\frac{r}{\sigma}} \quad (1.14)$$

with adjustable constants σ and A . These two laws are more realistic since they consider compressibility properties of atoms.

The electrostatic interaction is of both attractive and repulsive forms. The exponentially damped

Table 1.2: Types and nature of interatomic attraction and repulsion

Attraction			
Type	Coulomb	Covalent	van der Waals
Nature	Electrostatics	Exchange Interaction (1 st -order th.)	Dynamical Deformation of Electron Hull (2 nd -order th.)
$\Phi(r)$	$-1/r$	$-\exp(-r)$	$-1/r^6$
Chemical Bonding	Heteropolar	Homopolar	Dispersion Forces
Example	Ionic Crystals, e.g. <i>NaCl</i>	Semiconductors, e.g. <i>C</i> , <i>Ge</i> , <i>Si</i>	Solid Inert Gases, <i>H₂</i> , <i>HCl</i> , <i>CH₄</i> , Organic Crystals

Repulsion		
Type	Coulomb	Pauli
Nature	Electrostatics	Pauli's Exclusion Principle
$\Phi(r)$	$1/r$ or $\exp(-r)/r$ (Yukawa Potential)	$1/r^{12}$ or $\exp(-r)$

Coulomb potential with screening length σ is also known as Yukawa potential

$$\Phi_{rep}^{Yuk}(r) = + \frac{Z_1 Z_2 e^2}{r} e^{-\frac{r}{\sigma}} \quad (1.15)$$

where $Z_1 e$ and $Z_2 e$ are charges of the concerned particles. The potential (1.15) was originally introduced to describe the nuclear interaction between protons and neutrons due to pion exchange. Note that the Yukawa potential, in dependence on the sign of involved charges, can also describe a screened coulomb attraction.

A short but important remark should be made at this place. Namely, the repulsive forces are mainly responsible for melting whereas the attractive forces are mainly responsible for boiling, see e.g. Israelachvili [41], chapter 7.

Finally, the table 1.2 brings together and systemizes all statements and definitions of this section.

1.3 Modelling of Various Chemical Bonds

Now, after the nature of chemical bonds is discussed and dependence of these different bonding types on the separation is stated, the citation at the beginning of this chapter should be recalled in the reference to how the total energy of a crystal can be computed. The required microscopic energy function $E^{tot}(\mathbf{r}_i^{host}, \mathbf{r}_k^{el})$ should explicitly account for each atom i with coordinates \mathbf{r}_i^{host} in the body of interest. The 2nd group of arguments \mathbf{r}_k^{el} relates to the electronic degrees of freedom. Practically, any total energy calculation is an approximation and therefore a simplification of the full microscopic Hamiltonian opens the discussion. The simplifying approaches can be classified into three main classes, see Phillips [73]:

- the electronic degrees of freedom are completely removed (pair potential, pair functional, angular force schemes, cluster functionals):

$$E_{exact}^{tot}(\mathbf{r}_i^{host}, \mathbf{r}_k^{el}) \rightarrow E_{approx}^{tot}(\mathbf{r}_i^{host})$$

- the electronic degrees of freedom are accounted explicitly (tight-binding models):

$$E_{exact}^{tot}(\mathbf{r}_i^{host}, \mathbf{r}_k^{el}) \rightarrow E_{approx}^{tot}(\mathbf{r}_i^{host}, \mathbf{r}_k^{el})$$

- the electronic degrees of freedom are accounted implicitly in dependence of the total energy on the electron density $\rho(\mathbf{r})$ (density functional theory):

$$E_{exact}^{tot}(\mathbf{r}_i^{host}, \mathbf{r}_k^{el}) \rightarrow E_{approx}^{tot}(\mathbf{r}_i^{host}, \rho(\mathbf{r}))$$

1.3.1 The full Hamiltonian and its Series Expansion

According to Born-Oppenheimer approximation, the motion of electrons can be separated from motion of nuclei due to large difference between masses of electrons and nuclei. In terms of quantum mechanics, it means that the wave function of the total system $\Psi(\mathbf{r}_i^{host}, \mathbf{r}_k^{el})$ can be represented as a product of the electronic wave function $\psi(\mathbf{r}_n^{el}; \mathbf{r}_i^{host})$ depending on the electronic degrees of freedom and host degrees of freedom as fixed parameters and of the host wave function $\chi(\mathbf{r}_i^{host})$. Such representation of the total wave function allows the formulation of two separate Schrödinger equations for host atoms and for electrons:

$$\left[\hat{H}_{kin}^{el} + \hat{H}_{ee} + \hat{H}_{en} \right] \psi(\mathbf{r}_n^{el}; \mathbf{r}_i^{host}) = E^{el} \psi(\mathbf{r}_n^{el}; \mathbf{r}_i^{host}) \quad (1.16)$$

$$\left[\hat{H}_{kin}^{host} + \hat{H}_{nn} + E^{el} \right] \chi(\mathbf{r}_i^{host}) = E^{host} \chi(\mathbf{r}_i^{host}) \quad (1.17)$$

Here, \hat{H}_{kin}^{host} and \hat{H}_{kin}^{el} describe the host and electronic kinetic energy respectively; \hat{H}_{ee} electron-electron, \hat{H}_{nn} nucleus-nucleus and \hat{H}_{en} electron-nucleus interaction energies. Thereby, the effective Hamiltonian of the host problem involves the energy E^{el} of electronic problem.

First, only the host hamiltonian should be discussed with the label *host* being omitted in the following considerations for simplification. The host Hamiltonian \hat{H} consists of three terms, two of them

describe the potential energy of the host consisting of N atoms. These terms can be represented as a sum over many-body contributions of different orders, see e.g. Martin [53, 54, 55]:

$$\begin{aligned} \hat{H}_{nn} + E^{el} \equiv \Phi(\mathbf{r}_1, \dots, \mathbf{r}_N) = & \Phi_0 + \sum_{i=1}^N \Phi_1(\mathbf{r}_i) + \frac{1}{2!} \sum_{i=1}^N \sum_{j=1}^N \Phi_2(\mathbf{r}_i, \mathbf{r}_j) + \dots \\ & + \frac{1}{N!} \sum_{i=1}^N \sum_{j=1}^N \dots \sum_{n=1}^N \Phi_N(\mathbf{r}_i, \mathbf{r}_j \dots \mathbf{r}_n) \end{aligned} \quad (1.18)$$

Here, the summation is so organised that all indices take different values. The terms Φ_0 and Φ_1 lie out of interest. The 1st of the two reflects the choice of the zero level of energy and can be set to zero; the 2nd term is the mentioned above E^{el} and represents the potential energy of external field. Other terms such as Φ_2 , Φ_3 etc. describe the two-particle, three-particle, etc. interactions and should be discussed here. An important property of the many-body Hamiltonian is the invariance under interchange of any two particles. Furthermore, the Hamiltonian (1.18) is invariant under arbitrary translations and rotations resulting in the reduction of the number of independent variables in Φ from $3N$ to $3N - 3$ due to translation invariance. The rotation invariance reduces the number of variables again by three for $N > 2$ and by two for $N = 2$, see Martin [53, 54, 55]. Apart from Φ_2 , which depends on only one independent variable - separation between two particles, each further term has $3N - 6$ variables. Thus, Φ_3 depends on 3 and Φ_4 depends on 6 variables.

For non-directed bonds, it is sufficient to consider the only pairwise interactions whereas all higher-order interactions can be neglected. The pairwise interactions are described by so-called pair potentials discussed below.

1.3.2 Pair Potentials

To consider that time unknown intermolecular forces, the Dutch physicist J. D. van der Waals wrote his famous state equation of gases and liquids in 1873

$$(P + a/V^2)(V - b) = RT,$$

whereby the term a/V^2 describes the influence of these forces, which nowadays are known as van der Waals forces. In 1903, **Mie** proposed a semiempirical interaction pair potential in the following format:

$$\Phi(r) = -\frac{A}{r^n} + \frac{B}{r^m} \quad (1.19)$$

This potential was a first one including both a repulsive and an attractive part. The celebrated **Lennard-Jones**¹⁹ potential is a particular case of Mie potential with $n = 6$ and $m = 12$:

$$\Phi^{LJ}(r) = 4\varepsilon \left[\left[\frac{\sigma}{r} \right]^{12} - \left[\frac{\sigma}{r} \right]^6 \right] \quad (1.20)$$

whereby parameters σ and ε are explained in fig. 1.10²⁰. To describe the covalent bond, the **Morse**

¹⁹see Lennard-Jones [51]

²⁰The spring constant of the harmonic potential has the following connection to the parameters ε and σ of the Lennard-Jones potential:

$$c = \frac{24\varepsilon}{\sigma^2} \left[26 \cdot 2^{-14/6} - 7 \cdot 2^{-8/6} \right]$$



Figure 1.9: Left: Johannes D. van der Waals (1837 - 1923); right: Sir John Edward Lennard-Jones (1894 - 1954)

pair potential was proposed in 1929, see Morse [62]. This potential consists of the exponential repulsion and attraction:

$$\Phi^{Morse}(r) = \varepsilon \left[e^{2\alpha(1-\frac{r}{r_0})} - 2e^{\alpha(1-\frac{r}{r_0})} \right] \quad (1.21)$$

with parameters ε , r_0 and α . The behaviour of Morse potential is depicted in fig. 1.10. An adjustable parameter α determines the range of the interparticle forces. If α decreases, the range of the attractive part of the potential increases and softens the repulsive wall. The LJ potential has the same curvature at the bottom of the well as the Morse potential when $\alpha = 6$. The Morse potential has softer repulsion than the Lennard-Jones potential. Note that covalent bond is strongly oriented and a description of radial stretching is not sufficient to describe this bond.

A further Lennard-Jones-like pair potential is the **Buckingham potential**

$$\Phi^{Buck}(r) = A e^{\alpha(1-\frac{r}{r_0})} - \frac{B}{r^6} \quad (1.22)$$

consisting of more physical exponential Born-Meyer repulsion and the van der Waals attraction, see fig 1.11 (a). Unfortunately, the exponent becomes smaller than the inverse power law at very short ranges and the potential drops rapidly to minus infinity (so called Buckingham catastrophe), see fig. 1.11 (b). At these separations, the potential becomes unphysical. To bring the Buckingham and the Lennard-Jones potentials to a common equilibrium distance r_0 and to a common well depth ε , the following connection between the Lennard-Jones parameters ε and σ and the Buckingham parameters A , B and α have been derived:

$$A = \frac{1}{2} - \varepsilon, \quad B = \sigma^6, \quad \alpha = \frac{3}{\frac{1}{2} - \varepsilon} \quad (1.23)$$

All the pair potentials neglect the electronic contribution to the total energy and are related to the 1st class of simplifying procedures characterised by

$$E_{exact}^{tot}(\mathbf{r}_i^{host}, \mathbf{r}_k^{el}) \rightarrow E_{approx}^{tot}(\mathbf{r}_i^{host})$$

As shown e.g. by Phillips [73], a quantum mechanical 2nd-order perturbation theory yields a total energy correction which can be represented in the form of pair potentials depending on the coordinates

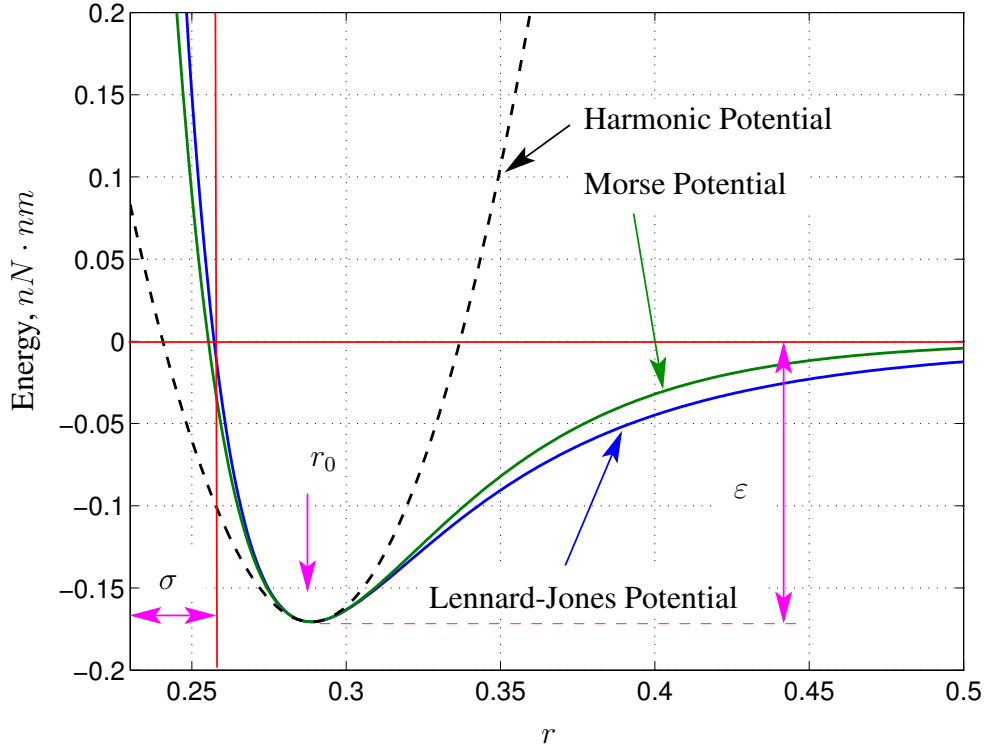


Figure 1.10: Lennard-Lones (LJ) pair potential compared with the Morse (M) potential and a harmonic potential $c \frac{(r - r_0)^2}{2} - \varepsilon$ (dashed line). Common parameters of LJ and M potentials are ε i.e. the pair well depth and the equilibrium separation $r_0 = \sigma 2^{1/6}$, which results from the condition $d\Phi^{LJ}(r)/dr = 0$. The 2nd parameter of LJ potential σ is the separation, at which the interaction energy vanishes. For this example, the values $\sigma = 0.257$ and $\varepsilon = 0.171$ are used. The 3rd parameter of M potential α is equal to 6 in this example so that M potential has the same curvature at the bottom of the well as LJ potential.

\mathbf{r}_i^{host} of the host atoms. The calculation is based on the simple model of metal: a box containing electrons and positive charged ions. The weak periodic field caused by the ionic host is viewed as a perturbation of the gas of free electrons. Thereby, the 2nd-order correction of the total energy is given by

$$\Delta E^{tot} = \frac{1}{2} \sum_{i,j} \Phi^{eff}(|\mathbf{r}_i - \mathbf{r}_j|) \quad (1.24)$$

with an effective pair potential Φ^{eff} , which is a complicated integral expression depending on the pseudopotential characterising the interaction of the valent electrons with the nuclei. By such a simplifying approach, the dependence of the calculated total energy on the electronic degrees of freedom is implicitly accounted in the form of a dependence on the mean electron density $\bar{\rho}$:

$$E_{exact}^{tot}(\mathbf{r}_i^{host}, \mathbf{r}_k^{el}) \rightarrow E_{approx}^{tot}(\mathbf{r}_i^{host}, \bar{\rho})$$

Reduction of the total energy in the modelling of metals by taking into account of only pairwise interactions leads to the following discrepancies between theory and experiment:

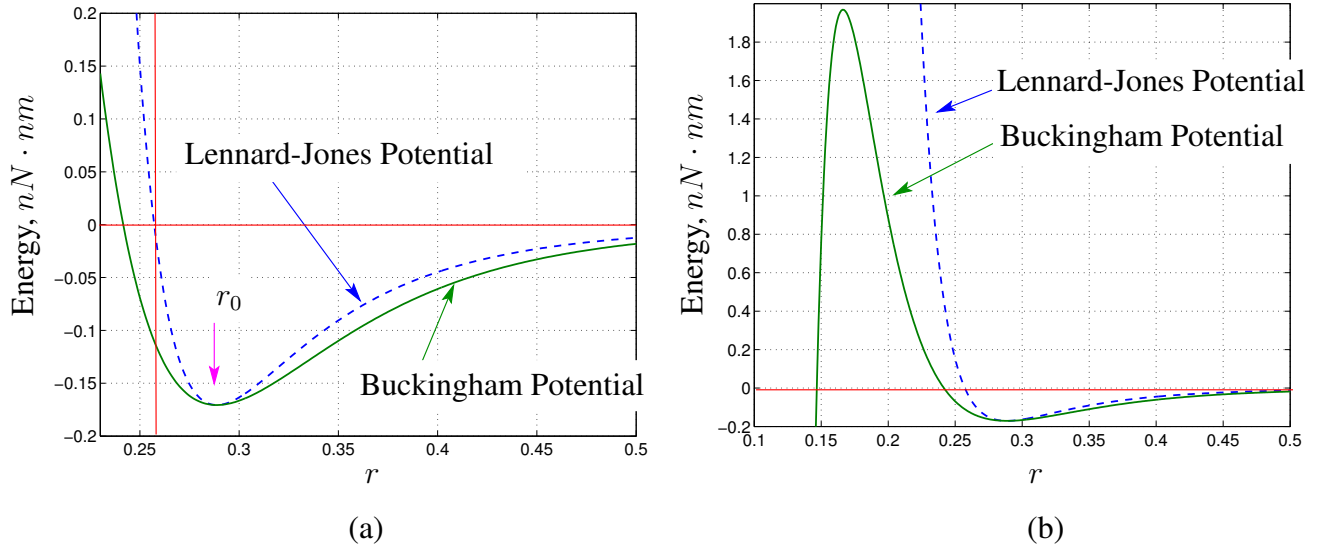


Figure 1.11: (a) The Buckingham and the Lennard-Jones potentials (dashed line). (b) The Buckingham catastrophe: the Buckingham potential drops rapidly to minus infinity at short separations

- the bond strength is independent of the environment i.e. on the number of the next neighbours of an atom;
- the computation of elastic modules using pair-potential-based total energy yields the classical Cauchy relation $C_{12} = C_{44}$ which is not valid in the general case;
- the formation energy of vacancies is always overestimated by pair potentials;
- the prediction of the inward relaxation of the outer layer of atoms at a metal surface yields incorrect results ²¹

These failures of pair potentials have led to the development of such potentials where the local environment of an atom is incorporated into the potential through many-body effects to produce a more faithful description of the interatomic interactions.

1.3.3 Many-Body Potentials for Modelling of Covalent Bonds

To describe a material with a low coordination number and strong directed bonds (predominantly the silicon Si), the **Stillinger-Weber (SW) potential** has been developed, see Stillinger and Weber [83]. This potential is based on a two-body and a three-body term:

$$E^{tot} = \frac{1}{2} \sum_{i,j} \Phi_2(|\mathbf{r}_i - \mathbf{r}_j|) + \frac{1}{3!} \sum_{i,j,k} \Phi_3(\mathbf{r}_i, \mathbf{r}_j, \mathbf{r}_k) \quad (1.25)$$

²¹The ratio of the vacancy energy, E_{vac} , which is the energy needed to remove an atom from the bulk and place it on the surface, to the cohesive energy, E_{coh} , which is the energy of an atom in the bulk, is always overestimated by a pair potential as it does not account for the effect of the local coordination environment at the vacancy on the bonding (for a pair potential $E_{vac} \equiv E_{coh}$).

The two-body term is discussed in the previous section. The three-body term provides the dependence of the total energy not only on the atomic separation but also on the bond angle, which has an equilibrium value minimizing the total energy. Consequently, for the SW potential, the angular term has the form

$$\Phi_3(\mathbf{r}_i, \mathbf{r}_j, \mathbf{r}_k) = h(r_{ij}, r_{ik}, \theta_{jik}) + h(r_{ji}, r_{jk}, \theta_{ijk}) + h(r_{ki}, r_{kj}, \theta_{ikj}) \quad (1.26)$$

$$\text{with } h(r_{ij}, r_{ik}, \theta_{ijk}) = \lambda e^{\gamma/(r_{ij}-a)} e^{\gamma/(r_{ik}-a)} \left[\cos \theta_{ijk} + \frac{1}{3} \right]^2 \quad (1.27)$$

Here $r_{ij} \doteq |\mathbf{r}_i - \mathbf{r}_j|$, θ_{jik} is the angle formed by the ij bond and the ik bond, λ and γ are parameters. Thus, the angular term is minimized for $\theta \approx 109.47^\circ$ corresponding to the tetrahedral bonding angle of the diamond structure. This potential gives a rather realistic description of crystalline silicon. However, it cannot predict the correct energies of the non-tetrahedral structures. Such potentials using only geometrical features such as distances and bond angles as variables are also called force fields and are successfully applied for prediction of structural and dynamical properties of organic systems.

A further celebrated potential, which should be mentioned in this section is the **Tersoff potential**, which is based on the assumption that the strength of a bond between two atoms is not constant, but depends on the local environment, see Tersoff [90]. The total energy in this case looks like the pair potential:

$$E^{tot} = \frac{1}{2} \sum_{i,j} [\Phi^r(r_{ij}) + b_{ij} \Phi^a(r_{ij})], \quad (1.28)$$

where Φ^a and Φ^r are the repulsive and attractive potentials of the form $A_r e^{-\lambda_r r_{ij}}$ and $A_a e^{-\lambda_a r_{ij}}$ respectively. The coefficients b_{ij} are not constant and involve both the angular and environmental dependence of the energy:

$$b_{ij} = \left[1 + \beta^n \left[\sum_{k \neq i,j} f_c(r_{ik}) g(\theta_{ijk}) \right]^n \right]^{(-1/2n)} \quad (1.29)$$

Here, $f_c(r)$ is a cut-off function vanishing at distances close to the interaction or cut-off radius r_c and $g(\theta)$ has the form

$$g(\theta) = 1 + \frac{c^2}{d^2} - \frac{c^2}{d^2 + (h - \cos \theta)^2} \quad (1.30)$$

On the one hand, the bond ij is weakened by the presence of other bonds ik involving atom i . On the other hand, to create a realistic model, the angular terms are introduced. This potential has a broader application field as the SW potential, but the main user problem is caused by number of functions which should be fitted.

Besides these two potentials, the **Modified Embedded Atom Method (MEAM)** should be called among advanced potentials providing realistic description of directed bonds. This potential is discussed in the following section.

The table 1.3 summarises discussed potentials.

Table 1.3: Energetic Potentials for Modelling of Chemical Bonds

Pair Potentials		
Name	Usage	Analytical Expression, $\Phi_2(r)$
Lennard-Jones	van der Waals interaction	$4\varepsilon \left[\left[\frac{\sigma}{r} \right]^{12} - \left[\frac{\sigma}{r} \right]^6 \right]$
Buckingham	van der Waals interaction	$A e^{\alpha \left(1 - \frac{r}{r_0}\right)} - \frac{B}{r^6}$
Morse	Covalent interaction, bond stretch	$\varepsilon \left[e^{2\alpha \left(1 - \frac{r}{r_0}\right)} - 2 e^{\alpha \left(1 - \frac{r}{r_0}\right)} \right]$
Many-Body Potentials		
Name	Usage	Analytical Expression
Stillinger-Weber	Covalent interaction	$\Phi_3(\mathbf{r}_i, \mathbf{r}_j, \mathbf{r}_k) = h(r_{ij}, r_{ik}, \theta_{jik}) + h(r_{ji}, r_{jk}, \theta_{ijk}) + h(r_{ki}, r_{kj}, \theta_{ikj})$ $h(r_{ij}, r_{ik}, \theta_{ijk}) = \lambda e^{\gamma/(r_{ij} - a)} e^{\gamma/(r_{ik} - a)} \left[\cos \theta_{ijk} + \frac{1}{3} \right]^2$
Tersoff	Covalent interaction	$\frac{1}{2} \sum_{i,j} [\Phi^r(r_{ij}) + b_{ij} \Phi^a(r_{ij})],$ $b_{ij} = \left[1 + \beta^n \left[\sum_{k \neq i,j} f_c(r_{ik}) g(\theta_{ijk}) \right]^n \right]^{(-1/2n)}$

1.3.4 Many-Body Potentials for Modelling of Metals

A number of approaches for realistic description of solids based on the so called first-principles or quantum mechanical calculations has been developed in recent decades. These methods account for the environmental dependence of the bond strength. **Effective medium theory** [42], **Finnis-Sinclair potential** [29], **glue models** [25] and **embedded atom method (EAM)** [8] are known among others. In this work, only the EAM has been applied and should therefore be overviewed in detail.

The EAM belongs to the so-called pair functionals and represents the 3rd class of simplifying ap-

proaches where, as mentioned above

$$E_{exact}^{tot}(\mathbf{r}_i^{host}, \mathbf{r}_k^{el}) \rightarrow E_{approx}^{tot}(\mathbf{r}_i^{host}, \rho(\mathbf{r}));$$

Milestones of (M)EAM

The EAM is based on the earlier works of Hohenberg and Kohn [39] and Stott and Zaremba [84]. It is dealt in [39] with a ground state of an interacting electron gas in an external field. Thereby, the existence of a universal functional of the electronic density, which is independent of this external field is proven, the general form of such functional is proposed and an explicit format is given for two simple cases.

Based upon the Hohenberg-Kohn theorem, the energy of an atom embedded in a non-homogeneous host electronic system has been treated in [84]. Thereby, the concept of so called **quasiatom** i.e. an electrical neutral system consisting of the impurity ion together with the screening electron cloud has been introduced. The difference between the energy of a free ion and the energy of the ion embedded in the electronic system has been then defined as the embedding energy.

The concept of the EAM appears explicitly for the first time in [7] in connection with an investigation of brittle fractures in transition metal (Ni) in a presence of hydrogen. The idea of the quasiatom has been generalised so that each atom in a solid was considered as an impurity embedded in the host consisting of all other atoms. Thereby, the total energy of a crystal is given by a sum over all atomic contributions:

$$E^{tot} = \sum_i E_i = \sum_i \left[F_i(\rho_i) + \frac{1}{2} \sum_{j \neq i} \Phi(r_{ij}) \right] \quad (1.31)$$

Here, the energy functional F_i is the embedding energy of Atom i in terms of [84]; r_{ij} is the distance between atoms i and j and $\Phi(r_{ij})$ is a pair potential describing possibly screened electrostatic interaction of the host atoms. It was obtained that the atomic contribution $E_i = E_i(r_{i1}, r_{i2}, \dots)$ depends only on separations between the atom i and all other atoms.

In this original paper, the embedding function F_{Ni} and the pair potential Φ_{Ni-Ni} as well as other needed functionals and pair potentials have been obtained by fitting to some experimental data for Ni such as the lattice constant, the elastic modules and the sublimation energy. The explicit format of F_H has been taken over by the work of Puska et al. [75]. The newly proposed in [7] method has been systematically represented in [8] by the same authors.

Consequently, the embedding functions and the pair potentials for a variety of *fcc*-metals such as *Cu*, *Ag*, *Au*, *Ni*, *Pd*, *Pt* and their alloys have been explicitly obtained in the following work [31]. Unfortunately, the attempt to describe the shear behaviour of the covalent crystals such as *Si* by using the bond-angular-independent EAM potential led to a conflict with an experimental data related to elastic constants. In particular, it has been obtained that

- $C_{11} = C_{12}$ whereas this is not valid for *Si*;
- $C_{12} - C_{44} > 0$ whereas it should be negative.

The first discrepancy can be eliminated by involving more than only the next neighbours of an atom into its interaction sphere. The second one is related to the bond orientation and has been overcome by introduction of the angular-dependent electron density. This revised approach is known as modified

embedded atom method (MEAM), see Baskes [4], Baskes et al. [10], Baskes [5]. This last work is of a special importance since it summarises the theory and contains parameters for 26 elements: ten fcc, ten bcc, three diamond cubic, three gases. However, this extension is of an empirical character and cannot be captured within any theory. The MEAM for hcp metals appeared two years later, see Baskes and Jonson [9]

The MEAM has been developed under consideration that only the first next neighbours of an atom should be accounted. This proposition requires an introduction of a cut-off or screening function which changes the behaviour of the potential as well as its derivatives (at least the 1st one) so that they become smoothly zero at the predefined cut-off radius and the unphysical forces due to the cut-off procedure do not appear. Such screening functions have been firstly introduced in [5], but as shown in the more recent publication of Baskes [6], it leads to infinite forces. A new suitable screening function has been introduced in this recent paper. Moreover, a new functional dependence of the electron density on the angular terms has been proposed in this work. Thus, [5] should be used as a source of the MEAM potential for implementation, whereby all needed material parameters are listed there.

Further modification of the MEAM is related to the failure of this approach in some applications to bcc metals. This failure is connected only with the above mentioned consideration of the 1st next neighbours. The MEAM enhanced by taking the 2nd nearest neighbours into account has been developed for *Fe* by Lee and Baskes [49] and extended for a number of other bcc metals by Lee et al. [50]. A discussion of this enhancement lies outside this work.

Current Formulation of (M)EAM

To finish the overview of (M)EAM, the explicit format of the discussed potential should be given. The full expression for MEAM potential involving the possibility to consider a system with a different types of atoms is rather complicated and it seems to be purposeful to refer the reader to the works [5] and [6] mentioned above, in which this potential is given. In the present work, the only atomic-separation-dependent EAM potential for a monoatomic system of fcc type has been used and therefore, only this simplified (but complicated enough!) case should be represented here.

Thus, the contribution E_i of atom i to the total energy (1.31) has a format, see [5]

$$E_i = \frac{1}{Z} \sum_{\substack{j=1 \\ j \neq i}}^Z E^u(r_{ij}) + \left[F\left(\frac{\rho}{Z}\right) - \frac{1}{Z} \sum_{\substack{j=1 \\ j \neq i}}^Z F\left(\frac{\rho^0(r_{ij})}{Z}\right) \right] \quad (1.32)$$

Here E^u is the energy of an atom in the reference structure and is given by a universal energy function

$$E^u(r) = -\varepsilon \left(1 + \alpha \left[\frac{r}{r_0} - 1 \right] \right) e^{-\alpha \left[\frac{r}{r_0} - 1 \right]} \quad (1.33)$$

The embedding function F is the energy needed to embed an atom into the background electron density ρ at site of this atom and is a simple function of the electron density ρ :

$$F(\rho) = A \varepsilon \rho \ln \rho \quad (1.34)$$

ρ is the background electron density actually seen at the atom i and is an additive value consisting of the contributions of the atomic electron densities, see Herman and Skillman [37]:

$$\rho = \sum_{j \neq i} \rho^{(0)}(r_{ij}) \quad (1.35)$$

ρ^0 (do not confuse ρ^0 with $\rho^{(0)}$!) is the background electron density of the atom i in the reference structure:

$$\rho^0 = Z \rho^{(0)}, \quad (1.36)$$

whereby the spherical-averaged electron density $\rho^{(0)}$ of an atom decays exponentially with the inter-atomic separation:

$$\rho^{(0)} = e^{-\beta^{(0)} \left[\frac{r}{r_0} - 1 \right]} \quad (1.37)$$

The following parameters have been introduced here: the sublimation energy ε ; the equilibrium nearest-neighbour distance r_0 ; the number of nearest neighbours Z ; the exponential decay factor for the universal energy function α ; the scaling factor for the embedding energy A ; the exponential decay factor for the atomic densities $\beta^{(0)}$. By substituting (1.33)-(1.37) into (1.32), an explicit form of the EAM potential as a function of atomic separations can be obtained:

$$\begin{aligned} E_i = & -\frac{\varepsilon}{Z} \sum_{\substack{j=1 \\ j \neq i}}^Z \left(1 + \alpha \left[\frac{r_{ij}}{r_0} - 1 \right] \right) e^{-\alpha \left[\frac{r_{ij}}{r_0} - 1 \right]} \\ & + A \varepsilon \left[\left(\sum_{\substack{m=1 \\ m \neq i}}^Z e^{-\beta^{(0)} \left[\frac{r_{im}}{r_0} - 1 \right]} / Z \right) \ln \left(\sum_{\substack{k=1 \\ k \neq i}}^Z e^{-\beta^{(0)} \left[\frac{r_{ik}}{r_0} - 1 \right]} / Z \right) \right. \\ & \left. + \frac{1}{Z} \sum_{\substack{j=1 \\ j \neq i}}^Z \beta^{(0)} \left[\frac{r_{ij}}{r_0} - 1 \right] e^{-\beta^{(0)} \left[\frac{r_{ij}}{r_0} - 1 \right]} \right] \end{aligned} \quad (1.38)$$

Remark 1.1. In [49], another definition of the embedding function has been used:

$$F(\rho) = A \varepsilon (\rho/\rho^0) \ln (\rho/\rho^0)$$

It means that the electron density has been scaled other than in [5]. Note that $\rho^0 = Z \rho^{(0)}(r_0) = Z$ for fcc or bcc structures. Thus, the change of scaling is irrelevant to monoatomic fcc structure being treated in this work.

To obtain the shape of EAM potential, consider only two interacting atoms of the same type. In this case, (1.38) results in

$$\Phi^{EAM}(r) = -\varepsilon \left[1 + \alpha \left[\frac{r}{r_0} - 1 \right] \right] e^{-\alpha \left[\frac{r}{r_0} - 1 \right]} \quad (1.39)$$

where ε is a sublimation energy, r_0 is an equilibrium separation and α is an exponential decay factor. Fig. 1.12 shows the behaviour of this function together with its 1st derivative

$$(\Phi^{EAM}(r))' = \frac{\varepsilon \alpha^2}{r_0} \left[\frac{r}{r_0} - 1 \right] e^{-\alpha \left[\frac{r}{r_0} - 1 \right]} \quad (1.40)$$

Here, the following parameters of *Al* are used: $\varepsilon = 3.58\text{eV}$, $r_0 = 2.86 \text{ \AA}$, $\alpha = 4.61$.

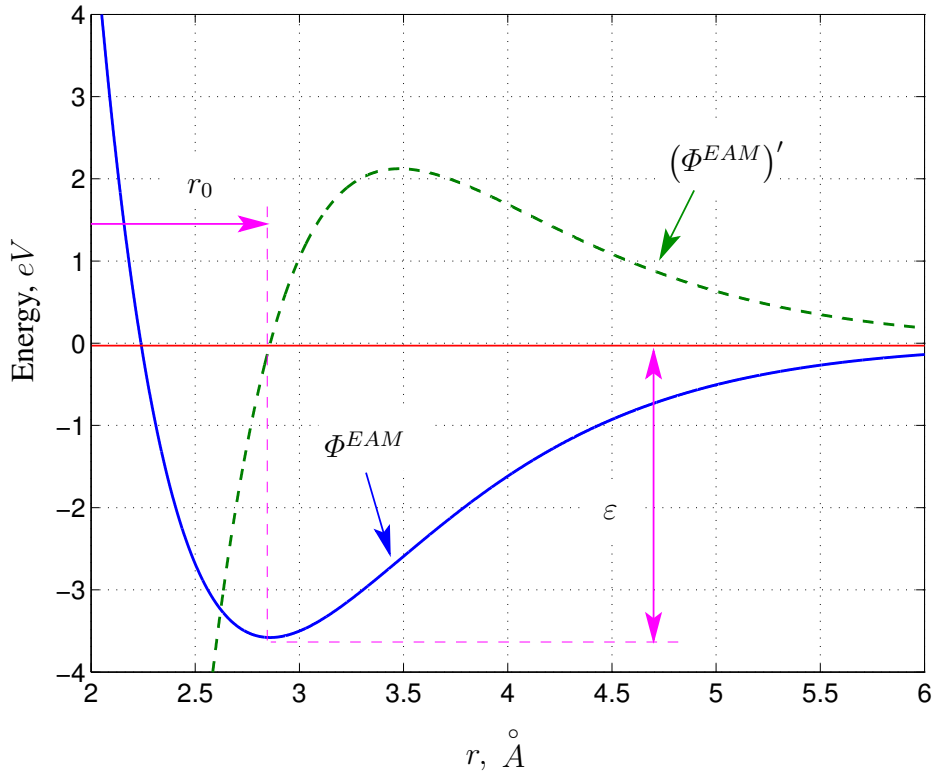


Figure 1.12: The EAM potential for two interacting atoms of the same type and its 1st derivative. Here, the parameters of *Al* $\varepsilon = 3.58\text{eV}$, $r_0 = 2.86 \text{ \AA}$, $\alpha = 4.61$ are used.

Chapter 2

Continuum-Atomistic Constitutive Modelling

“One of the key questions ... is how best to reconcile microscopic descriptions, which are presumed to represent the true mechanistic underpinnings of a given process, and phenomenological descriptions, whose aim is to capture the essential physics of a particular process, and to use this reduced description as a predictive tool.”

Rob Phillips, “Crystals, Defects and Microstructures”

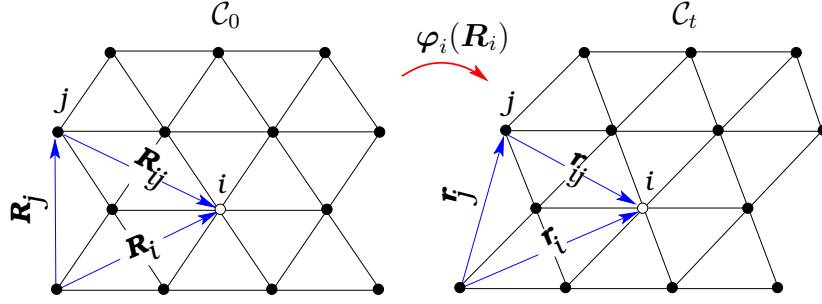
2.1 Atomistic Constitutive Modelling

To set the stage and to introduce several definitions, we start with a short review of the direct atomistic approach, whereby we restrict ourselves to classical lattice statics. For an overview on different approaches towards nanomechanics, we refer to Ortiz and Phillips [70]. We consider a crystallite body consisting of N interacting atoms. The kinematics are then typically represented by the distance vectors between two atoms labeled i and j , i.e. \mathbf{R}_{ij} and \mathbf{r}_{ij} in the material and spatial configuration, respectively

$$\mathbf{R}_{ij} = \mathbf{R}_i - \mathbf{R}_j \quad \mathbf{r}_{ij} = \mathbf{r}_i - \mathbf{r}_j \quad \text{with } r_{ij} = |\mathbf{r}_{ij}| \quad (2.1)$$

The position vectors \mathbf{R}_i and \mathbf{r}_i in both configurations are connected by the non-linear discrete map $\varphi_i(\mathbf{R}_i)$, see fig. 2.1. Assume that the total internal energy E^{int} of the crystal lattice can be represented as a sum over all atomic contributions as in (1.31).

$$E^{int} = \sum_i E_i \quad (2.2)$$

Figure 2.1: Material C_0 and spatial C_t crystal lattice configuration

whereby, in general, E_i depends on the coordinates of all N atoms in the lattice:

$$E_i = E_i(r_{i1}, r_{i2}, \dots, r_{iN}).$$

The derivative of the total internal energy E^{int} with respect to the position vector \mathbf{r}_i of the i -th atom then yields the force \mathbf{f}_i acting on this particular atom due to the interactions with all other atoms

$$\mathbf{f}_i = -E_{,\mathbf{r}_i}^{int} = \sum_{j \neq i} \mathbf{f}_{ij} \quad \text{with} \quad \mathbf{f}_{ij} = -\frac{E_{i,r_{ij}} + E_{j,r_{ji}}}{r_{ij}} \mathbf{r}_{ij}. \quad (2.3)$$

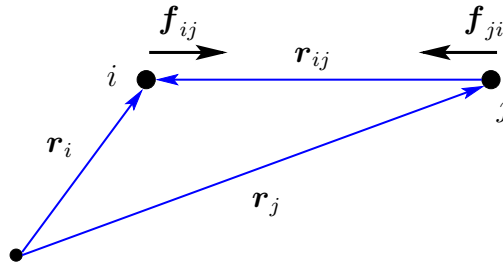
If the pair potentials $\Phi(r)$ are applied for the description of the interatomic interaction, the atomic contribution E_i has a format

$$E_i = \frac{1}{2} \sum_{j \neq i} \Phi(r_{ij}) \equiv \frac{1}{2} \sum_{j \neq i} \Phi_{ij} \quad (2.4)$$

The force \mathbf{f}_{ij} then has an explicit dependence on the pair potentials:

$$\mathbf{f}_{ij} = -\frac{\Phi'_{ij}}{r_{ij}} \mathbf{r}_{ij} \quad (2.5)$$

whereby the comma denotes partial differentiation and the prime $(\bullet)'$ denotes the derivative of (\bullet) with respect to r_{ij} , see e.g [1], eq. (5.2). Consequently, \mathbf{f}_{ij} represents the force acting on the atom i due to atom j , see fig. 2.2. This relation represents the underlying constitutive law of classical lattice

Figure 2.2: Definitions of the distance vectors \mathbf{r}_{ij} and the interaction force \mathbf{f}_{ij}

statics based on only pairwise interactions. Please note that here the summation convention is not

adopted to quantities related to atomistics. The principle of the minimum of the total potential energy representing the global equilibrium results locally in the equilibrium at each atom

$$E^{tot} = E^{int} + E^{ext} \longrightarrow \min_{\mathbf{r}_i} \iff \sum_{j \neq i} \mathbf{f}_{ij} + \mathbf{f}_i^{ext} \doteq \mathbf{0} \quad (2.6)$$

with the external force \mathbf{f}_i^{ext} acting on the atom i . Within an iterative solution strategy, the second derivative of the total energy E^{tot} with respect to \mathbf{r}_j is needed. This results in the atomic level stiffness \mathbf{k}_{ij} . If the atomic contribution E_i is again a function of the coordinates of all atoms, \mathbf{k}_{ij} takes the format

$$\mathbf{k}_{ij} \doteq -E_{,\mathbf{r}_i \mathbf{r}_j}^{int} = \mathbf{k}_{ij}^{(0)} + \sum_{\substack{m \neq i \\ m \neq j}} \mathbf{k}_{ij}^{(m)}, \quad i \neq j \quad (2.7)$$

with the following notions:

$$\mathbf{k}_{ij}^{(0)} \doteq \frac{E_{i,r_{ij}} + E_{j,r_{ji}}}{r_{ij}} \mathbf{I} + \left[\frac{E_{i,r_{ij}r_{ij}} + E_{j,r_{ji}r_{ji}}}{r_{ij}^2} - \frac{E_{i,r_{ij}} + E_{j,r_{ji}}}{r_{ij}^3} \right] \mathbf{r}_{ij} \otimes \mathbf{r}_{ij} \quad (2.8)$$

and

$$\mathbf{k}_{ij}^{(m)} \doteq \frac{E_{i,r_{ij}r_{im}} + E_{j,r_{ji}r_{mi}}}{r_{im}r_{ij}} \mathbf{r}_{ij} \otimes \mathbf{r}_{im}. \quad (2.9)$$

Here, $E_{i,r_{ij}r_{im}}$ denotes the 2nd derivative of E_i with respect to r_{ij} and r_{im} :

$$E_{i,r_{ij}r_{im}} \doteq \frac{\partial^2 E_i}{\partial r_{ij} \partial r_{im}} = \frac{\partial E_{i,r_{ij}}}{\partial r_{im}}.$$

It is remarkable that the diagonal elements \mathbf{k}_{ii} of the total atomic level stiffness tensor can be represented as a sum over the corresponding off-diagonal elements \mathbf{k}_{ij}

$$\mathbf{k}_{ii} = -E_{,\mathbf{r}_i \mathbf{r}_i}^{int} = - \sum_{j \neq i} \mathbf{k}_{ij}. \quad (2.10)$$

In the case of pair potentials, E_i takes the format (2.4) and $E_{i,r_{ij}r_{im}} = 0$ for each m so that all $\mathbf{k}_{ij}^{(m)}$ vanish and the atomic level stiffness can be rewritten as

$$\mathbf{k}_{ij} = \frac{\Phi'_{ij}}{r_{ij}} \mathbf{I} + \left[\frac{\Phi''_{ij}}{r_{ij}^2} - \frac{\Phi'_{ij}}{r_{ij}^3} \right] \mathbf{r}_{ij} \otimes \mathbf{r}_{ij}, \quad i \neq j \quad (2.11)$$

The bandwidth of the atomic level stiffness is thereby related to the interaction or cut-off radius r_c .

2.2 1st– Order Hyperelastic Continua

In this section, we give a short description of the continuum mechanics framework. In this approach, the body is defined by a collection of material points. The non-linear deformation map $\varphi(\mathbf{X})$ relates the material placement \mathbf{X} to the spatial placement $\mathbf{x} = \varphi(\mathbf{X})$, see fig. 2.3. Thereby, the deformation

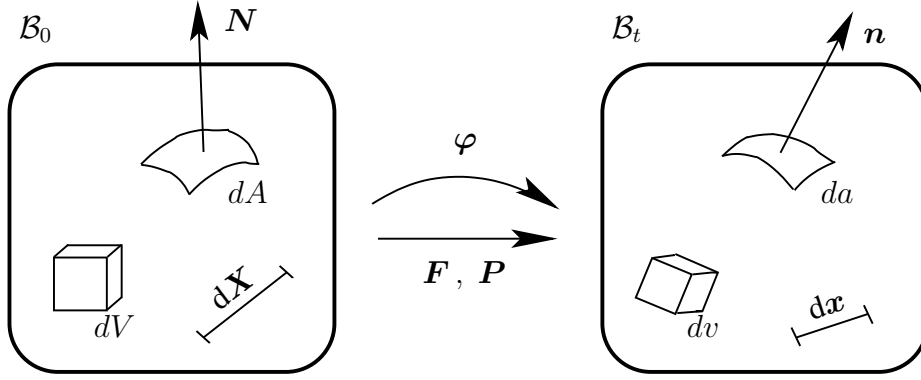


Figure 2.3: A non-linear mapping in the continuum modelling. A line, area and volume elements in both material and spatial configurations are shown.

gradient \mathbf{F} defines a linear tangent map and is given by the two-point tensor

$$\mathbf{F} \doteq \frac{\partial \varphi(\mathbf{X})}{\partial \mathbf{X}} \equiv \nabla_{\mathbf{X}} \varphi \quad (2.12)$$

By virtue of the continuity of both configurations, the mapping should be unique with the consequence for the determinant \mathbf{F} :

$$\det \mathbf{F} \neq 0.$$

The deformation gradient transforms a linear element $d\mathbf{X}$ in the material configuration \mathcal{B}_0 into a linear element $d\mathbf{x}$ in the spatial configuration \mathcal{B}_t :

$$d\mathbf{x} = \mathbf{F} \cdot d\mathbf{X}. \quad (2.13)$$

For the transformations of an area element and of a volume element depicted in fig. 2.3, the following rules are valid ¹:

$$d\mathbf{a} \doteq \mathbf{n} da = \det \mathbf{F} \cdot \mathbf{F}^{-t} \cdot \mathbf{N} dA \doteq \det \mathbf{F} \cdot \mathbf{F}^{-t} \cdot d\mathbf{A} \quad (2.14)$$

$$dv = \det \mathbf{F} dV \quad (2.15)$$

Then for hyperelastic material response, the strain energy W_0 per unit volume in the material configuration is a function of the deformation gradient \mathbf{F} and the position vector \mathbf{X} in the material configuration, i.e.

$$W_0 = W_0(\mathbf{F}; \mathbf{X}) \quad (2.16)$$

Note that the dependence of W_0 on \mathbf{X} corresponds to the subscript i of the i^{th} atom's energy within the atomistic approach. The strain energy is usually phenomenologically defined based on an appropriate set of invariants of the right Cauchy-Green tensor $\mathbf{C} = \mathbf{F}^t \cdot \mathbf{F}$. Based on this classical set-up, the constitutive law results from the first derivative of the strain energy with respect to the deformation gradient and renders the first Piola-Kirchhoff stress tensor \mathbf{P} , which is again a two-point tensor

$$\mathbf{P} \doteq \frac{\partial W_0}{\partial \mathbf{F}} \quad (2.17)$$

¹The rule (2.14) is due to Nanson, see e.g. Ogden [68].

We now reiterate the well known derivation of the equilibrium equations of a 1st-order hyperelastic continuum and the corresponding boundary conditions in the usual way by minimisation of the total potential energy

$$E^{tot} = \int_{\mathcal{B}_0} W_0(\mathbf{F}) dV + E^{ext} \rightarrow \min \quad (2.18)$$

with the potential E^{ext} of the external forces

$$E^{ext} = - \int_{\mathcal{B}_0} \mathbf{b}_0 \cdot \boldsymbol{\varphi} dV - \int_{\partial\mathcal{B}_0} \mathbf{t}_0^P \cdot \boldsymbol{\varphi} dA, \quad (2.19)$$

whereby \mathbf{b}_0 is the body force and \mathbf{t}_0^P is the nominal surface traction in the material configuration. In what follows “:” denotes a double contraction of rank-two tensors \mathbf{P} and \mathbf{F} , i.e. $P_{iJ} F_{iJ}$. According to the classical approach in the calculus of variations (see next chapter), the 1st variation of E^{tot} should vanish to fulfill (2.18):

$$\begin{aligned} \delta E^{tot} &= \delta \int_{\mathcal{B}_0} W_0(\mathbf{F}) dV + \delta E^{ext} \\ &= \int_{\mathcal{B}_0} \frac{\partial W_0}{\partial \mathbf{F}} : \nabla_X \delta \boldsymbol{\varphi} dV - \int_{\mathcal{B}_0} \mathbf{b}_0 \cdot \delta \boldsymbol{\varphi} dV - \int_{\partial\mathcal{B}_0} \mathbf{t}_0^P \cdot \delta \boldsymbol{\varphi} dA = 0 \end{aligned} \quad (2.20)$$

Note that this equation is also known as a weak formulation of an equilibrium with the virtual displacement $\delta \boldsymbol{\varphi}$ as a test function.

After application of partial integration and making use of the Gauss theorem, eq. (2.20) yields the familiar local equilibrium equations with the conventional Neumann-type boundary conditions in the well-known format

$$\text{Div} \mathbf{P} + \mathbf{b}_0 = \mathbf{0} \quad \text{in } \mathcal{B}_0 \quad (2.21)$$

$$\mathbf{P} \cdot \mathbf{N} = \mathbf{t}_0^P \quad \text{on } \partial\mathcal{B}_0 \quad (2.22)$$

with the material surface normal \mathbf{N} to $\partial\mathcal{B}_0$. Here, the operator Div denotes the corresponding divergence operation with respect to the material coordinates \mathbf{X} .

Finally, linearisation of the stress tensor yields the 4th-order tangent operator \mathbb{L} , which relates the increment in \mathbf{P} to the increment in \mathbf{F}

$$\mathbb{L} = \frac{\partial^2 W_0}{\partial \mathbf{F} \otimes \partial \mathbf{F}} \quad \text{with} \quad d\mathbf{P} = \mathbb{L} : d\mathbf{F} \quad (2.23)$$

The pull-back operation applied to \mathbf{P} or \mathbb{L} yields the 2nd Piola-Kirchhoff stress tensor

$$\mathbf{S} \doteq \mathbf{F}^{-1} \cdot \mathbf{P}$$

and the tangent operator denoted \mathbb{C}_1 . A direct calculation yields the connection between \mathbb{L} and \mathbb{C}_1 :

$$\mathbb{C}_1 = \mathbf{F}^{-1} \cdot \mathbb{L} : [\mathbf{F}^{-t} \overline{\otimes} \mathbf{I}] , \quad \mathbb{L} = \mathbf{F} \cdot \mathbb{C}_1 : [\mathbf{F}^t \overline{\otimes} \mathbf{I}] \quad (2.24)$$

or in the component representation:

$$(C_1)_{MJPL} = (F^{-1})_{iM} L_{iJkL} (F^{-1})_{kP} , \quad L_{iJkL} = F_{iM} (C_1)_{MJPL} F_{kP} .$$

On the other hand, an analogous calculation leads to the connection between \mathbb{L} and

$$\mathbb{C} \doteq 2 \frac{\partial \mathbf{S}}{\partial \mathbf{C}}, \quad d\mathbf{S} = \mathbb{C} : \frac{1}{2} d\mathbf{C}$$

which relates an increment in \mathbf{S} to the increment in the right Cauchy-Green tensor $\mathbf{C} \doteq \mathbf{F}^t \cdot \mathbf{F}$:

$$\mathbb{C} = \mathbf{F}^{-1} \cdot \mathbb{L} : [\mathbf{F}^{-t} \overline{\otimes} \mathbf{I}] - [\mathbf{F}^{-1} \cdot \mathbf{F}^{-t}] \overline{\otimes} \mathbf{S}, \quad \mathbb{L} = \mathbf{F} \cdot \mathbb{C} : [\mathbf{F}^t \overline{\otimes} \mathbf{I}] + \mathbf{I} \overline{\otimes} \mathbf{S} \quad (2.25)$$

or in the component representation:

$$C_{MJPL} = (F^{-1})_{Mi} L_{iJkL} (F^{-1})_{Pk} - (F^{-1})_{Mi} (F^{-1})_{Pi} S_{LJ}, \quad L_{iJkL} = F_{iM} C_{MJPL} F_{kP} + \delta_{ik} S_{LJ}.$$

The comparison of (2.24) with (2.25) yields a connection between \mathbb{C}_1 and \mathbb{C} :

$$2 \frac{\partial \mathbf{S}}{\partial \mathbf{C}} = \mathbb{C} = \underbrace{\mathbb{C}_1}_{p.b.(\mathbb{L})} - [\mathbf{F}^{-1} \cdot \mathbf{F}^{-t}] \overline{\otimes} \mathbf{S} \quad (2.26)$$

or by components:

$$C_{MJPL} = (C_1)_{MJPL} - (F^{-1})_{Mi} (F^{-1})_{Pi} S_{LJ} = (F^{-1})_{Mi} L_{iJkL} (F^{-1})_{Pk} - (F^{-1})_{Mi} (F^{-1})_{Pi} (F^{-1})_{Lj} P_{jJ}.$$

Analogously, the push-forward operation yields the Kirchhoff stress tensor

$$\boldsymbol{\tau} \doteq \mathbf{P} \cdot \mathbf{F}^t$$

and the corresponding tangent operator \mathbb{E}_1 , see Steinmann [81]:

$$\mathbb{E}_1 = [\mathbf{I} \overline{\otimes} \mathbf{F}] : \mathbb{L} : [\mathbf{I} \overline{\otimes} \mathbf{F}^t] \quad (2.27)$$

or in the component representation:

$$(E_1)_{ijkl} = F_{jN} L_{iNkP} F_{lP}$$

In contrast to the push-forward operation, the linearisation of $\boldsymbol{\tau}$ yields another tangent operator \mathbb{E}_2 which determines the relative (Lie-type) sensitivity $\mathcal{L}\boldsymbol{\tau} \doteq \mathbf{F} \cdot d\mathbf{S} \cdot \mathbf{F}^t$ of $\boldsymbol{\tau}$ in terms of the relative (Lie-type) increment $\mathcal{L}\mathbf{g} \doteq \mathbf{F}^{-t} \cdot d\mathbf{C} \cdot \mathbf{F}^{-1}$ of the spatial metric $\mathbf{g} = \mathbf{F}^{-t} \cdot \mathbf{C} \cdot \mathbf{F}^{-1}$, see Miehe [57]:

$$\mathcal{L}\boldsymbol{\tau} = \mathbb{E}_2 : \frac{1}{2} \mathcal{L}\mathbf{g}$$

The connection between \mathbb{E}_1 and \mathbb{E}_2 is given by, see Steinmann [81]:

$$2 \frac{\partial \boldsymbol{\tau}}{\partial \mathbf{g}} = \mathbb{E}_2 = \underbrace{\mathbb{E}_1}_{p.f.(\mathbb{L})} - \mathbf{I} \overline{\otimes} \boldsymbol{\tau} \quad (2.28)$$

or by component representation:

$$(E_2)_{ijkl} = (E_1)_{ijkl} - \delta_{ik} \tau_{jl} = F_{jN} L_{iNkP} F_{lP} - \delta_{ik} P_{jM} F_{lM}$$

Note that \mathbb{E}_2 is a push-forward of \mathbb{C} :

$$\mathbb{E}_2 = [\mathbf{F} \overline{\otimes} \mathbf{F}] : \mathbb{C} : [\mathbf{F}^t \overline{\otimes} \mathbf{F}^t] \quad (2.29)$$

or in the componentwise representation, see Miehe [57]:

$$(E_2)_{abcd} = C_{ABCD} F_{aA} F_{bB} F_{cC} F_{dD}$$

2.3 1st- Order Cauchy-Born Rule

Next, we pursue a description of the mixed continuum-atomistic approach mentioned above, which is e.g. employed among other, more sophisticated concepts by Shenoy *et al.* [78], Tadmor [88], Tadmor *et al.* [69]. The key idea here is to replace the phenomenological macroscopic strain energy

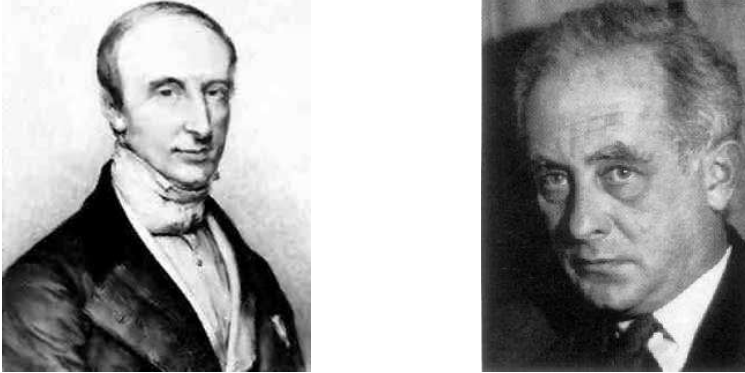


Figure 2.4: Augustin-Louis Cauchy (1789-1857), on the left, and Max Born (1882-1970)

density W_0 per unit volume in the material configuration by appropriate atomistic potentials. This step allows the natural consideration of a real crystal structure with the appropriate anisotropic energy density in the setting of continuum mechanics. In the sequel, we will denote this hybrid model as **the continuum-atomistic model**. Thereby, the important step is to find a correspondence between an atomistic energy function E_i and a specific strain energy density W_0 . By the assumption that the individual atomic contributions to the total energy can be defined and that the energy of each atom i is uniformly distributed over the volume V_i of its Voronoi polyhedron in fig. 2.5, see Tadmor [88], both energies can be related as follows

$$W_0 \doteq \frac{E^{int}}{N V_i} = \frac{1}{N V_i} \sum_{i=1}^N E_i(r_{i1}, \dots, r_{iN}) = W_0(r_{i1}, \dots, r_{iN}) \quad (2.30)$$

The remaining problem is now to establish a relation between the continuum deformation and the atomic distance vectors. Here, we shall follow the Cauchy-Born rule (CBR), which is denoted as the 1st-order CBR. The 2nd-order CBR is related to the higher-order theory and is stated in the last chapter of the present work.

The conceptual idea here is to consider homogeneous deformations of an infinite representative crystallite, whereby the kinematical relation is given by the 1st-order Cauchy-Born rule. In 1828-1829, Cauchy [17, 16, 19, 18] supposed that the gross motion corresponds to the atomic motion in a solid during the deformation. In 1915, Born [13, 14] generalized this hypothesis by assumption an additional relaxation of inner microstructure. The inner relaxation is used e.g. in the already cited works of Martin [53, 54, 55] and is also a main subject of chapters 4 and 5 in the present work.

In the mathematical expression of the Cauchy-Born-Rule is assumed that the lattice vectors \mathbf{r}_{ij} of the spatial configuration result from the corresponding \mathbf{R}_{ij} in the material configuration by the application of the local deformation gradient $\mathbf{F} = \nabla_{\mathbf{X}} \varphi$ (which in general varies with \mathbf{X}), see fig. 2.5,

$$\mathbf{r}_{ij} = \mathbf{F} \cdot \mathbf{R}_{ij} \quad (2.31)$$

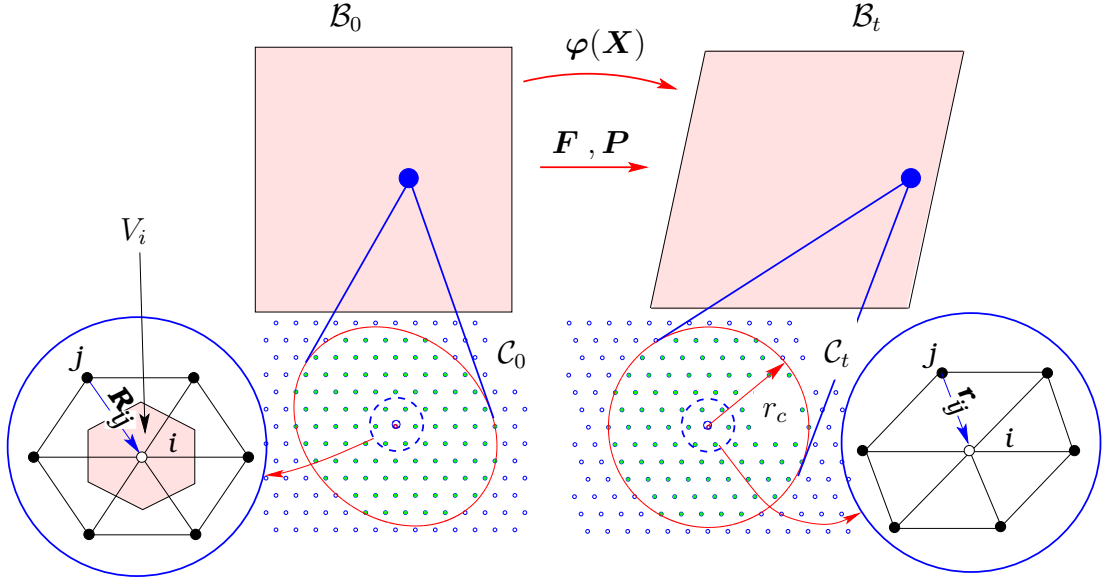


Figure 2.5: The 1st-order Cauchy-Born rule for the case of homogeneous deformation

The strain energy density W_0 defined in (2.30) then depends only on relative distances r_{ij} between the atom i and all other atoms and can formally be represented as a function of the deformation gradient and the fixed distance vectors \mathbf{R}_{ij} in the material configuration

$$W_0 = W_0(r_{i1}, \dots, r_{iN}) = W_0(|\mathbf{F} \cdot \mathbf{R}_{i1}|, \dots, |\mathbf{F} \cdot \mathbf{R}_{iN}|) = W_0(\mathbf{F}) \quad (2.32)$$

Here, the constant distance vectors \mathbf{R}_{ij} in the material configuration are given and depend only on the underlying geometrical crystal lattice structure. Thus, each point of the continuum is modeled by an infinite crystal, which deforms homogeneously. In practice, the cut-off radius r_c of the pair potential limits the extension of that part of the crystal that has to be considered, see again fig. 2.5. For the case of the homogeneous deformation, the energies E_i of all atoms are equivalent, and the expression (2.30) obtains a more simple format:

$$W_0 = \frac{1}{N V_i} N E_i(r_{i1}, \dots, r_{iN}) = \frac{E_i(r_{i1}, \dots, r_{iN})}{V_i} = W_0(r_{i1}, \dots, r_{iN}) \quad (2.33)$$

Thus, in this case, the energy of only one atom of lattice is sufficient to compute the strain energy density in the entire lattice. Moreover, for the case of pair potentials, W_0 can be expressed in terms of interatomic pairwise interactions:

$$W_0 = \frac{1}{2V_i} \sum_{j \neq i} \Phi_{ij} \quad (2.34)$$

The constitutive law given by eq. (2.17) results under consideration of (2.30)-(2.32) in the following explicit format ² :

$$\begin{aligned} \mathbf{P} &= \frac{1}{NV_i} \sum_i \frac{\partial E_i}{\partial \mathbf{F}} = \frac{1}{NV_i} \sum_i \sum_{j \neq i} \frac{\partial E_i}{\partial r_{ij}} \frac{\partial r_{ij}}{\partial \mathbf{F}} = \frac{1}{NV_i} \sum_i \sum_{j \neq i} \frac{E_{i,r_{ij}}}{r_{ij}} \mathbf{r}_{ij} \otimes \mathbf{R}_{ij} \\ &= \frac{1}{N} \sum_i \frac{1}{2V_i} \sum_{j \neq i} \frac{E_{i,r_{ij}} + E_{j,r_{ji}}}{r_{ij}} \mathbf{r}_{ij} \otimes \mathbf{R}_{ij} = \frac{1}{N} \sum_i \frac{1}{2V_i} \sum_{j \neq i} \mathbf{f}_{ji} \otimes \mathbf{R}_{ij} \equiv \frac{1}{N} \sum_i \mathbf{P}_i \end{aligned} \quad (2.35)$$

with the interatomic force $\mathbf{f}_{ji} = -\mathbf{f}_{ij}$ introduced in (2.3) and the notation

$$\mathbf{P}_i \doteq \frac{1}{2V_i} \sum_{j \neq i} \mathbf{f}_{ji} \otimes \mathbf{R}_{ij}. \quad (2.36)$$

As a consequence, the appropriate push-forward, i.e. the spatial Kirchhoff stress features the expected symmetry properties:

$$\mathbf{P} : \nabla_X \delta \varphi = [\mathbf{P} \cdot \mathbf{F}^t] : \nabla_x \delta \varphi = \left[\frac{1}{2NV_i} \sum_i \sum_{j \neq i} \mathbf{f}_{ji} \otimes \mathbf{r}_{ij} \right] : \nabla_x \delta \varphi. \quad (2.37)$$

In the case of the homogeneous deformation provided by the standard Cauchy-Born rule,

$$\mathbf{P} = \frac{1}{N} N \mathbf{P}_i = \mathbf{P}_i. \quad (2.38)$$

Likewise, the 4th-order tangent operator \mathbb{L} relating the material rate of \mathbf{P} to the material rate of \mathbf{F} takes the format

$$\mathbb{L} \doteq \frac{\partial^2 W_0}{\partial \mathbf{F} \otimes \partial \mathbf{F}} = \frac{1}{N} \sum_i \frac{\partial \mathbf{P}_i}{\partial \mathbf{F}} \equiv \frac{1}{N} \sum_i \mathbb{L}_i \quad (2.39)$$

with the following definition of the ‘‘local’’ tangent \mathbb{L}_i :

$$\mathbb{L}_i \doteq \frac{\partial \mathbf{P}_i}{\partial \mathbf{F}}.$$

An explicit expression for \mathbb{L}_i can be obtained simply by using (2.36) and considering (2.8) and (2.9)³:

$$\mathbb{L}_i = \frac{1}{2V_i} \sum_{j \neq i} \left[\mathbf{k}_{ij}^{(0)} \overline{\otimes} [\mathbf{R}_{ij} \otimes \mathbf{R}_{ij}] + \sum_{\substack{m \neq i \\ m \neq j}} \mathbf{k}_{ij}^{(m)} \overline{\otimes} [\mathbf{R}_{ij} \otimes \mathbf{R}_{im}] \right] \quad (2.40)$$

²A more implicit format of the constitutive law without resorting explicitly to the atomistic interaction forces can be found e.g. in [88].

³The non-standard dyadic product $\overline{\otimes}$ emerging in (2.40) is introduced here for 2nd-order tensors \mathbf{A} , \mathbf{B} and \mathbf{C} as

$$[\mathbf{A} \overline{\otimes} \mathbf{B}] : \mathbf{C} = \mathbf{A} \cdot \mathbf{C} \cdot \mathbf{B}^t \quad \text{or} \quad [\mathbf{A} \overline{\otimes} \mathbf{B}]_{ijkl} \doteq A_{ik} B_{jl}$$

Under consideration of pair potentials, (2.40) can again be simplified since all $\mathbf{k}_{ij}^{(m)}$ vanish in this case:

$$\mathbb{L}_i = \frac{1}{2V_i} \sum_{j \neq i} \mathbf{k}_{ij} \bar{\otimes} [\mathbf{R}_{ij} \otimes \mathbf{R}_{ij}] \quad (2.41)$$

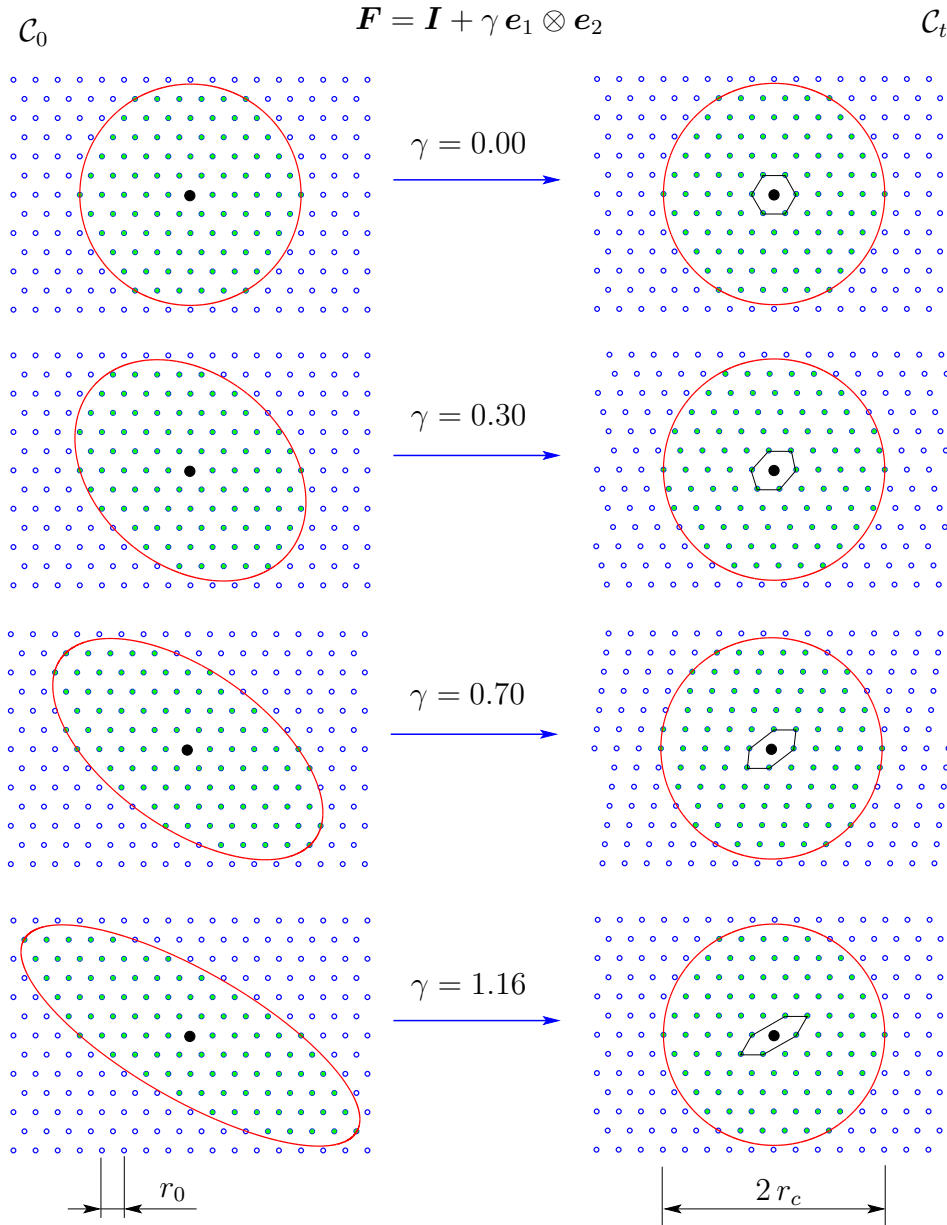


Figure 2.6: Application of the 1st-order Cauchy-Born rule: simple shear deformation characterised by shear number γ and by a deformation gradient $\mathbf{F} = \mathbf{I} + \gamma \mathbf{e}_1 \otimes \mathbf{e}_2$ applied to the material lattice configuration (on the left). The circles with radius r_c on the right (spatial lattice configuration) contain the next neighbours of the middle atom and are called cut-off circles. Due to the Cauchy-Born rule, they form various stretched and rotated ellipses in the material configuration similar to the Cauchy stretch ellipsoid in the classical theory of elasticity. Here, r_0 denotes the lattice constant.

with $\mathbf{k}_{ij} \equiv \mathbf{k}_{ij}^{(0)}$. For the case of the homogeneous deformation, the “global” tangent \mathbb{L} and the “local” tangent \mathbb{L}_i are equal:

$$\mathbb{L} = \frac{1}{N} N \mathbb{L}_i = \mathbb{L}_i. \quad (2.42)$$

It is remarkable that the quantities, which are defined for the underlying atomistic model show up

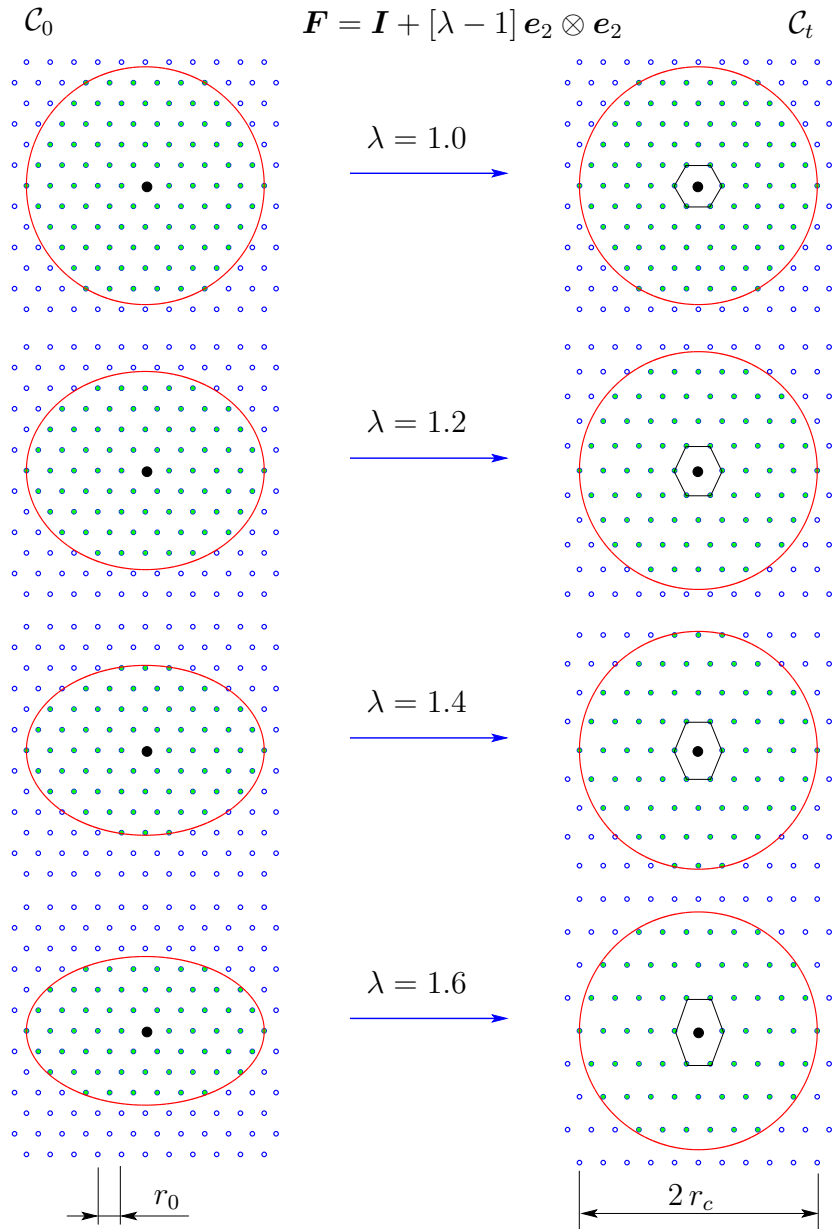


Figure 2.7: Application of the 1st-order Cauchy-Born rule: uniaxial extension characterised by stretch λ and by a deformation gradient $\mathbf{F} = \mathbf{I} + [\lambda - 1]\mathbf{e}_2 \otimes \mathbf{e}_2$ applied to the material lattice configuration (on the left). The circles with radius r_c on the right (spatial lattice configuration) contain the next neighbours of the middle atom and are called cut-off circles. Due to the Cauchy-Born rule, they form various stretched ellipses in the material configuration. Here, r_0 denotes the lattice constant.

in a simple format in the relations for \mathbf{P} and \mathbb{L} , thus reflecting the atomistic features in the continuum setting.

Fig. 2.6 and 2.7 show an application of the 1st-order Cauchy-Born rule for a simple shear deformation and for a uniaxial extension. The same material lattice configuration \mathcal{C}_0 is shown on the left. On the right are shown spatial lattice configurations \mathcal{C}_t for different values of the shear number γ (fig. 2.6) or of the stretch λ (fig. 2.7). The circles with radius r_c on the right (spatial lattice configuration) contain the next neighbours of the middle atom and are called cut-off circles. Due to the Cauchy-Born rule, they form various stretched and rotated ellipses in the material configuration .

In practical applications, the cut-off or interaction radius must be chosen to reduce the summation over all atoms to a summation over the next neighbours only. The choice of this radius depends on the used potential: an interatomic interaction on the separations greater than r_c should be negligible in comparison to the interaction within the cut-off circle. If this requirement is not fulfilled as e.g. in the case of EAM potential accounting only the first next neighbours, a screening function should be introduced to bring the truncated potential smoothly to zero, see Baskes [6]. If the energy does not smoothly reach zero at the cut-off radius, pure numerical forces arise and the solver can become very unstable, see Tadmor [88]. It is important that such a screening function also brings the first derivative of the energy to zero at r_c .

Fig. 2.8 explains the choice of r_c in the case presented here. The upper figure depicts a strain energy density W_0 computed according to (2.32) for the simple shear deformation with the cut-off radius $r_c = n r_0$ for different integer scaling factors $n = \overline{1, 5}$. It is easy to recognise that the energy converges to a constant value with the increasing n . The difference between the energy curve with $n = 12$ (denoted as $W_0^{(12)}$), which is not shown here and the curve with $n = 5$ (denoted as $W_0^{(5)}$) is negligible in comparison to the difference between $W_0^{(5)}$ and $W_0^{(3)}$, see the lower diagram in fig. 2.8. Thus, $r_c = 5r_0$ is chosen as the cut-off radius. However, for more complicated applications, $n = 3$ has been used for the sake of efficiency.

As expected, the Cauchy-Born strain energy density W_0 shows a periodical behaviour for the simple shear deformation due to the implemented lattice periodicity. It becomes possible due to the computation of the actual neighbours contained in the cut-off sphere after each load increment. Fig. 2.9 displays again the strain energy density W together with the components of the Kirchhoff stress tensor $\boldsymbol{\tau} = \mathbf{P} \cdot \mathbf{F}^t$. Note that the parameters ε and σ of the Lennard-Jones potential are chosen under requirement of the stress-free material configuration so that all stress components vanish at $\mathbf{F} = \mathbf{I}$.

The Cauchy-Born rule naturally considers atomic features of the crystal such as the lattice symmetry. The influence of the underlying crystal orientation on the computed strain energy density and the components of the Kirchhoff stress tensor is shown in fig. 2.10. Here, the same simple shear deformation with the shear number γ running from zero to 3 is applied to two different material lattice configurations: one oriented as in the previous figures and another one rotated by 30° with respect to the 1st one. The upper figure then shows a different behaviour of the strain energy density and the shear component of the Kirchhoff stress tensor .

Thus, an application of the 1st-order Cauchy-Born rule provides a macroscopic material law, which contains implicitly all atomic features considered in the corresponding microscopic model. Unfortunately, the Cauchy-Born rule may be applied only within a relatively narrow band of the admissible deformations close to identity. The failure of the Cauchy-Born rule and the methodology to overcome this failure phenomena is discussed in detail in the next two chapters.

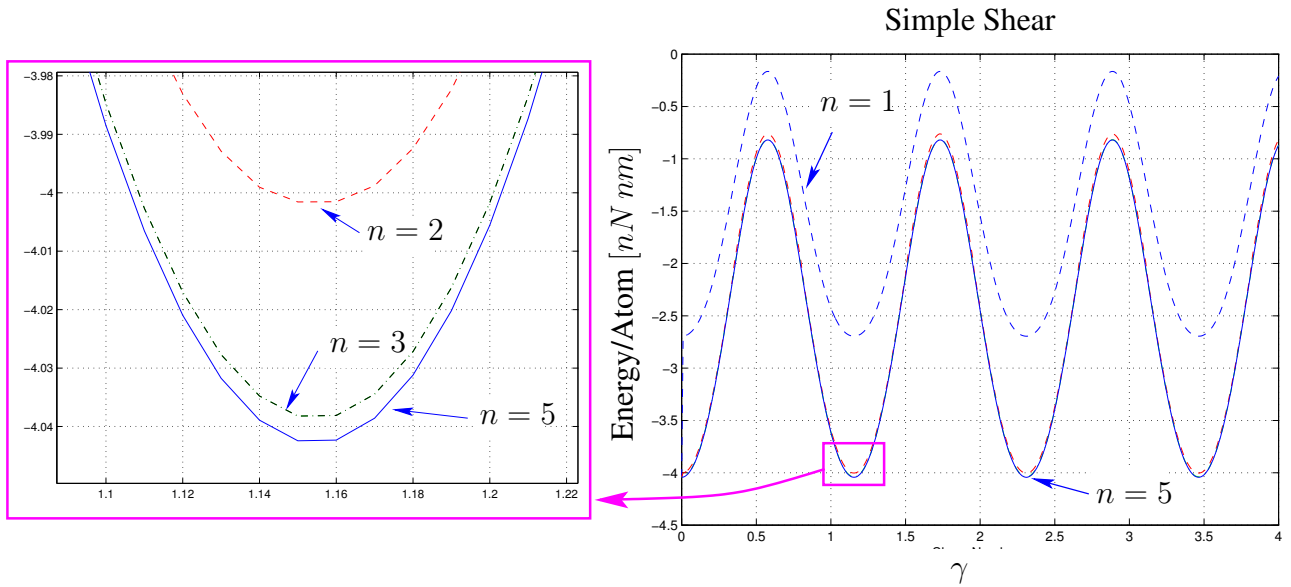


Figure 2.8: The choice of the cut-off radius. A strain energy density computed according to (2.32) for the simple shear deformation with the cut-off radius $r_c = n r_0$ for different integer scaling factors $n = \overline{1, 5}$. The strain energy density converges to a constant value with the increasing n .

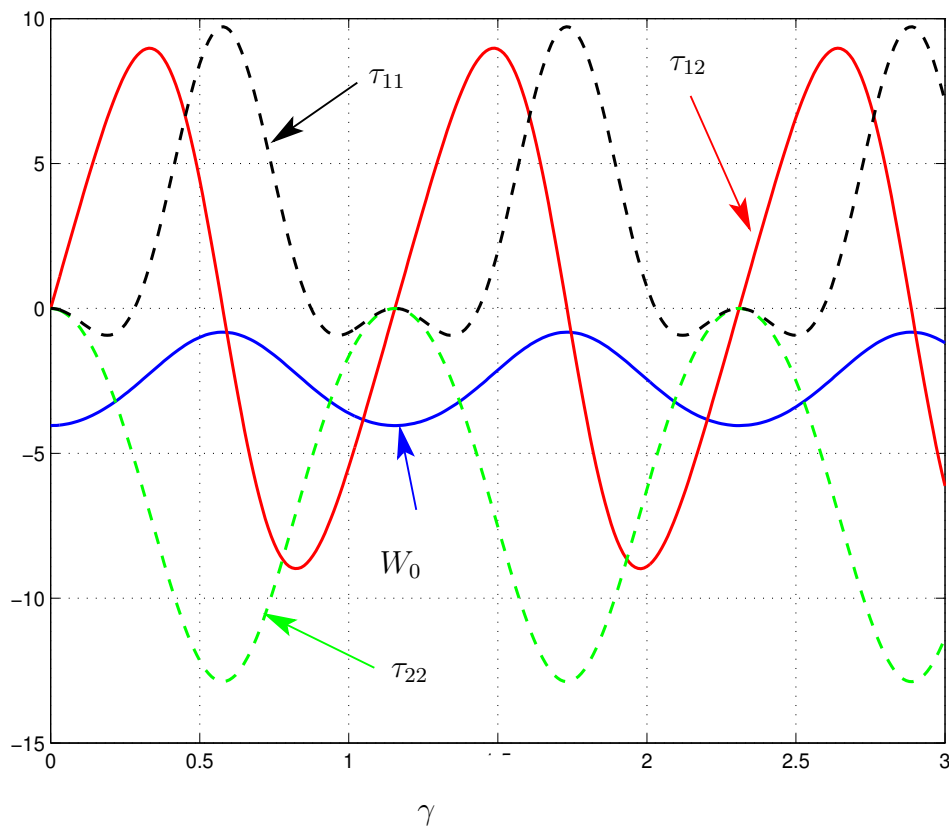
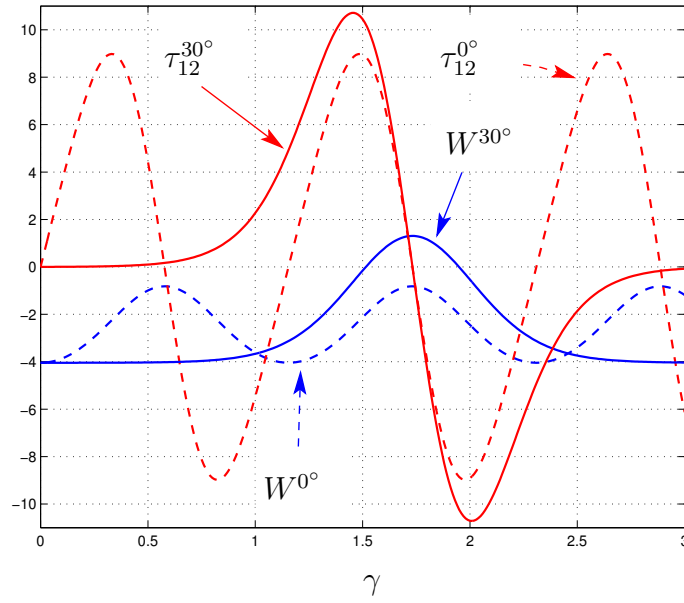
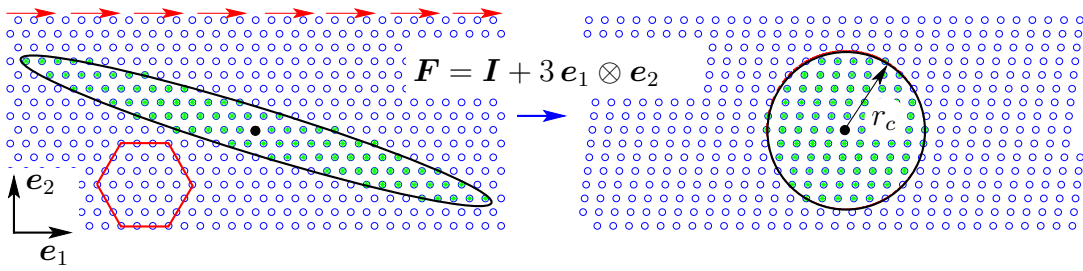


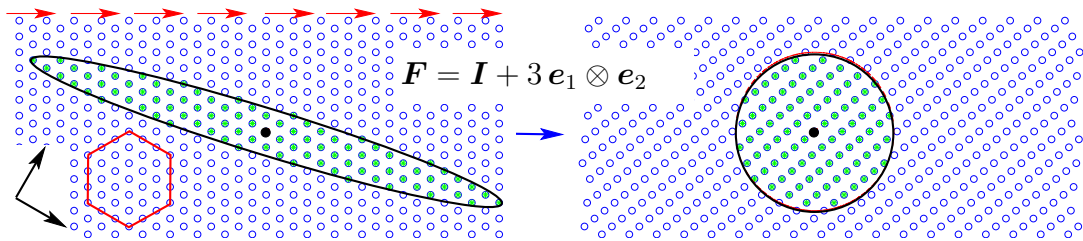
Figure 2.9: The strain energy density W and the components of the Kirchhoff stress tensor $\tau = P \cdot F^t$ display a periodic behaviour due to the computation of the actual neighbours contained in the cut-off sphere after each load increment



Originally Oriented Crystallite: $W^{0^\circ}, \tau_{12}^{0^\circ}$



Crystallite rotated by 30°: $W^{30^\circ}, \tau_{12}^{30^\circ}$



\mathcal{C}_0

Simple Shear

\mathcal{C}_t

Figure 2.10: The influence of the crystallite orientation on the strain energy density and the Kirchhoff stress tensor.

2.4 Scale Transition: Continuation and Homogenisation

The 1st-order Cauchy-Born rule can be viewed as a simple kind of averaging when all atoms in the spatial lattice configuration follow the prescribed macroscopic deformation $\bar{\mathbf{F}}$. In this section, the result (2.36) is obtained from the main principle of the homogenisation i.e. from the equivalence of the virtual macro and micro power, see Hill. Furthermore, it is proven that the Cauchy-Born deformation on the boundary also follows from this principle.

A short overview of the continuous homogenisation should be represented in this section for a better understanding.

2.4.1 Continuous homogenisation

The aim of the homogenisation is to average local field values such as the 1st Piola-Kirchhoff stress tensor \mathbf{P} or the deformation gradient \mathbf{F} over a sufficient inhomogeneous body of interest to obtain the homogenised values $\bar{\mathbf{P}}$ and $\bar{\mathbf{F}}$ respectively. The connection between the local and the homogenised field values is given by assuming

$$\bar{\mathbf{F}} = \frac{1}{V_0} \int_{\mathcal{B}_0} \mathbf{F} dV \quad \bar{\mathbf{P}} = \frac{1}{V_0} \int_{\mathcal{B}_0} \mathbf{P} dV \quad (2.43)$$

with the volume V_0 of the material configuration. The power requirement mentioned above is given by

$$\mathcal{W}_{macro} = \mathcal{W}_{micro} \quad \Rightarrow \quad \bar{\mathbf{P}} : \dot{\bar{\mathbf{F}}} \doteq \frac{1}{V_0} \int_{\mathcal{B}_0} \mathbf{P} : \dot{\mathbf{F}} dV \quad (2.44)$$

For further considerations, the following two identities are needed:

$$\text{Div}(\boldsymbol{\varphi} \otimes \mathbf{I}) = \text{Grad} \boldsymbol{\varphi} \cdot \mathbf{I}^t + \boldsymbol{\varphi} \otimes \text{Div} \mathbf{I} = \mathbf{F} \cdot \mathbf{I} + \boldsymbol{\varphi} \otimes \mathbf{0} = \mathbf{F} \quad (2.45)$$

$$\text{Div}(\mathbf{X} \otimes \mathbf{P}) = \text{Grad} \mathbf{X} \cdot \mathbf{P}^t + \mathbf{X} \otimes \text{Div} \mathbf{P} = \mathbf{I} \cdot \mathbf{P}^t + \mathbf{X} \otimes \mathbf{0} = \mathbf{P}^t \quad (2.46)$$

Here, the equilibrium condition (2.21) is used; $\text{Div} \equiv \nabla_{\mathbf{X}} \cdot (\bullet)$ and $\text{Grad} \equiv \nabla_{\mathbf{X}} (\bullet)$ denote the usual differential operations of divergence and gradient with respect to the material configuration. By using these identities and the Gauss theorem, the volume integrals in (2.43) can be easily transformed in the area integrals:

$$\bar{\mathbf{F}} = \frac{1}{V_0} \int_{\mathcal{B}_0} \text{Div}(\boldsymbol{\varphi} \otimes \mathbf{I}) dV = \frac{1}{V_0} \int_{\partial \mathcal{B}_0} \boldsymbol{\varphi} \otimes \mathbf{I} \cdot \mathbf{N} dA = \frac{1}{V_0} \int_{\partial \mathcal{B}_0} \boldsymbol{\varphi} \otimes \mathbf{N} dA \quad (2.47)$$

$$\bar{\mathbf{P}} = \frac{1}{V_0} \left[\int_{\mathcal{B}_0} \text{Div}(\mathbf{X} \otimes \mathbf{P}) dV \right]^t = \frac{1}{V_0} \int_{\partial \mathcal{B}_0} [\mathbf{P} \cdot \mathbf{N}] \otimes \mathbf{X} dA \equiv \frac{1}{V_0} \int_{\partial \mathcal{B}_0} \mathbf{T} \otimes \mathbf{X} dA \quad (2.48)$$

where \mathbf{N} is the normal vector to the micro-scale material configuration and $\mathbf{T} \doteq \mathbf{P} \cdot \mathbf{N}$ is the traction in the material configuration. Recall that for a 2nd-order tensor $\boldsymbol{\sigma}$ and for a vector \mathbf{a} the following transformation is valid:

$$\text{Div}(\boldsymbol{\sigma} \cdot \mathbf{a}) = \text{Div} \boldsymbol{\sigma}^t \cdot \mathbf{a} + \text{Grad} \mathbf{a} : \boldsymbol{\sigma}^t \quad (2.49)$$

Now, from the power requirement (2.44) under consideration of (2.47)-(2.49) follows

$$\begin{aligned}
 \bar{\mathbf{P}} : \dot{\bar{\mathbf{F}}} &= \frac{1}{V_0} \int_{\mathcal{B}_0} \mathbf{P} : \text{Div}(\dot{\boldsymbol{\varphi}} \otimes \mathbf{I}) dV = \frac{1}{V_0} \int_{\mathcal{B}_0} \mathbf{P} : \text{Grad} \dot{\boldsymbol{\varphi}} dV \\
 &= \frac{1}{V_0} \int_{\mathcal{B}_0} [\text{Div}(\mathbf{P}^t \cdot \dot{\boldsymbol{\varphi}}) - \text{Div} \mathbf{P} \cdot \dot{\boldsymbol{\varphi}}] dV = \frac{1}{V_0} \int_{\mathcal{B}_0} \text{Div}(\mathbf{P}^t \cdot \dot{\boldsymbol{\varphi}}) dV \\
 &= \frac{1}{V_0} \int_{\partial \mathcal{B}_0} \mathbf{P}^t \cdot \dot{\boldsymbol{\varphi}} \cdot \mathbf{N} dA = \frac{1}{V_0} \int_{\partial \mathcal{B}_0} \mathbf{T} \cdot \dot{\boldsymbol{\varphi}} dA
 \end{aligned} \tag{2.50}$$

On the other hand

$$\bar{\mathbf{P}} : \dot{\bar{\mathbf{F}}} = \left[\frac{1}{V_0} \int_{\partial \mathcal{B}_0} \mathbf{T} \otimes \mathbf{X} dA \right] : \dot{\bar{\mathbf{F}}} = \frac{1}{V_0} \int_{\partial \mathcal{B}_0} \mathbf{T} \otimes \mathbf{X} : \dot{\bar{\mathbf{F}}} dA = \frac{1}{V_0} \int_{\partial \mathcal{B}_0} \mathbf{T} \cdot \dot{\bar{\mathbf{F}}} \cdot \mathbf{X} dA \tag{2.51}$$

Finally, the comparison of the right-hand parts of (2.50) and (2.51) yields the desired result:

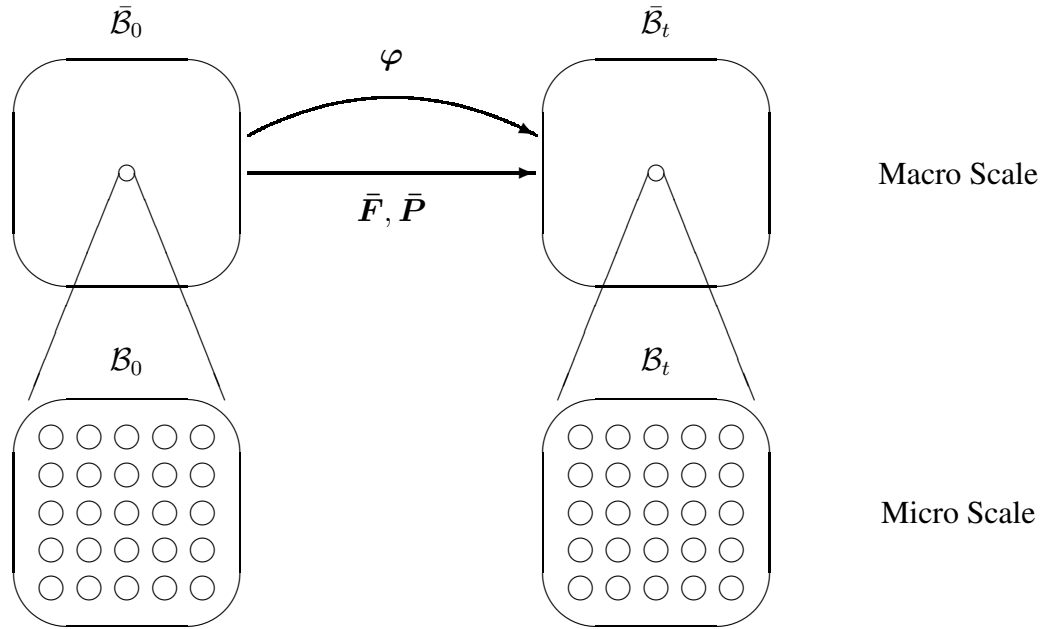


Figure 2.11: A non-homogeneous micro scale and a homogenised macro scale.

$$\int_{\partial \mathcal{B}_0} \mathbf{T} \cdot [\boldsymbol{\varphi} - \bar{\mathbf{F}} \cdot \mathbf{X}] dA \doteq 0 \tag{2.52}$$

Last equation states that the power requirement is satisfied for

1. the periodicity on $\partial \mathcal{B}_0$;
2. $\boldsymbol{\varphi} = \bar{\mathbf{F}} \cdot \mathbf{X}$ in \mathcal{B}_0 ;
3. $\boldsymbol{\varphi} = \bar{\mathbf{F}} \cdot \mathbf{X}$ on $\partial \mathcal{B}_0$.

Similar to the continuous case, the homogeneous Cauchy-Born boundary conditions have been derived in this section using a discrete analog of (2.43) and (2.44). In general, the application of the Cauchy-Born rule can be divided into two global steps: the continuisation i.e. the transition from a discrete representative volume element (RVE) to a continuous non-homogeneous RVE (discrete micro scale \Rightarrow continuous micro scale) and the homogenisation i.e. the transition from a continuous non-homogeneous RVE to a continuous homogeneously deformed body (continuous micro scale \Rightarrow continuous macro scale). Such averaging strategy is displayed in the fig. 2.12. Both the continuisation and the homogenisation are discussed below.

2.4.2 Continuisation

The continuisation is represented by the lower part of the fig. 2.12. This procedure states the connection between the discrete atomistic features such as the interatomic forces \mathbf{f}_{ij} and the relative atomic separations \mathbf{r}_{ij} , and the continuous local field values such as the 1st Piola-Kirchhoff stress tensor \mathbf{P}_i and the deformation gradient \mathbf{F}_i which are constant in the next environment of the atom i . The power requirement in this case provides the power equivalence of the discrete and continuous system at the micro level:

$$\mathcal{W}_{micro}^{conti} = \mathcal{W}_{micro}^{discrete} \Rightarrow \frac{1}{V_0} \sum_i \mathbf{P}_i : \dot{\mathbf{F}}_i V_i \doteq \frac{1}{2V_0} \sum_i \sum_{j \neq i} \mathbf{f}_{ji} \cdot \dot{\mathbf{r}}_{ij}. \quad (2.53)$$

For the continuous micro system, the volume integral is replaced by the sum over all cells in the discrete RVE. It is easy to prove that the Cauchy-Born rule is necessary for (2.53) in the whole discrete lattice system i.e.

$$\mathbf{r}_i = \bar{\mathbf{F}} \cdot \mathbf{R}_i \quad \forall \mathbf{R}_i \in \mathcal{C}_0 \cup \partial\mathcal{C}_0 \quad \Leftrightarrow \quad \mathbf{F}_i = \bar{\mathbf{F}} \quad \forall i = \overline{1, N}, \quad (2.54)$$

where N is the number of atoms in the discrete lattice RVE. Indeed, if (2.54) is valid, the right-hand side of (2.53) can be transformed as shown below:

$$\begin{aligned} \mathbf{P}_i : \dot{\mathbf{F}}_i &= \frac{1}{2V_i} \sum_{j \neq i} \mathbf{f}_{ji} \cdot \dot{\mathbf{r}}_{ij} = \frac{1}{2V_i} \sum_{j \neq i} \mathbf{f}_{ji} \cdot \left[\dot{\bar{\mathbf{F}}} \cdot \mathbf{R}_{ij} \right] \\ &= \frac{1}{2V_i} \sum_{j \neq i} \left[\mathbf{f}_{ji} \otimes \mathbf{R}_{ij} \right] : \dot{\bar{\mathbf{F}}} = \left[\frac{1}{2V_i} \sum_{j \neq i} \mathbf{f}_{ji} \otimes \mathbf{R}_{ij} \right] : \dot{\bar{\mathbf{F}}} \equiv \mathbf{P} : \dot{\bar{\mathbf{F}}} \end{aligned} \quad (2.55)$$

where

$$\mathbf{P} \equiv \mathbf{P}_i \doteq \frac{1}{2V_i} \sum_{j \neq i} \mathbf{f}_{ji} \otimes \mathbf{R}_{ij} \quad (2.56)$$

Remember that the expression (2.55) has been obtained according to the definition of the 1st Piola-Kirchhoff stress tensor as the 1st derivative of the strain energy density W_0 , see (2.36).

Assume that the Cauchy-Born rule is valid only in a local environment of each atom and is not true for the whole RVE i.e.

$$\mathbf{r}_{ij} \approx \mathbf{F}_i \cdot \mathbf{R}_{ij} \quad \forall j \neq i \quad \text{no summation!} \quad (2.57)$$

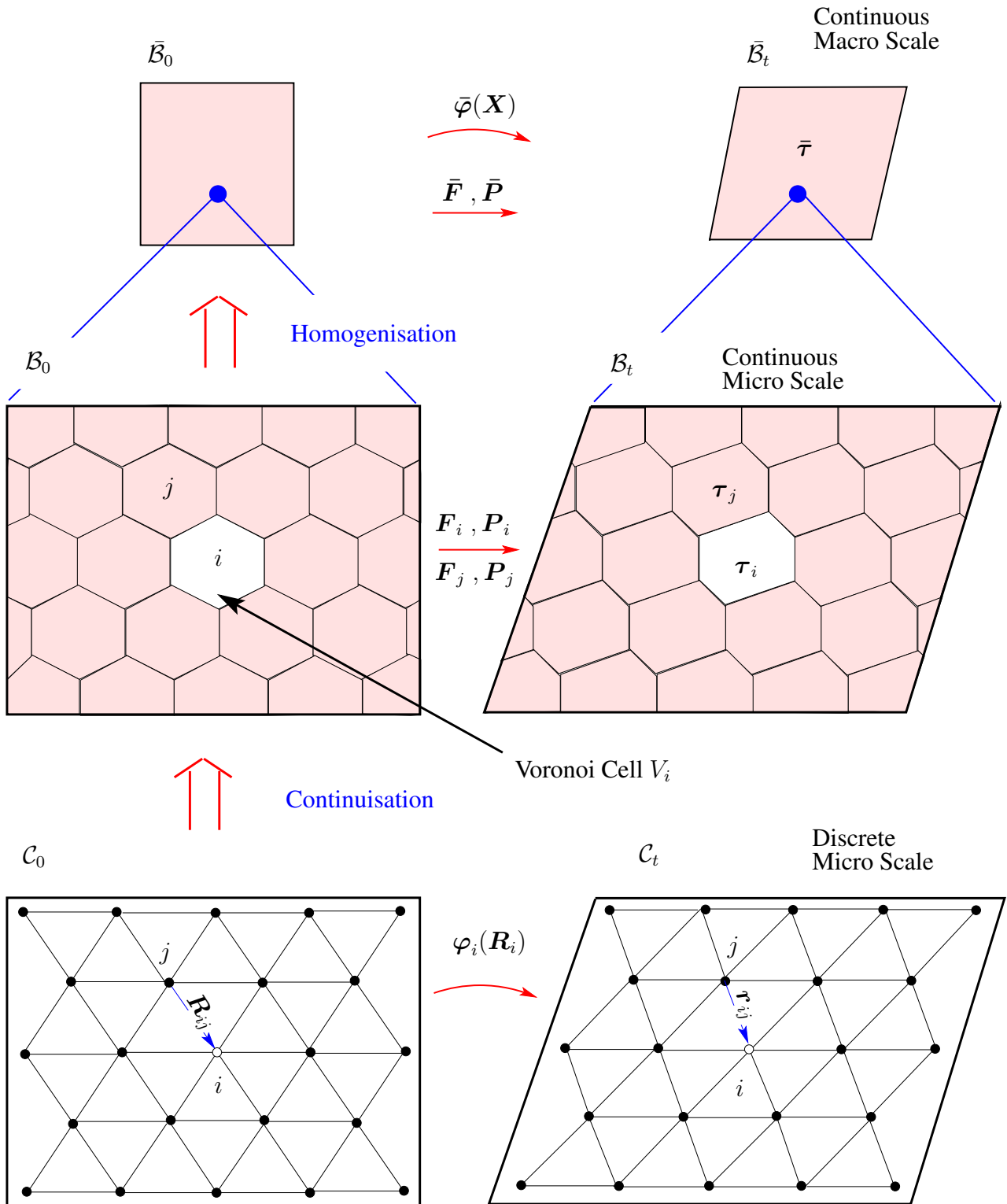


Figure 2.12: Two-step transition from a discrete micro scale to a continuous macro scale: continuation and homogenisation.

The local deformation gradient \mathbf{F}_i for this local or cellwise Cauchy-Born rule can be obtained by the following minimisation problem:

$$\frac{1}{2} \sum_{j \neq i} |\mathbf{r}_{ij} - \mathbf{F}_i \cdot \mathbf{R}_{ij}|^2 \rightarrow \min_{\mathbf{F}_i} \quad (2.58)$$

whereby the vectors \mathbf{r}_i of the spatial lattice configuration \mathcal{C}_t are the solutions of the lattice statics problem with e.g. the Cauchy-Born boundary conditions

$$\mathbf{r}_i = \bar{\mathbf{F}} \cdot \mathbf{R}_i \quad \forall \mathbf{R}_i \in \partial \mathcal{B}_0.$$

Also in this case, the cellwise Cauchy-Born rule (2.57) is necessary for the power requirement (2.53). This necessity is proven below. From (2.58) follows:

$$\begin{aligned} \delta \left\{ \frac{1}{2} \sum_{j \neq i} |\mathbf{r}_{ij} - \mathbf{F}_i \cdot \mathbf{R}_{ij}|^2 \right\} = 0 &\Rightarrow \sum_{j \neq i} [\mathbf{r}_{ij} - \mathbf{F}_i \cdot \mathbf{R}_{ij}] \otimes \mathbf{R}_{ij} = \mathbf{0} \\ &\Downarrow \\ \sum_{j \neq i} \mathbf{r}_{ij} \otimes \mathbf{R}_{ij} &= \mathbf{F}_i \cdot \left[\sum_{j \neq i} \mathbf{R}_{ij} \otimes \mathbf{R}_{ij} \right] \end{aligned} \quad (2.59)$$

If the matrix $\sum_{j \neq i} \mathbf{R}_{ij} \otimes \mathbf{R}_{ij}$ is invertible, (2.59) results in an expression for \mathbf{F}_i :

$$\mathbf{F}_i = \left[\sum_{j \neq i} \mathbf{r}_{ij} \otimes \mathbf{R}_{ij} \right] \cdot \left[\sum_{j \neq i} \mathbf{R}_{ij} \otimes \mathbf{R}_{ij} \right]^{-1} \quad (2.60)$$

A detailed investigation of $\sum_{j \neq i} \mathbf{R}_{ij} \otimes \mathbf{R}_{ij}$ is given in the appendix. It is shown that for a sufficiently symmetric atomic arrangement, this sum is proportional to the identity matrix with a constant scaling factor ρ (cf. (A.6)):

$$\sum_{j \neq i} \mathbf{R}_{ij} \otimes \mathbf{R}_{ij} = \rho \mathbf{I} \quad (2.61)$$

and (2.61) can be rewritten as

$$\mathbf{F}_i = \frac{1}{\rho} \sum_{j \neq i} \mathbf{r}_{ij} \otimes \mathbf{R}_{ij} \quad (2.62)$$

In view of (2.57) and (2.62), an expression identical to (2.56) can be obtained for the local 1st Piola-Kirchhoff stress tensor \mathbf{P}_i . Note that this case contains the Cauchy-Born rule (2.54) as a particular case. Thus, the necessity of the Cauchy-Born rule is proven.

2.4.3 Discrete homogenisation

The discrete homogenisation means a transition from the local deformation gradient \mathbf{F}_i and the local 1st Piola-Kirchhoff stress tensor \mathbf{P}_i at the micro scale to the averaged deformation gradient $\bar{\mathbf{F}}$ and the averaged 1st Piola-Kirchhoff stress tensor $\bar{\mathbf{P}}$ at the macro scale, see the upper part of fig. 2.12. These values are connected according to the following assumption, which is a discrete analog of (2.43):

$$\bar{\mathbf{F}} \doteq \frac{1}{V_0} \sum_i \mathbf{F}_i V_i \quad \bar{\mathbf{P}} \doteq \frac{1}{V_0} \sum_i \mathbf{P}_i V_i \quad (2.63)$$

An expression for the homogenised 1st Piola-Kirchhoff stress tensor $\bar{\mathbf{P}}$ results from (2.56) and (2.63):

$$\bar{\mathbf{P}} = \frac{1}{V_0} \sum_i \left[\frac{1}{2V_i} \sum_{j \neq i} \mathbf{f}_{ji} \otimes \mathbf{R}_{ij} \right] V_i = \frac{1}{2V_0} \sum_i \sum_{j \neq i} \mathbf{f}_{ji} \otimes \mathbf{R}_{ij} \quad (2.64)$$

Now, the sufficiency of the Cauchy-Born rule for the whole RVE can simply be derived from (2.63) under consideration of the cellwise Cauchy-Born rule (2.57) and its consequence (2.56) as well as the corresponding power requirement

$$\mathcal{W}_{macro} = \mathcal{W}_{micro}^{discrete} \Rightarrow \bar{\mathbf{P}}^t : \dot{\bar{\mathbf{F}}} \doteq \frac{1}{2V_0} \sum_i \sum_{j \neq i} \mathbf{f}_{ji} \cdot \dot{\mathbf{r}}_{ij} \quad (2.65)$$

Indeed,

$$\begin{aligned} \bar{\mathbf{P}}^t : \dot{\bar{\mathbf{F}}} &= \left[\frac{1}{V_0} \sum_i \mathbf{P}_i V_i \right] : \dot{\bar{\mathbf{F}}} = \frac{1}{V_0} \sum_i \mathbf{P}_i : \dot{\bar{\mathbf{F}}} V_i = \frac{1}{2V_0} \sum_i \sum_{j \neq i} [\mathbf{f}_{ji} \otimes \mathbf{R}_{ij}] : \dot{\bar{\mathbf{F}}} \\ &= \frac{1}{2V_0} \sum_i \sum_{j \neq i} \mathbf{f}_{ji} \cdot [\dot{\bar{\mathbf{F}}} \cdot \mathbf{R}_{ij}] = \text{(on the other hand)} \frac{1}{2V_0} \sum_i \sum_{j \neq i} \mathbf{f}_{ji} \cdot \dot{\mathbf{r}}_{ij} \quad (2.66) \\ &\quad \Downarrow \\ &\quad \sum_i \sum_{j \neq i} \mathbf{f}_{ji} \cdot [\mathbf{r}_{ij} - \bar{\mathbf{F}} \cdot \mathbf{R}_{ij}] \doteq 0 \end{aligned}$$

It means that the power requirement is satisfied for

1. the periodicity on $\partial\mathcal{C}_0$;
2. $\mathbf{r}_{ij} = \bar{\mathbf{F}} \cdot \mathbf{R}_{ij}$ in \mathcal{C}_0 ;

It was thus proven that the global Cauchy-Born rule (2.54) follows from both the homogenisation assumption (2.63) and the power requirement (2.65) under consideration of the cellwise Cauchy-Born rule (2.57). But the real aim of the homogenisation is to obtain the validity of the Cauchy-Born rule on the boundary of RVE from (2.63) and the power requirement

$$\mathcal{W}_{macro} = \mathcal{W}_{micro}^{conti} \Rightarrow \bar{\mathbf{P}} : \dot{\bar{\mathbf{F}}} \doteq \frac{1}{V_0} \sum_i \mathbf{P}_i : \dot{\bar{\mathbf{F}}}_i V_i \quad (2.67)$$

without any additional assumption. Thereby, the sum over all atoms should be replaced by a sum over the only boundary atoms, i.e. a discrete analogue of the Gauss theorem should be considered⁴. The derivation of the Cauchy-Born or affine boundary conditions and consequently, a proof of

⁴Recall the Gauss theorem. Let $\mathbf{H} : \mathbb{R}^3 \rightarrow \mathcal{B}_0 \subset \mathbb{R}^3$ be a vector-valued function with the components $[P(X, Y, Z) \ Q(X, Y, Z) \ R(X, Y, Z)]$. Let \mathbf{H} be continuous and continuous differentiable in $\mathcal{B}_0 \cup \partial\mathcal{B}_0$. Then

$$\iiint_{\mathcal{B}_0} \left[\frac{\partial P}{\partial x} + \frac{\partial Q}{\partial y} + \frac{\partial R}{\partial z} \right] dx dy dz = \iint_{\partial\mathcal{B}_0} [P dy dz + Q dx dz + R dx dy].$$

This theorem can be rewritten in the vectorial format:

$$\iiint_{\mathcal{B}_0} \text{Div} \mathbf{H} dV = \iint_{\partial\mathcal{B}_0} \mathbf{H} \cdot \mathbf{N} dA$$

with the surface normal vector \mathbf{N}

the sufficiency of such boundary conditions is discussed in the appendix. But because of the large scale of the needed transformations, the question concerning the sufficiency of the affine boundary conditions also in the discrete case remains open. For further applications within the present work, an assumption about the Cauchy-Born deformation for the whole RVE is considered.

2.5 Finite Element Implementation

In this section, an application of the Continuum-Atomistic model based on the 1st-order Cauchy-Born rule within the frame of a standard non-linear finite element method (FEM) should be discussed. A non-linear FEM setting is described in the appendix. Further detailed description lies outside this work.

2.5.1 Continuum-Atomistic Constitutive Law

The main concept of the continuum-atomistic modelling has been discussed in section 2.3. Remember that according to the continuum-atomistic principle, the macroscopic strain energy density W_0 is a volume averaged energy of a crystallite corresponding to a point of continuum, see (2.30). Thereby, the format of the energy E_i of an atom with a number i has not be specified. Here, an application of two different energy functions should be discussed in detail. One of them is based on the Lennard-Jones pair potential (1.20), and the other is the EAM potential in the more complicated format (1.38).

The Lennard-Jones Pair Potential

The 1st two derivatives of the Lennard-Jones pair potential are given by

$$\frac{d\Phi^{LJ}(r)}{dr} = -\frac{24\varepsilon}{\sigma} \left[2 \left[\frac{\sigma}{r} \right]^{13} - \left[\frac{\sigma}{r} \right]^7 \right] \quad (2.68)$$

$$\frac{d^2\Phi^{LJ}(r)}{dr^2} = +\frac{24\varepsilon}{\sigma^2} \left[26 \left[\frac{\sigma}{r} \right]^{14} - 7 \left[\frac{\sigma}{r} \right]^8 \right] \quad (2.69)$$

According to (2.34) and under consideration of (1.20) and (2.32), the strain energy density in the material configuration obtains the following explicit format in this case:

$$W_0(\mathbf{F}) = \frac{2\varepsilon}{V_i} \sum_{j \neq i} \left[\left[\frac{\sigma}{|\mathbf{F} \cdot \mathbf{R}_{ij}|} \right]^{12} - \left[\frac{\sigma}{|\mathbf{F} \cdot \mathbf{R}_{ij}|} \right]^6 \right] \quad (2.70)$$

Due to the assumption (2.31), displacements of all atoms are equivalent and the necessity to average over the whole crystallite is therefore omitted. The atom i is then an atom inside the crystallite, say, the middle atom, see e.g. fig. 2.6. It is thereby important to check whether the whole cut-off circle lies within the representative cell, see Tadmor [88]. If this is not the case, the size of the cell must be chosen larger to obtain correct results. The size of the representative crystallite should generally be changed in dependence of the type of the external macroscopic load. Note that in general, a new representative crystallite of different size, structure and rotation can be defined for each element.

The material lattice configuration \mathcal{C}_0 with the site vectors \mathbf{R}_i , see. fig. 2.1, should be defined at the beginning of the simulation. For all simulations in this work, a close-packed two-dimensional lattice

is considered. Such lattice is characterised by a hexagonal atomic arrangement and corresponds to the (111)–plane of the fcc-structure highlighted in fig. 1.6 (b).

The expression (2.38) for the 1st Piola-Kirchhoff stress tensor in view of (2.5), (2.31), (2.32), (2.56) and (2.68) can be rewritten as

$$\begin{aligned} \mathbf{P}(\mathbf{F}) = \mathbf{P}_i &= \frac{1}{2V_i} \sum_{j \neq i} \frac{(\Phi_{ij}^{LJ})'}{r_{ij}} \mathbf{r}_{ij} \otimes \mathbf{R}_{ij} \\ &= -\frac{12\varepsilon}{V_i \sigma^2} \sum_{j \neq i} \left[2 \left[\frac{\sigma}{|\mathbf{F} \cdot \mathbf{R}_{ij}|} \right]^{14} - \left[\frac{\sigma}{|\mathbf{F} \cdot \mathbf{R}_{ij}|} \right]^8 \right] \mathbf{F} \cdot [\mathbf{R}_{ij} \otimes \mathbf{R}_{ij}] \end{aligned} \quad (2.71)$$

Finally, an explicit format for the tangent operator (2.41) results from (2.11), (2.31), (2.32), (2.68) and (2.69) in

$$\begin{aligned} \mathbb{L}(\mathbf{F}) &= \frac{1}{2V_i} \sum_{j \neq i} \left[\frac{(\Phi_{ij}^{LJ})'}{r_{ij}} \mathbf{I} \bar{\otimes} [\mathbf{R}_{ij} \otimes \mathbf{R}_{ij}] + \left[\frac{(\Phi_{ij}^{LJ})''}{r_{ij}^2} - \frac{(\Phi_{ij}^{LJ})'}{r_{ij}^3} \right] [\mathbf{r}_{ij} \otimes \mathbf{r}_{ij}] \bar{\otimes} [\mathbf{R}_{ij} \otimes \mathbf{R}_{ij}] \right] \\ &= -\frac{12\varepsilon}{V_i \sigma^4} \sum_{j \neq i} \left\{ \sigma^2 \left[2 \left[\frac{\sigma}{|\mathbf{F} \cdot \mathbf{R}_{ij}|} \right]^{14} - \left[\frac{\sigma}{|\mathbf{F} \cdot \mathbf{R}_{ij}|} \right]^8 \right] \mathbf{I} \bar{\otimes} [\mathbf{R}_{ij} \otimes \mathbf{R}_{ij}] \right. \\ &\quad \left. - \left[28 \left[\frac{\sigma}{|\mathbf{F} \cdot \mathbf{R}_{ij}|} \right]^{16} - 8 \left[\frac{\sigma}{|\mathbf{F} \cdot \mathbf{R}_{ij}|} \right]^{10} \right] [\mathbf{F} \otimes \mathbf{F}] \bar{\cdot} [\mathbf{R}_{ij} \otimes \mathbf{R}_{ij}] \bar{\otimes} [\mathbf{R}_{ij} \otimes \mathbf{R}_{ij}] \right\} \end{aligned} \quad (2.72)$$

The explicit expressions (2.71) and (2.72) for $\mathbf{P}(\mathbf{F})$ and $\mathbb{L}(\mathbf{F})$ respectively can now be substituted into the corresponding expressions for the nodal contribution to the internal force \mathbf{F}_I^{int} (C.17) and for the tangential stiffness matrix \mathbf{K}_{TIJ}^e (C.35). However, these explicit expressions have a rather complicated format and, moreover, are only applicable to the Lennard-Jones pair potential. It therefore seems to be reasonable to implement the general results (2.36) and (2.40) and then compute \mathbf{f}_{ij} , $\mathbf{k}_{ij}^{(m)}$ and $\mathbf{k}_{ij}^{(0)}$ separately for each type of potential according to (2.3), (2.8) and (2.9) respectively.

EAM Potential

In this case, the expression for the strain energy density takes the format (2.30) with the atomic contribution E_i given in (1.38). Note that E_i cannot now be represented as a sum over pairwise interactions Φ_{ij} as in the case with the Lennard-Jones pair potential. The 1st Piola-Kirchhoff stress tensor \mathbf{P} is given by (2.36). To obtain \mathbf{f}_{ji} according to (2.3), the derivative $E_{i,r_{ij}}$ is needed. A direct

calculation under consideration of (1.32)-(1.38) yields an explicit expression for $E_{i,r_{ij}}$:

$$\begin{aligned} E_{i,r_{ij}} &= \frac{1}{Z} \frac{\partial E^u}{\partial r_{ij}} + \frac{\partial \rho^{(0)}}{\partial r_{ij}} \left[\frac{\partial F(\rho/Z)}{\partial \rho} - \frac{\partial F(\rho^0/Z)}{\partial \rho^0} \right] \\ &= \frac{\varepsilon}{Z r_0} \left[\alpha^2 \left[\frac{r_{ij}}{r_0} - 1 \right] e^{-\alpha \left[\frac{r_{ij}}{r_0} - 1 \right]} - A\beta^{(0)} e^{-\beta^{(0)} \left[\frac{r_{ij}}{r_0} - 1 \right]} \ln(I) \right] \end{aligned} \quad (2.73)$$

with the notation

$$I = \frac{\sum_{\substack{k=1 \\ k \neq i}}^Z e^{-\beta^{(0)} \left[\frac{r_{ik}}{r_0} - 1 \right]}}{Z e^{-\beta^{(0)} \left[\frac{r_{ij}}{r_0} - 1 \right]}}. \quad (2.74)$$

An explicit expression $\mathbf{P}(\mathbf{F})$ is given below:

$$\begin{aligned} \mathbf{P}(\mathbf{F}) = \mathbf{P}_i &= \frac{\varepsilon}{Z r_0 V_i} \sum_{j \neq i} \left\{ \alpha^2 \left[\frac{|\mathbf{F} \cdot \mathbf{R}_{ij}|}{r_0} - 1 \right] e^{-\alpha \left[\frac{|\mathbf{F} \cdot \mathbf{R}_{ij}|}{r_0} - 1 \right]} \right. \\ &\quad \left. - A\beta^{(0)} e^{-\beta^{(0)} \left[\frac{|\mathbf{F} \cdot \mathbf{R}_{ij}|}{r_0} - 1 \right]} \ln(I(\mathbf{F})) \right\} \frac{\mathbf{F} \cdot [\mathbf{R}_{ij} \otimes \mathbf{R}_{ij}]}{|\mathbf{F} \cdot \mathbf{R}_{ij}|}. \end{aligned} \quad (2.75)$$

The expression (2.40) for \mathbb{L}_i contains parts of the atomic-level stiffness \mathbf{k}_{ij} ; the tensors $\mathbf{k}_{ij}^{(0)}$ and $\mathbf{k}_{ij}^{(m)}$ are given in (2.8) and (2.9) respectively. To calculate these tensors, $E_{i,r_{ij}r_{ij}}$ and $E_{i,r_{ij}r_{im}}$, the 2nd derivatives of E_i with respect to r_{ij} and r_{im} , $m \neq j$ are needed. Simple but tedious direct calculations using (2.73) and (2.74) lead to the following results:

$$\begin{aligned} E_{i,r_{ij}r_{ij}} \doteq \frac{\partial E_{i,r_{ij}}}{\partial r_{ij}} &= E_{j,r_{ji}r_{ji}} = \frac{\varepsilon}{Z r_0^2} \left[\alpha^2 \left[1 - \alpha \left[\frac{r_{ij}}{r_0} - 1 \right] \right] e^{-\alpha \left[\frac{r_{ij}}{r_0} - 1 \right]} \right. \\ &\quad \left. - A\beta^{(0)2} e^{-\beta^{(0)} \left[\frac{r_{ij}}{r_0} - 1 \right]} \left[\ln(I) - \frac{1}{ZI} + 1 \right] \right] \end{aligned} \quad (2.76)$$

$$E_{i,r_{ij}r_{im}} \doteq \frac{\partial E_{i,r_{ij}}}{\partial r_{im}} \Big|_{\substack{m \neq i \\ m \neq j}} = E_{j,r_{ji}r_{mi}} = \frac{\varepsilon}{Z r_0^2} A\beta^{(0)2} e^{-\beta^{(0)} \left[\frac{r_{ij}}{r_0} - 1 \right]} e^{-\beta^{(0)} \left[\frac{r_{im}}{r_0} - 1 \right]} \frac{1}{I}. \quad (2.77)$$

Substituting (2.73), (2.74), (2.76) and (2.77) into (2.8) and (2.9) yields an explicit expression for $\mathbb{L} \equiv \mathbb{L}_i$ according to (2.40). Note that in this case, $\mathbf{k}_{ij}^{(m)}$ differ from zero, and hence \mathbb{L} contains a 2^{nd} sum over m . The ansatz $r_{ij} = |\mathbf{F} \cdot \mathbf{R}_{ij}|$ allows to represent \mathbb{L} again as a function of \mathbf{F} . The whole explicit expression for $\mathbb{L}(\mathbf{F})$ cannot be given here because of its length and complexity. However, the explicit derivatives given above are sufficient for the implementation.

Pull-Back and Push-Forward

The pull-back and push-forward operations of the two-field tensors $\mathbf{P}(\mathbf{F})$ and $\mathbb{L}(\mathbf{F})$ are especially simple. Indeed, to pull \mathbf{P} or \mathbb{L} back into the material configuration, \mathbf{r}_{ij} should simply be substituted by \mathbf{R}_{ij} in the corresponding expressions. Analogously, the push-forward operation can be carried out by substituting \mathbf{R}_{ij} by \mathbf{r}_{ij} .

2.5.2 The Structure of the Simulation Code

The code consists of two parts. The 1st one is the usual non-linear finite element frame described in appendix. The 2nd part is related to the description of the representative crystallite and contains a computation of homogenised stresses and tangent operators. The main idea of the simulation is that a representative crystal lattice corresponds to each integration point. The macroscopic deformation gradient in the integration point represents generally the boundary condition for the microscopic RVE. For the simulations in the present chapter, only a homogeneous deformation for the whole RVE is considered so that the Cauchy-Born rule (2.31) is valid for all atoms in the RVE. This principle is schematically represented in fig. 2.13.

After the load step of $n - 1$, an application of the new macroscopic deformation gradient \mathbf{F}_e^{n-1} computed for the element e at the macro scale on the basis of the homogenised 1st Piola-Kirchhoff stress \mathbf{P}_e^{n-1} to the representative crystallite at the micro scale causes the new displacements of the lattice atoms and hence, the next-neighbours list of the atom i must be updated after each step. Due to such an update, the new \mathbf{P}_e^n can be computed according to (2.36), whereby the summation runs over the only current next-neighbours of i . These uncompensated element stresses are then used as an input for the next equilibrium iteration, which yields the new deformation gradient \mathbf{F}_e^n .

An important question is the choice of units. Because of the possible application to the nano or micro mechanics, the nanometer ($1 \text{ nm} = 10^{-9} \text{ m}$) is chosen as the unit length and the nanoNewton ($1 \text{ nN} = 10^{-9} \text{ N}$) as the unit force. Another units result from both defined units. E.g. the energy E has the dimension

$$\dim[E] = nN \cdot nm = 10^{-18} \text{ J}$$

where $1 \text{ J} = \frac{\text{kg} \cdot \text{m}^2}{\text{s}^2}$. The strain energy density W_0 has principally the same dimension as the elasticity modules such as the Young's modulus i.e. the dimension of pressure. W_0 obtains the following dimension:

$$\dim[W_0] = \dim[E/V] = nN/nm^2 = \text{GPa}; \quad 1 \text{ Pa} = N/m^2$$

For the structure of the underlying crystallite, the material constants of Aluminium have been used. The 1st parameter is the minimal atomic separation in Al: $r_0 = 0.286 \text{ nm}$. Another one is the sublimation energy i.e. the energy needed to remove an atom from the crystal⁵: $E_0 = 3.58 \text{ eV/atom} =$

⁵1 eV = 1.602 · 10⁻¹⁹ J

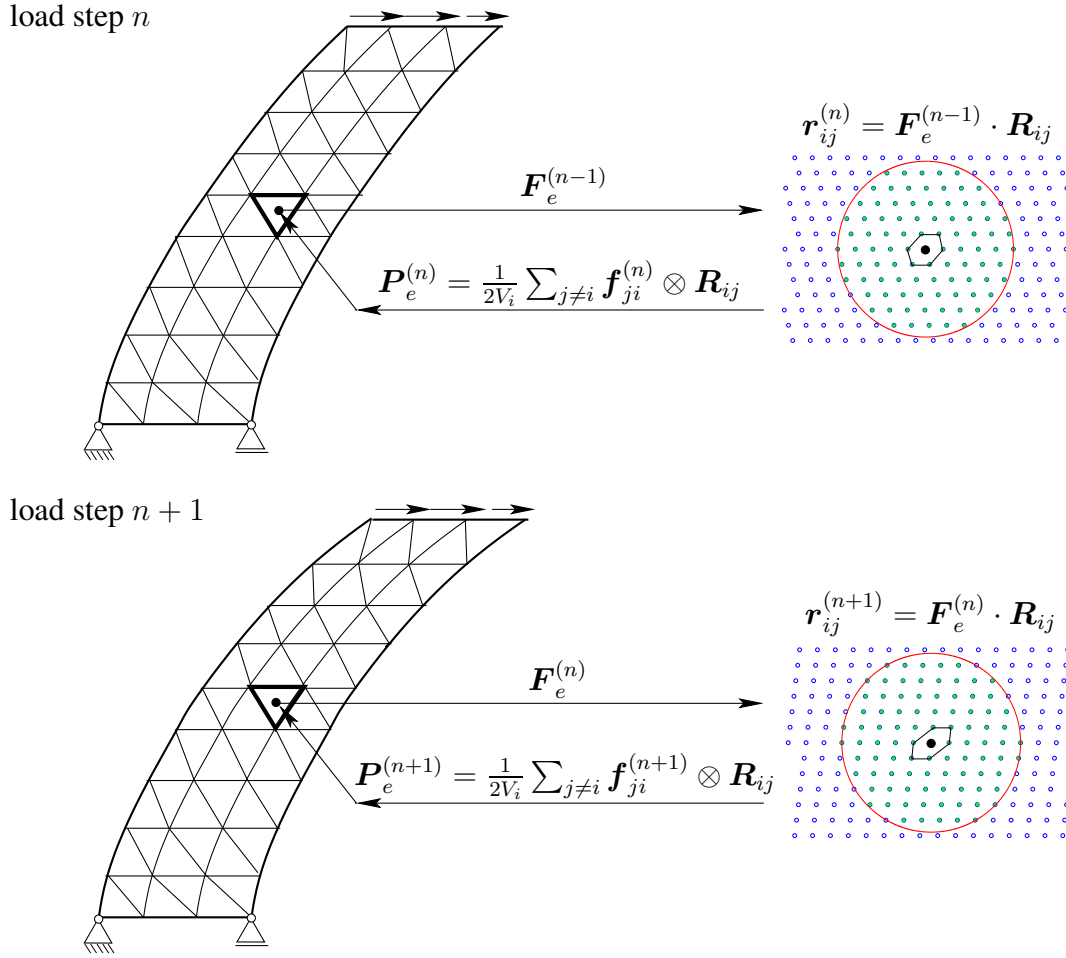


Figure 2.13: Operating mode of the two-scale continuum-atomistic model. Note that both deformed configurations are considered arbitrary and not a result of any simulation.

$0.574 nN \cdot nm/atom$. These parameters have been used to find parameters ϵ and σ for different number of the next neighbours. Thereby, the 1st requirement is the stress-free material lattice configuration \mathcal{C}_0 . It means that the norm of the 1st Piola-Kirchhoff stress tensor (2.71) must vanish in this configuration. The 2nd one is that the energy of an atom in the unloaded lattice calculated according to (2.70) must yield the sublimation energy. These two non-linear equations with the unknowns σ and ϵ have been solved for different length of the cut-off radius using MATLAB optimisation tools. Some results are given below in tab. 2.1. For all examples discussed in this chapter, $r_c = 3r_0$ has been used, cf. fig. 2.8.

In the case of the EAM potential, the only next neighbours of the atom i are considered. A set of parameters for Al given in [5] for simulations using this type of energy function is shown in tab. 2.2. Here, Z is the coordination number i.e. the number of the next neighbours in the lattice. For the planar case considered here $Z = 6$; in the three-dimensional lattice $Z = 12$ for Al. A further parameter to be defined is the area V_i (the volume in the three-dimensional case) of the Voronoi polyhedron displayed

n	$\varepsilon, nN \cdot nm$	σ, nm
1	$E_0/3$	$2^{-1/6}r_0$
2	0.1729	0.2569
3	0.1706	0.2572
4	0.1701	0.2573
5	0.1699	0.2573
12	0.1697	0.2573

Table 2.1: Parameters ε and σ of the Lennard-Jones pair potential for different cut-off radii $r_c = n r_0$ with the lattice constant $r_0 = 0.286 nm$ and the sublimation energy $E_0 = 0.574 nN \cdot nm/atom$

$\varepsilon, nN \cdot nm$	r_0, nm	α	$\beta^{(0)}$	Z	A
E_0	r_0	4.61	2.21	6	1.07

Table 2.2: Parameters for the EAM potential for a monoatomic system of fcc type

in fig. 2.6. A simple calculation leads to the following value in the planar case:

$$V_i = \sqrt{3} r_0^2 / 2 = 0.071 nm^2$$

2.6 Examples

Some results of the continuum-atomistic computation are presented in this section. Thereby, both the Lennard-Jones and the EAM potentials described above state a constitutive law in these simulations. Note that the model considered in all simulations only works in the elastic region and fails as soon as the elastic limit is reached. The elastic-plastic transition is discussed in the following chapters.

2.6.1 Indentation Test

The indentation test is an important method for determining of elastic as well as plastic material properties. The indentation at the nanoscale or the nanoindentation allows to determine such properties of e.g. thin films and other low-dimensional structures. A number of researchers deal with the simulation of the indentation at nanoscale, see e.g. Tadmor [88], Huber [40]. The example presented here contains a 2D simulation of the indentation with a flat, pyramidal and spherical indenters. Thereby, each indenter is assumed to be absolutely rigid and the friction between the indenter and sample is not considered. The load is applied during several load steps by using displacement boundary conditions. Fig. 2.14 shows the sample to be indented with constraints. Because of the problem symmetry in x-direction, the symmetry boundary conditions have been applied to reduce the size of the problem. For the discretisation, the isoparametric triangular three-node elements described in appendix have been used. The triangulation has been done with the commercial code PATRAN and is shown in fig. 2.15. The FE model consists of 1012 elements and 1072 nodes.

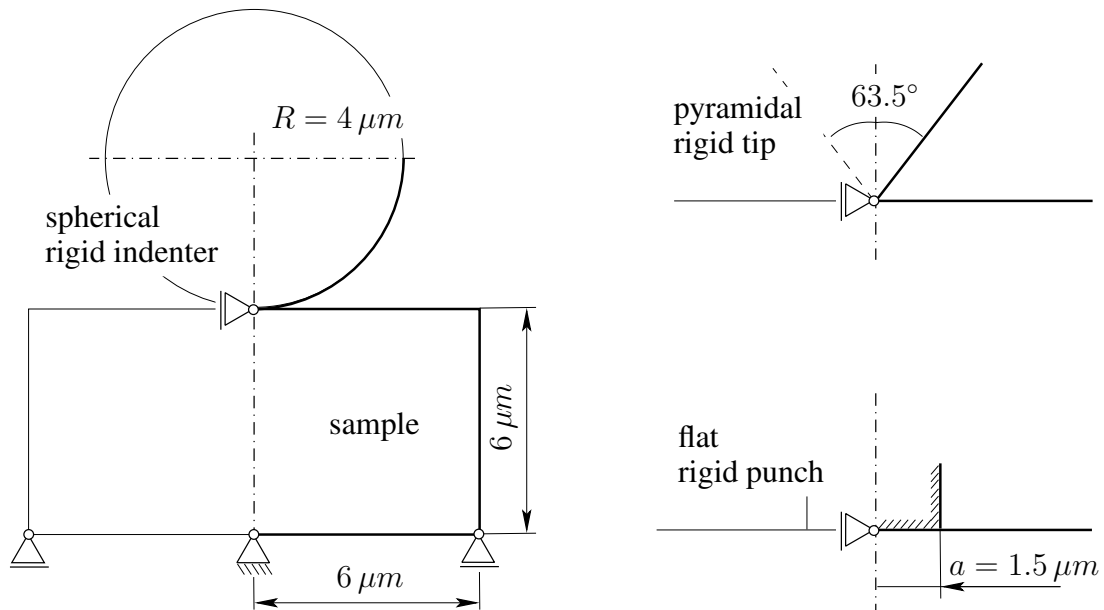


Figure 2.14: Geometrical settings of the indentation test. A rectangular sample (on the left) with the rigid spherical indenter. On the right: two additional indenters, a pyramidal Berkovich tip and a flat punch.

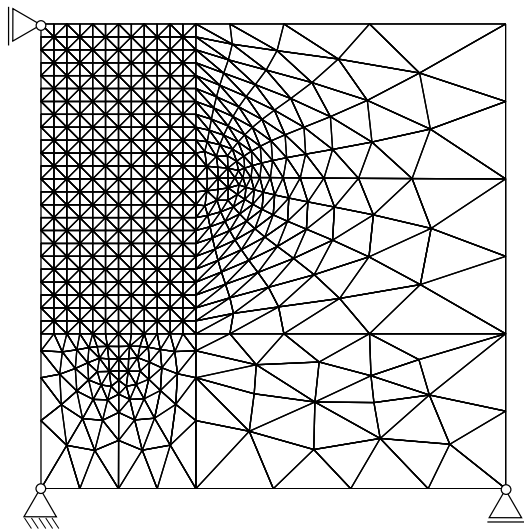
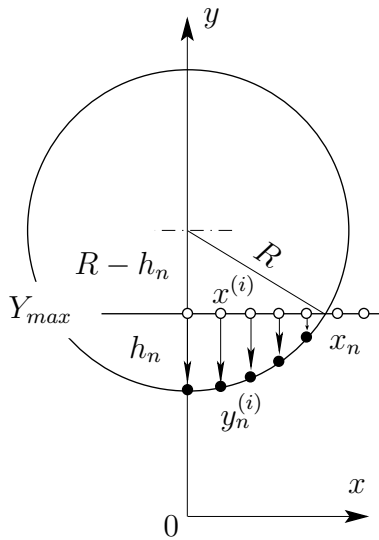


Figure 2.15: Discretized sample. The isoparametrical triangular three-nodes elements have been used here.

Spherical Indenter

In this case, the beginning contact takes place in only one node at the top left corner. But already after the 1st step, more than one node take part in the contact. After the load step $n - 1$, a new penetration depth h_n should be prescribed. Simple geometrical consideration shown in fig. 2.16 permits the determination of the contact area x_n and the new prescribed nodal positions y_n according to (2.78) where Y_{max} denotes the y -coordinate of the sample's top edge and $x^{(i)}$ is the x -coordinate of the node i in the material configuration. As soon as x_n is known, the new set of nodes taking part in the contact can be determined and the new displacement boundary conditions can be stated.



$$x_n = \sqrt{2Rh_n - h_n^2}$$

$$y_n^{(i)} = Y_{max} + (R - h_n) - \sqrt{R^2 - (x_n^{(i)})^2} \quad (2.78)$$

Figure 2.16: On the determination of a new nodal position after the step $n - 1$. The white-filled circles exhibit the initial nodal positions at the top edge of the sample. The black-filled circles are the newly prescribed nodal positions for the step n computed according to (2.78).

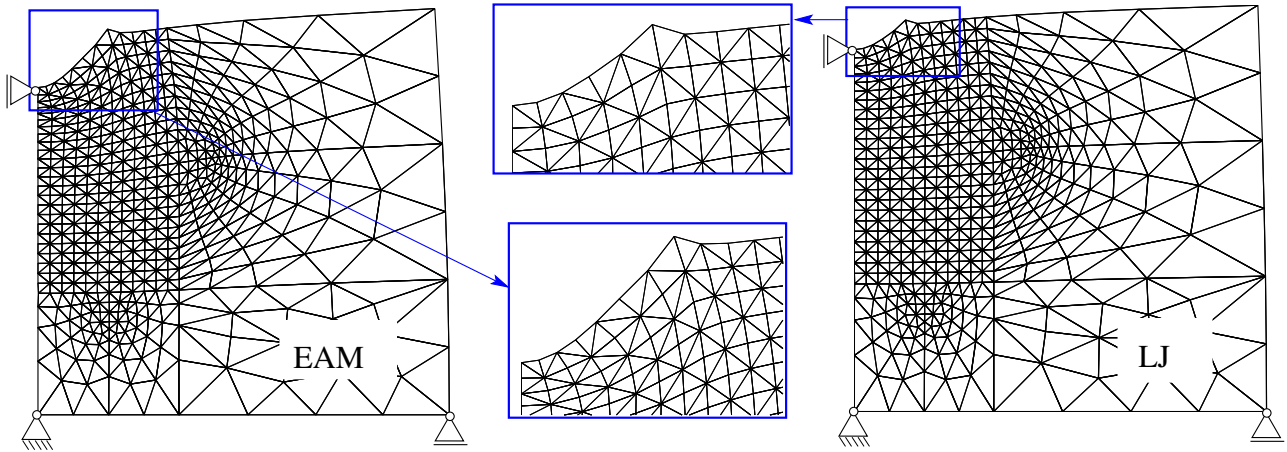


Figure 2.17: Spatial configuration corresponding to the maximum achievable elastic deformation according to the Cauchy-Born rule for both Lennard-Jones and EAM energy functions. The displacements are represented with a scaling factor 5 in comparison to the true displacements.

Spatial configurations obtained by using the LJ and the EAM energy potentials are exhibited in fig. 2.17. These configurations correspond to the maximum achievable elastic deformation applied according to the Cauchy-Born rule. To achieve a better resolution, all displacements are scaled with a factor 5. Evidently, the EAM potential allows higher elastic deformations than the LJ potential.

The corresponding load-displacement diagrams for both potentials compared with an experimental curve ⁶ are shown in fig. 2.18. The vertical displacement h of the top left corner corresponding to the middle point of the indenter is plotted in the x-axis. The computed material response P i.e. the internal force (y-axis) consists of the contributions of the nodes taking part in the contact. The jumps in the

⁶The indentation test was made by Dipl.-Ing. T. Dietz at the Institut für Materialforschung II, Forschungszentrum Karlsruhe, with the nanoindenter XP from MTS System. A sample consisting of the 99.99% Al has been indented with three different diamond tips: flat punch with the circular cross section of radius $5 \mu\text{m}$, spherical indenter with the radius of $10 \mu\text{m}$ and the Berkovich 3-face pyramid with the cone angle of 65.3° .

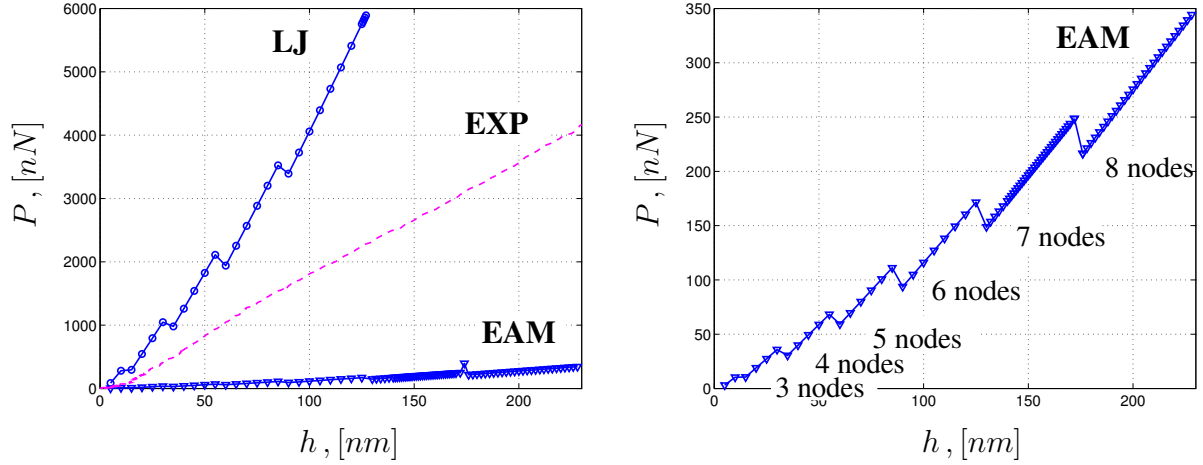


Figure 2.18: On the left: load-displacement diagrams for the indentation of the spherical indenter obtained by using the Lennard-Jones (\circ) and the EAM (∇) energy functions compared with the experimental curve (dashed line). The prescribed vertical displacement h of the top left corner corresponding to the middle point of the indenter is plotted in the x-axis. The computed material response P is plotted in the y-axis. Thereby, the exhibited internal force is the sum over the contributions of all nodes taking part in the contact. On the right: load-displacement diagram for the EAM energy function. The jumps in the displacement correspond to an inclusion of a new node in the contact and are mesh-dependent.

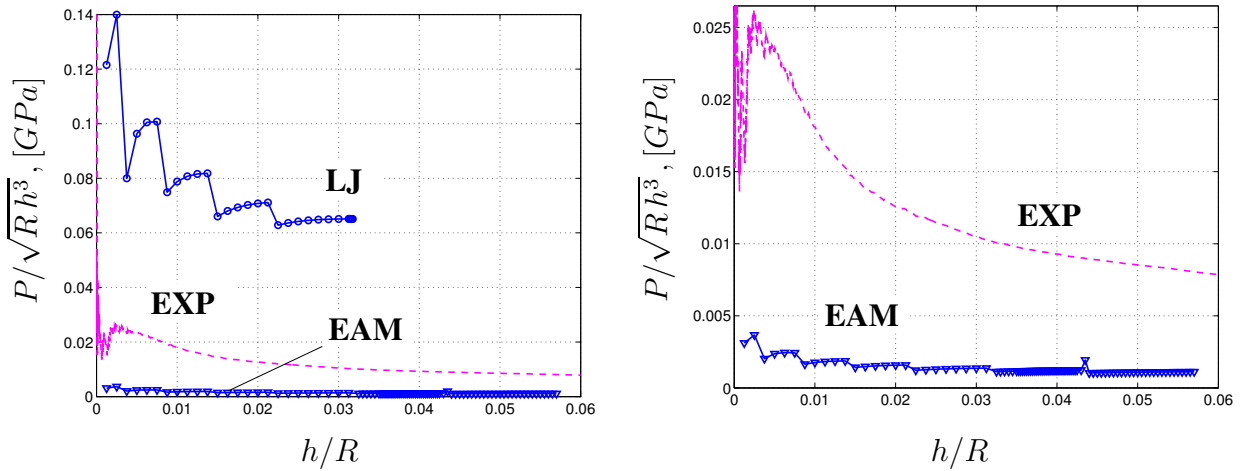


Figure 2.19: $P/\sqrt{R}h^3 - vs. - h/R$ -curves obtained by using the Lennard-Jones (\circ) and the EAM (∇) energy functions compared with an experimental curve (dashed line). On the right: experimental and EAM $P/\sqrt{R}h^3 - vs. - h/R$ -curves drawn to a larger scale.

displacement are caused by involvement a new node in the contact. The 1st jump corresponds e.g. to the involvement of the 3rd node; the 2nd jump - to the involvement of the 4th node and so on. These jumps are mesh-dependent. The maximum penetration depth, which is achieved with the Lennard-Jones (LJ) potential is 127 nm whereas the EAM potential allows to reach the depth of about 230 nm. Thereby, the material response is about 6 μN and 0.35 μN respectively.

The experimental curve lies between the curves for both potentials. However, a direct comparison with experiment cannot be carried out since the indenters in the simulation and in the experiment have different sizes. Admittedly, the following expression, which is valid for a spherical indenter in the elastic region is proportional to the Young's modulus and therefore, is independent of the size of indenter, see e.g. Huber [40]:

$$\frac{P}{\sqrt{R}h^3} = const \quad (2.79)$$

This expression is shown in fig. 2.19 as a function of the dimensionless penetration depth h/R . Firstly, all curves exhibit the same qualitative behaviour. Moreover, the EAM curve quantitatively tends to the experimental curve stronger than the LJ curve.

Pyramidal Tip

As in the previous case, the contact takes place first in only one node. This situation however remains unchanged for all load steps so that the model contains a singularity similar to the application of a single force. This results in a relatively small elastic deformation in the simulation, which already fails at relatively small penetration depths. Note that indentation experiments yield same result. The contact area x_n and the newly prescribed nodal positions y_n can be determined according to (2.81). The corresponding geometrical considerations are explained in fig. 2.20.

The maximum achievable elastically deformed configurations are shown in fig. 2.21. The displacements are scaled with a factor 3. The EAM potential allows to reach a higher penetration depth also in this case.

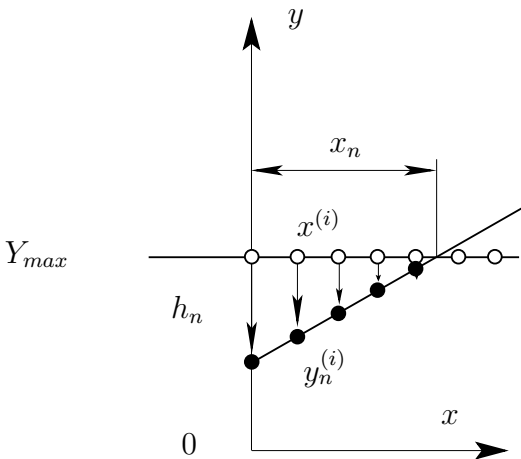
The load-displacement diagrams are shown in fig. 2.22. Here, the prescribed vertical displacement of the left top corner of the sample vs. the computed vertical internal force at this corner is shown. In view of the constant number of nodes taking part in contact during the simulation, the load-displacement curves exhibit no jumps as in the previous case.

The cone angle of 63.5° used in the simulation is a standard angle of the Berkovich pyramid used in the corresponding indentation test. Therefore, the simulation results can directly be compared with the experimental results. The comparison shows that the EAM curve again qualitatively tends to the experimental curve.

Note that also for a pyramidal indenter exists an expression similar to (2.79), which is proportional to the Young's modulus, see e.g. Huber [40]:

$$\frac{P}{h^2} = const \quad (2.80)$$

This expression is plotted in fig. 2.23 as a function of the penetration depth h . The quantitative agreement of the EAM and the experimental curves can be found also here.



$$\begin{aligned} x_n &= h_n \tan \alpha \\ y_n^{(i)} &= Y_{max} + h_n \left(\frac{x^{(i)}}{x_n} - 1 \right) \end{aligned} \quad (2.81)$$

Figure 2.20: On the determination of a new nodal position after the step $n - 1$. The white-filled circles exhibit the initial nodal positions at the top edge of the sample. The black-filled circles are the newly prescribed nodal positions for the step n computed according to (2.81).

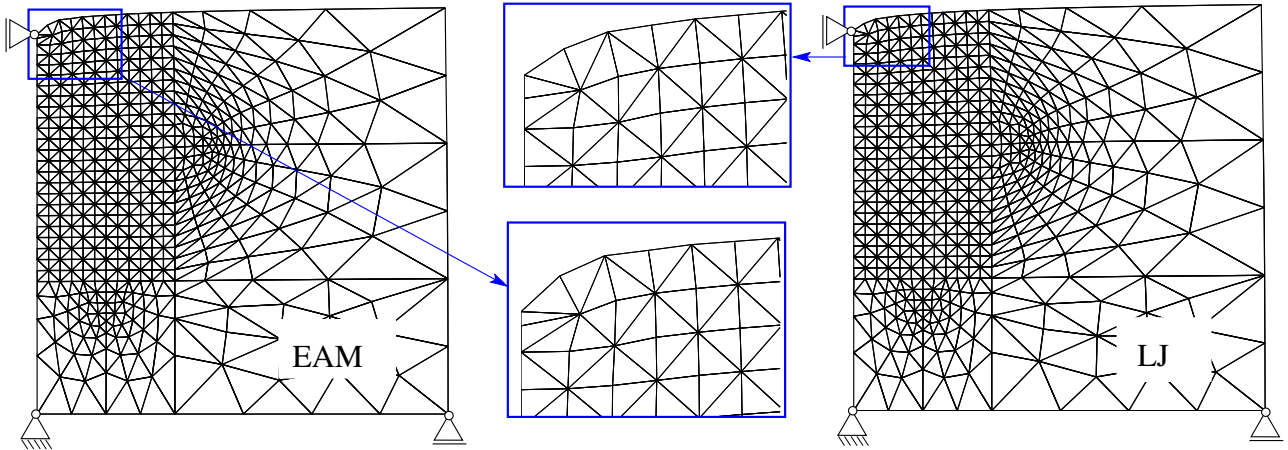


Figure 2.21: Spatial configuration corresponding to the maximum achievable elastic deformation according to the Cauchy-Born rule for both Lennard-Jones and EAM energy functions. The displacements are represented with a scaling factor 3 in comparison to the true displacements.

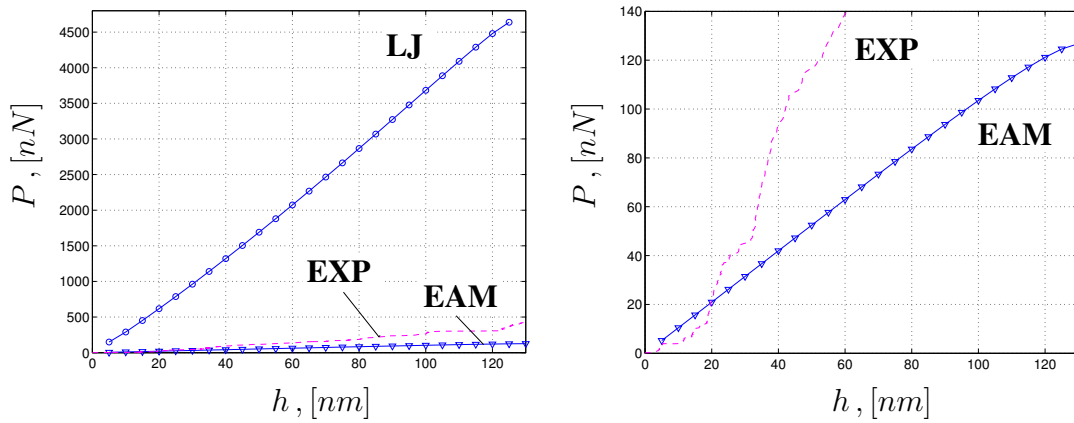


Figure 2.22: On the left: load-displacement diagrams for the indentation of the pyramidal (Bercovich) tip obtained by using the Lennard-Jones (\circ) and the EAM (∇) energy functions compared with the experimental curve (dashed line). The prescribed vertical displacement h of the top left corner corresponding to the middle point of the tip is plotted in the x-axis. The computed material response P is plotted in the y-axis. On the right: load-displacement diagram for the EAM energy function compared with the experimental curve.

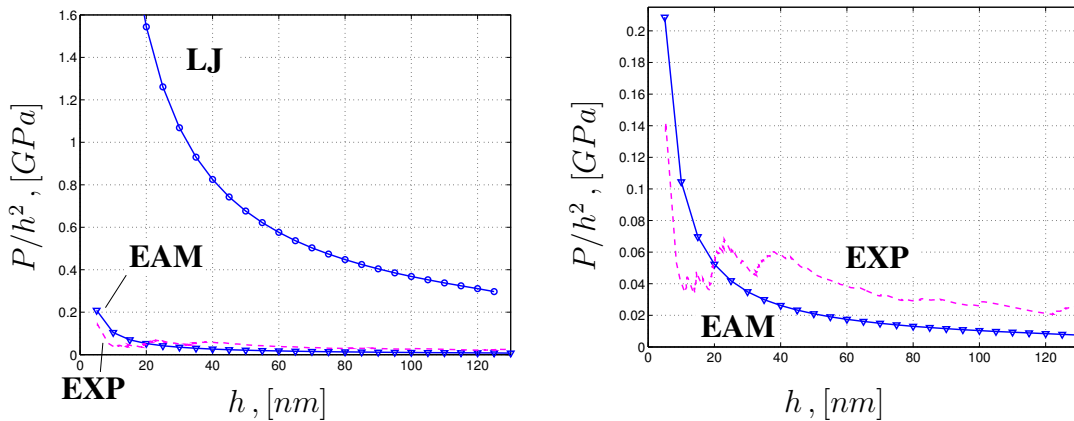


Figure 2.23: $P/h^2 - vs. - h$ -curves obtained by using the Lennard-Jones (\circ) and the EAM (∇) energy functions compared with an experimental curve (dashed line). On the right: experimental and EAM $P/h^2 - vs. - h$ -curves drawn to a larger scale.

Flat Indenter

In the case of the indentation with a flat punch, the nodes taking part in the contact (10 in this problem) are defined at the beginning and this set remains unchanged during the simulation so that the load is distributed among these nodes. After each load step, all nodes underlying the displacement boundary conditions obtain a new identical displacement. The deformed configurations for the maximum elastic deformation reached by using the LJ and the EAM potentials are shown in fig. 2.24.

The corresponding load-displacement diagrams are depicted in fig. 2.25. The comparison with other

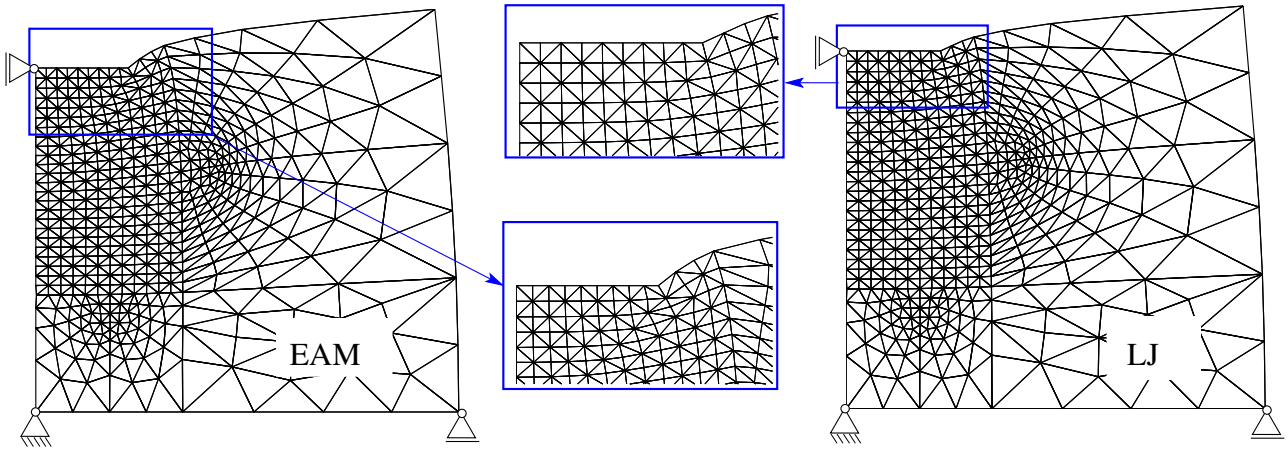


Figure 2.24: Spatial configuration corresponding to the maximum achievable elastic deformation according to the Cauchy-Born rule for both Lennard-Jones and EAM energy functions. The displacements are presented with a scaling factor 2 in comparison to the true displacements.

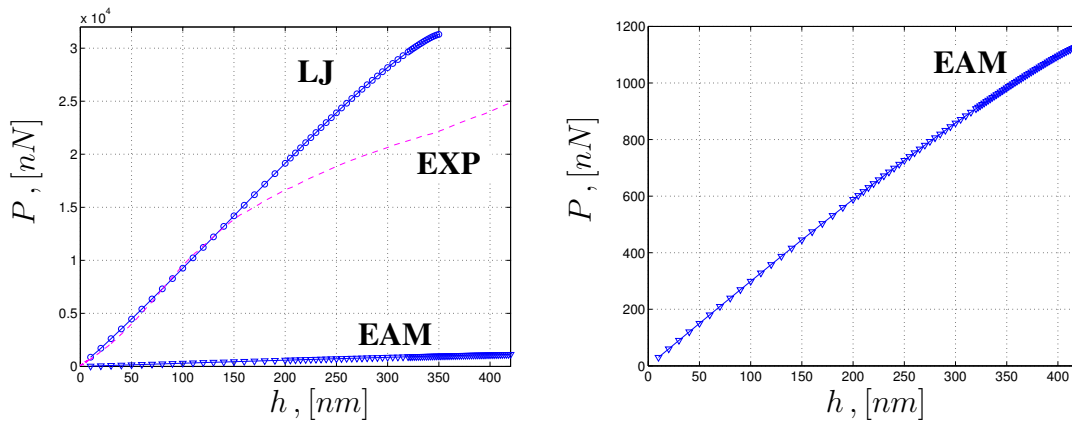


Figure 2.25: On the left: load-displacement diagrams for the indentation of the flat punch obtained by using the Lennard-Jones (\circ) and the EAM (∇) energy functions compared with the experimental curve (dashed line). The prescribed vertical displacement h of the top left corner corresponding to the middle point of the indenter is plotted in the x-axis. The computed material response P is plotted in the y-axis. Thereby, the exhibited internal force is the sum over the contributions of all nodes taking part in contact. On the right: load-displacement diagram for the EAM energy function.

cases described above shows that the possible elastic deformation is the largest for the flat punch.

Note that the application of the EAM potential leads to a higher penetration depth also in this case. The cross section radius a of the experimental punch differs from those used in the simulation. For this reason, the expression

$$\frac{P}{ah} = const, \quad (2.82)$$

which is similar to (2.79) and (2.80) has been used to compare the experimental and simulation results. It follows from the diagrams in fig. 2.26 that the EAM potential yields quantitatively better results than the LJ potential although a good agreement of the experimental and LJ load-displacement curves.

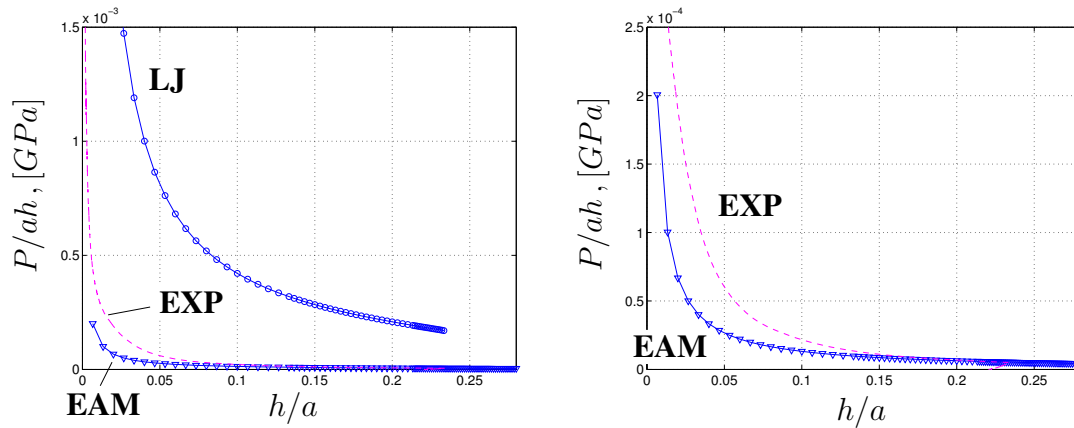


Figure 2.26: $P/ah - vs. - h/a$ -curves obtained by using the Lennard-Jones (\circ) and the EAM (∇) energy functions compared with an experimental curve (dashed line). On the right: experimental and EAM $P/h^2 - vs. - h$ -curves drawn to a larger scale.

All Three Types of Indenters

A comparison of the load-displacement diagrams for all three types of indenters is shown in fig. 2.27 (a) and (b) for the LJ and EAM potentials respectively. Except for the mesh-dependent jumps, the indentations with spherical and pyramidal tips give rise to similar material responses. In contrast, the flat punch causes considerably higher internal forces for the same deformations. The experimental data shown on the right diagram of this fig. exhibit the same qualitative behaviour and therewith support the simulation results.

Experimental and computed $P/h^2 - vs. - h$ - curves depicted in fig. 2.28 exhibit also an identical qualitative behaviour.

Unfortunately, it is impossible to compare yield stresses obtained from the simulations with the experimental yield stress due to unavailable unloading data.

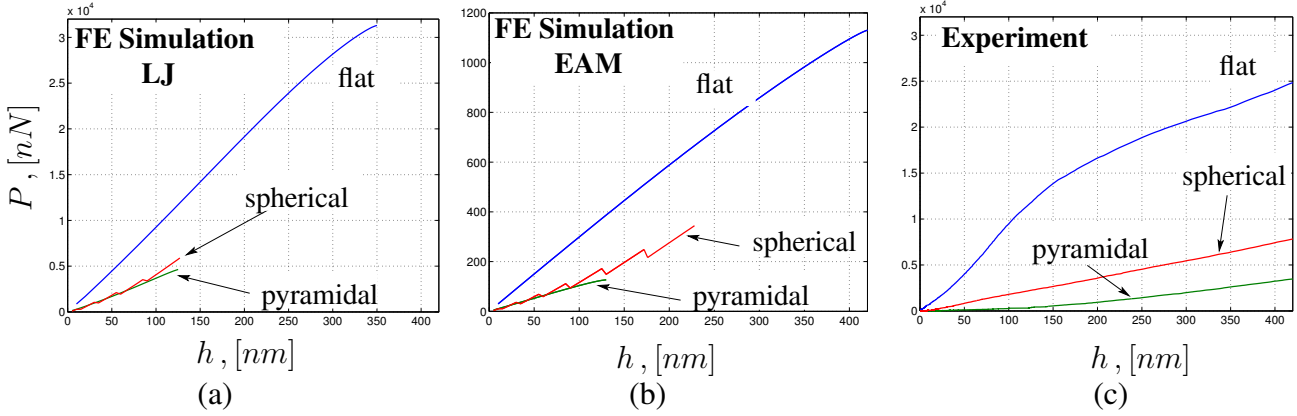


Figure 2.27: Comparison of the load-displacement diagrams for the indentation with the spherical, pyramidal and flat tips: indentation experiment (c) and continuum-atomistic simulation using the Lennard-Jones (a) and the EAM (b) potentials. Whereas the indentation with the spherical and pyramidal tips cause a similar material response, the indentation with the flat punch leads to higher internal forces for the same deformations.

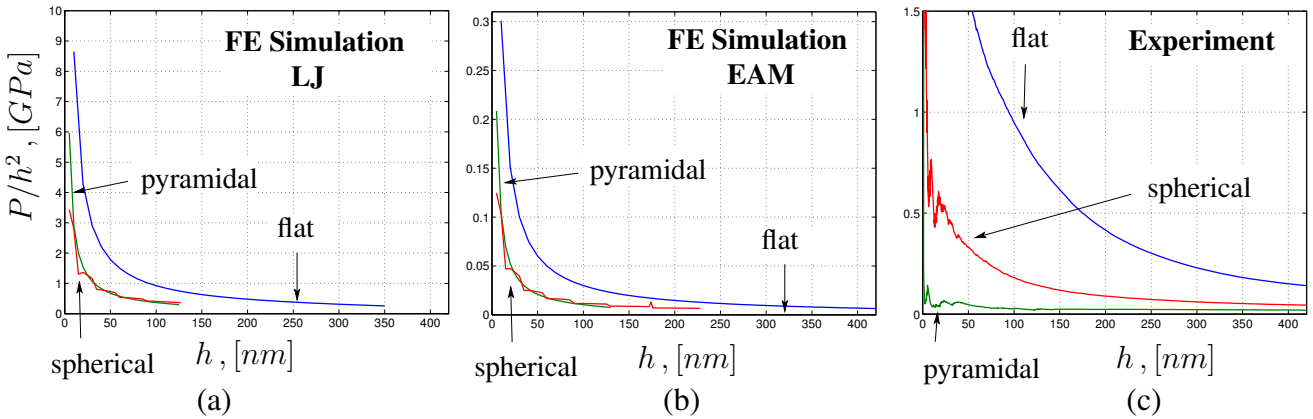


Figure 2.28: Comparison of the P/h^2 – vs. – h – curves for the indentation with the spherical, pyramidal and flat tips: indentation experiment (c) and continuum-atomistic simulation using the Lennard-Jones (a) and the EAM (b) potentials.

2.6.2 Horizontal Shearing

Consider a 2D rectangular plate with the dimensions shown in fig. 2.29 (a). The bottom edge of the plate is fixed and only a horizontal displacement is permitted at the top edge. A distributed horizontal tilting load is applied to the top edge of the plate. The sample in this example has been meshed manually by an explicit definition of the nodal coordinates and element connections. The meshed sample is shown in fig. 2.29 (b). This simulation is force-controlled, i.e. the distributed force acting on the top edge obtains a prescribed increment after each load step. The discretised model consists of 60 elements and 39 nodes. The Lennard-Jones potential has been used as a constitutive law. The deformed configuration corresponding to the maximum elastic deformation is shown in fig. 2.30 together with the load-displacement diagram. This diagram exhibits the horizontal displacement of the left top corner vs. the sum of the internal forces acting in the loaded nodes on the top edge.

A study of the load-displacement diagrams obtained in all presented examples shows that in spite of a strong non-linear constitutive law, the simulations fail at the deformations near the linear limit. The origin of this failure is studied in the next chapter.

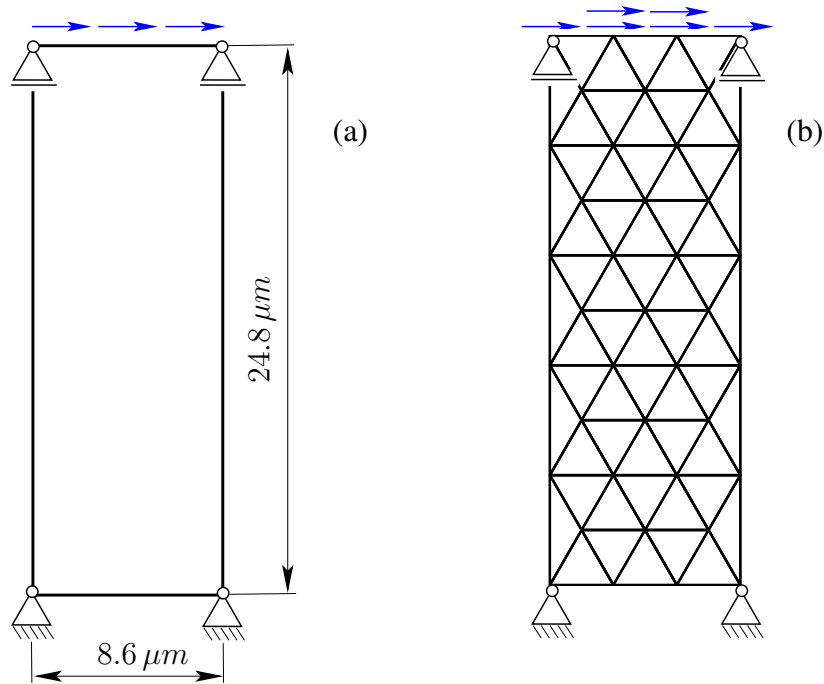


Figure 2.29: (a) Geometry of the sample being tested with the constraints and the loads; (b) initial manually generated FE mesh with the constraints and the discretised load.

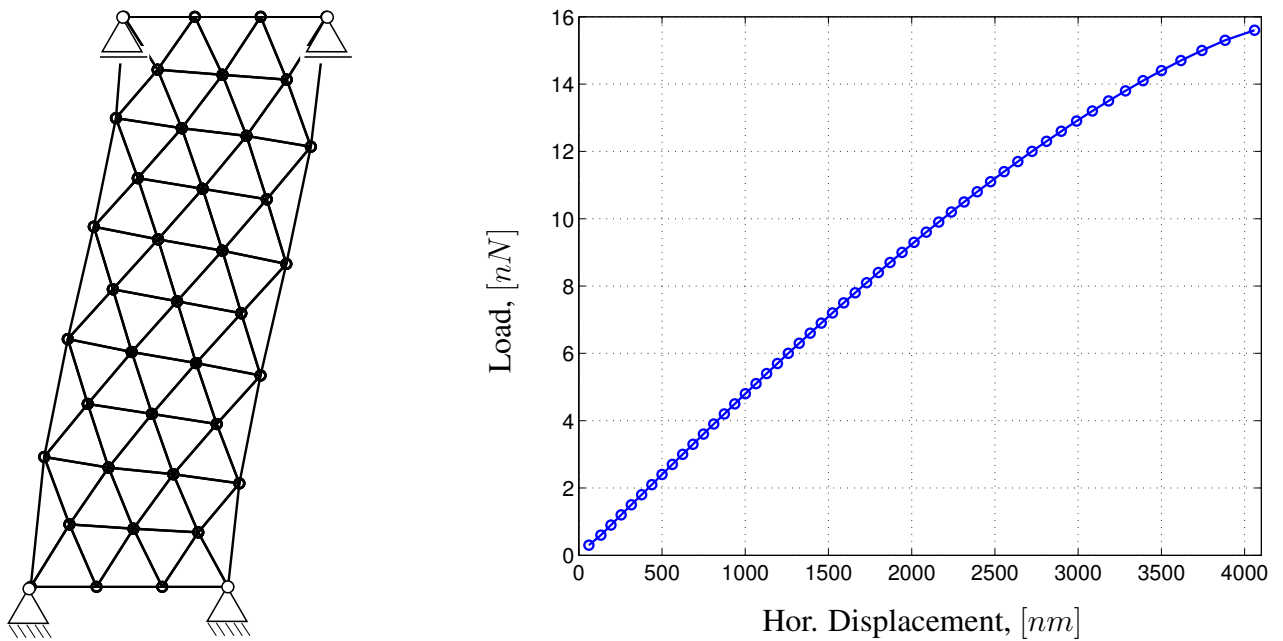


Figure 2.30: The maximum achievable elastically deformed configuration with the corresponding load-displacement diagram.

Chapter 3

Microstructures and Energy Minimisation

“Microstructures often develop on many different scales in space and in time, and to understand the formation, interaction, and overall effect of these structures is a great scientific challenge...”

Stefan Müller, “Variational models for microstructure and phase transitions”

In the previous part, the natural limit of the Cauchy-Born rule has been reached. In this chapter, the following questions should be discussed:

- Why does the Cauchy-Born rule fail?
- How can the critical deformation be detected?
- What should be done to overcome the failure of the Cauchy-Born rule?

To obtain plausible answers to these questions, the development of microstructures should be explained in terms of energy minimisation in variational problems. Another citation from the above mentioned lectures of Professor Müller can be included here: “The reason for the formation of such microstructure is typically that no exact optimum exists and optimizing sequences have to develop finer and finer oscillations (which may only be limited by effects neglected in the model, such as the underlying atomic structure).” Fig. 3.1 gives some examples of microstructures in different materials.

Recall the setting of the problem. In this work, all materials are considered to be hyperelastic. As a consequence, the following minimisation problem has been handled:

$$I(\varphi) \doteq \int_{\mathcal{B}_0} W_0(\mathbf{F}) dV - \Pi(\varphi) \longrightarrow \inf \quad (3.1)$$

where

- $\mathcal{B}_0 \subset \mathbb{R}^2$ is a bounded open domain considered as the material configuration;



(a)



(b)

Figure 3.1: Microstructure in a single crystal of the shape-memory alloy $Cu - Al - Ni$. (a) The sets of needles ending at perpendicular interfaces. The different colours show the two variants of the martensite involved. The specimen normal is $[100]$. The specimens are under biaxial tension at room temperature (C. Chu and R. D. James, Department of Aerospace Engineering and Mechanics, Minneapolis). (b) Unloaded specimen after a uniaxial tension experiment with $[111]$ (vertical) tension axis (T. W. Shield, *J. Mech. Phys. Sol.*, 43(6), 1995, pp. 869-895).

- $\varphi \in W^{1,p}(\mathcal{B}_0; \mathbb{R}^2) : \mathcal{B}_0 \rightarrow \mathbb{R}^2$ is a given non-linear map, so that the spatial configuration is given by $\varphi(\mathcal{B}_0)$;
- $\mathbf{F} \doteq \nabla_{\mathbf{X}} \varphi \in \mathbb{R}_+^{2 \times 2}$, $\mathbf{X} \in \mathcal{B}_0$, is the deformation gradient;
- $W_0(\mathbf{X}; \mathbf{F}) : \mathcal{B}_0 \times \mathbb{R}_+^{2 \times 2} \rightarrow \mathbb{R}$ is a stored energy function;
- $\mathbb{R}^{2 \times 2}$ is the set of 2×2 matrices;
- $\mathbb{R}_+^{2 \times 2} \doteq \{\mathbf{F} \in \mathbb{R}^{2 \times 2} : \det \mathbf{F} > 0\}$

In this model, the elastic crystal is considered as a non-linear elastic continuum due to application of the Cauchy-Born rule, see e.g. Ericksen [27].

The calculus of variations consists of two main approaches: classical and direct method. The **classical** method goes back to Lagrange, Weierstrass, Jacobi, Hamilton and has been developed essentially in 19th century. According to this method, the zeros of the 1st variation of I should be found (the Euler-Lagrange equations) and then the positivity of the 2nd variation around the solution should be studied.

The **direct** methods have been developed by Hilbert and Lebesgue at the beginning of 20th century. To decide whether the variational problem has a solution, these methods deal directly with the functional I . Thereby, the existence of a minimiser for the stated problem is connected with the coercivity and the sequential weak lower semicontinuity of the functional I and furthermore with convexity properties of the function W , see Dacorogna [22]. The direct methods propose how a new variational problem should be formulated if the original problem has no solution. Main results of this theory are overviewed in the following sections of this chapter. The material of the present chapter is based

essentially on the works of Dacorogna [21, 22, 23] and Müller [63] as well as on the recent work of Friesecke and Theil [33].

3.1 Definitions and Statements

The problem (3.1) is a particular case of the following general variational problem¹:

$$\min \left\{ I(\varphi) \doteq \int_{\mathcal{B}} W(\mathbf{X}, \varphi(\mathbf{X}), \mathbf{F}) dV : \varphi \in W^{1,p}(\mathcal{B}; \mathbb{R}^m) \text{ and } \varphi = \varphi_0 \text{ on } \partial\mathcal{B} \right\} \quad (3.2)$$

Here, as in (3.1)

- $\mathcal{B} \subset \mathbb{R}^n$ is a bounded open domain;
- $\varphi : \mathcal{B} \rightarrow \mathbb{R}^m$;
- $\mathbf{F} \doteq \nabla_{\mathbf{X}} \varphi \in \mathbb{R}^{n \times m}$, $\mathbf{X} \in \mathcal{B}$;
- $W : \mathcal{B} \times \mathbb{R}^m \times \mathbb{R}^{n \times m} \rightarrow \mathbb{R}$ is a continuous function;
- φ_0 is a given function;
- $W^{1,p}(\mathcal{B}; \mathbb{R}^m)$ is a Sobolev space defined below.

A distinction is drawn between the **scalar case** (if either $n = 1$ or $m = 1$) and the **vectorial case** (if $m, n > 1$). This chapter concentrates on the vectorial case, which differs essentially from the scalar case.

3.1.1 Weak Convergence and Sequential Weak Lower Semicontinuity

It should be commenced with the definition of L^p and Sobolev spaces.

Definition 3.1. (Dacorogna [22])

- Let $1 \leq p < \infty$ and let $\mathcal{B} \subset \mathbb{R}^n$ be an open set. A measurable function $W : \mathcal{B} \rightarrow \mathbb{R}$ is said to be in $L^p(\mathcal{B})$ if

$$\|W\|_{L^p} \equiv \left(\int_{\mathcal{B}} |W(\mathbf{X})|^p dV \right)^{1/p} < \infty$$

- Let $p = \infty$ and let $\mathcal{B} \subset \mathbb{R}^n$ be an open set. A measurable function $W : \mathcal{B} \rightarrow \mathbb{R}$ is said to be in $L^\infty(\mathcal{B})$ if

$$\|W\|_{L^\infty} \equiv \inf\{\alpha : |W(\mathbf{X})| \leq \alpha \text{ a.e. in } \mathcal{B}\} < \infty$$

¹In the following sections of this chapter, the index 0 denoting the material configuration is omitted for the sake of simplicity

A conjugate exponent p' for $1 \leq p < \infty$ can be defined according to

$$\frac{1}{p} + \frac{1}{p'} = 1$$

Thereby, if $p = \infty$ then $p' = 1$ and conversely. In terms of this definition, the dual space of $L^p(\mathcal{B})$ is $L^{p'}(\mathcal{B})$.

Definition 3.2. (Dacorogna [22]) *Sobolev space*

- Let $1 \leq p \leq \infty$, let $\mathcal{B} \subset \mathbb{R}^n$ be an open set and $s \in \mathbb{N}$ (the set of integers). Then

$$W^{s,p}(\mathcal{B}) \doteq \{\varphi : \varphi \in L^p(\mathcal{B}), \nabla_X^\alpha \varphi \in L^p(\mathcal{B}), \alpha = 1, 2, \dots, s\}$$

- With the space $W^{s,p}(\mathcal{B})$ is associated the norm

$$\|\varphi\|_{W^{s,p}} \doteq \left(\sum_{\alpha=0}^s \|\nabla_X^\alpha \varphi\|_{L^p}^p \right)^{1/p} \quad \text{if } 1 \leq p < \infty$$

$$\|\varphi\|_{W^{s,\infty}} \doteq \max_{0 \leq \alpha \leq s} \{\|\nabla_X^\alpha \varphi\|_{L^\infty}^p\} \quad \text{if } p = \infty.$$

- $W_0^{s,p}$ denotes the closure of $C_0^\infty(\mathcal{B})$ in $W^{s,p}$.

Thus, $W^{s,p}$ is a Banach space, separable if $1 \leq p < \infty$ and reflexive if $1 < p < \infty$. If $\varphi : \mathcal{B} \subset \mathbb{R}^n \rightarrow \mathbb{R}^m$ is a vector valued function, the Sobolev space is denoted by $W^{s,p}(\mathcal{B}; \mathbb{R}^m)$.

Now, definition of the weak convergence in L^p can be introduced.

Definition 3.3. (Dacorogna [22]) Let $\mathcal{B} \subset \mathbb{R}^n$ be a bounded open set. The sequence $\varphi^\varepsilon : \mathcal{B} \rightarrow \mathbb{R}^m$

- **converges weakly** in $L^p(\mathcal{B})$, $1 \leq p < \infty$, to φ :

$$\varphi^\varepsilon \rightharpoonup \varphi \quad \text{in } L_m^p(\mathcal{B}), \quad \text{as } \varepsilon \rightarrow \infty$$

if

$$\int_{\mathcal{B}} \varphi^\varepsilon(\mathbf{X}) \cdot \psi(\mathbf{X}) dV \longrightarrow \int_{\mathcal{B}} \varphi(\mathbf{X}) \cdot \psi(\mathbf{X}) dV, \quad \text{as } \varepsilon \rightarrow \infty$$

for every $\psi \in L_m^{p'}(\mathcal{B})$; “ \cdot ” denotes the scalar product in \mathbb{R}^m .

- **converges weakly*** in $L^\infty(\mathcal{B})$ to φ if $p = \infty$:

$$\varphi^\varepsilon \xrightarrow{*} \varphi \quad \text{in } L_m^\infty(\mathcal{B})$$

for every $\psi \in L_m^1(\mathcal{B})$

Based on the definition of the weak convergence, an important definition of the (sequential) weak lower semicontinuity can be introduced.

Definition 3.4. (Dacorogna [21, 22]) Let \mathcal{X} be a Banach space; let $\varphi, \varphi^\varepsilon \in \mathcal{X}$ be such that

$$\varphi^\varepsilon \rightharpoonup \varphi.$$

Suppose that a continuous function $I : \mathcal{X} \rightarrow \bar{\mathbb{R}} = \mathbb{R} \cup \{+\infty\}$ is given. Then

1. I is **(sequentially) weakly continuous (wsc)** if

$$\liminf_{\varepsilon \rightarrow \infty} I(\varphi^\varepsilon) = I(\varphi);$$

2. I is **(sequentially) weakly lower semicontinuous (wslsc)** if

$$\liminf_{\varepsilon \rightarrow \infty} I(\varphi^\varepsilon) \geq I(\varphi);$$

3. I is **coercive** over \mathcal{X} if

$$I(\varphi) \geq \alpha \|\varphi\| + \beta$$

for every $\varphi \in \mathcal{X}$ and for some $\alpha > 0, \beta \in \mathbb{R}$.

The next theorem states a sufficient condition for the existence of minimiser for the problem

$$\inf\{I(\varphi) : \varphi \in \mathcal{X}\} \tag{3.3}$$

without any assumption about the dependence $I(\varphi)$ on φ .

Theorem 3.1. (Dacorogna [22]) Let \mathcal{X} be a reflexive Banach space, $I : \mathcal{X} \rightarrow \bar{\mathbb{R}}$ be wslsc and coercive over \mathcal{X} . Also assume that there exists $\tilde{\varphi} \in \mathcal{X}$ with $I(\tilde{\varphi}) < \infty$, then (3.3) has at least one solution $\bar{\varphi} \in \mathcal{X}$, i.e.

$$I(\bar{\varphi}) = \inf\{I(\varphi) : \varphi \in \mathcal{X}\}.$$

It is usually difficult to determine whether a functional is wslsc or not. On the other hand, as later shown, the weak lower semicontinuity is connected with some convexity properties of the integrand (in our case of the function W). Thus, some notions of convexity should be introduced before the theorems stating the connection between the weak lower semicontinuity of I and convexity properties of W are subsequently formulated.

3.1.2 Notions of Convexity

The convexity and coercivity of the integrand W are sufficient for the existence of a minimiser for problem (3.2) in both scalar and vectorial cases, see Dacorogna [22], 3.4, theorem 4.1. Contrary to the scalar case, convexity of W is not a necessary condition in the vectorial case. In this case, the quasiconvexity introduced by Morrey [61] is of a special importance and replaces the notion of convexity. However, the quasiconvexity is an integral condition and its verification is not simpler than a verification of the weak lower semicontinuity. To overcome this difficulty, a slightly weaker rank-one convexity and stronger polyconvexity conditions have been introduced, see Ball [3]. In this subsection, all these notions are introduced and their hierarchy is stated.

For a matrix $\mathbf{F} \in \mathbb{R}^{n \times m}$ let

• $\mathbf{M}(\mathbf{F}) : \mathbb{R}^{n \times m} \rightarrow \mathbb{R}^{\tau(n,m)}$ denote a vector consisting of all $s \times s$ subdeterminants of the matrix \mathbf{F} , $1 \leq s \leq m \wedge n = \min\{m, n\}$ and

• $\tau(n, m) = \sum_{s=1}^{m \wedge n} \binom{n}{s} \binom{m}{s}$ denotes its length. Here $\binom{m}{s} \doteq \frac{m!}{s!(m-s)!}$

Definition 3.5. (Dacorogna [22], Müller [63]) A function $W : \mathbb{R}^{n \times m} \rightarrow \bar{\mathbb{R}} = \mathbb{R} \cup \{+\infty\}$ is

1. **convex** if

$$W(\lambda \mathbf{F}_A + [1 - \lambda] \mathbf{F}_B) \leq \lambda W(\mathbf{F}_A) + [1 - \lambda] W(\mathbf{F}_B)$$

for every $\mathbf{F}_A, \mathbf{F}_B \in \mathbb{R}^{n \times m}$ and every $\lambda \in (0, 1)$;

2. **polyconvex** if a convex function $\tilde{W} : \mathbb{R}^{\tau(n,m)} \rightarrow \bar{\mathbb{R}}$ exists such that

$$W(\mathbf{F}) = \tilde{W}(\mathbf{M}(\mathbf{F}))$$

3. **quasiconvex** if

$$\int_{\mathcal{B}} W(\mathbf{F} + \nabla_X \tilde{\varphi}) dV \geq \int_{\mathcal{B}} W(\mathbf{F}) dV = W(\mathbf{F}) V$$

for every bounded domain $\mathcal{B} \subset \mathbb{R}^n$ with $\text{meas}(\mathcal{B}) \doteq V$ and $\text{meas}(\partial \mathcal{B}) = 0$, for every $\mathbf{F} \in \mathbb{R}^{n \times m}$ and for every $\tilde{\varphi} \in W_0^{1,\infty}(\mathcal{B}; \mathbb{R}^m)$ whenever the integral on the left-hand side exists.

4. **rank-1 convex** if W is convex along rank-1 laminates, i.e. if

$$W(\lambda \mathbf{F}_A + [1 - \lambda] \mathbf{F}_B) \leq \lambda W(\mathbf{F}_A) + [1 - \lambda] W(\mathbf{F}_B)$$

for every $\mathbf{F}_A, \mathbf{F}_B \in \mathbb{R}^{n \times m} : \text{rank}(\mathbf{F}_A - \mathbf{F}_B) \leq 1$ and for every $\lambda \in (0, 1)$;

The following theorem states hierarchy of the notions introduced in the recent definition

Theorem 3.2. (Dacorogna [22], Müller [63])

1. If $n \geq 2, m \geq 2$ then

$$W \text{ convex} \begin{array}{l} \Rightarrow \\ \Leftrightarrow \end{array} W \text{ polyconvex} \begin{array}{l} \Rightarrow \\ \Leftrightarrow \end{array} W \text{ quasiconvex} \begin{array}{l} \Rightarrow \\ \Leftrightarrow \end{array} W < \infty \begin{array}{l} \Rightarrow \\ \Leftrightarrow \end{array} \text{if } m \geq 3 \quad W \text{ rank-1 convex}$$

2. If $n = 1$ or $m = 1$, then all these notions are equivalent.

3. if $W \in C^2(\mathbb{R}^m)$, then rank-1 convexity is equivalent to Legendre-Hadamard (or **ellipticity condition**):

$$[\mathbf{m} \otimes \mathbf{N}] : \frac{\partial^2 W(\mathbf{F})}{\partial \mathbf{F} \otimes \partial \mathbf{F}} : [\mathbf{m} \otimes \mathbf{N}] \geq 0 \quad (3.4)$$

for every $\mathbf{N} \in \mathbb{R}^n$, $\mathbf{m} \in \mathbb{R}^m$ and $\mathbf{F} \in \mathbb{R}^{n \times m}$

Remark 3.1.

- The question whether rank-1 convexity implies quasiconvexity for $m = 2$, $n \geq 2$ is open.
- The rank-1 convexity of W is necessary and sufficient condition for quasiconvexity of W if W is quadratic, see Dacorogna [22]. In this case, the ellipticity of the Euler equations is equivalent to the weak lower semicontinuity of the functional.
- An application of the Legendre-Hadamard condition within the localisation analysis is discussed in detail in the next chapter.

A physical meaning of the different notions of convexity defined above should now be discussed, see also Lambrecht [47].

Convexity

For a better understanding of the convexity condition, the following notations should be introduced:

$$\mathbf{F}_B \doteq \mathbf{F}, \quad \mathbf{F}_A \doteq \mathbf{F} + \Delta \mathbf{F}.$$

Then the convexity inequality given in definition (3.5) can be transformed to

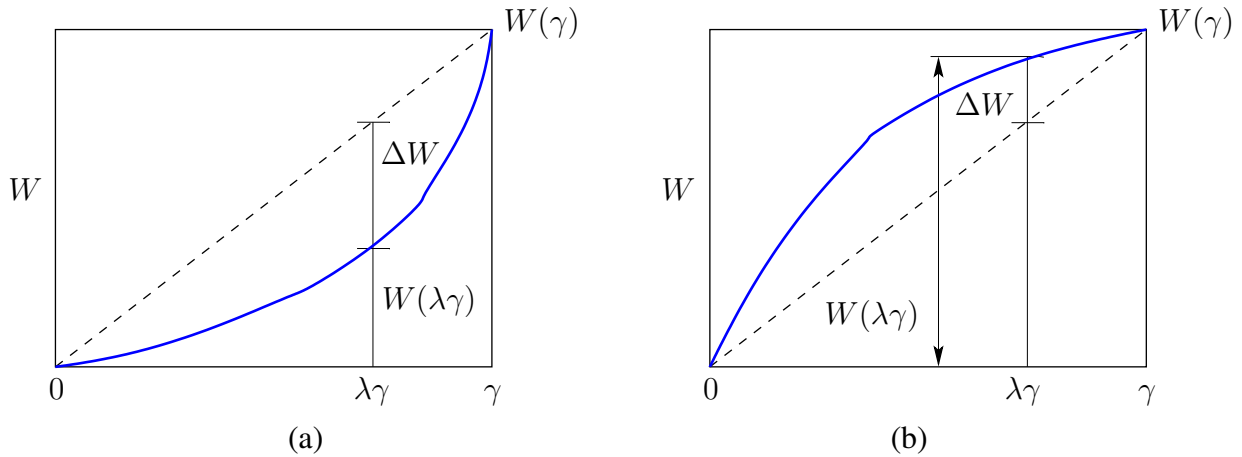


Figure 3.2: A convex (a) and a non-convex (b) curves

$$W(\mathbf{F} + \lambda \Delta \mathbf{F}) - W(\mathbf{F}) \leq \lambda [W(\mathbf{F} + \Delta \mathbf{F}) - W(\mathbf{F})] \quad (3.5)$$

with λ as in (3.5). In terms of non-linear elasticity, this inequality states stability of a system with the strain energy density $W(\mathbf{F})$ with respect to an arbitrary perturbation $\Delta\mathbf{F}$ of a deformation gradient. It is explained in fig. 3.2 for 1D-case. Here, the deformation gradient depends only on the scalar number γ as e.g. in the case of the simple shear: $\mathbf{F} = \mathbf{I} + \gamma \mathbf{e}_1 \otimes \mathbf{e}_2$. Then, the strain energy density becomes a function of γ and the case becomes quasi one-dimensional. Without loss of generality, a zero level of the energy is chosen so that $W(0) = 0$; this state is considered to be unperturbed. It now immediately follows from fig. 3.2 (a):

$$\frac{W(\lambda\gamma) + \Delta W}{W(\gamma)} = \frac{\lambda}{1} \Rightarrow W(\lambda\gamma) = \lambda W(\gamma) - \Delta W \leq \lambda W(\gamma)$$

what corresponds to (3.5), i.e. the curve in this figure is convex. It can be analogously obtained from fig. 3.2 (b) that

$$\frac{W(\lambda\gamma) - \Delta W}{W(\gamma)} = \frac{\lambda}{1} \Rightarrow W(\lambda\gamma) = \lambda W(\gamma) + \Delta W \geq \lambda W(\gamma)$$

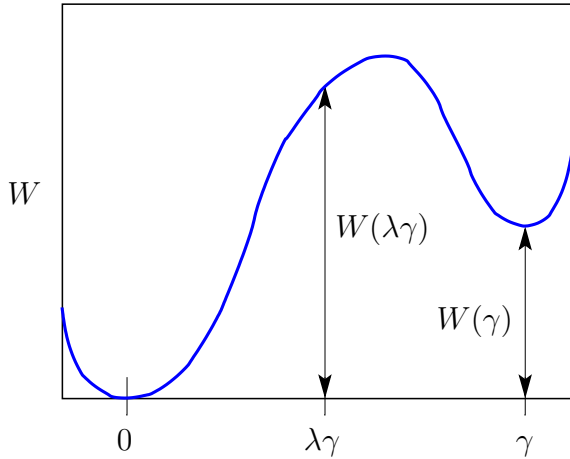


Figure 3.3: A double-well problem

and this curve is no longer convex. If a curve is convex, only a single well can exist. A non-convex curve can exhibit further minima corresponding to other equilibrium configurations, see fig. 3.3. It is easy to recognise that for the curve shown in this figure, the convexity condition fails:

$$W(\lambda\gamma) > W(\gamma) \geq \lambda W(\gamma)$$

since $\lambda \in (0, 1)$. In this case, a perturbation can lead to a new equilibrium configuration with the energy $W(\gamma)$

Polyconvexity

The notion of polyconvexity is not used in this work. Nevertheless, it should be briefly overviewed. In the planar case $n = m = 2$ and $\tau(n, m) = 5$. The integrand W is a function of \mathbf{F} and $\det \mathbf{F}$:

$$W(\mathbf{F}) = \tilde{W}(\mathbf{F}, \det \mathbf{F}).$$

In 3D-case, the $\text{cof} \mathbf{F} \doteq \det \mathbf{F} \mathbf{F}^{-t}$ represents the 3^{rd} submatrix of \mathbf{F} so that

$$W(\mathbf{F}) = \tilde{W}(\mathbf{F}, \text{cof} \mathbf{F}, \det \mathbf{F}).$$

According to the definition of polyconvexity, W must be convex with respect to each of these arguments i.e. it must be stable with respect to arbitrary perturbation in \mathbf{F} , $\text{cof} \mathbf{F}$ and $\det \mathbf{F}$, which

describe a changing of a line, surface and volume elements. It means that the polyconvexity requires stability of material with respect to an arbitrary perturbation of the length, surface and volume in each material point.

Quasiconvexity

The physical meaning of quasiconvexity is straightforward and can easily be seen in its definition. This definition states stability of a homogeneously deformed body with respect to any perturbation.

Rank-1 Convexity

Analogous to convexity, the rank-1 convexity requires the stability of a body with respect to perturbations of rank one. If this requirement is no longer fulfilled, the homogeneous deformation yields no equilibrium, and the body changes to a new equilibrium configuration consisting of two phases A and B deformed homogeneously with deformation gradients \mathbf{F}_A and \mathbf{F}_B respectively. Thereby, λ and $1 - \lambda$ show the volume fractions of each phase. Tangential continuity of φ on the interfaces between the phases can be expressed as

$$\mathbf{F}_A \cdot \boldsymbol{\tau}_0 = \mathbf{F}_B \cdot \boldsymbol{\tau}_0 \quad \Rightarrow \quad [\mathbf{F}_A - \mathbf{F}_B] \cdot \boldsymbol{\tau}_0 = 0 \quad (3.6)$$

where $\boldsymbol{\tau}_0$ is a tangent vector to interface in the material configuration so that $\boldsymbol{\tau}$ is its push-forward, see fig. 3.4 (a). From this condition follows that the difference $\mathbf{F}_A - \mathbf{F}_B$ must be of rank one as the

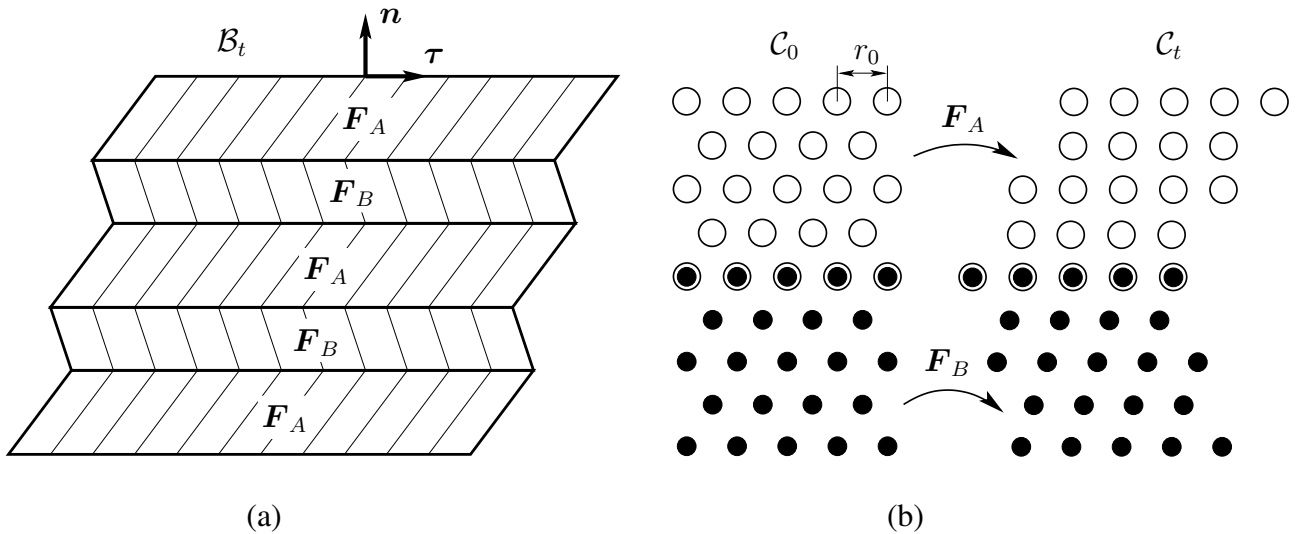


Figure 3.4: Rank-1 laminates in the spatial configuration: (a) a continuum case; (b) the case of a discrete crystal lattice

matrix of a homogeneous equation system, which have a non-trivial solution and can be represented as $\mathbf{m} \otimes \mathbf{N}$. Here \mathbf{N} is pull-back of \mathbf{n} , the normal vector to the interface and \mathbf{m} is an arbitrary vector, whose meaning is discussed below.

For a discrete system, such as a crystal lattice, the condition (3.6) cares for compatibility of two lattices obtained by affine deformations \mathbf{F}_A and \mathbf{F}_B of the same reference lattice. The compatibility

requires that the interface between the phases is invariant with respect to the deformations \mathbf{F}_A and \mathbf{F}_B , see 3.4 (b). In this case, the length of τ_0 should be equal to the atomic spacing r_0 along the interface. From the condition (3.6) also follows that both homogeneously deformed lattices differ by a simple shear deformation $\mathbf{m} \otimes \mathbf{N}$. A number of microstructures based on rank-1 connections such as twin crossings or wedge microstructures is known from experiments, see e.g. Müller [63]. These structures consist of more than 2 different phases.

Infinitesimal Rank-1 Convexity

Before the introduction of the infinitesimal rank-1 convexity, the Taylor series expansion of the convexity inequality (3.5) in the neighbourhood of \mathbf{F} up to quadratic terms should be considered:

$$\begin{aligned} & \left[W(\mathbf{F}) + \lambda \frac{\partial W(\mathbf{F})}{\partial \mathbf{F}} : \Delta \mathbf{F} + \frac{1}{2} \lambda^2 \Delta \mathbf{F} : \frac{\partial^2 W(\mathbf{F})}{\partial \mathbf{F} \otimes \partial \mathbf{F}} : \Delta \mathbf{F} \right] - W(\mathbf{F}) \\ & \leq \lambda \left[\left[W(\mathbf{F}) + \frac{\partial W(\mathbf{F})}{\partial \mathbf{F}} : \Delta \mathbf{F} + \frac{1}{2} \Delta \mathbf{F} : \frac{\partial^2 W(\mathbf{F})}{\partial \mathbf{F} \otimes \partial \mathbf{F}} : \Delta \mathbf{F} \right] - W(\mathbf{F}) \right] \end{aligned}$$

After simplification of this expression, the only quadratic terms remain:

$$\frac{1}{2} \lambda [1 - \lambda] \Delta \mathbf{F} : \frac{\partial^2 W(\mathbf{F})}{\partial \mathbf{F} \otimes \partial \mathbf{F}} : \Delta \mathbf{F} \geq 0 \quad \Rightarrow \quad \Delta \mathbf{F} : \frac{\partial^2 W(\mathbf{F})}{\partial \mathbf{F} \otimes \partial \mathbf{F}} : \Delta \mathbf{F} \geq 0 \quad (3.7)$$

This last inequality states the condition of the infinitesimal convexity. A definition of the infinitesimal rank-1 convexity is given by the same inequality with the perturbation $\Delta \mathbf{F} = \mathbf{m} \otimes \mathbf{N}$ and takes the format (3.4).

The notion of infinitesimal rank-1 convexity is of a special importance in the present work and will be recalled in the next chapters.

3.1.3 Different Envelopes of a Function

The convex, polyconvex, quasiconvex and rank-1 convex hulls or envelopes of W are the largest convex, polyconvex, quasiconvex and rank-1 convex functions below W and can be defined as follows

Definition 3.6. (Dacorogna [23])

$$\begin{aligned} CW &= \sup \{ W^c \leq W : W^c \text{ convex} \}, \\ PW &= \sup \{ W^{pc} \leq W : W^{pc} \text{ polyconvex} \}, \\ QW &= \sup \{ W^{qc} \leq W : W^{qc} \text{ quasiconvex} \}, \\ RW &= \sup \{ W^{rc} \leq W : W^{rc} \text{ rank-1 convex} \}, \end{aligned}$$

whereby, as follows from the above theorem

$$CW \leq PW \leq QW \leq RW \leq W$$

The format of these envelopes is defined by the next theorem. For our application, only quasiconvex hull is of interest.

Theorem 3.3. (Dacorogna [22, 23]) *Let $W : \mathbb{R}^{n \times m} \rightarrow \bar{\mathbb{R}}$. Then*

$$1. \quad CW = \inf \left\{ \sum_{i=1}^{mn+1} \lambda_i W(\mathbf{F}_i) : \mathbf{F} = \sum_{i=1}^{mn+1} \lambda_i \mathbf{F}_i \right\}$$

$$2. \quad PW = \inf \left\{ \sum_{i=1}^{\tau+1} \lambda_i W(\mathbf{F}_i) : \tilde{W}(\mathbf{F}) = \sum_{i=1}^{\tau+1} \lambda_i \tilde{W}(\mathbf{F}_i) \right\}$$

3. Let $R_0 W = W$ and

$$R_{i+1} W(\mathbf{F}) = \inf \left\{ \begin{array}{l} \lambda R_i W(\mathbf{F}_1) + [1 - \lambda] R_i W(\mathbf{F}_2) : \lambda \in (0, 1), \\ \mathbf{F} = \lambda \mathbf{F}_1 + [1 - \lambda] \mathbf{F}_2, \text{rank}(\mathbf{F}_1 - \mathbf{F}_2) = 1 \end{array} \right\}.$$

Then $RW = \inf_{i \in \mathbb{N}} R_i W(\mathbf{F})$.

4. If $W : \mathbb{R}^{n \times m} \rightarrow \mathbb{R}$ is locally bounded and Borel measurable then

$$QW(\mathbf{F}) = \inf_{\tilde{\varphi} \in W_0^{1,\infty}} \frac{1}{V} \left\{ \int_{\mathcal{B}} W(\mathbf{F} + \nabla_X \tilde{\varphi}) dV \right\}$$

3.1.4 Existence of minimiser; Relaxation

It is stated in theorem (3.1) that the functional I should be wslsc and coercive to have a minimiser. The following theorem states the connection between the quasiconvexity of W and the sequential weak lower semicontinuity of I and consequently a connection between the quasiconvexity of W and existence of minimiser of I .

Theorem 3.4. Müller [63])

1. Let I be as in (3.2) and $W(\mathbf{X}, \varphi(\mathbf{X}), \mathbf{F}) \equiv W(\mathbf{F})$. Then I is weak* sequentially lower semicontinuous (w*slsc) on $W^{1,\infty}(\mathcal{B}; \mathbb{R}^m)$ if and only if $W(\mathbf{X}, \varphi(\mathbf{X}), \mathbf{F})$ is quasiconvex in the last variable.

2. Suppose in addition that

$$0 \leq W(\mathbf{F}) \leq C [|\mathbf{F}|^p + 1]$$

for some $p \in [1, \infty)$. If W is quasiconvex then I is wslsc on $W^{1,p}(\mathcal{B}; \mathbb{R}^m)$

Remark 3.2. The quasiconvexity of W is sufficient and necessary for the weak* sequential lower semicontinuity of I even for $W = W(\mathbf{X}, \varphi(\mathbf{X}), \mathbf{F})$ satisfying some growth conditions, see Dacorogna [22].

In the next theorem, W is again a function of only \mathbf{F} . The general case $W = W(\mathbf{X}, \varphi(\mathbf{X}), \mathbf{F})$ is treated in e.g. Dacorogna [22]. In this case, W should satisfy some additional growth and coercivity conditions.

Theorem 3.5. (Müller [63]) *Suppose that $p \in (1, \infty)$, $c > 0$ and that W satisfies*

$$c|\mathbf{F}|^p \leq W(\mathbf{F}) \leq C [|\mathbf{F}|^p + 1].$$

1. *If W is quasiconvex and $\psi \in W^{1,p}(\mathcal{B}; \mathbb{R}^m)$ then I attains its minimum in the class*

$$\psi \in W_{\psi}^{1,p}(\mathcal{B}; \mathbb{R}^m) \doteq \{\varphi \in W^{1,p}(\mathcal{B}; \mathbb{R}^m) : \varphi - \psi \in W_0^{1,p}(\mathcal{B}; \mathbb{R}^m)\}.$$

2. *If $\bar{I} \doteq \int_{\mathcal{B}} W^{qc}(\mathbf{F})$ then $\inf_{W_{\psi}^{1,p}} I = \min_{W_{\psi}^{1,p}} \bar{I}$*

3. *A function $\bar{\varphi}$ is a minimiser of \bar{I} in $W_{\psi}^{1,p}$ if and only if it is a cluster point (with respect to weak convergence in $W^{1,p}$) of a minimising sequence for I .*

The passage from I to \bar{I} is called **relaxation**. Thereby, the quasiconvex function W^{qc} yields the solution of a new variational problem formulated instead of the original problem, which has no solution. The format of the quasiconvex envelope W^{qc} is given in theorem 3.3 and the definition of the relaxed functional \bar{I} , see theorem 3.5, enables to explain the relaxation from the physical point of view as the passage from the microscopic energy I to a macroscopic energy \bar{I} averaged over fine scale oscillations, see Müller [63]. Such form of relaxation is called **quasiconvexification**. To obtain the quasiconvex hull W^{qc} , the integral equation given in theorem 3.3-4 should be solved. For this reason, the problem of the quasiconvexification is rather complicated. Instead of that, relaxation in terms of polyconvexification, convexification or rank-1 convexification can be considered.

3.2 Application to a Discrete Lattice System

All previous theoretical results of this chapter apart from the considerations of the infinitesimal rank-1 convexity are related to the continuum theory. An application of these results to a discrete lattice requires some adaptation and is treated in this section.

As mentioned above, the idea to treat an elastic crystal within the frame of non-linear continuum theory stems from Ericksen [27]. Then, the equilibrium problem of crystals under different loads has been treated in terms of variational methods by Ericksen [26, 28], Chipot and Kinderlehrer [20], Fonseca [32] and many others. In the often cited book of Dacorogna [22], an overview of the results obtained in [20, 32] is given.

The special feature of a discrete lattice system is the periodicity of the atomic arrangement which leads to periodicity of the crystal energy as a function of the atomic positions. A usual way to describe such system is to choose the origin at one of the atoms and three linearly independent lattice vectors \mathbf{a}_i , $i = 1, 2, 3$. The position of any atom in the lattice is then given by linear combination of these vectors. A 3×3 matrix with i -th column consisting of the components of the vector \mathbf{a}_i is denoted

as $\mathbf{A} \doteq (\mathbf{a}_1 \ \mathbf{a}_2 \ \mathbf{a}_3)$. The periodical lattice structure leads to additional assumptions about the frame indifference and invariance of the Helmholtz free energy Φ under a change of lattice basis:

$$\Phi = \Phi(\mathbf{A}^t \cdot \mathbf{A}) = \Phi([\mathbf{M}^t \cdot \mathbf{A}^t] \cdot [\mathbf{A} \cdot \mathbf{M}]) \quad (3.8)$$

for every $\mathbf{M} \in GL(\mathbb{Z}^3) \doteq \{\mathbf{M} \in \mathbb{R}^{3 \times 3} : \det \mathbf{M} = \pm 1 \text{ and } m_{ij} \in \mathbb{Z}, i, j = 1, 2, 3\}$ with the set of relative integers \mathbb{Z} . For a fixed basis \mathbf{A} , the strain energy density per unit reference volume is a function of the deformation gradient $\mathbf{F} \in \mathbb{R}_+^{3 \times 3} \doteq \{\mathbf{F} \in \mathbb{R}^{3 \times 3} : \det \mathbf{F} > 0\}$:

$$W(\mathbf{F}) = \Phi([\mathbf{A}^t \cdot \mathbf{F}^t] \cdot [\mathbf{F} \cdot \mathbf{A}]) \quad (3.9)$$

A further invariance property of W can be derived² from (3.8) and (3.9):

$$W(\mathbf{F}) = W(\mathbf{Q} \cdot \mathbf{F} \cdot \mathbf{H}) \quad (3.10)$$

for every

- $\mathbf{F} \in \mathbb{R}_+^{3 \times 3}$,
- $\mathbf{Q} \in \mathcal{R}^+ : \{\mathbf{Q} \in \mathbb{R}^{3 \times 3} : \mathbf{Q}^t \cdot \mathbf{Q} = \mathbf{I} \text{ and } \det \mathbf{Q} = 1\}$,
- $\mathbf{H} \in \mathbf{A} \cdot [GL(\mathbb{Z}^3)] \cdot \mathbf{A}^{-1}$ which is the conjugate group of $GL(\mathbb{Z}^3)$.

The frame indifference under finite rotations \mathbf{Q} requires that W cannot be quadratic in \mathbf{F} so that the constitutive law must be non-linear, see Friesecke and Theil [33]. If W is quadratic in \mathbf{F} , the frame indifference is valid only for infinite small rotations.

A further assumption is related to the behaviour of W :

$$\left\{ \begin{array}{l} W(\mathbf{F}) \geq 0, \quad W(\mathbf{I}) = 0 \\ \lim_{\det \mathbf{F} \rightarrow 0} W(\mathbf{F}) = \infty \end{array} \right. \quad (3.11)$$

The variational problem like (3.2) associated with such W generally has in no solution because of the lacking coercivity and rank-1 convexity of W due to different invariances in the problem. It can be easily shown e.g. for familiar example of the simple shear. Recall that in this case, the deformation gradient has the format $\mathbf{F} = \mathbf{I} + \gamma \mathbf{e}_1 \otimes \mathbf{e}_2$ and W becomes a periodic function of the shear number γ . For smooth W , there exist regions where the infinitesimal rank-1 condition (3.4) is no longer fulfilled. Thus, the consideration of a relaxed problem is the only possibility to find a solution of the minimisation problem like (3.2). The following theorem is proven by Chipot and Kinderlehrer [20] and Fonseca [32]:

Theorem 3.6. (Dacorogna [22]) *Let W satisfy (3.10) and (3.11). Let*

$$h(t) \doteq \inf\{W(\mathbf{F}) : \det \mathbf{F} = t\}.$$

If PW and RW denote the polyconvex and rank-1 convex envelope of W , then for every $\mathbf{F} \in \mathbb{R}_+^{3 \times 3}$

1. $PW(\mathbf{F}) = RW(\mathbf{F}) = h^{**}(\det \mathbf{F})$,

²The derivation is given in the appendix

$$2. \quad h^{**}(\det \mathbf{F}) = \inf \left\{ \frac{1}{V} \int_{\mathcal{B}} W(\mathbf{F} + \nabla_{\mathbf{X}} \varphi) dV : \varphi \in W_0^{1,\infty}(\mathcal{B}; \mathbb{R}^3) \right\}$$

Here, the function h is the subenergy density of W .

While problem (3.2) has generally no solution, there are such particular \mathbf{F} , which provide the existence of minimiser for this problem. Friesecke and Theil [33] have recently studied the validity and failure of the Cauchy-Born rule on the basis of a 2D mass-spring model, see fig. 3.5. The non-linearity of this model is of a geometric origin caused by the frame indifference of the strain energy density mentioned above.

A particular result of this study states that the elastic energy density $W_{\mathcal{B}_L}(\mathbf{F})$ as a function of the

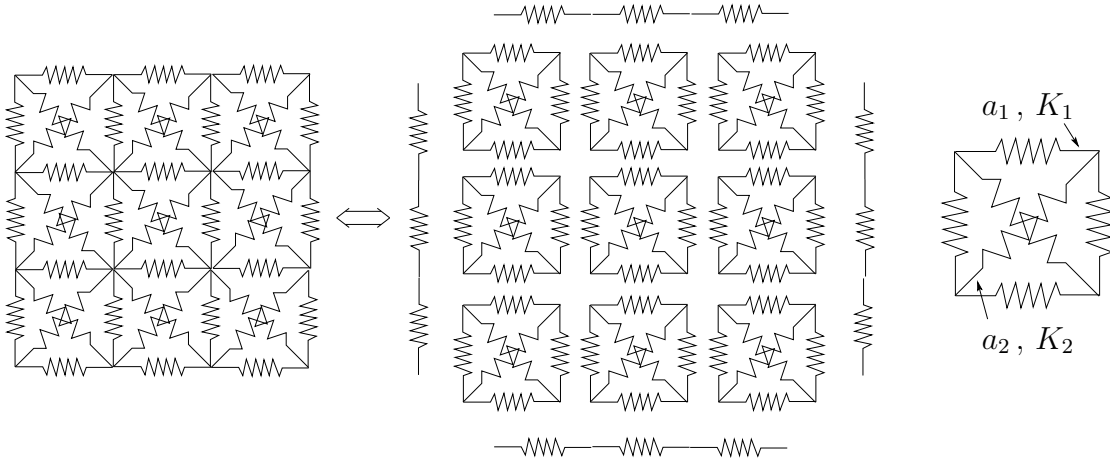


Figure 3.5: The 2D mass-spring model used by Friesecke and Theil in [33]. The system on the left can be divided into boundary and body parts, whereby the body part consists of separated cells. A single cell consists of the four masses on its corners connected by linear springs with the spring parameters K_1 and K_2 and the equilibrium length a_1 and a_2 .

macroscopic deformation $\varphi(\mathbf{X}) = \mathbf{F} \cdot \mathbf{X}$ prescribed on the boundary (i.e. $\forall \mathbf{X} \in \mathcal{C}_L$) converges to a limit $W(\mathbf{F})$ with the increase of the characteristic length L of the material configuration \mathcal{B}_L :

$$\lim_{L \rightarrow \infty} W_{\mathcal{B}_L}(\mathbf{F}) = W(\mathbf{F}) \quad \text{with} \quad W_{\mathcal{B}_L}(\mathbf{F}) \doteq \min_{\substack{\varphi \in \mathcal{A} \\ \varphi(\mathbf{X})|_{\mathbf{X} \in \partial \mathcal{C}_L} = \mathbf{F} \cdot \mathbf{X}}} \frac{E^{tot}(\{\varphi(\mathbf{X})\}_{\mathbf{X} \in \mathcal{C}_L})}{V_L} \quad (3.12)$$

Here $\mathcal{C}_L = r_0 \mathbb{Z}^2 \cap \mathcal{B}_L$ denotes the material lattice configuration i.e. a collection of the atomic sites within \mathcal{B}_L and $r_0 = f(K_1, K_2, a_1, a_2)$ is the lattice constant, see fig. 3.5. Further notations include V_L as the volume of \mathcal{B}_L and E^{tot} as the total internal energy of the atomic collection. The class \mathcal{A} of admissible deformations is defined by

$$\mathcal{A} \doteq \{ \varphi : \mathcal{C}_L \rightarrow \mathbb{R}^2 \mid \det'(\nabla'_{\mathbf{X}} \varphi) \geq 0 \quad \forall \mathbf{X} \in \mathcal{C}'_L \} \quad (3.13)$$

Here

- \mathcal{C}'_L is the set of bottom left corners of unit cells:

$$\mathcal{C}'_L \doteq \{ \mathbf{X} \in \mathcal{C}_L \mid \mathbf{X}, \mathbf{X} + r_0 \mathbf{e}_1, \mathbf{X} + r_0[\mathbf{e}_1 + \mathbf{e}_2], \mathbf{X} + r_0 \mathbf{e}_2 \in \mathcal{C}_L \};$$

- $\nabla'_X(\bullet)$ is a generalised gradient taking additional atomistic degrees of freedom of the unit cell with bottom left corner \mathbf{X} into account:

$$\nabla'_X \varphi \doteq \frac{1}{r_0} [\varphi(\mathbf{X}) - \bar{\varphi} \mid \varphi(\mathbf{X} + r_0 \mathbf{e}_1) - \bar{\varphi} \mid \varphi(\mathbf{X} + r_0[\mathbf{e}_1 + \mathbf{e}_2]) - \bar{\varphi} \mid \varphi(\mathbf{X} + r_0 \mathbf{e}_2) - \bar{\varphi}] \in \mathbb{R}^{2 \times 4}$$

with $\bar{\varphi} \doteq [\varphi(\mathbf{X}) + \varphi(\mathbf{X} + r_0 \mathbf{e}_1) + \varphi(\mathbf{X} + r_0[\mathbf{e}_1 + \mathbf{e}_2]) + \varphi(\mathbf{X} + r_0 \mathbf{e}_2)]/4$;

- for an arbitrary function $G = [\mathbf{g}_1 \mid \mathbf{g}_2 \mid \mathbf{g}_3 \mid \mathbf{g}_4] \in \mathbb{R}^{2 \times 4}$

$$\det'(G) \doteq \frac{1}{2} [\det(\mathbf{g}_2 - \mathbf{g}_1) \mid \det(\mathbf{g}_4 - \mathbf{g}_1) + \det(\mathbf{g}_4 - \mathbf{g}_3) \mid \det(\mathbf{g}_2 - \mathbf{g}_3)];$$

geometrically $\det'(\nabla'_X \varphi)$ is the area of the unit cell in the spatial configuration with the bottom left corner $\varphi(\mathbf{X})$ divided by the area of the unit cell in the material configuration.

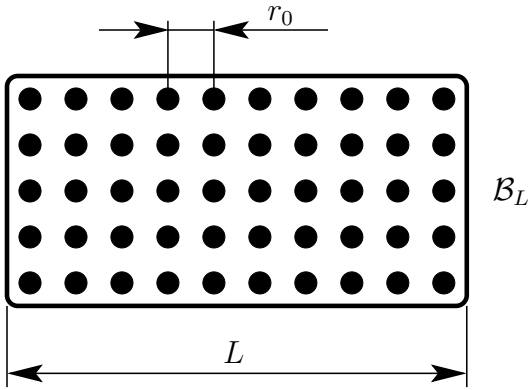


Figure 3.6: The material configuration \mathcal{B}_L characterised by the linear size L . The collection of the black points (atoms) represents the material lattice configuration $\mathcal{C}_L = r_0 \mathbb{Z}^2 \cap \mathcal{B}_L$, whereby r_0 is the lattice constant.

In particular, the generalised gradient $\det'(\nabla'_X \varphi)$ is a discrete null-Lagrangian³ i.e. if φ and $\bar{\varphi}$ are two mappings from \mathcal{C}_L to \mathbb{R}^2 , which agree on $\partial \mathcal{C}_L$ then

$$\sum_{\mathbf{X} \in \mathcal{C}'_L} \det'(\nabla'_X \varphi) = \sum_{\mathbf{X} \in \mathcal{C}'_L} \det'(\nabla'_X \bar{\varphi}).$$

The main result of [33] is that the Cauchy-Born rule is a theorem for favourable values of the spring constants and spring equilibrium lengths and for all \mathbf{F} in some open neighbourhood of $SO(2)$ so that

$$W(\mathbf{F}) = W^{CB}(\mathbf{F}) \quad (3.14)$$

whereby $W^{CB}(\mathbf{F})$ is the strain energy density of the homogeneously deformed lattice when each cell follows the linear deformation prescribed on the boundary:

$$W^{CB}(\mathbf{F}) \doteq \lim_{L \rightarrow \infty} \frac{E^{tot}(\{\mathbf{F} \cdot \mathbf{X}\}_{\mathbf{X} \in \mathcal{C}_L})}{V_L} \quad (3.15)$$

To prove this proposition and to overcome the non-convexity of the lattice energy, Friesecke and Theil have introduced a new notion of lattice polyconvexity, which is a discrete analog of the polyconvexity.

³Integrands W for which the integral $\int W(\nabla_X \varphi) dV$ only depends on the boundary values of φ are called **null Lagrangians**, since the Euler-Lagrange equations are automatically satisfied for all functions φ .

Definition 3.7. (Friedrichs and Theil [33]) Let \mathcal{C} be a subset of $\mathbb{R}^{2 \times 4}$, which is invariant under translations

$$[\mathbf{g}_1, \mathbf{g}_2, \mathbf{g}_3, \mathbf{g}_4] \mapsto [\mathbf{g}_1 + \mathbf{d}, \mathbf{g}_2 + \mathbf{d}, \mathbf{g}_3 + \mathbf{d}, \mathbf{g}_4 + \mathbf{d}], \quad \mathbf{d} \in \mathbb{R}^2.$$

A translation-invariant function $E : \mathcal{C} \rightarrow \mathbb{R}$ is called **lattice-polyconvex** if a convex function exists

$$\tilde{E} : \mathcal{C} \times \{a \in \mathbb{R} \mid a = \det' \mathbf{F}' \text{ for some } \mathbf{F}' \in \mathcal{C}\} \rightarrow \mathbb{R},$$

such that $E(\mathbf{G}) = \tilde{E}(\mathbf{G}, \det' \mathbf{G})$.

Thereby, the lattice polyconvexity reduces to the classical continuum polyconvexity for generalised deformation gradients $\nabla'_X \varphi$ of affine lattice deformation given by Cauchy-Born lattice map $\varphi \doteq \mathbf{F} \cdot \mathbf{X} + \mathbf{c}$ ($\mathbf{X} \in \mathcal{C}_L$).

The theory represented in previous sections is sufficient to answer the questions posed at the beginning of the current chapter. The answers are given below together with the questions.

- *Q:* Why does the Cauchy-Born rule fail?
A: The Cauchy-Born rule provides a homogeneous lattice deformation and fails when the strain energy density W of a homogeneously deformed crystal becomes non-quasiconvex, so that the corresponding macroscopic total energy I is no longer swlsc and the problem (3.1) has no solution.
- *Q:* How can the critical deformation be detected?
A: Within the finite element implementation, the fulfillment of the infinitesimal rank-1 convexity condition (3.7) should be evaluated for each load step and for each quadrature point. The loss of infinitesimal rank-1 convexity is a necessary condition for the loss of quasiconvexity.
- *Q:* What should be done to overcome the failure of the Cauchy-Born rule?
A: The homogeneously deformed lattice should obtain a possibility to relax. Thereby, a development of microstructures is expected.

A practical implementation of the last two points is the topic of the next chapter.

Chapter 4

Transition to Plasticity in Continuum-Atomistics

“The bifurcation analysis is straightforward if the following fundamental problem can be solved

Fundamental problem *Find the equilibrium curves going through a given equilibrium point. ”*

Quoc Son Nguen, “Stability and Nonlinear Solid Mechanics”

4.1 Loss of Infinitesimal Rank-1 Convexity

According to the plan proposed in the last chapter, the verification of the criterion (3.7) should first be discussed. This criterion allows the detection of the beginning of the strain localisation, which is reviewed below. For an advanced treatment of different problems of stability and in particular, of the strain localisation, the reader is referred to a fundamental work of Quoc Son Nguen [66].

4.1.1 Localisation Analysis in Continuum Mechanics

Localisation is essentially a transition from a spatially homogeneous to a spatially concentrated inhomogeneous deformation state. The appearance of narrow zones of accumulated inelastic deformations usually accompanies this process, whereby other parts of the body can simultaneously exhibit unloading. Note that concerning the hierarchy of failure, both the velocity and velocity gradient remain continuous fields for diffuse failure.

$$[[\dot{\varphi}]] = 0 \quad \text{and} \quad [[\dot{\mathbf{F}}]] = 0 \quad (4.1)$$

In contrast to this, discontinuities of certain field values can be considered for localised failure. Thereby, the appearance of a discontinuity of the velocity gradient (weak discontinuity, see e.g. Rice [77])

$$[[\dot{\varphi}]] = [[\dot{\mathbf{F}}]] \neq 0 \quad (4.2)$$

corresponds to the loss of ellipticity of the appropriate quasi-static field equations according to the classification of partial differential equations. Here a jump of a field quantity $[[\bullet]] \doteq (\bullet)^+ - (\bullet)^-$ is defined as a difference between the magnitudes of this value on the positive and negative side of

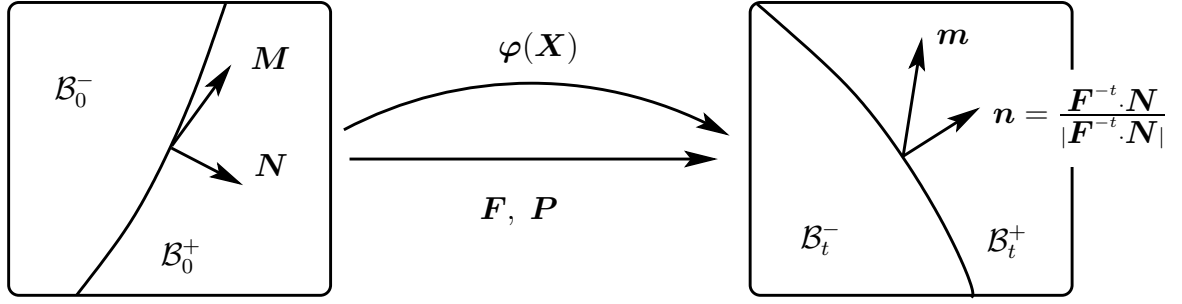


Figure 4.1: Zone of localised inelastic deformation in the spatial configuration; \mathbf{m} and \mathbf{n} denote the polarization vector and the normal to the localisation surface, respectively

the failure surface. The concept of strong discontinuity states a more general kinematical approach assuming the discontinuity of both the velocity and the velocity gradient fields

$$[[\dot{\varphi}]] \neq \mathbf{0} \quad \text{and} \quad [[\dot{\mathbf{F}}]] \neq \mathbf{0}, \quad (4.3)$$

see e.g. Steinmann *et al.* [82]. The strong discontinuity case can be reduced to the weak discontinuity by introduction of a regularisation method, see Steinmann [81]. Therefore, the only case of the weak discontinuity is considered here.

A presence of a discontinuity in the velocity gradient tensor is then kinematically expressed according to Maxwell's consistency condition, see Maxwell [56] and Truesdell and Toupin [92], as a rank-1 tensor weighted with a jump magnitude ξ

$$[[\dot{\mathbf{F}}]] = \xi \mathbf{m} \otimes \mathbf{N} \quad (4.4)$$

Here \mathbf{m} denotes the jump or rather polarisation vector in the spatial configuration and \mathbf{N} represents the normal to the failure surface converted back to the material configuration, see fig. 4.1. Thereby, the connection between \mathbf{n} and \mathbf{N} is given by the Nanson formula (2.14). The equilibrium condition across the failure surface requires continuity of the nominal traction vector \mathbf{t}_0 . By application of the Cauchy theorem, this condition results in

$$[[\mathbf{t}_0]] = \mathbf{t}_0^+ - \mathbf{t}_0^- = \mathbf{0} \quad \implies \quad [[\mathbf{t}_0]] = [[\dot{\mathbf{P}}]] \cdot \mathbf{N} = [[\mathbb{L} : \dot{\mathbf{F}}]] \cdot \mathbf{N} = \mathbf{0} \quad (4.5)$$

with \mathbf{P} and \mathbb{L} defined in (2.17) and (2.23), respectively. Under the assumption of a continuous tangent operator (so called linear comparison solid, see e.g. Hill [38], resulting in the so called continuous bifurcation), we obtain from eq. (4.4) and (4.5) the following localisation condition in terms of an eigenvalue problem for the localisation tensor \mathbf{q}

$$[[\mathbb{L} : [\mathbf{m} \otimes \mathbf{N}]]] \cdot \mathbf{N} = \mathbf{q}(\mathbf{N}) \cdot \mathbf{m} = \mathbf{0} \quad \text{with} \quad \mathbf{q} \doteq \mathbb{L} \mathbin{\text{?}} [\mathbf{N} \otimes \mathbf{N}] \quad (4.6)$$

or in componentwise representation ¹:

$$q_{pr} = L_{pQrS} N_Q N_S$$

¹The non-standard double contraction $\mathbin{\text{?}}$ can be introduced in terms of the non-standard dyadic product $\overline{\otimes}$ emerging in (2.40) for 2^{nd} -order tensors \mathbf{A} , \mathbf{B} and \mathbf{C} as

$$[\mathbf{A} \overline{\otimes} \mathbf{B}] \mathbin{\text{?}} \mathbf{C} = \mathbf{A}[\mathbf{B} : \mathbf{C}] \quad \text{or} \quad [\mathbf{A} \overline{\otimes} \mathbf{B}]_{pQrS}, C_{QS} \doteq A_{pr} B_{QS} C_{QS}$$

Thus, the appearance of non-zero solutions of eq. (4.6) indicates the possibility of strain localisation. A homogeneous equation system renders non-trivial solutions if its determinant vanishes. Therefore, the localisation condition can be reduced to

$$\det \mathbf{q}(\mathbf{N}) = 0 \iff \text{loss of ellipticity, possible discontinuities in } \llbracket \dot{\mathbf{F}} \rrbracket \quad (4.7)$$

The fact that $\det \mathbf{q}(\mathbf{N})$ becomes zero or negative thus corresponds to the possible occurrence of localisation in the form of continuous bifurcation. The sign-change of $\det \mathbf{q}(\mathbf{N})$ must therefore be checked during an incremental loading history for all spatial directions \mathbf{N} . The corresponding stress is the critical stress and \mathbf{N}^{crit} determines the failure direction corresponding to $\mathbf{N}^{crit} = \arg \min_{\mathbf{N}} \{\det \mathbf{q}\}$.

4.1.2 Derivation of the Localisation Criterion for Continuum-Atomistic Modelling

Finally, the localisation tensor \mathbf{q} takes an especially simple and elegant format within the framework of the continuum-atomistic approach. By substitution of the tangent operator \mathbb{L} given by the expression (2.40) into the definition of the localisation tensor (4.6), the following format of the acoustic tensor can be obtained:

$$\mathbf{q} = \frac{1}{2V_i} \sum_{j \neq i} \left[\mathbf{k}_{ij}^{(0)} [\mathbf{R}_{ij} \cdot \mathbf{N}]^2 + \sum_{\substack{m \neq i \\ m \neq j}} \mathbf{k}_{ij}^{(m)} [\mathbf{R}_{im} \cdot \mathbf{N}] [\mathbf{R}_{ij} \cdot \mathbf{N}] \right] \quad (4.8)$$

Note that the acoustic tensor is defined in the spatial configuration. If the pair potentials are used, (4.8) reduces to simple format since $\mathbf{k}_{ij}^{(m)} = 0$ and $\mathbf{k}_{ij} \equiv \mathbf{k}_{ij}^{(0)}$ in this case:

$$\mathbf{q} = \frac{1}{2V_i} \sum_{j \neq i} \mathbf{k}_{ij} [\mathbf{R}_{ij} \cdot \mathbf{N}]^2 \quad (4.9)$$

The localisation tensor in this case thus consists of the weighted sum over atomistic level stiffnesses. This statement is supported by the fact that the localisation tensor describes wave propagation in continuous media for the dynamic case, whereas the atomistic level stiffness does the same for discrete media.

4.1.3 Examples

To illustrate the developments discussed above, two different homogeneous deformations have been applied to the (111)–plane of *fcc*–type crystals and the behaviour of the localisation tensor as a function of crystal directions and applied deformation has been studied. In the computations, the sublimation energy and lattice constant of aluminium, $E_s = 3.58 \text{ eV} = 0.574 \text{ nNm}$ and $r_0 = 0.286 \text{ nm}$ respectively have been used to fit the parameters ε and σ of the Lennard-Jones potential as described in chapter 2. The cut-off radius r_c is chosen to be $5r_0$, and table 2.1 yields the values of the Lennard-Jones parameters ε and σ corresponding to $n = 5$. In the plane, the following setting for \mathbf{N} has been used:

$$\mathbf{N} = \cos \phi \mathbf{e}_1 + \sin \phi \mathbf{e}_2. \quad (4.10)$$

Simple Shear

The simple shear deformation is characterised by the deformation gradient

$$\mathbf{F} = \mathbf{I} + \gamma [\mathbf{e}_1 \otimes \mathbf{e}_2]$$

with the unit tensor \mathbf{I} and the shear number $\gamma = \tan \alpha$, see fig. 5.3, whereby \mathbf{e}_i denotes the cartesian

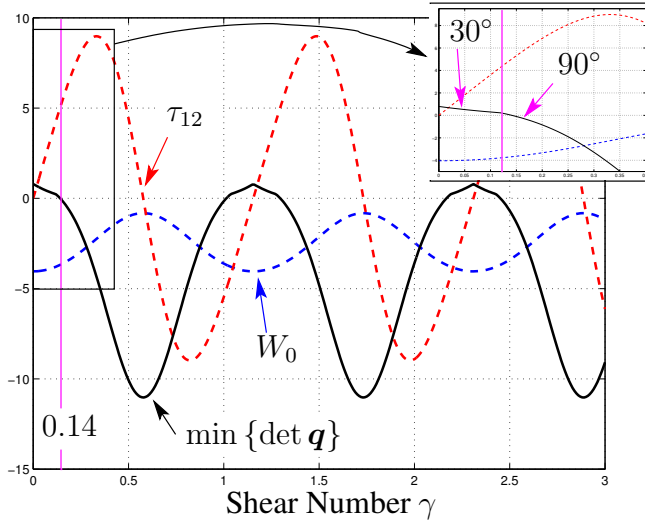


Figure 4.2: The strain energy density W_0 , the Kirchhoff shear stress τ_{12} and the minimum of the acoustic tensor determinant $\det \mathbf{q}$ as a functions of the shear number γ . The change of curvature of $\min\{\det \mathbf{q}\}$ is caused by shifting of its position ϕ from 30° to 90° at $\gamma \approx 0.14$.

unit vectors. During the deformation, atomic planes (or atomic rows for the planar case) slip relative to each other and the atomistic arrangement of the undeformed configuration repeats itself periodically. This can be recognised again on both bottom images of fig. 2.6. The undeformed (on the left) and the sheared structures are equivalent. Therefore, a periodical behaviour of the strain energy density

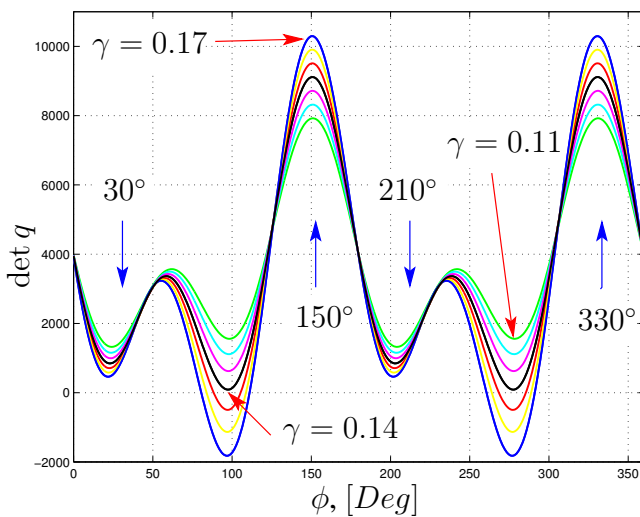


Figure 4.3: Determinant of the acoustic tensor vs. directions in the plane for different shear numbers between 0.11 and 0.17. At $\gamma \approx 0.14$, a change of the position of the minimum takes place: the minimum shifts from 30° to 90° .

and stress tensor components is expected. This periodicity can indeed be obtained by computing the actual neighbours contained in the cut-off sphere after every load increment, see fig. 2.9. It is expected

that the determinant of the localisation tensor $\det \mathbf{q}$ also exhibits a periodical behaviour. In fact, this periodical behaviour can be obtained by using equation(4.9). The minimum of the determinant of acoustic tensor is shown in fig. 4.2 as a function of the shear number γ . Thereby, the determinant is negative for the part of deformations. It means that the configurations corresponding to such shear numbers are not favourable from an energetical point of view. They would relax if the atoms would not be fully constrained. Furthermore, it is easy to recognise that the $\min\{\det \mathbf{q}\}$ -curve exhibits a change of curvature at $\gamma \approx 0.14$. This can be explained in terms of the abrupt shifting of the position ϕ of this minimum, see fig. 4.3. $\det \mathbf{q}$ vs. ϕ -curves for different γ between 0.11 and 0.17 are shown in this figure. The minimum of $\det \mathbf{q}$ lies at 30° for $\gamma < 0.14$ and at 90° for $\gamma \geq 0.14$ and becomes negative directly after the hanging of its position. It is remarkable that all the curves have a local extremum for ϕ corresponding to the normals to the slip directions in the (111) -plane. For instance, $\mathbf{N} \doteq [\cos 150^\circ \ \sin 150^\circ]$ is the normal to the slip direction $[\bar{1}01]$, see fig. 4.4. Recall that the obtained

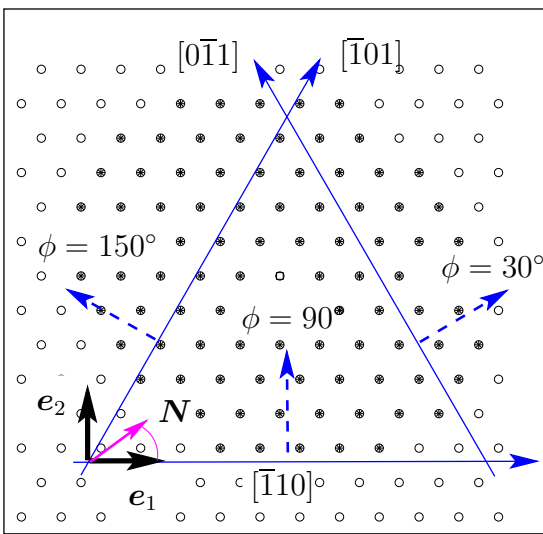


Figure 4.4: Slip system of fcc -type crystal in the (111) -plane

results depend on the orientation of the representative crystallite. For example, crystallites rotated by 60° relative to the original crystallite yield identical results due to symmetry. Fig. 2.10 compares strain energy densities and shear stresses of the Kirchhoff stress tensor for unrotated crystallites and crystallites rotated by 30° .

Uniaxial Extension without Lateral Contraction

The deformation gradient for uniform extension without lateral contraction shown in fig. 2.7 can be considered as

$$\mathbf{F} = \mathbf{I} + [\lambda - 1] \mathbf{e}_2 \otimes \mathbf{e}_2$$

with the unit tensor \mathbf{I} and the stretch λ . This deformation is not as spectacular as the simple shear deformation since it yields no periodicity in the appropriate quantities. The strain energy and the components of the Cauchy stress tensor $\boldsymbol{\sigma} \doteq \boldsymbol{\tau} / \det \mathbf{F}$ are displayed simultaneously with the values of $\min\{\det \mathbf{q}\}$ in fig. 4.5. The fact that a sign-change of $\min\{\det \mathbf{q}\}$ corresponds approximately to the maximum tension stress σ_{22} is in a good agreement with theoretical expectations. As in the previous case, a change of curvature of the minimum of $\det \mathbf{q}$ occurs shortly before the $\min\{\det \mathbf{q}\}$

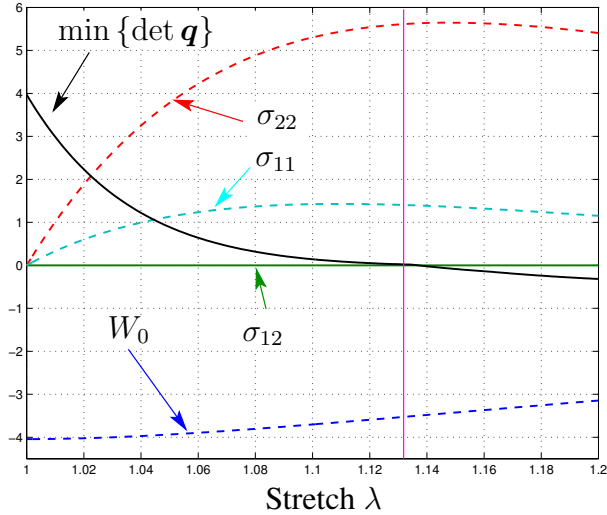


Figure 4.5: The strain energy density W_0 , the components of the Cauchy stress tensor σ and the minimum of the acoustic tensor determinant $\det \mathbf{q}$ as a functions of the stretch λ . The change of curvature of $\min\{\det \mathbf{q}\}$ is caused by shifting of its position ϕ from 90° to 0° at $\lambda \approx 1.135$.

becomes negative. This can be recognised in fig. 4.6, which shows $\det \mathbf{q}$ vs. ϕ curve for the values of the stretch λ close to the point of the sign-change of $\det \mathbf{q}$. At $\lambda \approx 1.135$, a change of the position of the minimum takes place: the minimum shifts from 90° to 0° . This mode becomes plausible if one remembers that there is no lateral contraction, i.e. the left and right edges are fixed and a tension in the horizontal direction occurs.

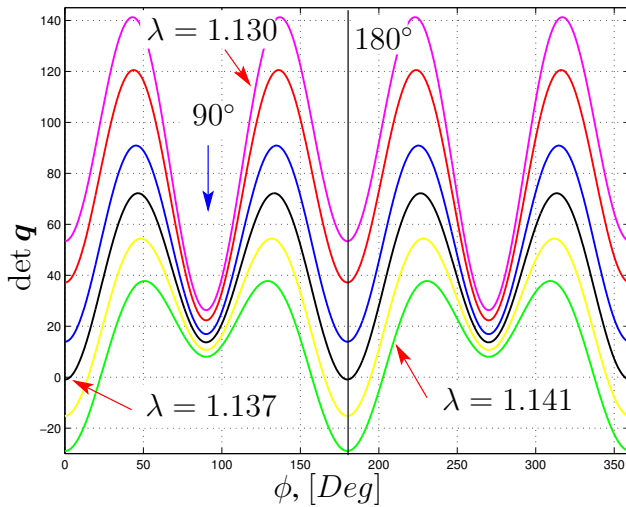


Figure 4.6: Determinant of the acoustic tensor vs. directions in the plane for different stretches between 1.130 and 1.141. At $\lambda \approx 1.135$, a change of the position of the minimum takes place: the minimum shifts from 90° to 0° . At $\lambda \approx 1.137$, the determinant of the acoustic tensor becomes negative.

4.1.4 Computation of Failure Surface

By making use of the derived localisation criterion (3.7) in terms of the eigenvalue problem for the acoustic tensor given by (4.9), a macroscopic failure surfaces for single crystals can be obtained. The following flow chart can be proposed for the computation of a single point of the failure surface in the principal stress space.

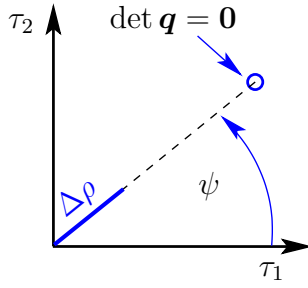


Figure 4.7: An illustration of the flow chart for the computation of a failure surface. $\Delta\rho$ is an increment in the length of the vector in the principal stress state with direction given by ψ .

1. Define Atomistic Arrangement (Structure, Rotation)
2. Define Polar Angle ψ in Principal Stress Space

3. Set $\tau^{pr} = n \Delta\rho \begin{bmatrix} \cos \psi & 0 \\ 0 & \sin \psi \end{bmatrix}$

4. Compute Deformation Gradient \mathbf{F} :

$$\frac{1}{2V} \sum_{j \neq i} \mathbf{f}_{ji}(\mathbf{F}) \otimes \mathbf{r}_{ij} - \tau^{pr} \longrightarrow \min$$

5. Compute Determinant of localisation Tensor

$$\det \mathbf{q}(\mathbf{N}) = \det \frac{1}{2V} \sum_{j \neq i} [\mathbf{R}_{ij} \cdot \mathbf{N}]^2 \mathbf{k}_{ij}(\mathbf{F})$$

6. Check localisation Condition

```

IF      det  $\mathbf{q}(\mathbf{N}) < 0$    $\Rightarrow$    $\tau^{pr} = \tau^{crit}$   AND   $\mathbf{N} = \mathbf{N}^{crit}$ 
ELSE     $\Rightarrow$    $n = n + 1$  ; GOTO 3
ENDIF

```

Here, τ^{pr} and $\Delta\rho$ denote the prescribed Kirchhoff's stress tensor and an increment in the length of the vector in the principal stress space with direction given by the polar angle ψ , respectively. $n = 1, 2, \dots$ is the step number. Fig. 4.7 illustrates the flow chart given above.

In this way, a discrete number of points of a failure surface can be obtained for any desired ratio of principal stresses τ_1 and τ_2 . The results of this computational procedure for both Lennard-Jones and EAM potentials are shown in fig. 4.8. The failure surfaces are open in the third quadrant i.e. in the region of compression. This is associated with the absence of a compression limit within the used atomic potential. Due to the special format of the employed potentials, the strain energy can increase during compression without limit. The failure surface is pronounced antisymmetric 1) due to the anisotropy of the underlying crystal structure and 2) due to the asymmetry of the used potentials mentioned above. For instance, the difference between the critical stresses τ_1 during uniaxial tension

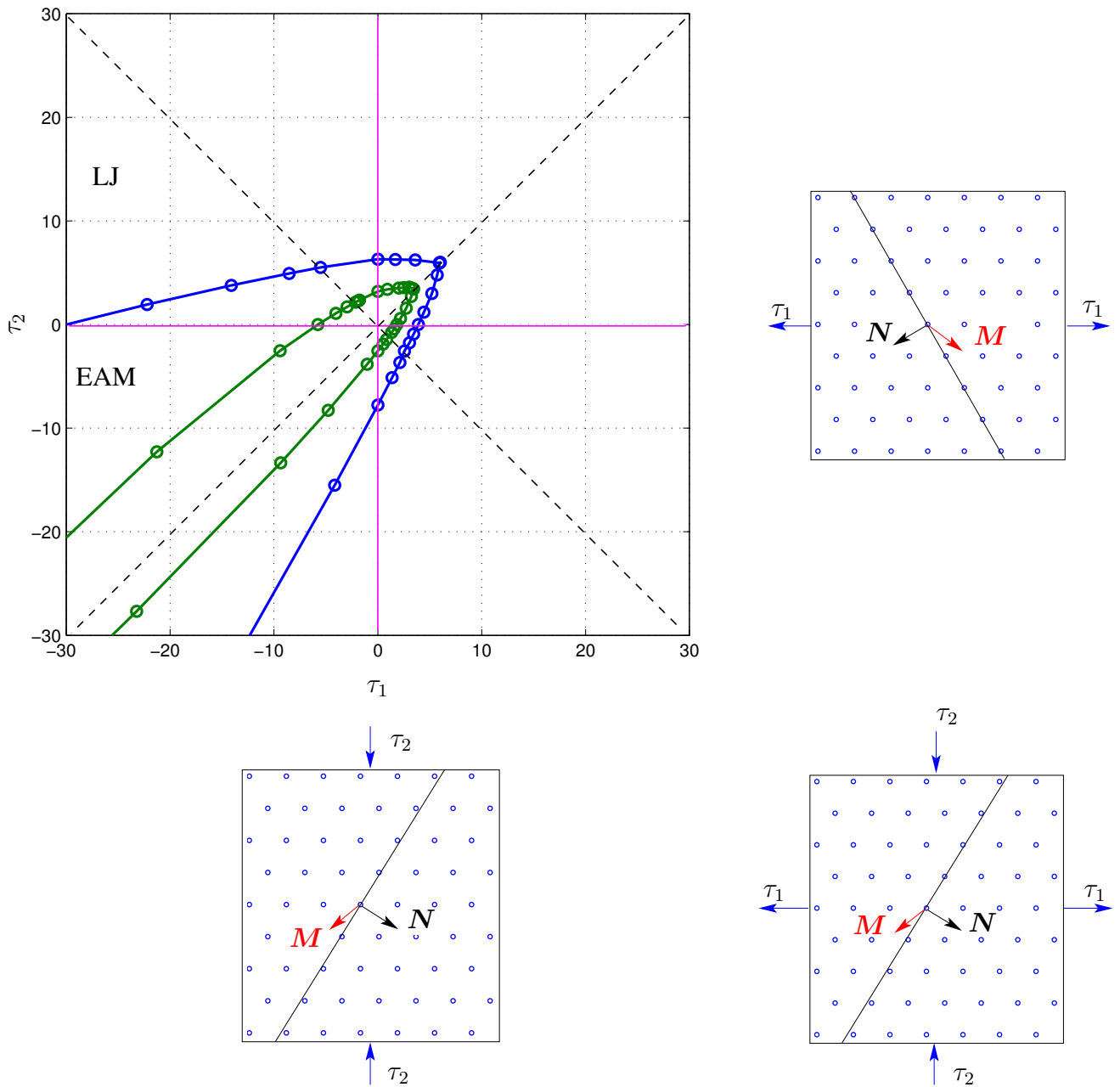


Figure 4.8: Failure surfaces computed for both Lennard-Jones and EAM potentials. They are open in the region of compression due to absence of compression limit in the used model. localisation modes corresponding to the uniaxial extension in x and y directions and to the pure shear are shown.

and compression ($\tau_2 = 0$) could probably be related to the activation of several modes of instability during compression whereas for tension, only one mode is available. This idea can be checked by comparing the normal vector \mathbf{N} and the polarisation vector \mathbf{m} corresponding to critical compression and tensile stresses. Indeed, the difference of the directions of the jumps in $[[\dot{\mathbf{F}}]]$ or the normals to the localisation surfaces for both critical stress states reflects an activation of different modes of instability during the deformation process.

The orientation of the underlying crystal structure with respect to the principal stress axes influences the results of the failure surface computation. Fig. 4.9 shows two such surfaces computed for the Lennard-Jones potential in the first quadrant of the principal plane stress space for two crystallites rotated by 30° relative to each other. Due to the cubic symmetry of the employed atomic arrangement, rotation by 30° corresponds simultaneously to a rotation by 90° . For this reason, both failure surfaces are symmetric with respect to the diagonal of the first quadrant. The computed surfaces look

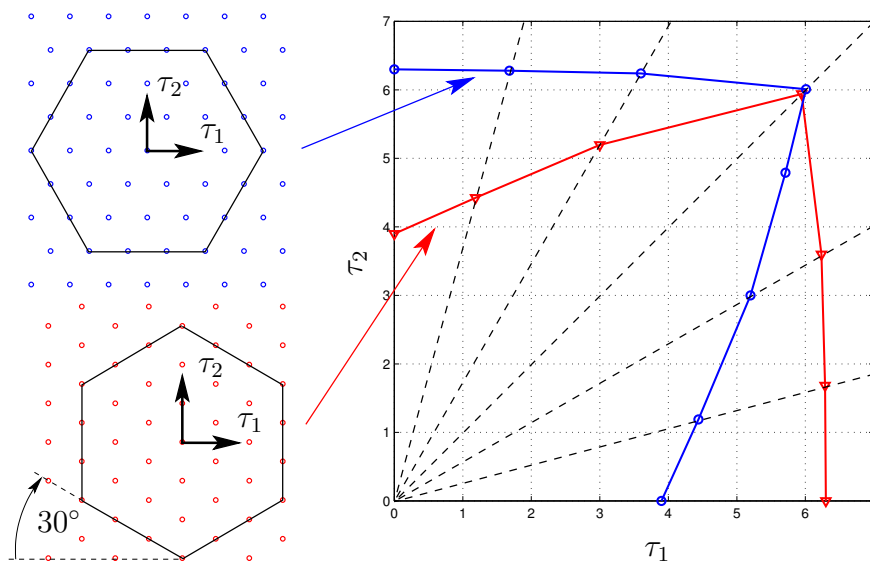


Figure 4.9: Influences of the underlying crystal structure orientation with respect to the principal stress axes on the failure surface.

qualitatively realistic and is similar to e.g yield surfaces for granular materials and concrete. The only problem, which must be understood, is that the computed failure modes, i.e. the combinations \mathbf{M} , \mathbf{N} cannot be interpreted plausibly since the computed glide directions differ from the known glide directions in the (111) -plane of fcc -crystals. To understand this phenomenon, the load history for a number of stress states has been studied. The results for the $\psi = 30^\circ, 44.9^\circ, 90^\circ, 135^\circ, 180^\circ$ are represented in appendix ??.

4.2 Finite Element Implementation

In previous section, the loss of infinitesimal rank-one convexity has been used as a method, which allows to detect the elastic limit. In the present section, a finite element implementation of this

criterion is discussed. For the sake of demonstration, the examples from chapter 2 are extended by such additional investigation and placed in this section.

4.2.1 Indentation Test

At first, the results of the indentation test with different shaped tips are represented.

Spherical Indenter

The computation of the minimum of $\det \mathbf{q}$ after each load step indicates the loss of ellipticity in 2 elements already at the penetration depth of about 90 nm and 175 nm for the Lennard-Jones (LJ) and EAM potentials respectively. Nevertheless, an application of further deformation remains still

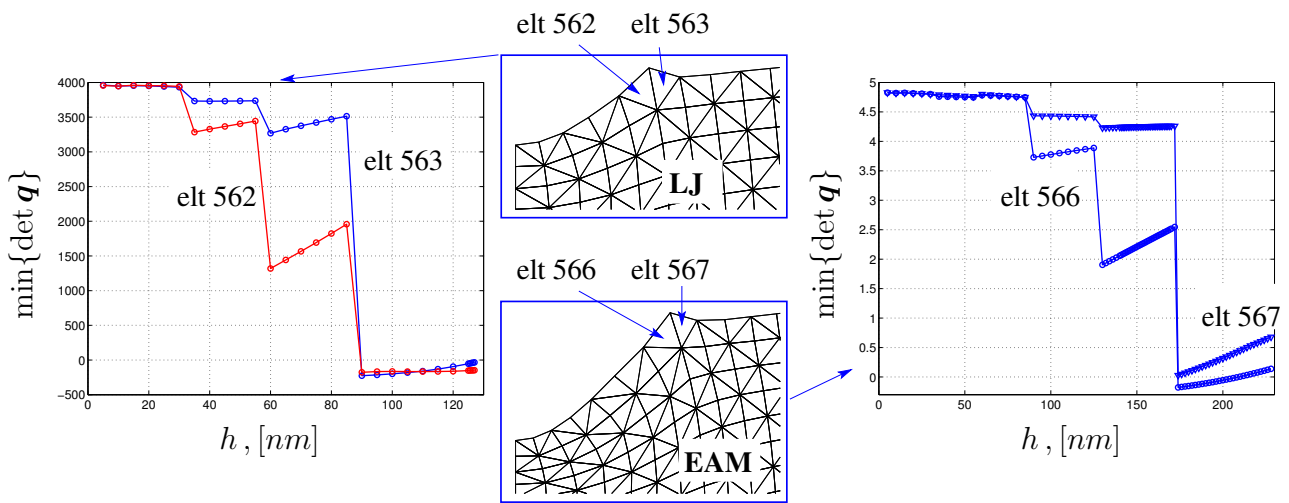


Figure 4.10: Minimum of the determinant of acoustic tensor in failed elements with element numbers 562 and 563 (LJ) and 566 and 567 (EAM) vs. the penetration depth h . Each jump corresponds to an inclusion of a new node in the contact, cf. fig. 2.18. At the penetration depth of about 90 nm and 175 nm for the LJ and EAM potentials respectively, $\det \mathbf{q}$ becomes negative in both elements.

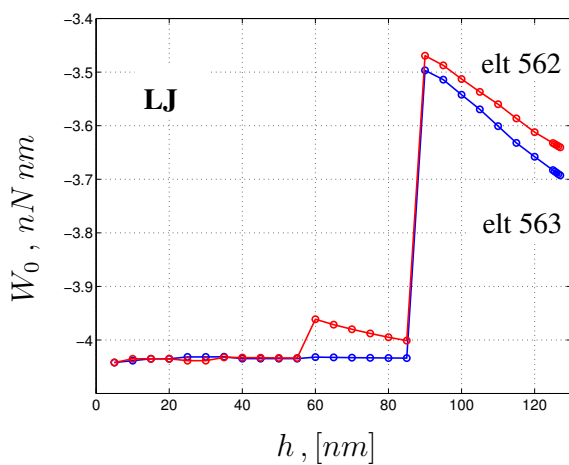


Figure 4.11: Strain energy density W_0 in both failed elements vs. the penetration depth h for the LJ potential. At the same penetration depth of about 90 nm when $\min\{\det \mathbf{q}\}$ becomes negative, W_0 increases considerably in both elements, so that an instability of the homogeneous Cauchy-Born deformation of the underlying crystallites occurs.

possible during the next several steps. Then the iterative solution strategy fails. Fig. 4.10 shows the behaviour of the minimum of $\det \mathbf{q}$ during the deformation in both elements where the loss of infinitesimal rank-one convexity takes place. Each jump in the curves corresponds to an inclusion of a new node in the contact, cf. fig. 2.18. After a next node has been involved, the distribution of the deformation becomes more homogeneous and $\min\{\det \mathbf{q}\}$ increases during several load steps. At the penetration depth of about 90 nm , $\det \mathbf{q}$ becomes negative in both elements. The curves shows an increase even in the region where they lie below zero. Admittedly, this post-critical behaviour has no importance for a finite element simulation including plasticity: as soon as the $\det \mathbf{q}$ of an element becomes negative, an appropriate plasticity model should be used in this element.

At the same penetration depth of about 90 nm when $\min\{\det \mathbf{q}\}$ becomes negative by using the LJ potential, the strain energy density W_0 increases considerably in both elements, see fig. 4.11, and an instability of the homogeneous Cauchy-Born deformation of the underlying crystallites occurs. During further deformation, W_0 exhibits a decrease indicating a stabilisation of the homogeneous deformation. As mentioned chapter 2, the jumps and consequently, the critical deformation corresponding to the loss of ellipticity should be mesh-dependent. Therefore, the obtained results must be verified by using differently refined meshes.

Pyramidal Tip

In this case, the element 553 exhibits the highest deformation, so that the failure first takes place in this element for both used potentials. Fig.4.12 shows the behaviour of the minimum of $\det \mathbf{q}$ in this element and in element 529 as a function of the penetration depth h . The strain energy density of both elements obtained by using the LJ potentials and depicted in fig. 4.13 exhibits no jumps and looks similar to the case of the the horizontal shearing.

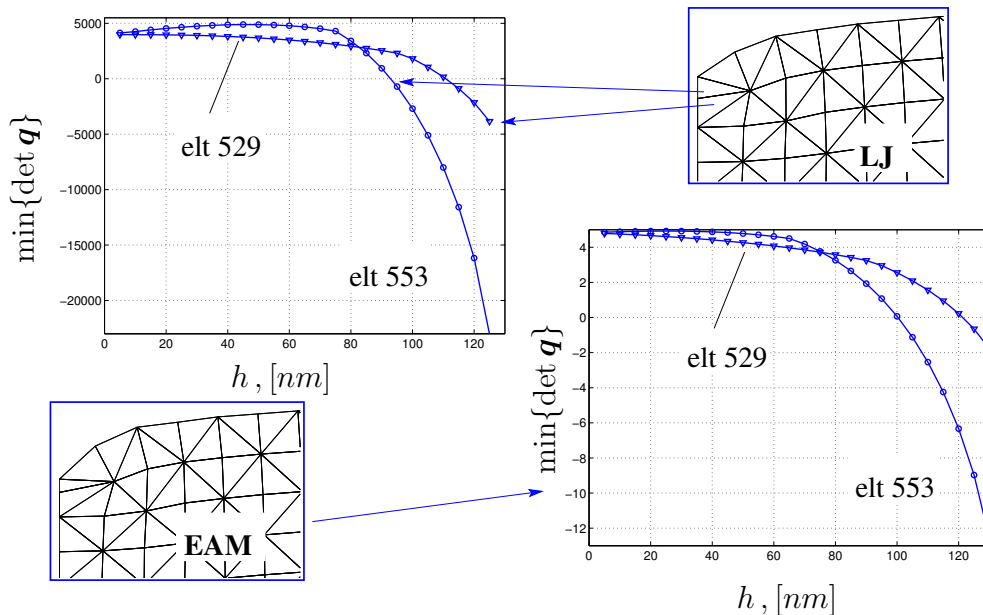


Figure 4.12: Minimum of the determinant of acoustic tensor in failed elements with element number 553 and 529 vs. the penetration depth h . At the penetration depth of about 90 nm , $\det \mathbf{q}$ becomes negative in the element 553 for both potentials.

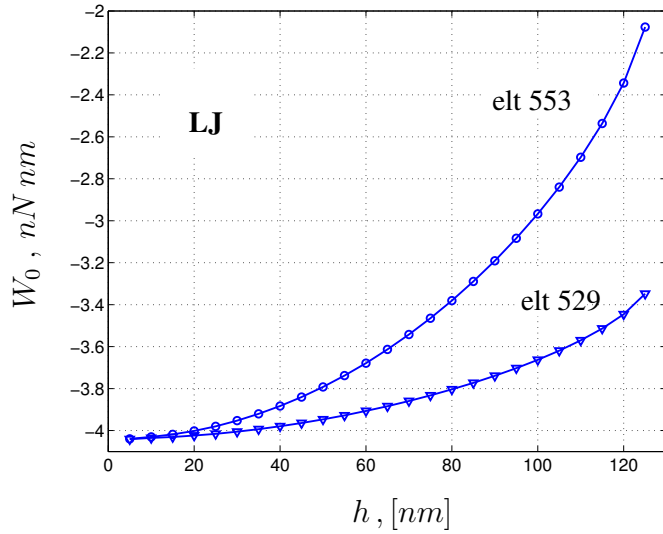


Figure 4.13: Strain energy density W_0 in the failed elements vs. the penetration depth h for the LJ potential. The behaviour of W_0 is similar to its behaviour in the shear experiment, see example with horizontal shearing.

Flat Indenter

As mentioned above, an indentation with the flat punch is characterised by a large elastic deformation, which becomes possible due to a load distributed among the nodes taking part in contact. The failure history is mirrored in fig. 4.14. The loss of ellipticity first occurs in element 547 at the penetration depth h of about 260 nm by using the LJ potentials and in element 570 at the penetration depth h of about 285 nm by using the EAM potentials.

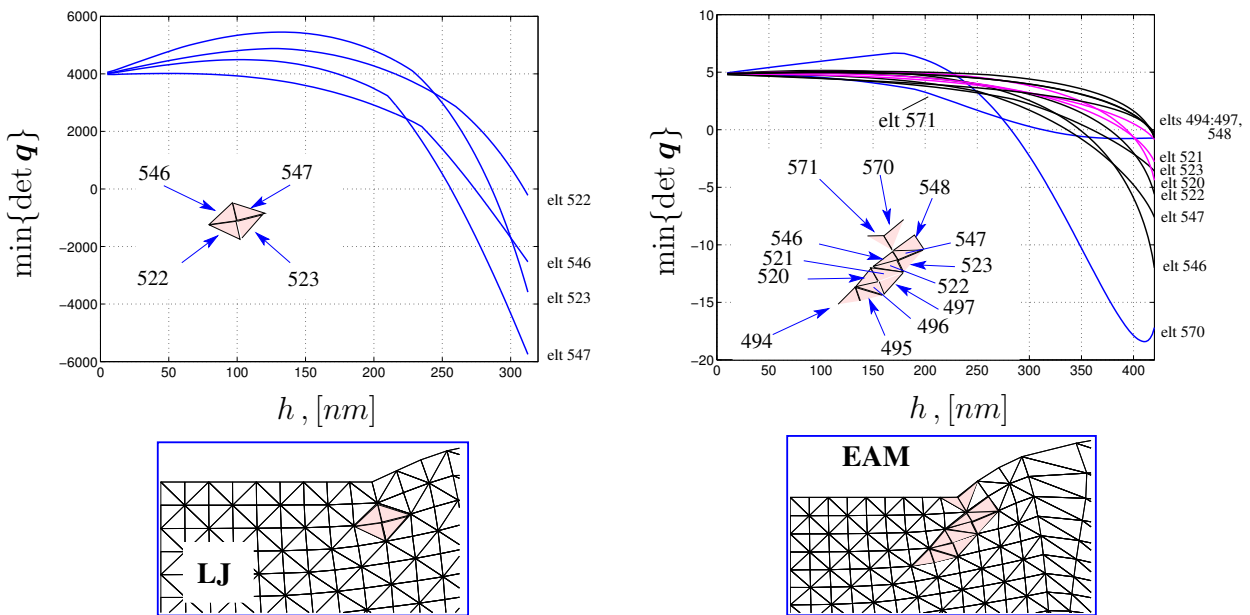


Figure 4.14: Minimum of the determinant of acoustic tensor in failed elements vs. the penetration depth. At the penetration depth of about 260 nm and 285 nm , $\det \mathbf{q}$ becomes negative in the elements 547 and 570 for the LJ and EAM potentials respectively.

This failure does not affect the convergence of the iterative solution. Element 523 fails at the penetration depth of 274 nm ; element 546 at 286 nm and element 522 at 310 nm by using the LJ potential. A loss of the convergence has consequently been obtained at $312, 6 \text{ nm}$ for this potential. As mentioned above, the EAM potential allows a higher elastic deformation: a loss of the convergence occurs firstly at 420 nm when elements 570, 571, 547, 546, 523, 522, 521, 520, 497, 494, 495, 496, and 548 fail.

The behaviour of the strain energy density W_0 in the failed elements is shown in fig. 4.15 for the LJ potential. All energies increase with the increasing deformation and the corresponding (homogeneously) deformed structures becomes instable if a critical energy level is reached. This level corresponds approximately to the highest energy in element 522, where the loss of ellipticity took place a few small load steps ago.

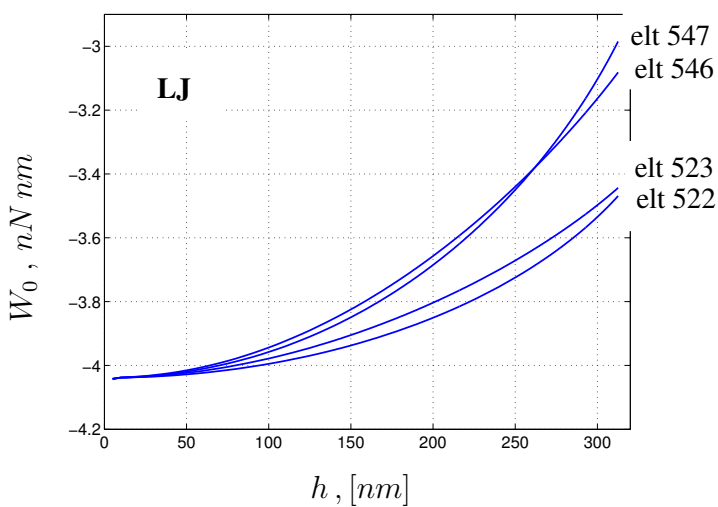


Figure 4.15: Strain energy density W_0 in the failed elements vs. the penetration depth h for the LJ potential. The behaviour of W_0 is similar to its behaviour in the shear experiment, see example with horizontal shearing.

Flat Indenter: another Example

Another example of an indentation with the flat punch seems to be interesting since it yields results, which are qualitative similar to the slip-line field solution developed by Prandtl [74] for such indentation problem on a semi-infinite medium without friction.

The sample's geometry in this example is similar to that shown in fig. 2.14 with the width of $28.6 \mu\text{m}$ and the height of $10 \mu\text{m}$; the punch has a width of $\approx 11.4 \mu\text{m}$. Contrary to the previous problem, all degrees of freedom on the bottom edge of the sample are fixed in this example. The manually meshed sample with the applied boundary conditions is shown in the upper part of fig. 4.16. The LJ potential has been used for this simulation.

According to the Prandtl's solution, the triangular area lying directly beneath the punch moves down as an entire body. Such behaviour can easily be recognised in the lower part of fig. 4.16, where the deformed sample is depicted. The loss of the infinitesimal rank-one convexity takes place in the highlighted elements representing a localisation zone. The corresponding $\min\{\det \mathbf{q}\}$ vs. penetration depth—curves for the failed elements are represented additionally. Since the problem exhibits a full symmetry with respect to the vertical axis, the only curves for the highlighted elements of the right-hand part of the sample are depicted.

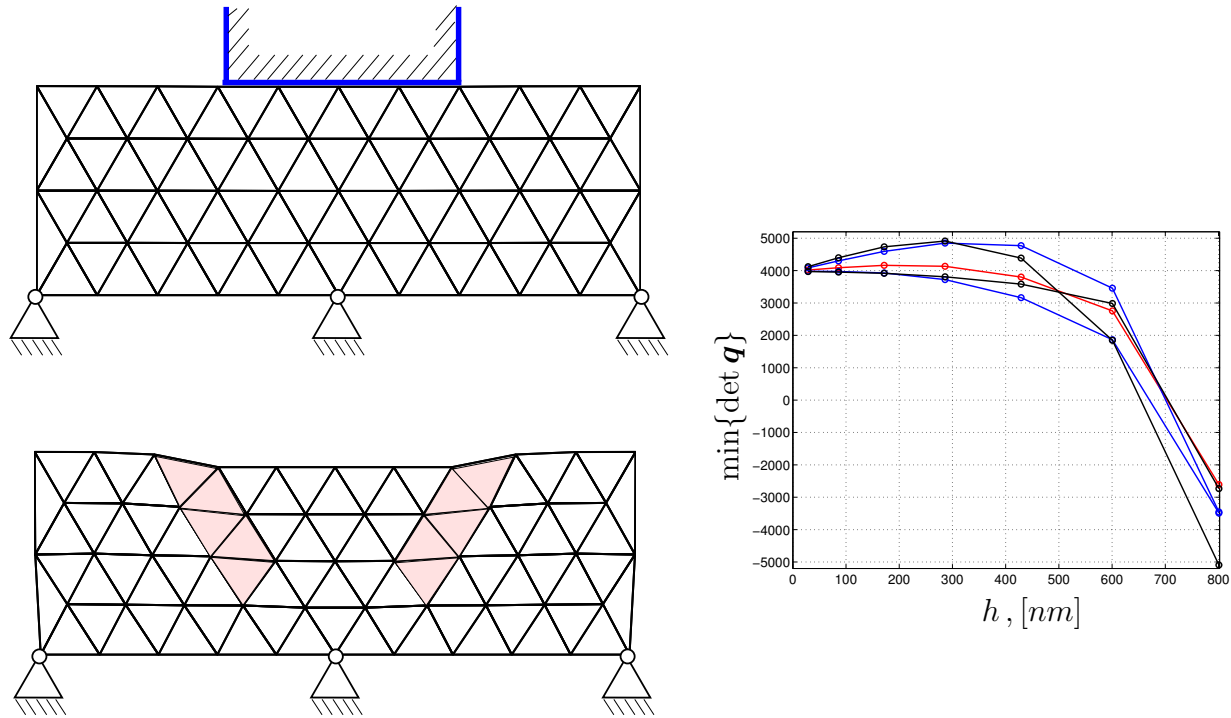


Figure 4.16: The meshed undeformed sample with the constraints (upper part) and the deformed sample with the highlighted elements, where the criterion of the loss of the infinitesimal rank-one convexity fails (lower part). The $\min\{\det \mathbf{q}\}$ vs. *penetration depth*–curves for the failed elements are shown additionally.

4.2.2 Horizontal Shearing

In this example, the 1st element (with number 55) fails when the horizontal displacement of the top left corner reaches approx. 3183 nm corresponding to the 45th load step. The total number of the failed elements reaches 7 after the last possible 52nd load step is completed. All the failed elements are highlighted in fig. 4.17. A minimum of the corresponding determinant of the acoustic tensor is shown for each element. $\det \mathbf{q}$ has a minimal value in element 55 where the loss of ellipticity occurs at first. The failure of the whole simulation takes place shortly after failure in this element. The strain energy densities in the failed elements are shown in fig. 4.18 as functions of the horizontal displacement of the left top corner. A maximal value is thereby reached as expected in element 55. The asymmetry in the placement of failed elements can be explained by the force-controlled simulation.

Using the terminology of the particle physics, it could be stated that these “excited” energetic states become unstable. Whereas in the case of, say, an excited electron it would reduce its energy by emission of a photon, in the case of a homogeneously deformed mechanical system, a relaxation due to development of a microstructure should occur.

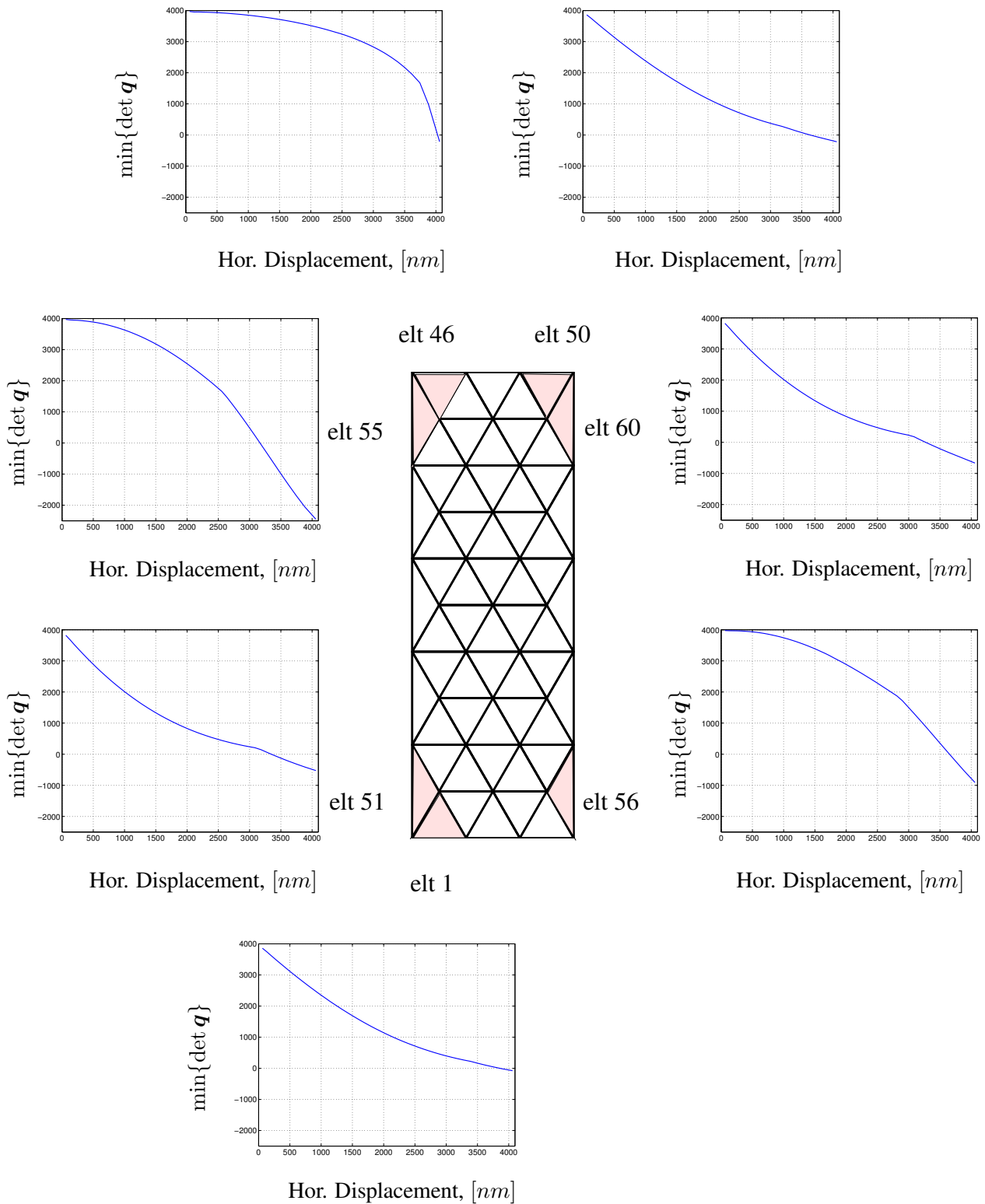


Figure 4.17: Minimum of the determinant of acoustic tensor in failed elements with element numbers 55, 60, 51, 50, 56, 1 and 46 vs. the horizontal displacement of the left top corner. At the displacement of about 3183 nm, $\det \mathbf{q}$ of element 55 becomes negative.

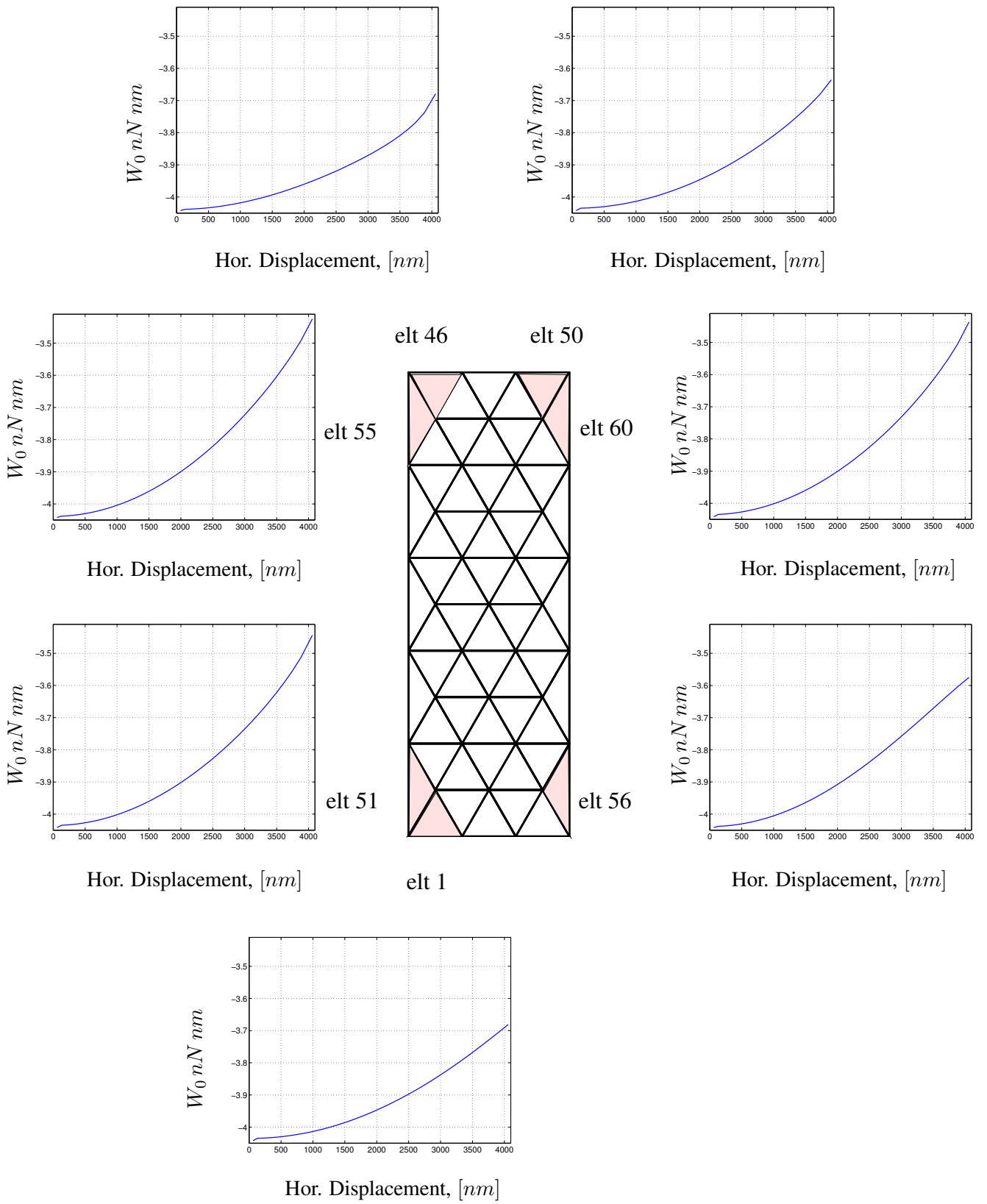


Figure 4.18: Strain energy density W_0 in the failed elements vs. the horizontal displacement of the left top corner.

4.3 Relaxation

The topic of this section is how to overcome the loss of quasiconvexity of the strain energy density or in other words, how the transition from elasticity to plasticity can be realised within the frame of continuum-atomistic modelling. As mentioned at the end of previous chapter, it could be done if the homogeneously deformed lattice obtains a possibility to relax, i.e. if each atom in RVE obtains additional degrees of freedom relative to the prescribed homogeneous deformation, which allow it to occupy a new position minimising the total energy in comparison with the homogeneous Cauchy-Born deformation, cf. Tadmor et al. [89]. A quasiconvex envelope for a scalar-valued tensor function $W(\mathbf{F})$ in a continuous case is given in theorem 3.3 (4). In this case, the total energy must be minimised with respect to an arbitrary perturbation $\nabla_X \tilde{\varphi}$ of the deformation gradient \mathbf{F} .

A similar construction can be considered for the discrete lattice system being handled here. Let us extend the Cauchy-Born rule (2.31) by an unknown term:

$$\mathbf{r}_i = \mathbf{F} \cdot \mathbf{R}_i + \mathbf{a}_i = \mathbf{F} \cdot [\mathbf{R}_i + \mathbf{A}_i] \quad (4.11)$$

with the additional inner material displacements \mathbf{A}_i . Then the strain energy density W_0 given in (2.30) is now a function of the deformation gradient and these displacements:

$$\begin{aligned} W_0 &= \frac{1}{NV_i} \sum_{i=1}^N E_i(r_{i1}, \dots, r_{iN}) = \frac{1}{NV_i} \sum_{i=1}^N E_i(|\mathbf{F} \cdot [\mathbf{R}_{i1} + \mathbf{A}_{i1}]|, \dots, |\mathbf{F} \cdot [\mathbf{R}_{iN} + \mathbf{A}_{iN}]|) \\ &= W_0(\mathbf{F}, \mathbf{A}_1, \dots, \mathbf{A}_N) \end{aligned} \quad (4.12)$$

where $\mathbf{R}_{ij} + \mathbf{A}_{ij} \doteq \mathbf{R}_i + \mathbf{A}_i - \mathbf{R}_j - \mathbf{A}_j$. The relaxed strain energy density can be written in the following format:

$$\widetilde{W}_0(\mathbf{F}) = \inf_{\mathbf{A}_{ij}} \left\{ \frac{1}{NV_i} \sum_{i=1}^N E_i(|\mathbf{F} \cdot [\mathbf{R}_{i1} + \mathbf{A}_{i1}]|, \dots, |\mathbf{F} \cdot [\mathbf{R}_{iN} + \mathbf{A}_{iN}]|) \right\}, \quad (4.13)$$

which is analogous to $QW(\mathbf{F})$ introduced in theorem 3.3 (4). Use of the pair potentials leads to a simplification of (4.13):

$$\widetilde{W}_0(\mathbf{F}) = \inf_{\mathbf{A}_{ij}} \left\{ \frac{1}{2NV_i} \sum_{i=1}^N \sum_{j \neq i}^N \Phi(|\mathbf{F} \cdot [\mathbf{R}_{ij} + \mathbf{A}_{ij}]|) \right\}. \quad (4.14)$$

4.3.1 Derivation of Equilibrium Conditions

The minimisation of W_0 defined in (4.12) results in the following equilibrium conditions:

$$\left. \frac{\partial W_0}{\partial \mathbf{A}_i} \right|_{\mathbf{F}=\text{const}} = \mathbf{0}. \quad (4.15)$$

Simple but tedious calculations yield the following explicit format of these conditions:

$$\frac{1}{NV_i} \sum_{j \neq i}^N \mathbf{F}^t \cdot \mathbf{f}_{ji} \doteq \mathbf{0} \quad (4.16)$$

with $f_{ji} = f_{ij}$ defined in (2.3). To solve the non-linear equation system (4.16) by e.g. Newton-Raphson method described in chapter 2, the 2nd-order tangent operator

$$\mathbf{b}_{ij} \doteq \left. \frac{\partial^2 W_0}{\partial \mathbf{A}_i \otimes \partial \mathbf{A}_j} \right|_{\mathbf{F}=\text{const}}$$

is needed. Direct derivation of (4.16) with respect to \mathbf{A}_j yields in view of (2.3) a simple format for \mathbf{b}_{ij}

$$\mathbf{b}_{ii} = -\frac{1}{N V_i} \mathbf{F}^t \cdot \mathbf{k}_{ii} \cdot \mathbf{F}, \quad \mathbf{b}_{ij} = -\frac{1}{N V_i} \mathbf{F}^t \cdot \mathbf{k}_{ij} \cdot \mathbf{F} \quad (4.17)$$

with the atomic-level stiffnesses \mathbf{k}_{ii} and \mathbf{k}_{ij} introduced in (2.10) and (2.7) respectively. Note that (4.16) and (4.17) are derived without any special assumptions about the energy function and are based on the general format (4.12) for the total energy. They are therefore valid for pair potentials as well as for many-body potentials like EAM.

As soon as the inner displacements \mathbf{A}_i are found, the relaxed atomic positions \mathbf{r}_i can be computed according to (4.11). The knowledge of new \mathbf{r}_i allows the computation of the 1st Piola-Kirchhoff stress tensor as well as the 4th-order tangent operator \mathbb{L} according to their definitions (2.17) and (2.23) respectively. However, due to the additional dependence of W_0 on the inner displacements the expressions for \mathbf{P} and \mathbb{L} now contain the 3rd-order tensor $\partial \mathbf{A}_i / \partial \mathbf{F}$, see Tadmor et al. [89]:

$$\mathbf{P} = \frac{\partial W_0}{\partial \mathbf{F}} + \sum_i \frac{\partial W_0}{\partial \mathbf{A}_i} \cdot \frac{\partial \mathbf{A}_i}{\partial \mathbf{F}} \quad (4.18)$$

$$\mathbb{L} = \frac{\partial^2 W_0}{\partial \mathbf{F} \otimes \partial \mathbf{F}} + \sum_i \frac{\partial^2 W_0}{\partial \mathbf{F} \otimes \partial \mathbf{A}_i} \cdot \frac{\partial \mathbf{A}_i}{\partial \mathbf{F}} \quad (4.19)$$

Thereby, the expressions must be evaluated at the constant relaxed $\mathbf{A}_i \forall i = \overline{1, N}$. It also is shown in [89] that the non-trivial derivative can be represented as

$$\frac{\partial \mathbf{A}_i}{\partial \mathbf{F}} = - \left(\frac{\partial^2 W_0}{\partial \mathbf{A}_i \otimes \partial \mathbf{A}_j} \right)^{-1} \cdot \frac{\partial^2 W_0}{\partial \mathbf{F} \otimes \partial \mathbf{A}_j} \quad (4.20)$$

Direct calculations lead to an explicit format for the 3rd-order tensor $\frac{\partial^2 W_0}{\partial \mathbf{F} \otimes \partial \mathbf{A}_j}$:

$$\mathbb{B}_i \doteq \frac{\partial^2 W_0}{\partial \mathbf{F} \otimes \partial \mathbf{A}_i} = \frac{1}{N V_i} \sum_{j \neq i} \mathbb{B}_{ij} \quad \text{with}$$

$$\mathbb{B}_{ij} \doteq \frac{1}{N V_i} \sum_{j \neq i} \left[\mathbf{F}^t \cdot \mathbf{k}_{ij}^{(0)} \otimes [\mathbf{R}_{ij} + \mathbf{A}_{ij}] + \mathbf{F}^t \cdot \sum_{\substack{m \neq i \\ m \neq j}} \mathbf{k}_{ij}^{(m)} \otimes [\mathbf{R}_{im} + \mathbf{A}_{im}] + f_{ji} [\mathbf{I} \otimes \mathbf{F}] \cdot [\mathbf{R}_{ij} + \mathbf{A}_{ij}] \right] \quad (4.21)$$

where $f_{ji} = |\mathbf{f}_{ji}|$. Note that the subscripts are related to the atomic numbering and do not denote the tensor components. The deformation of crystallite RVE is no longer homogeneous, so that \mathbf{P} and \mathbb{L} in (4.18) and (4.19) respectively are averaged in the volume of RVE and can be represented as

$$\mathbf{P} = \frac{1}{N} \sum_i^N \mathbf{P}_i, \quad \mathbb{L} = \frac{1}{N} \sum_i^N \mathbb{L}_i \quad (4.22)$$

Indeed, the 1st terms on the right-hand sides of (4.18) and (4.19) are given in (2.35) and (2.39). However, \mathbf{R}_{ij} must be replaced by $\mathbf{R}_{ij} + \mathbf{A}_{ij}$ for all possible i and j . A substitution of (4.16) and (4.21) into the 2nd terms of (4.18) and (4.19) respectively results in (4.22) with the following notations:

$$\mathbf{P}_i \doteq \frac{1}{V_i} \sum_{j \neq i} \left[\frac{1}{2} \mathbf{f}_{ji} \otimes [\mathbf{R}_{ij} + \mathbf{A}_{ij}] + \mathbf{F}^t \cdot \mathbf{f}_{ji} \cdot \frac{\partial \mathbf{A}_i}{\partial \mathbf{F}} \right] \quad (4.23)$$

$\mathbb{L}_i \doteq$

$$\frac{1}{V_i} \sum_{j \neq i} \left[\frac{1}{2} \left[\mathbf{k}_{ij}^{(0)} \overline{\otimes} [[\mathbf{R}_{ij} + \mathbf{A}_{ij}] \otimes [\mathbf{R}_{ij} + \mathbf{A}_{ij}]] + \sum_{\substack{m \neq i \\ m \neq j}} \mathbf{k}_{ij}^{(m)} \overline{\otimes} [[\mathbf{R}_{ij} + \mathbf{A}_{ij}] \otimes [\mathbf{R}_{im} + \mathbf{A}_{im}]] \right] + \mathbb{B}_{ij} \cdot \frac{\partial \mathbf{A}_i}{\partial \mathbf{F}} \right] \quad (4.24)$$

The practical aim of the relaxation procedure is thus to find a correct relaxed environment for each atom from the representative cell to be able to compute a correct stress according to (4.23).

4.3.2 Implementation at the Micro Scale

The equilibrium condition (4.17) states a pure lattice statics problem at the microscale. The solution algorithm of this problem is shown below:

(•) Load step n

1. Update the deformation gradient: $\mathbf{F}^{(n)} = \mathbf{F}^{(n-1)} + \Delta \mathbf{F}$

2. Set an initial value:

$$\mathbf{r}_i^{(n)start} \doteq \mathbf{r}_i^{(n-1)end} = \mathbf{F}^{(n-1)} \cdot [\mathbf{R}_i + \mathbf{A}_i^{(n-1)end}] \neq \mathbf{F}^{(n)} \cdot \mathbf{R}_i$$

3. Find relaxed spatial placement $\mathbf{r}_i^{(n)end}$, which fulfills the equilibrium conditions

$$\sum_{j \neq i} \mathbf{f}_{ji}(\mathbf{r}_i^{(n)}) \cdot \mathbf{F}^{(n)} = \mathbf{0} \text{ by using the Newton-Raphson scheme}$$

In general, there are two possibilities to define the starting value for the Newton-Raphson iterations at the beginning of the step n :

- (1) $\mathbf{r}_i^{(n)start} \doteq \mathbf{F}^{(n)} \cdot \mathbf{R}_i = \mathbf{F}^{(n-1)} \cdot \mathbf{R}_i + \Delta \mathbf{F} \cdot \mathbf{R}_i$
- (2) $\mathbf{r}_i^{(n)start} \doteq \mathbf{r}_i^{(n-1)end} = \mathbf{F}^{(n-1)} \cdot \mathbf{R}_i + \mathbf{F}^{(n-1)} \cdot \mathbf{A}_i^{(n-1)}$.

In the 1st case, the whole lattice should be homogeneously deformed according to the Cauchy-Born rule and then it obtains a possibility to relax. Unfortunately, this approach does not provide a development of microstructures. In the 2nd case, the relaxed atomic configuration $\mathbf{r}_i^{(n-1)end}$ computed during the previous step $n - 1$ should be used as the start values for the step n . This 2nd approach has been used in this work.

After each Newton-Raphson iteration, the next-neighbours list should be updated for each atom in

RVE. The RVE i.e. a rectangular 2D atomic lattice in this case, has finite extensions but it must describe an infinite crystallite without any boundary. It means that the periodical boundary conditions (PBC) should be formulated for the representative crystallite in order to exclude the boundary effects. Note that the application of PBC has a bearing on the stiffness matrix. Indeed, in the case of PBC, the displacements of corresponding atoms on opposite sides of the cell must be identical. To understand how the global stiffness matrix \mathbf{K}_T must be changed, consider only one such pair of corresponding atoms, say i and k . The PBC require:

$$\mathbf{u}_i = \mathbf{u}_k \Leftrightarrow (\mathbf{u}_i)_x = (\mathbf{u}_k)_x, \quad (\mathbf{u}_i)_y = (\mathbf{u}_k)_y \quad (4.25)$$

where $\mathbf{u}_i \doteq \mathbf{r}_i - \mathbf{R}_i$. Remember that the system of the linear algebraic equations to be solved within the Newton-Raphson approach is given by (C.24). The degrees of freedom corresponding to the x

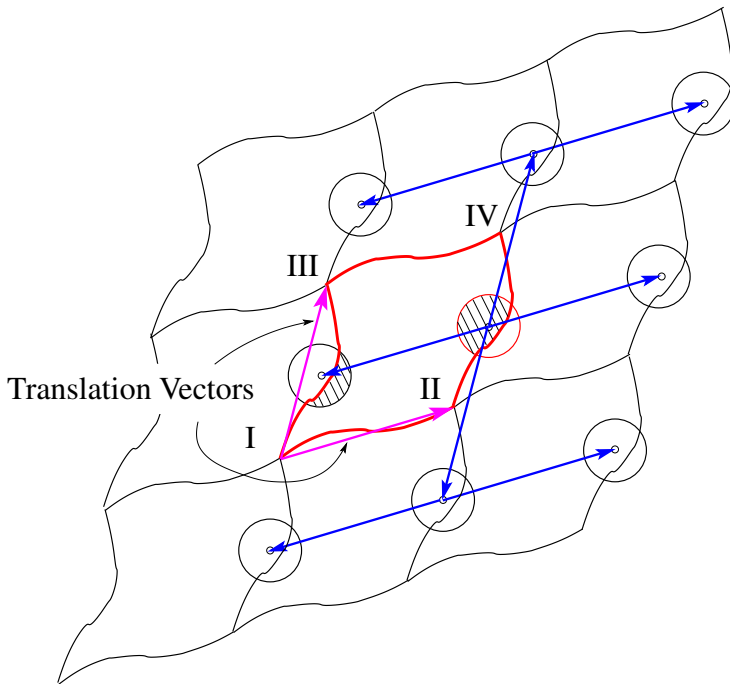


Figure 4.19: On the computation of the next-neighbours under consideration of PBC.

and y displacements of the atom i usually have numbers $2i - 1$ and $2i$ respectively so that 2 lines with these numbers correspond to \mathbf{u}_i in the stiffness matrix. The same is valid for \mathbf{u}_k . Let the atom k be a master atom and the atom i be a slave atom, i.e. the atom i has no its own degrees of freedom and their displacements results from (4.25). Then the lines $2i - 1$ and $2i$ of \mathbf{K}_T consist of zeros except for columns $2i - 1$ and $2i$ as well as $2k - 1$ and $2k$. The lines $2i - 1$ and $2i$ of the residual force in (C.24) must be set to zero. The whole system of equations then obtains the following format:

$$\begin{array}{c} 2i-1 \\ 2i \end{array} \begin{bmatrix} \ddots & \vdots & \vdots & \dots & \vdots & \vdots & \ddots \\ 0 \dots 0 & 1 & 0 & \dots & -1 & 0 & 0 \dots 0 \\ 0 \dots 0 & 0 & 1 & \dots & 0 & -1 & 0 \dots 0 \\ \ddots & \vdots & \vdots & \dots & \vdots & \vdots & \ddots \end{bmatrix} \begin{bmatrix} \vdots \\ \Delta(\mathbf{u}_i)_x \\ \Delta(\mathbf{u}_i)_y \\ \vdots \end{bmatrix} = \begin{bmatrix} \vdots \\ 0 \\ 0 \\ \vdots \end{bmatrix} \quad (4.26)$$

In principle, such lines corresponding to the slave degrees of freedom can be removed from \mathbf{K}_T and the size of the system can therewith be reduced. The next problem is how to compute the next neighbours of each atom in the cell under consideration of PBC. The method suggested in this work is explained in fig. 4.19. The main idea is to create 8 mappings of the original atom ² together with its next-neighbours circle in the spatial configuration. The translation vectors can be computed as follows:

$$\mathbf{v}_1 = \mathbf{r}_{II} - \mathbf{r}_I, \quad \mathbf{v}_2 = \mathbf{r}_{III} - \mathbf{r}_I \quad (4.27)$$

where r_I , r_{II} and r_{III} are the position vectors of the RVE's corners. The atoms contained in all 9 circles are then the current next neighbours of the original atom. Thereby, the double presented boundary and corner atoms must be eliminated. Thus, only one if any corner atom may be presented in the next-neighbours list. Fig. 4.21 illustrates this method for different placed original atoms. If the original atom lies within the RVE together with its cut-off circle, all mapped circles are empty as shown in the left top figure. In all other cases, at least one or more mapped circles contain a part from the effective environment of the original atom.

The square-shaped atomic arrangement shown in fig. 4.20 (a) has been used as a representative crystallite for examples represented below. A displacement according to the Cauchy-Born rule has been applied to the top and bottom edges of this cell, whereas the left and the right edges are subjected to PBC, see fig. 4.20 (b).

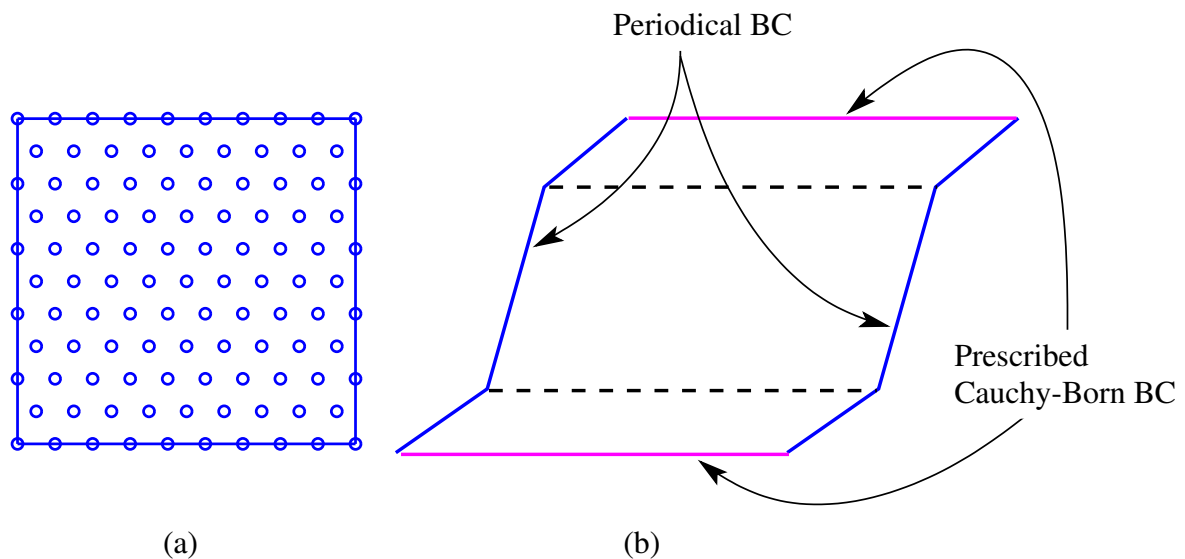


Figure 4.20: (a) The representative crystallite; (b) displacements according to the Cauchy-Born rule are applied to the top and bottom edges of the cell; the left and right edges are subjected to PBC.

²in the figur this atom lies within the parent cell)

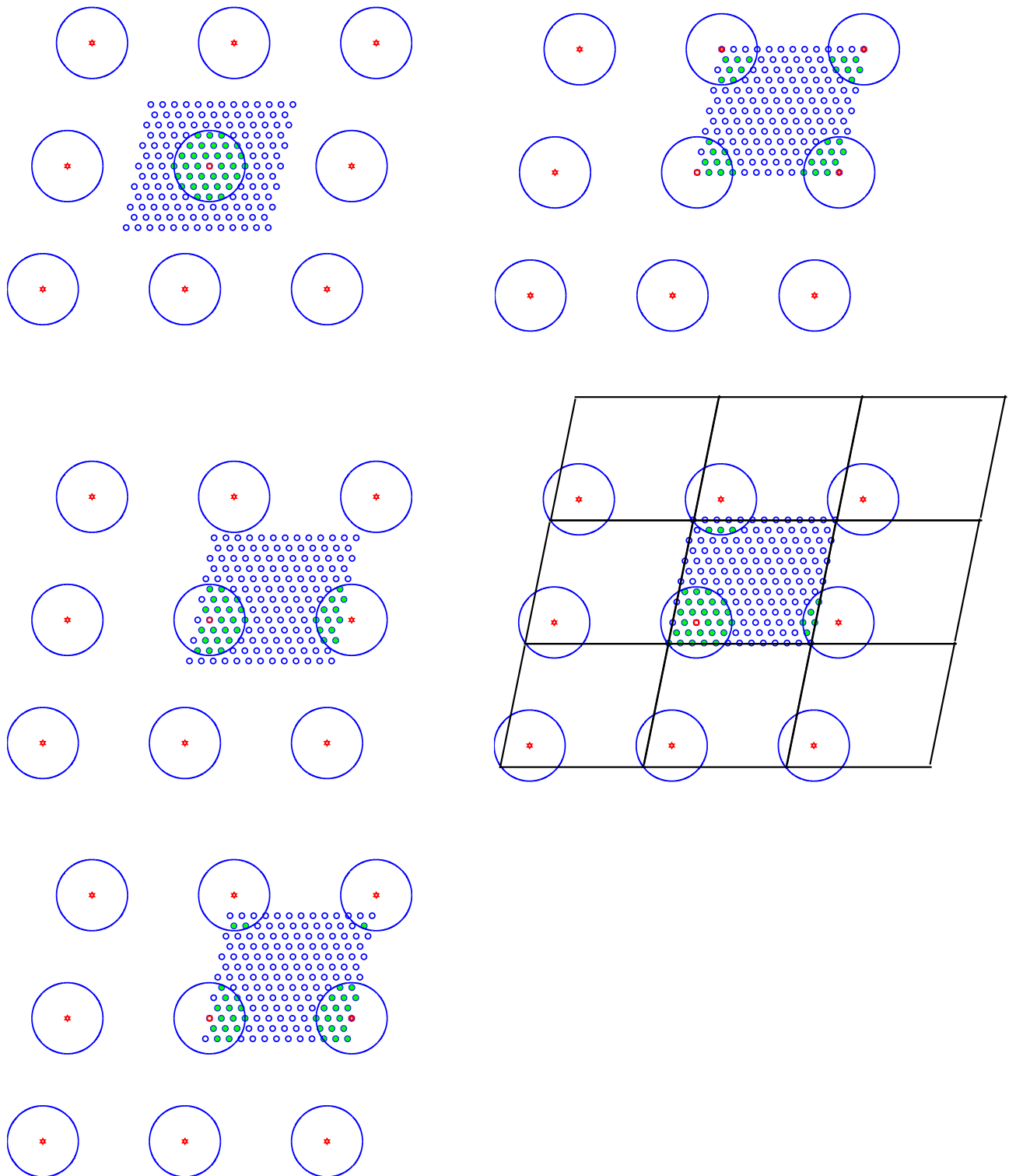


Figure 4.21: Mapped cut-off circles for different placed original atom, which must lie within the RVE or on its boundary.

A simple shear deformation with the deformation gradient given by

$$\mathbf{F} = \mathbf{I} + \gamma \mathbf{e}_1 \otimes \mathbf{e}_2$$

has been applied to the top and bottom edges of RVE. The 7 relaxed energy curves shown in fig. 4.22 are obtained by changing of the step width $\delta\gamma$ ³. All the curves exhibit an identical behaviour until a critical deformation corresponding to $\gamma^c \approx 0.13$. At this critical deformation, the loss of infinitesimal rank-one convexity must occur so that the homogeneous deformation no longer yields a minimum for the energy. A critical strain energy density W_0^c of about -3.8 nN nm corresponds to γ^c . All jumps in the energy curves or a failure of simulation (for e.g. step width 0.0012) take place at this W_0^c . To understand what happens at this energy, the behaviour of the determinant of acoustic tensor has been studied. The corresponding curves are depicted in fig. 4.23. A comparison of the curves shows that the loss of ellipticity indeed occurs as soon as the critical deformation is reached. The energy

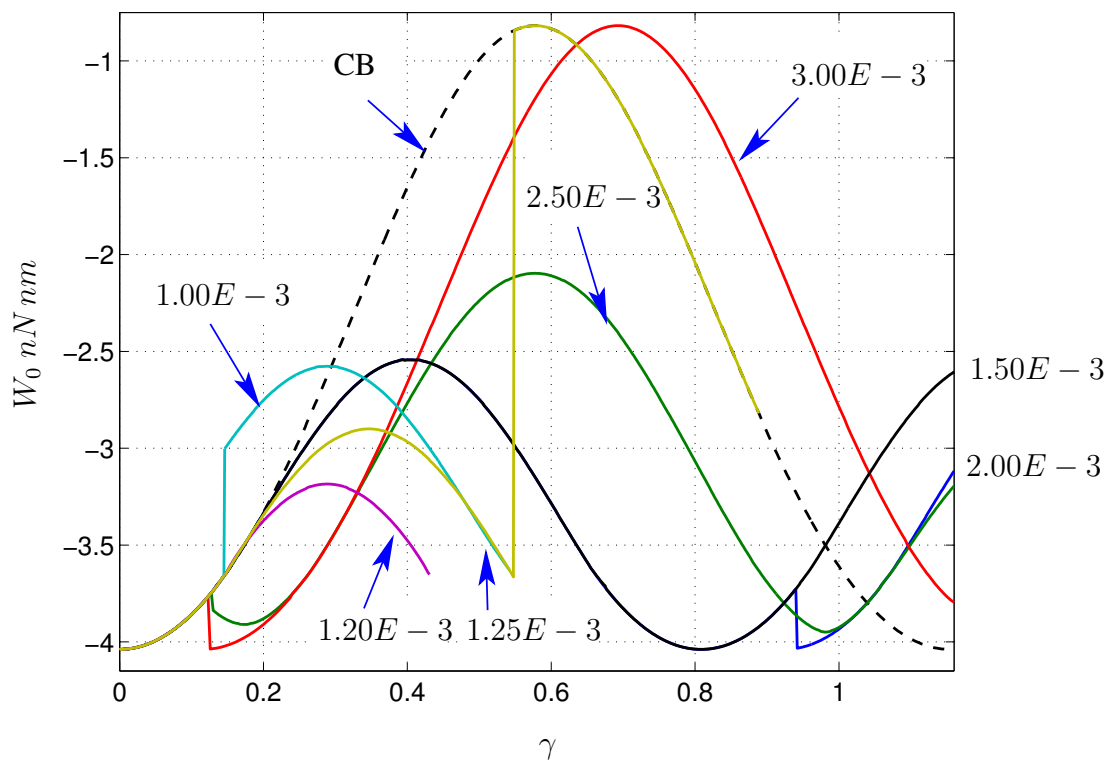


Figure 4.22: Relaxed strain energy density curves corresponding to different load step widths from 0.001 to 0.003 vs. the shear number. The unrelaxed Cauchy-Born energy of a homogeneously deformed RVE is highlighted with the dashed line.

reduction becomes possible due to a rearrangement of the atoms in RVE. Some structure snap-shots are exhibited in fig. 4.24 for two different relaxed energies. A development of microstructures, here of the shear bands, can be easily recognised in both figures. Of course, due to PBC no dislocation can occur and only a whole atomic row can glide in the shear direction. Nevertheless, the development of

³Note that in principle further curves could be obtained by this method, but it seems to be aimless since the only aim of this study was to obtain a development of microstructures.

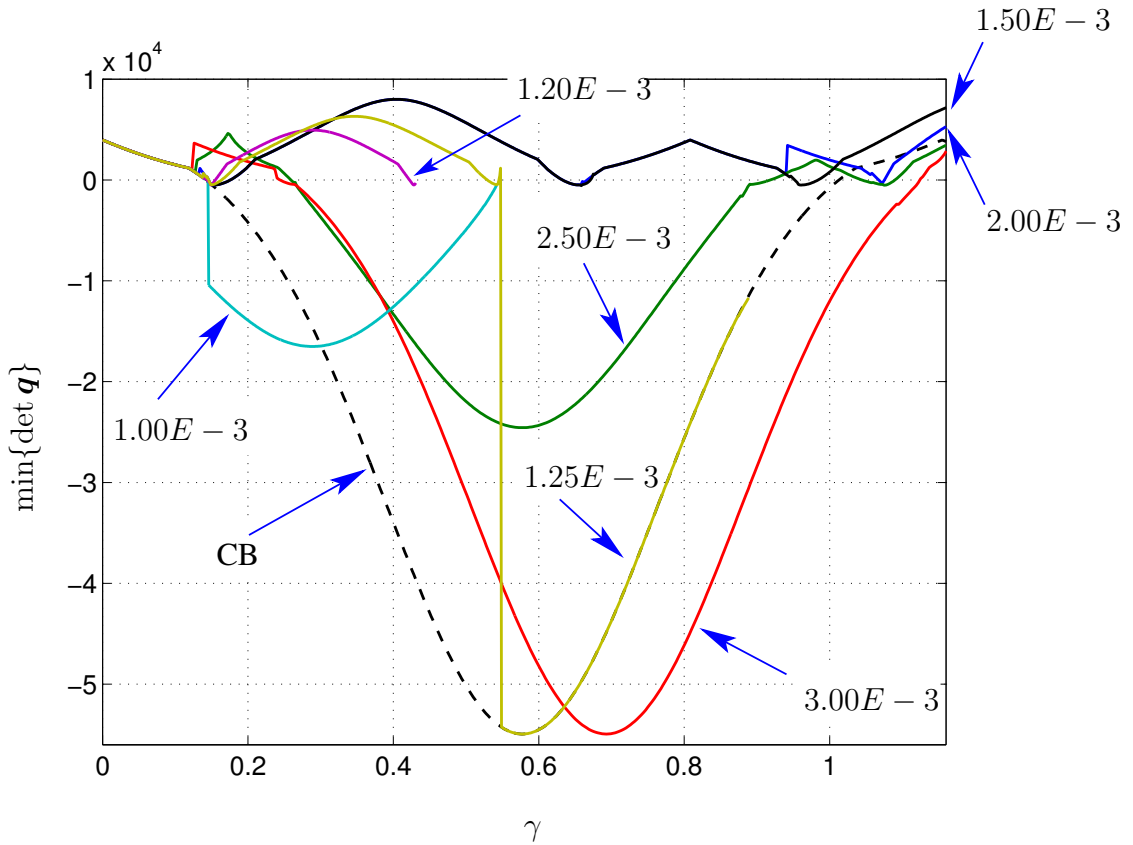


Figure 4.23: Minimum of the determinant of acoustic tensor \mathbf{q} corresponding to different load step widths from 0.001 to 0.003 vs. the shear number. The minimum of $\det \mathbf{q}$ for the unrelaxed Cauchy-Born energy is highlighted with the dashed line.

the shear bands is an irreversible deformation. It means that due to the relaxation, a transition from (hyper)elasticity to plasticity occurs within the continuum-atomistic approach.

Thus, due to the described relaxation procedure, a development of microstructures in an expected form of the shear bands has been obtained. However, the main problem remains unsolved since even the relaxed energy density is not rank-1-convex an arbitrary shear number, see fig. 4.23. On the other hand, there are a lot of possible configurations with the energy less than the Cauchy-Born energy at the bifurcation point and the result of relaxation depends on the load step width. Therefore, a robust relaxation procedure is required, which forces the system to jump into an energy branch corresponding to the absolute minimum of energy.

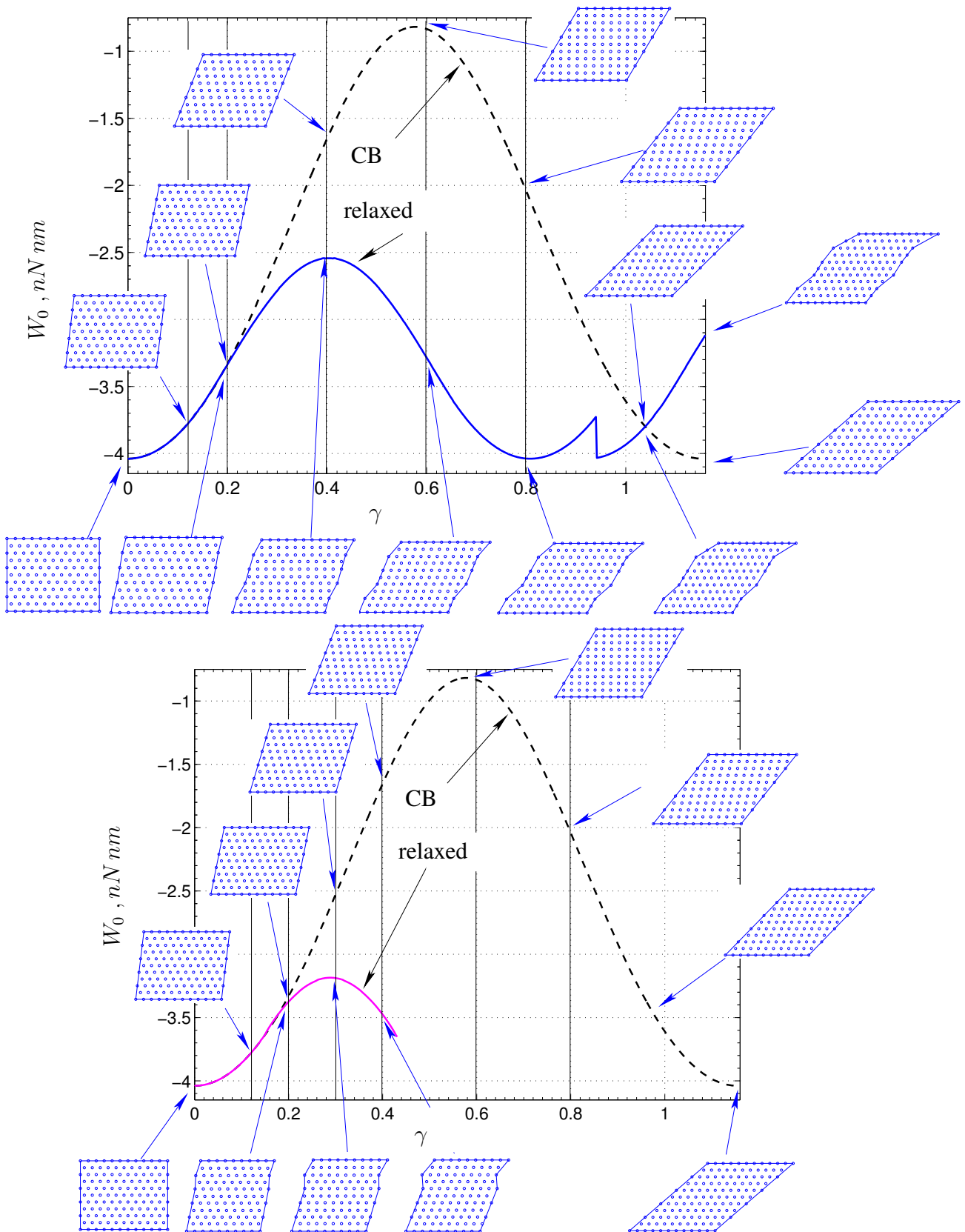


Figure 4.24: Cauchy-Born (dashed) and relaxed (step width = 0.0020 in the upper and 0.0012 in the lower figure) strain energy curves together with the corresponding structures.

4.3.3 Stability Criterion and Path-Change Procedure

Such a method has been proposed by Wagner and Wriggers, see [94, 93]. This method allows the detection of a bifurcation point where the system becomes unstable, the number of the branches in this point and, finally, prescribes how to perturb the system to jump in a stable branch corresponding to a minimum of the energy. The method uses the fact that more than one equilibrium state exists for the same load level at the bifurcation point. This leads to the eigenvalue problem for the global stiffness matrix \mathbf{K}_T . The algorithm is shown in fig. 4.25. Here, φ_j and λ_j denote the eigenvectors and eigenvalues respectively. Thus, the eigenvalue problem for \mathbf{K}_T should be solved after each load step. The occurrence of one or more zero eigenvalues indicates that the bifurcation point is reached. Thereby, the corresponding eigenvectors φ_j prescribe the direction, which should be followed to compute a secondary branch and hence they can be interpreted as perturbations of the solution at the bifurcation point. An eigenvector corresponding to a zero eigenvalue should be added to the

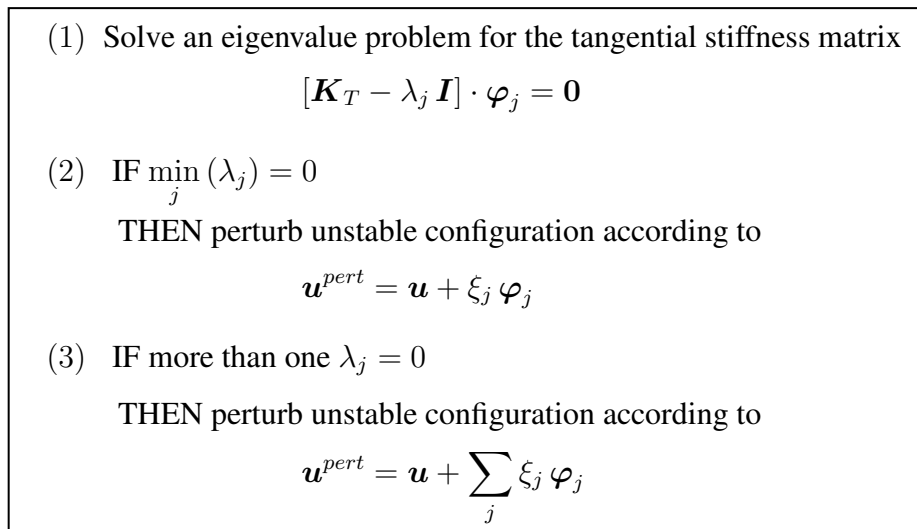


Figure 4.25: Algorithm describing the path-change procedure.

solution (in this case, to the homogeneously deformed configuration) with the scaling factor ξ_j . In the case of multiple zero eigenvalues, the perturbation takes the format of a linear combination of the corresponding eigenvectors with the unknown scaling factors. Unfortunately, there is no proposition how these scaling factors can be determined. The problem of determining ξ_j is discussed below.

Note that the global stiffness matrix being investigated must include only such columns and rows, which correspond to unconstrained degrees of freedom. For instance, DOF's prescribed for boundary conditions as well as the slave DOF's introduced for PBC must be eliminated to provide the symmetry of \mathbf{K}_T (left and top boundary as well as all corner atoms in this work).

A stability investigation of \mathbf{K}_T reduced in this manner has been carried out for examples discussed in the previous section. The results are represented in fig. 4.26. Here, the $\min_j \{\lambda_j\}$ is shown as a function of the shear number γ . Comparison with fig. 4.23 shows that the loss of ellipticity occurs at the same deformations as the loss of stability. In principle, both criteria are equivalent.

Among all computed examples, only two are of interest: for the step width of 0.002 and 0.003. In these load cases, the energy jumps into a branch corresponding to an energy less than the Cauchy-

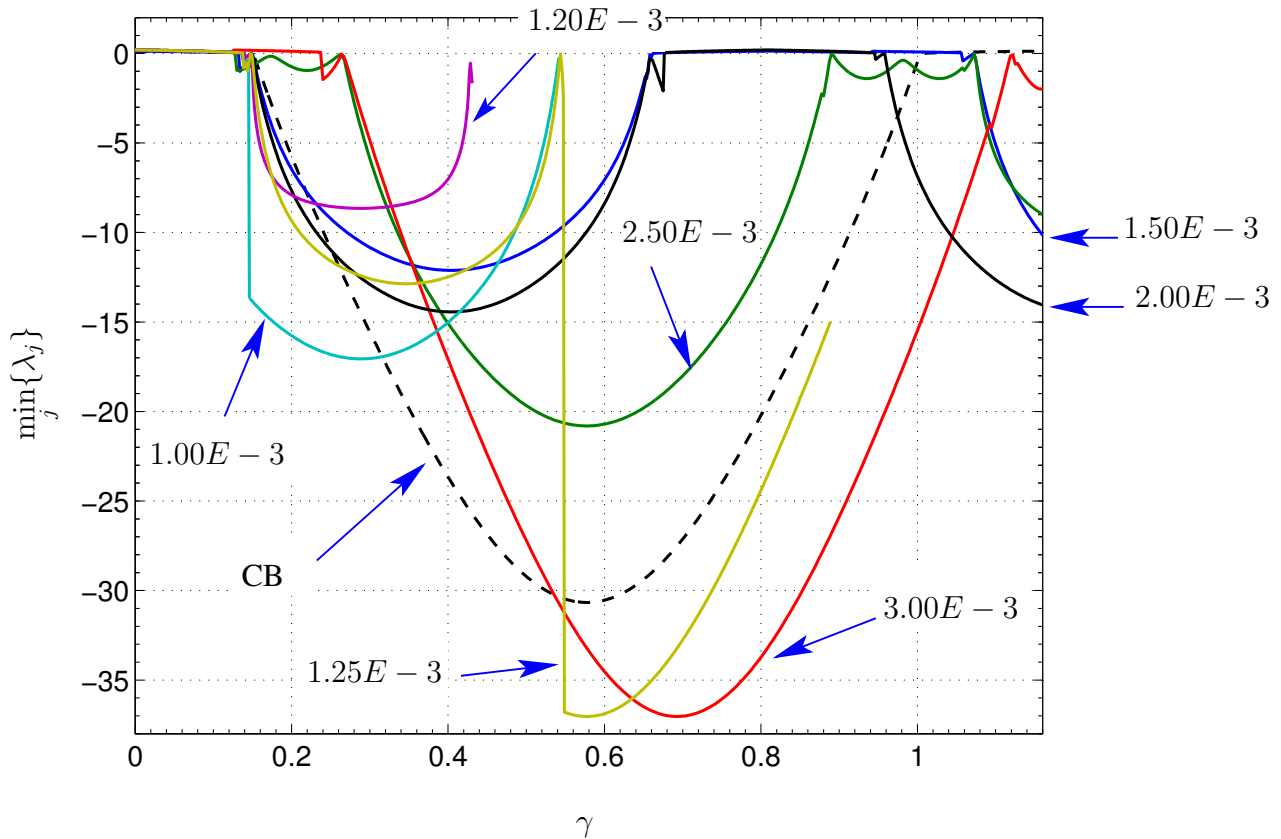


Figure 4.26: Minimum of eigenvalues of the global stiffness matrix \mathbf{K}_T vs. the shear number for different load step widths from 0.001 to 0.003 . The minimum of λ for the unrelaxed Cauchy-Born energy is highlighted by the dashed line.

Born energy. Due to this jump, the system remains stable for a longer time. The stable parts of the strain energy curves for these examples are shown in fig. 4.27 together with the stability criterion. Some snap-shots of the stable relaxed and unrelaxed configurations are exhibited additionally. Both energy curves can be viewed as two unconnected parts of the same relaxed energy, whereby the missed connection piece should have the same zigzag shape⁴. Each jump corresponds to the gliding of an atomic row by one interatomic distance. The averaged energy remains thereby constant. This model corresponds to the ideal plasticity without hardening. The corresponding stress curves depicted in fig. 4.28 advocate this proposition. Indeed, the averaged shear component of the stress remains constant, so that the deformation increases without additional external force.

Finally, a comparison of both criteria for these two chosen examples is shown in fig. 4.29. It is easy to recognise that the critical deformations resulting from the investigation of the loss of ellipticity are the same as was obtained from the investigation of loss of stability.

⁴It could be supposed in view of (3.12) and (3.15) that the behaviour of the relaxed energy curve depends probably on the size of the underlying crystallite L . This assumption can be verified by using lattice cells larger than the cell in the present work.

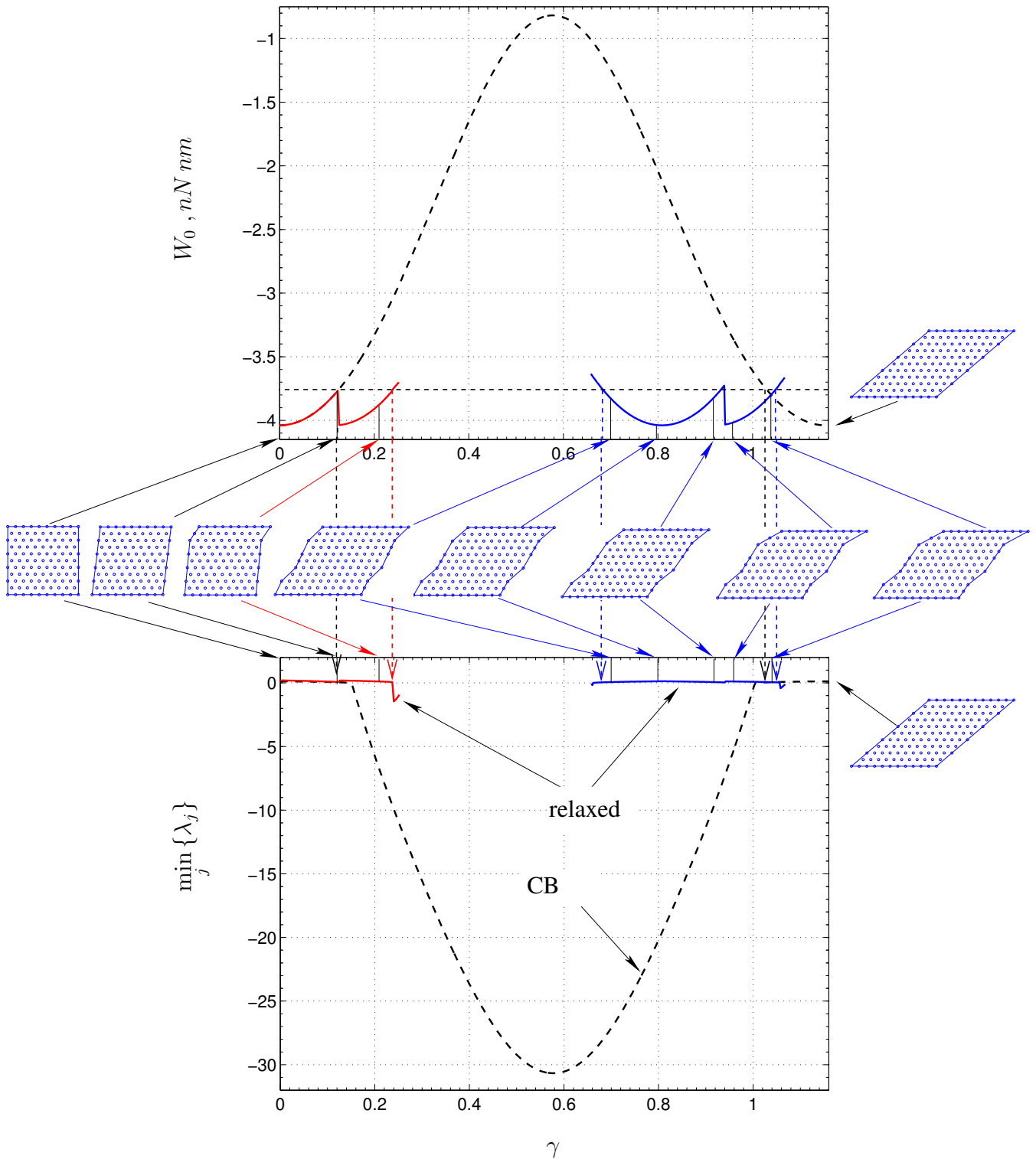


Figure 4.27: Strain energy density in the precritical region for two different step widths of 0.002 and 0.003. At the critical deformation, the system changes into a 2nd branch with the energy less than the Cauchy-Born energy (dashed line).

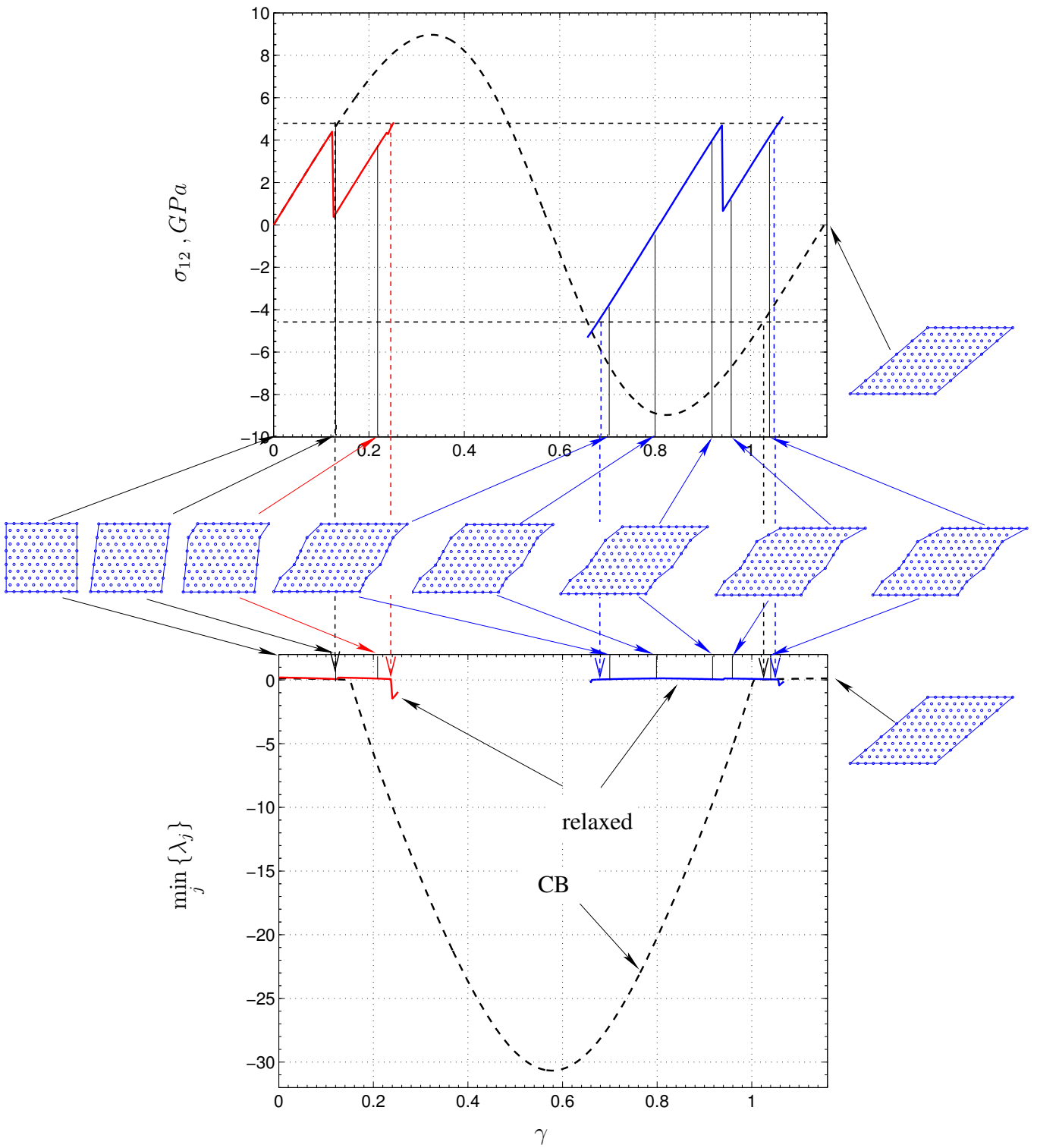


Figure 4.28: Shear stress in the precritical region for two different step widths of 0.002 and 0.003. An averaged value of the stress remains constant during the deformation.

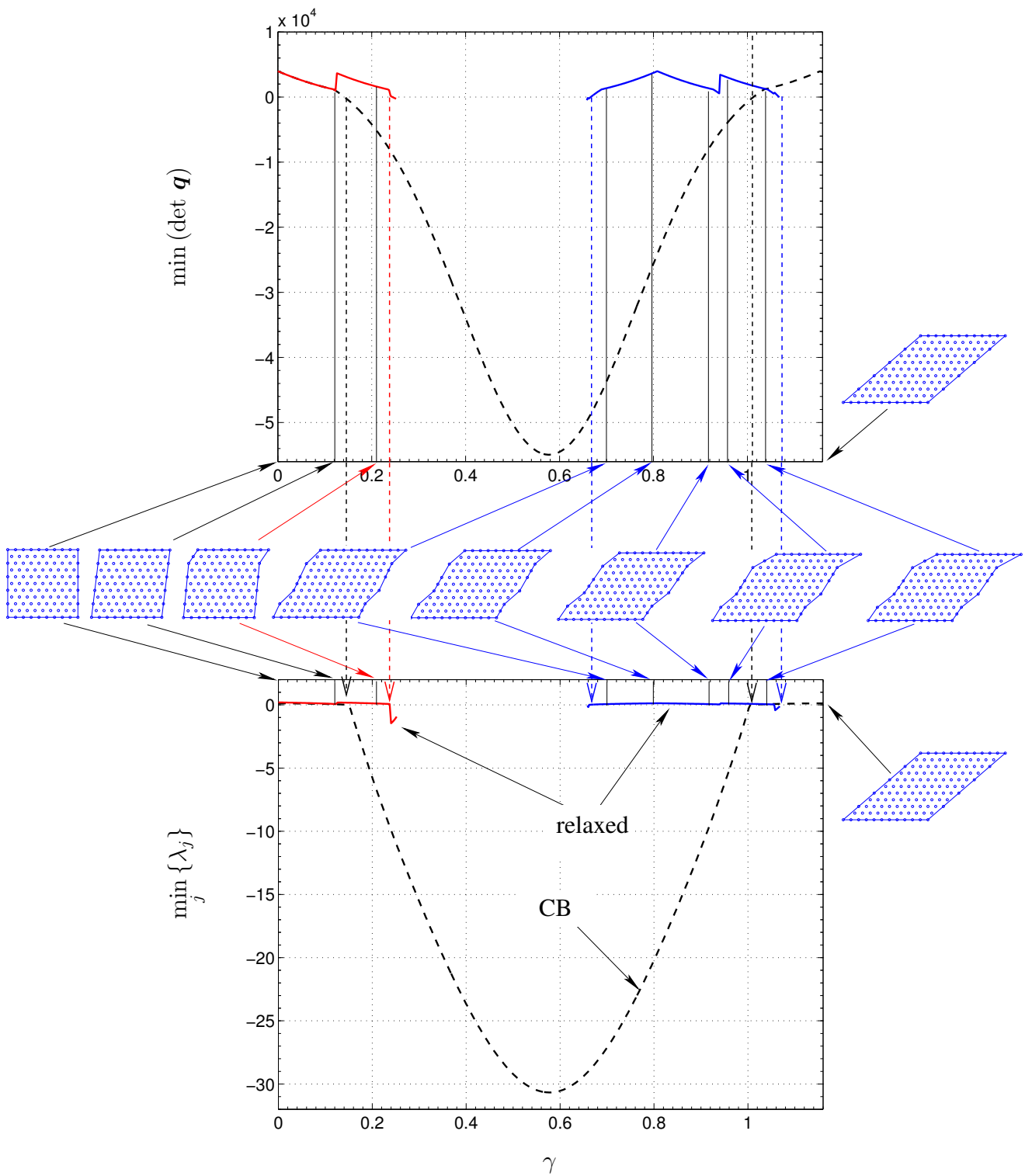


Figure 4.29: Comparison of two criteria: the loss of ellipticity and the loss of stability for two different step widths of 0.002 and 0.003.

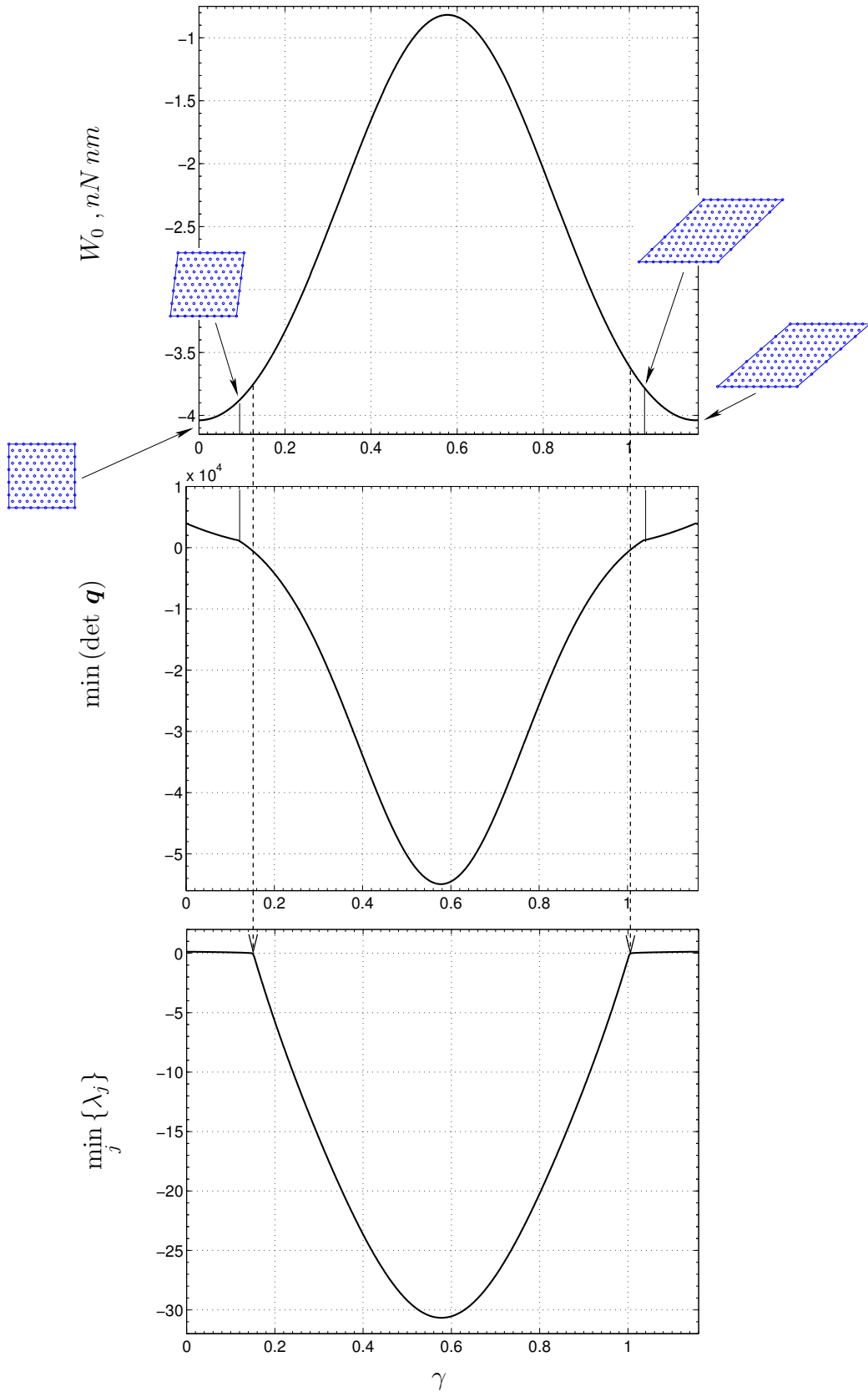


Figure 4.30: Strain energy density together with the minimum of $\det \mathbf{q}$ and of λ_j for a fully constrained system deformed according to the Cauchy-Born rule. Four configurations from the stable region are shown.

Thus, the functionality of the stability criterion is shown. Here, the general approach of the path-change procedure should be discussed. The simulation starts with the homogeneous deformation for the whole lattice cell according to the Cauchy-Born rule, whereby the stability criterion must be checked after each load step. Recall that only the micro scale is handled here. As soon as the critical deformation is reached (the vertical dashed line in fig. 4.30), the last homogeneously deformed configuration should be perturbed according to the scheme in fig. 4.25. In the case depicted in fig. 4.30, two zero eigenvalues appear at the bifurcation point. It is shown in fig. 4.31 and 4.32 how the corresponding eigenvectors can be applied as perturbation for the homogeneously deformed configuration, whereby the perturbation takes place only due to either 1st (fig. 4.31) or 2nd (fig.4.32)

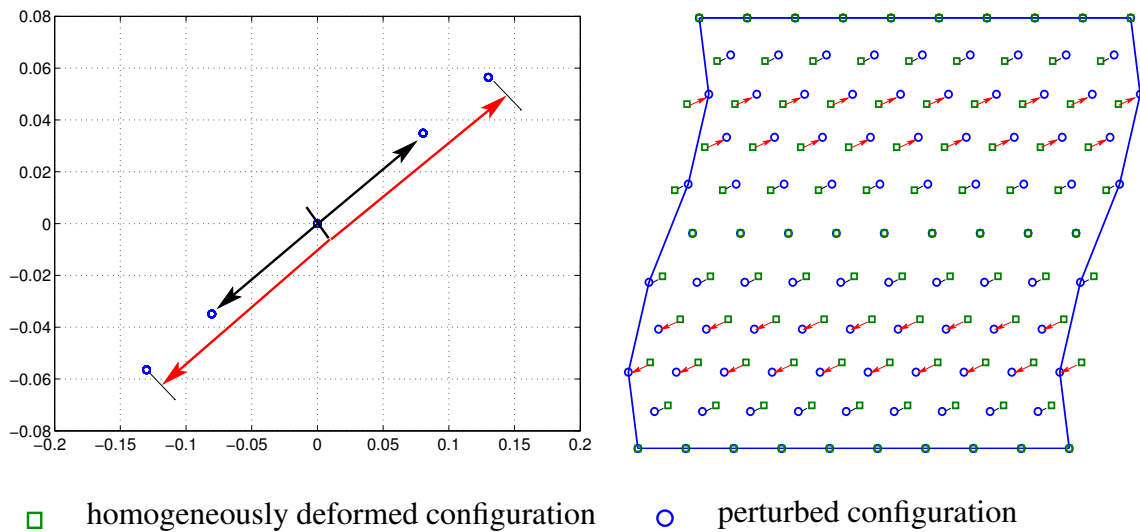


Figure 4.31: 1st zero eigenvector represented as a perturbation (on the left); perturbed homogeneously deformed configuration, whereby the perturbed atomic positions are depicted with circles whereas the unperturbed position with squares.

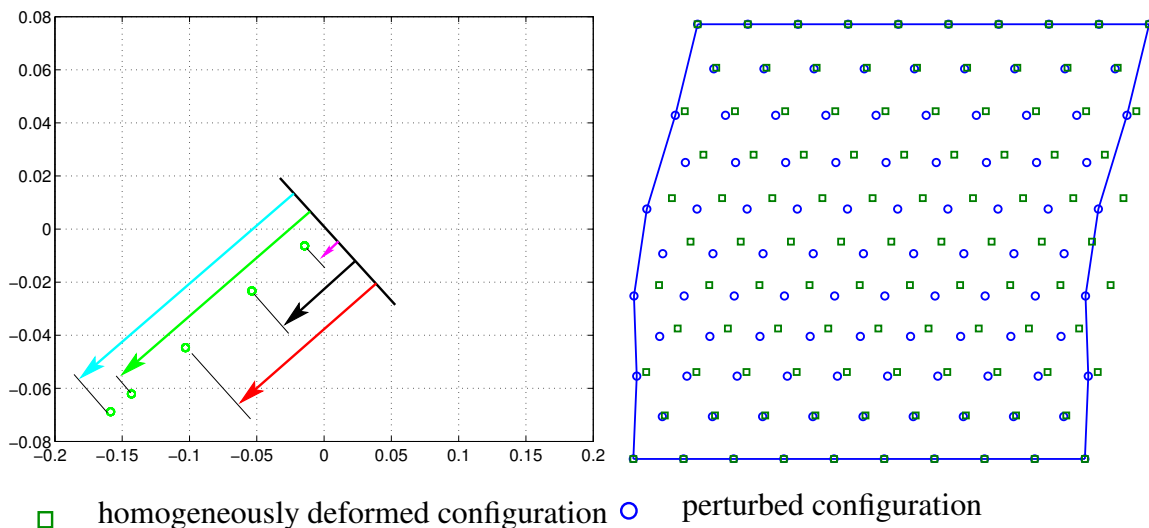


Figure 4.32: 2nd zero eigenvector represented as a perturbation (on the left); perturbed homogeneously deformed configuration, whereby the perturbed atomic positions are depicted with circles whereas the unperturbed position with squares.

eigenvector with the corresponding scaling factor equal to 1 and with the 2nd scaling factor equal to zero. The 1st eigenvector thereby defines two pairs of displacements, which have the same values and reverse directions in each pair. The corresponding perturbed structure therefore exhibits the same symmetry: the upper part can be obtained from the lower part as a result of a 180° rotation.

The 2nd eigenvector yields 5 different displacements, which are equivalently directed, see fig. 4.32. The perturbed structure exhibits no symmetry. Both perturbed structures are shown together in fig. 4.33. It is quite evident that both perturbations provide a development of shear bands. It is complicated to decide, which perturbed configuration is more favourable from the energetical point of view since each deformed cell contains relaxed bands with the structure similar to the undeformed configuration and, additionally, transition bands.

Now, the main question is how the convenient scaling factors can be determined. Firstly, it has

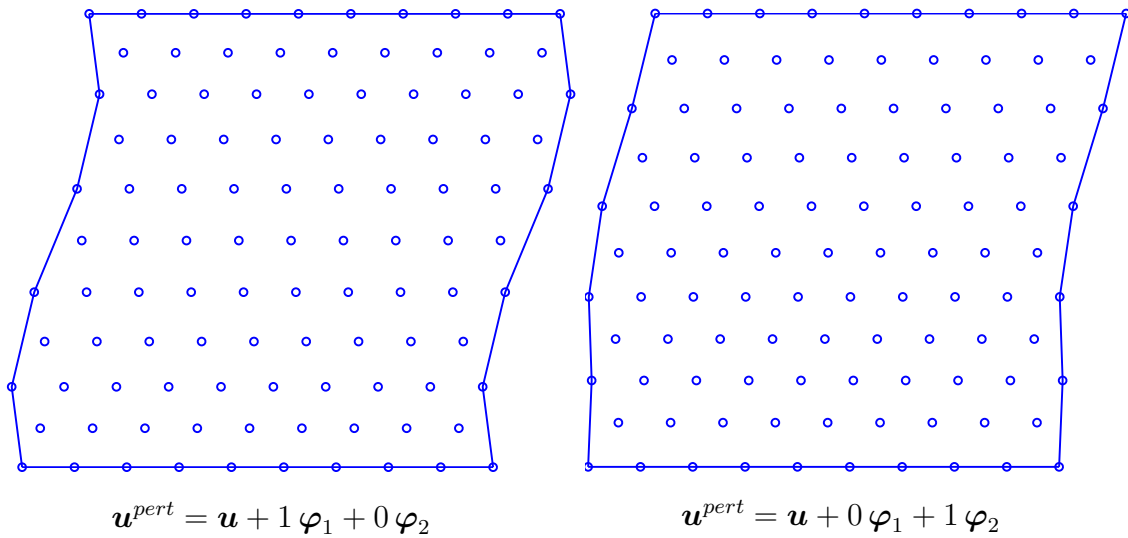


Figure 4.33: Perturbed configurations for two sets of scaling factors ξ_1, ξ_2 : $\{\xi_1 = 1, \xi_2 = 0\}$ and $\{\xi_1 = 0, \xi_2 = 1\}$.

been attempted to set a random values for ξ_1 and ξ_2 . Unfortunately, this method does not lead to a relaxed structure with a minimum of the strain energy density. Another proposition is to compute the strain energy density as a function of both scaling factors so that $W_0 = W_0(\xi_1, \xi_2)$ whereby ξ_1 and ξ_2 run from $-n$ to n near to zero. By this method, a minimum of W_0 can be detected and a corresponding pair $\{\xi_1, \xi_2\}$ should be chosen as the convenient scaling factors. The accuracy of the determination can be controlled by changing of the step width. Projections of such an energy surface at the bifurcation point are shown in fig. 4.34 for $n = 6$ and step width 0.2. The strain energy density reaches a minimum for $\xi_1 = \xi_2 = 0.2$. This means that the Cauchy-Born deformation does not provide an energetically favourable configuration. The whole energy surface at the bifurcation point is shown again in fig. 4.35 (a).

To check whether the Cauchy-Born deformation provides an energetically favourable configuration in the precritical region, an analogical energy surface has been computed for a deformation just at the beginning of the simulation. This surface is shown in fig. 4.35 (b). As expected, the minimum of the energy surface corresponds to $\xi_1 = \xi_2 = 0$ i.e. to the Cauchy-Born energy.

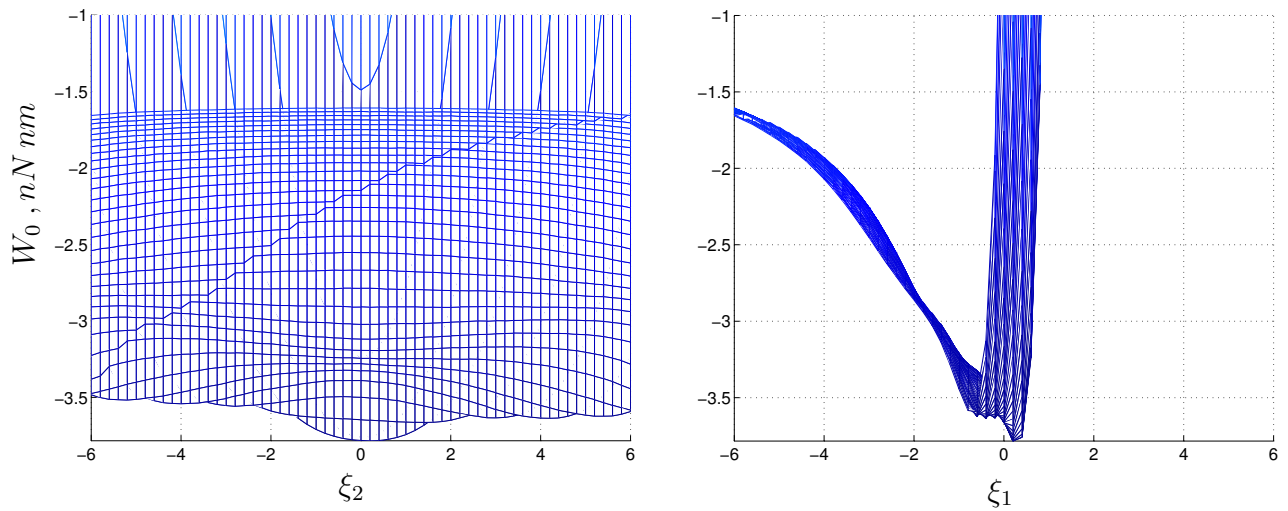


Figure 4.34: Projections of the energy surface. It is easy to recognise that the Cauchy-Born energy does not correspond to a favourable state.

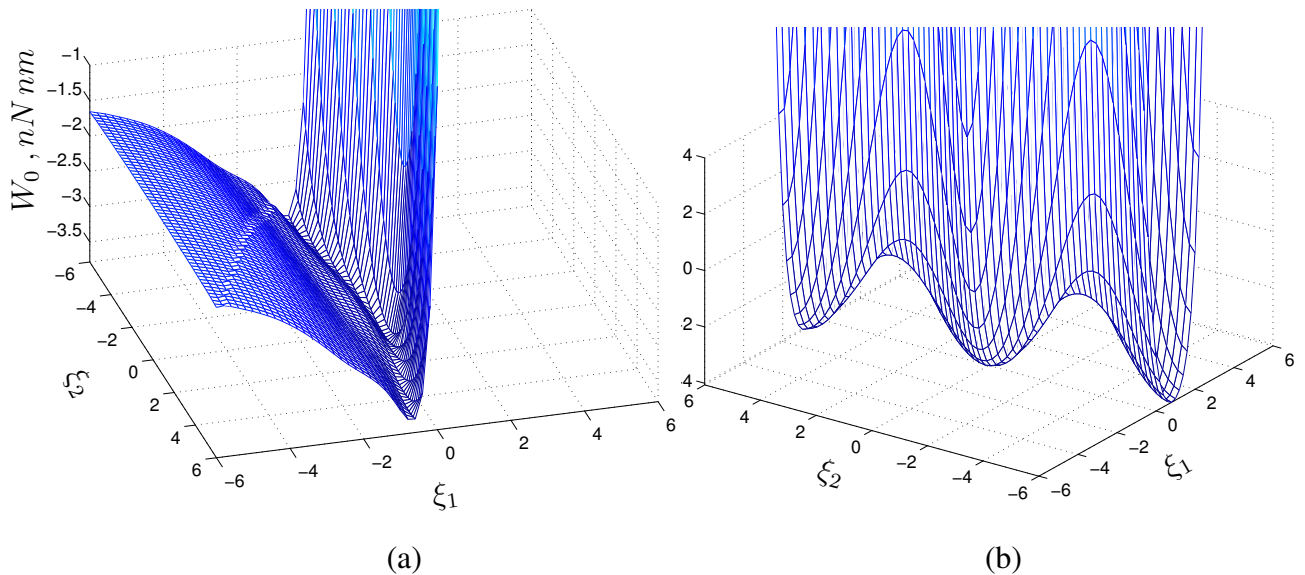


Figure 4.35: Strain energy density as a function of the scaling factors ξ_1 and ξ_2 . The step width is 0.2: (a) at the bifurcation point; (b) shortly after the beginning of deformation in the precritical region.

A usage of the obtained scaling factors unfortunately does not lead to a new relaxed structure. To increase the accuracy of the scaling factor determination, the range of the variation of ξ_1 and ξ_2 has been decreased whereas the resolution has been increased, so that the number of raster points does not increase dramatically. In other words, the following parameters have been used: $n = 0.4$ instead of 6 and the step width is equal to 0.01 instead 0.2. Thereby, it was found that the better resolution shifts the minimum of W_0 from $\xi_1 = \xi_2 = 0.2$ to $\xi_1 = 0.29$, $\xi_2 = 0.09$, see fig. 4.36. However, even this correction does not provide an appearance of a new relaxed structure and the problem of a robust definition of ξ_j remains open.

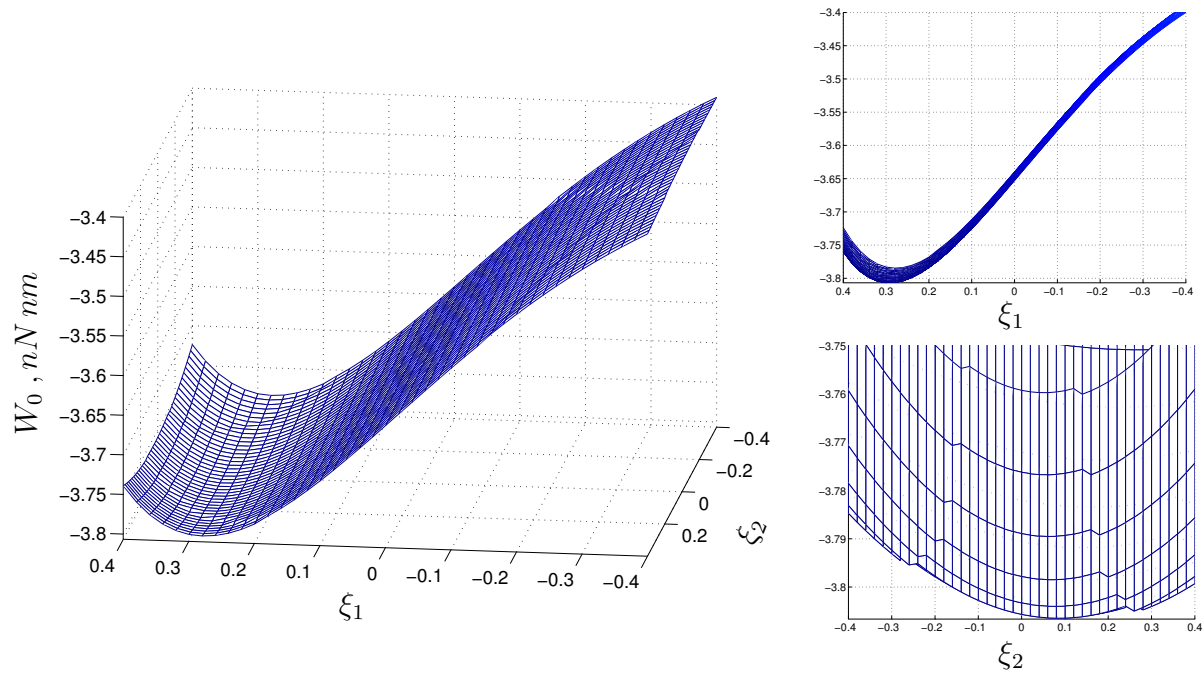


Figure 4.36: Energy surface at the bifurcation point with better resolution compared to the surface shown in fig. 4.34.

Thus, a robust procedure, which locates only the branch providing an absolute minimum of the strain energy density among numerous branches at the bifurcation point remains incomplete⁵. Without such a procedure, no finite element implementation can be considered.

⁵To improve the convergence, the damped Newton method, s. appendix, can be used instead of the classical Newton-Raphson approach.

Chapter 5

Higher – Order Gradients in Continuum-Atomistics

“In general, strain gradients are inversely proportional to the length scale over which plastic deformation occur. Thus, gradient effects become important for plastic deformations taking place at small scales.”

N. A. Fleck, “Strain gradient plasticity”

As obtained in chapter 4, the relaxation results in the development of microstructures with deformation inhomogeneity at the atomic length scale. In general, this inhomogeneity cannot be captured by the standard Cauchy-Born rule (2.31), see fig. 5.1. To remain within the realm of the continuum-atomistic model and nevertheless still obtain accurate results in this more general case of inhomogeneous deformations, the Cauchy-Born rule is considered in the classical form as the 1st term of a Taylor’s series expansion of the deformation field and enhanced by the 2nd, quadratic term including the higher-order deformation gradient. Based on these advanced kinematics, a full higher-order gradient framework is obtained by minimisation of the total energy of the body of interest.

In principle, the quasicontinuum formulation could subdivide the volume containing an inhomogeneity and linearly interpolate the shear. But the introduction of higher-order gradients is also motivated from studies of localisation limiters, see e.g. [30]. Here, the higher-order gradients provide an introduction of a lower size bound for the microstructures arising due to the relaxation.

The consideration of the higher-order expansion terms has only a kinematical meaning and serves to take the inhomogeneities in the deformation field into account. Thereby, the atomistic description remains unchanged and only the kinematic description within the existing interatomic potentials is modified.

This framework is similar to the Toupin-Mindlin theory of linear elasticity, see Toupin [91] and Mindlin [59, 60]. Nix and Gao [67] have investigated the indentation size effect using the notion of geometrically necessary dislocations connected with the strain gradient plasticity. Recently, the

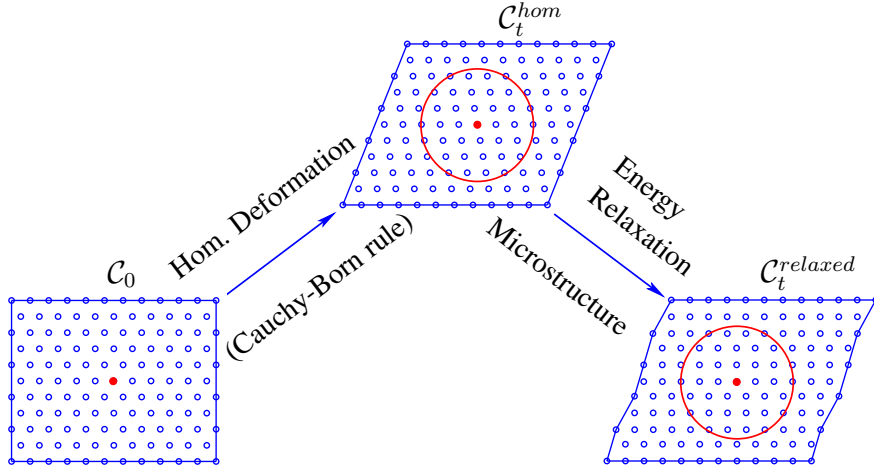


Figure 5.1: Material configuration \mathcal{C}_0 and two spatial configurations: \mathcal{C}_t^{hom} deformed homogeneously according to the Cauchy-Born rule and $\mathcal{C}_t^{relaxed}$ obtained during the energy minimisation procedure by relaxation. The circles display an interaction or cut-off-circle of the middle atom depicted in black and contain the current next neighbours of this atom. Atomic displacements within the cut-off-circle in $\mathcal{C}_t^{relaxed}$ are no longer homogeneous and can not be captured by the standard Cauchy-Born rule.

higher-order gradient theory for finite deformation has been elaborated by Geers et al. [35] and Kouznetsova et al. [46] within classical continuum mechanics in the context of homogenization approaches. Newly, Leamy et al. [48] have applied the higher-order gradient theory combined with the Cauchy-Born rule to analyse carbon nanotubes. A comparison of the various higher-order gradients theories can be found in the detailed overview elaborated by Fleck and Hutchinson [30].

Finally, note that this study relates to only one point of continuum and contains no FE implementation.

5.1 2^{nd} – Order Hyperelastic Continua

In the higher-order theory, the 2^{nd} -order deformation gradient \mathbf{G} , which is a rank-three tensor, must be introduced in addition to \mathbf{F} :

$$\mathbf{G} \doteq \frac{\partial^2 \varphi(\mathbf{X})}{\partial \mathbf{X} \otimes \partial \mathbf{X}} \equiv \nabla_{\mathbf{X}} \nabla_{\mathbf{X}} \varphi \quad (5.1)$$

The energy minimisation takes again a format similar to (2.20):

$$\begin{aligned} \delta E^{tot} &= \delta \int_{\mathcal{B}_0} W_0(\mathbf{F}, \mathbf{G}) dV + \delta E^{ext} \\ &= \int_{\mathcal{B}_0} \left[\frac{\partial W_0}{\partial \mathbf{F}} : \nabla_{\mathbf{X}} \delta \varphi + \frac{\partial W_0}{\partial \mathbf{G}} : \nabla_{\mathbf{X}} \nabla_{\mathbf{X}} \delta \varphi \right] dV + \delta E^{ext} = 0 \end{aligned} \quad (5.2)$$

Here “:” denotes a triple contraction of rank-three tensors \mathbf{Q} and \mathbf{G} , i.e. $Q_{iJK} G_{iJK}$. In addition to the 1^{st} Piola-Kirchhoff stress (2.17), the 2^{nd} -order stress \mathbf{Q} is introduced here as the 1^{st} derivative of the energy density with respect to the 2^{nd} -order deformation gradient \mathbf{G} :

$$\mathbf{Q} \doteq \frac{\partial W_0}{\partial \mathbf{G}} \quad (5.3)$$

It follows from (5.3) that the 2^{nd} -order stress is represented by a rank-three tensor. The symmetry properties of this tensor are determined by the symmetry of $\mathbf{G} = \nabla_X \nabla_X \boldsymbol{\varphi}$, which is symmetric in the second and third index because of the interchangeability of second partial derivatives. The variation of the external potential includes an additional term due to the 2^{nd} -order stress traction \mathbf{t}_0^Q on the surface $\partial\mathcal{B}_0$, see e.g. Mindlin [60] or Fleck and Hutchinson [30], and can be represented as a sum of three terms¹:

$$\delta E^{ext} = - \int_{\mathcal{B}_0} \delta \boldsymbol{\varphi} \cdot \mathbf{b}_0 dV - \int_{\partial\mathcal{B}_0} \delta \boldsymbol{\varphi} \cdot \mathbf{t}_0^P dA - \int_{\partial\mathcal{B}_0} \nabla_N \delta \boldsymbol{\varphi} \cdot \mathbf{t}_0^Q dA, \quad (5.4)$$

After simple but tedious transformations of (5.2) outlined in detail in the appendix, the following higher-order equilibrium equations and Neumann-type boundary conditions are obtained:

$$\text{Div}(\mathbf{P} - \text{Div} \mathbf{Q}) + \mathbf{b}_0 = \mathbf{0} \quad \text{in } \mathcal{B}_0 \quad (5.5)$$

$$[\mathbf{P} - \text{Div} \mathbf{Q}] \cdot \mathbf{N} + \mathfrak{L}(\mathbf{Q} \cdot \mathbf{N}) = \mathbf{t}_0^P \quad \text{on } \partial\mathcal{B}_0 \quad (5.6)$$

$$\mathbf{Q} : [\mathbf{N} \otimes \mathbf{N}] = \mathbf{t}_0^Q \quad \text{on } \partial\mathcal{B}_0, \quad (5.7)$$

whereby the partial integration, the Gauss theorem and the Stoke's surface divergence theorem are essentially involved. Here, $\mathfrak{L}(\mathbf{Q} \cdot \mathbf{N})$ denotes the following differential operator:

$$-\mathfrak{L}(\mathbf{Q} \cdot \mathbf{N}) \doteq K \mathbf{Q} : [\mathbf{N} \otimes \mathbf{N}] + \nabla_X^T(\mathbf{Q} \cdot \mathbf{N}) : \mathbf{I} \quad (5.8)$$

with the mean curvature $K \doteq -\nabla_X^T \mathbf{N} : \mathbf{I}$ of the surface $\partial\mathcal{B}_0$, see Brand [15], p. 222.

5.2 2^{nd} -Order Cauchy-Born Rule

The Cauchy-Born rule in the form (2.31) is insufficient to describe the kinematics for the case of inhomogeneous deformations. Furthermore, size effects cannot be taken into account, see e.g. Geers *et al.* [35] or Fleck and Hutchinson [30], if the problem size reaches the scale of the atomic spacing as in the case of nanomechanics. To get over this discrepancy, the 2^{nd} i.e. quadratic term in the Taylor's series expansion of the displacement field has been taken into account. Thereby, (2.31) is considered as the 1^{st} term in this expansion near the homogeneously deformed configuration. The extended Cauchy-Born rule of 2^{nd} -order can thus be expressed in the following format

$$\mathbf{r}_{ij} = \mathbf{F} \cdot \mathbf{R}_{ij} + \frac{1}{2} \mathbf{G} : [\mathbf{R}_{ij} \otimes \mathbf{R}_{ij}] \quad (5.9)$$

with the previously introduced 2^{nd} -order deformation gradient \mathbf{G} . The strain energy density W_0 now consequently depends on both \mathbf{F} and \mathbf{G} :

$$\begin{aligned} W_0 &= W_0(r_{i1}, \dots, r_{iN}) \\ &= W_0(|\mathbf{F} \cdot \mathbf{R}_{i1}|, \dots, |\mathbf{F} \cdot \mathbf{R}_{iN}|, \frac{1}{2} \mathbf{G} : [\mathbf{R}_{i1} \otimes \mathbf{R}_{iN}], \dots, \frac{1}{2} \mathbf{G} : [\mathbf{R}_{iN} \otimes \mathbf{R}_{iN}]) \\ &= W_0(\mathbf{F}, \mathbf{G}) \end{aligned} \quad (5.10)$$

¹The gradient operator can be decomposed into normal and tangential parts according to the following rule:

$$\nabla_X(\bullet) = [\nabla_X(\bullet) \cdot \mathbf{N}] \mathbf{N} + \nabla_X(\bullet) \cdot [\mathbf{I} - \mathbf{N} \otimes \mathbf{N}] \equiv \nabla_X^N(\bullet) + \nabla_X^T(\bullet)$$

with the normal gradient operator $\nabla_X^N(\bullet) \doteq [\nabla_X(\bullet) \cdot \mathbf{N}] \mathbf{N} \equiv \nabla_N(\bullet) \mathbf{N}$ and the tangential gradient operator $\nabla_X^T(\bullet) \doteq \nabla_X(\bullet) \cdot [\mathbf{I} - \mathbf{N} \otimes \mathbf{N}]$, whereby \mathbf{N} denotes the material surface normal vector.

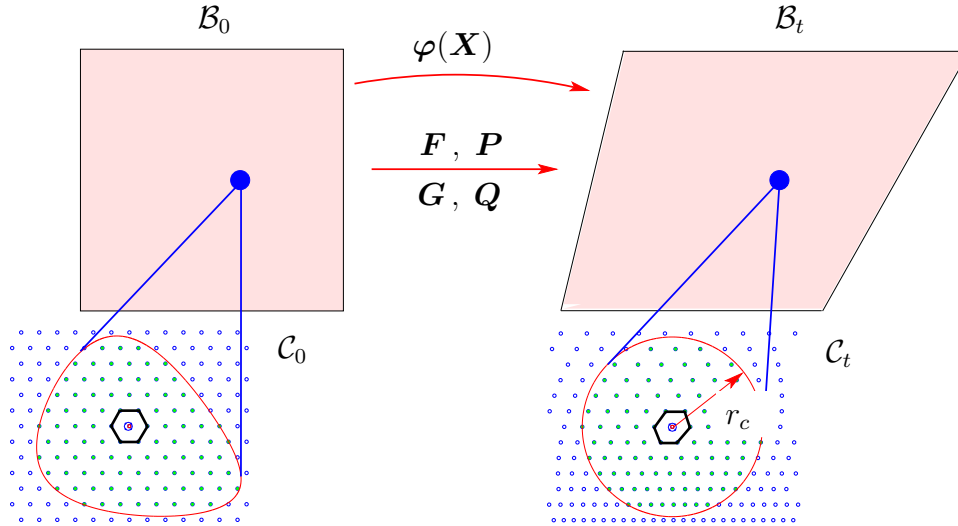


Figure 5.2: The 2^{nd} -order Cauchy-Born rule for the case of non-homogeneous deformation

The Euler-Lagrange equations corresponding to a potential depending on \mathbf{F} and \mathbf{G} are given by (5.5)-(5.7).

The explicit format of the constitutive law for the 1^{st} Piola-Kirchhoff stress retains its form previously given by (2.36). The definition (5.3) renders the following format for the 2^{nd} -order stress under consideration of (2.30) and (5.10):

$$\mathbf{Q} = \frac{1}{4V_i} \sum_{j \neq i} \mathbf{f}_{ji} \otimes \mathbf{R}_{ij} \otimes \mathbf{R}_{ij} \quad (5.11)$$

The push-forward operation in the case of the 2^{nd} -order theory is more complicated than in the 1^{st} -order theory. The specific virtual work transformation yields spatial stress tensors in the following explicit format ²:

$$\begin{aligned} & \mathbf{P} : \nabla_X \delta \varphi + \mathbf{Q} : \nabla_X \nabla_X \delta \varphi \\ = & [\mathbf{P} \cdot \mathbf{F}^t + \mathbf{Q} \overset{2,3}{:} \mathbf{G}] : \nabla_x \delta \varphi + [\mathbf{Q} : [\mathbf{F}^t \otimes \mathbf{F}^t]] : \nabla_x \nabla_x \delta \varphi \\ = & \left[\frac{1}{2V_i} \sum_{j \neq i} \mathbf{f}_{ji} \otimes \mathbf{r}_{ij} \right] : \nabla_x \delta \varphi + \left[\frac{1}{4V_i} \sum_{j \neq i} \mathbf{f}_{ji} \otimes \mathbf{r}_{ij}^1 \otimes \mathbf{r}_{ij}^1 \right] : \nabla_x \nabla_x \delta \varphi \end{aligned} \quad (5.12)$$

with the spatial distance vector $\mathbf{r}_{ij}^1 \doteq \mathbf{R}_{ij} \cdot \mathbf{F}^t$ of the 1^{st} -order theory. The linearisation of (5.11) contains various 2^{nd} derivatives of W_0 with respect to \mathbf{F} and \mathbf{G} :

$$\frac{\partial^2 W_0}{\partial \mathbf{F} \otimes \partial \mathbf{F}}, \quad \frac{\partial^2 W_0}{\partial \mathbf{F} \otimes \partial \mathbf{G}}, \quad \frac{\partial^2 W_0}{\partial \mathbf{G} \otimes \partial \mathbf{F}}, \quad \frac{\partial^2 W_0}{\partial \mathbf{G} \otimes \partial \mathbf{G}}.$$

²The operation $\overset{2,3}{:}$ denotes the double contraction of two rank-three tensors with respect to their 2^{nd} and 3^{rd} indices, e.g. $[\mathbf{Q} \overset{2,3}{:} \mathbf{G}]_{ab} \doteq Q_{aMN} G_{bMN}$.

The 1st one contributes to the linearisation of the 1st Piola-Kirchhoff stress and again takes the known format (2.40) or (2.41) for the case of pair potentials. Explicit expressions for the remaining three tensors must be derived. Usual simple calculations yield the following 6th and 5th order tangent operators³:

$$\mathbb{M}_{FG} \doteq \frac{\partial^2 W_0}{\partial \mathbf{F} \otimes \partial \mathbf{G}} = \frac{1}{4V_i} \sum_{j \neq i} [\mathbf{k}_{ij} \bar{\otimes} [\mathbf{R}_{ij} \otimes \mathbf{R}_{ij}]] \otimes \mathbf{R}_{ij} \quad (5.13)$$

$$\mathbb{M}_{GF} \doteq \frac{\partial^2 W_0}{\partial \mathbf{G} \otimes \partial \mathbf{F}} = \frac{1}{4V_i} \sum_{j \neq i} [\mathbf{k}_{ij} \underline{\otimes} [\mathbf{R}_{ij} \otimes \mathbf{R}_{ij}]] \otimes \mathbf{R}_{ij} \quad (5.14)$$

$$\mathbb{M}_{GG} \doteq \frac{\partial^2 W_0}{\partial \mathbf{G} \otimes \partial \mathbf{G}} = \frac{1}{8V_i} \sum_{j \neq i} [\mathbf{k}_{ij} \underline{\otimes} [\mathbf{R}_{ij} \otimes \mathbf{R}_{ij}]] \otimes [\mathbf{R}_{ij} \otimes \mathbf{R}_{ij}] \quad (5.15)$$

5.3 Examples

To investigate the influence of the higher-order deformation gradient contribution in the extended Cauchy-Born rule on the accuracy of the kinematic description, a special non-homogeneous simple-shear-like deformation has been chosen and studied.

5.3.1 Geometric Characterisation of a Prototype Deformation

Firstly, a short description of the deformation analysed in the sequel should be given.

Homogeneous Simple Shear Deformation

Before introducing the above mentioned non-homogeneous deformation, the main features of the familiar homogeneous simple shear deformation, see fig. 5.3, should be reviewed. The origin of the local coordinate system is chosen in the middle of the undeformed volume element. All straight vertical lines in the material configuration transform to straight but inclined lines with the same slope α in the spatial configuration. In this case, the deformation field φ can be represented as a linear map of the material position vectors \mathbf{X} as

$$[\varphi] = \begin{bmatrix} \varphi_1 \\ \varphi_2 \end{bmatrix} = \begin{bmatrix} X_1 & + & B X_2 \\ 0 & + & X_2 \end{bmatrix} \rightsquigarrow \varphi = \mathbf{F}^{hom} \cdot \mathbf{X} \quad (5.16)$$

with the constant deformation gradient in terms of the shear number γ

$$F_{iJ} = F_{iJ}^{hom}(B) = \frac{\partial \varphi_i}{\partial X_J} = \begin{bmatrix} 1 & \gamma \\ 0 & 1 \end{bmatrix} \quad \text{with} \quad \gamma \equiv B = \text{constant over } \mathcal{B}_0 \quad (5.17)$$

Clearly, the 2nd-order deformation gradient \mathbf{G} vanishes identically in this homogeneous case:

$$G_{iJ1} \equiv \frac{\partial F_{iJ}}{\partial X_1} = \begin{bmatrix} 0 & 0 \\ 0 & 0 \end{bmatrix} \quad G_{iJ2} \equiv \frac{\partial F_{iJ}}{\partial X_2} = \begin{bmatrix} 0 & 0 \\ 0 & 0 \end{bmatrix} \quad (5.18)$$

³Expressions (5.13)-(5.15) are valid for pair potentials only with \mathbf{k}_{ij} defined in (2.11).

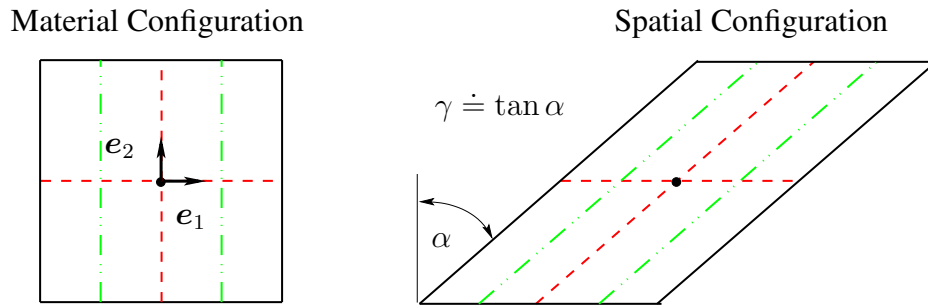


Figure 5.3: The homogeneous simple shear deformation with the spatially constant shear number γ

Non-Homogeneous Simple-Shear-like Deformation

To obtain a slightly perturbed simple shear deformation, a quadratic term with a small parameter $A \ll B$ has been added to the deformation field (5.16):

$$[\varphi] = \begin{bmatrix} \varphi_1 \\ \varphi_2 \end{bmatrix} = \begin{bmatrix} X_1 + B X_2 + A X_1 X_2 \\ X_2 \end{bmatrix} \rightsquigarrow \varphi = \mathbf{F}^{hom} \cdot \mathbf{X} + \frac{1}{2} \mathbf{G} : [\mathbf{X} \otimes \mathbf{X}] \quad (5.19)$$

Note that this deformation is precisely captured by the extended Cauchy-Born rule (5.9). The deformation gradient of the perturbed simple shear deformation

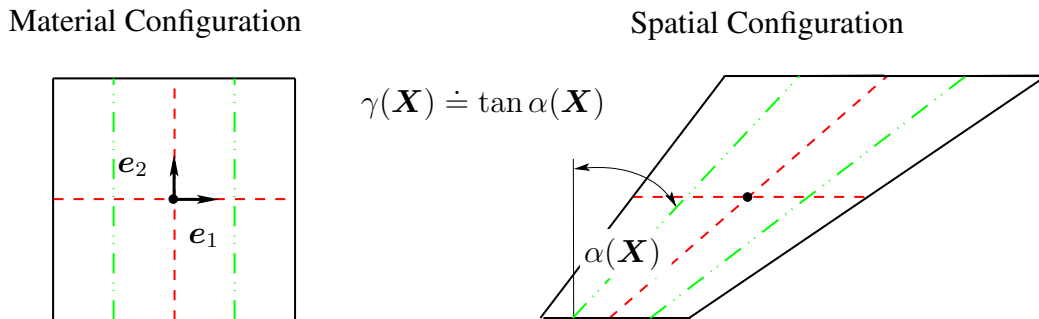


Figure 5.4: The non-homogeneous simple-shear-like deformation with the position-dependent shear number $\gamma(\mathbf{X})$

$$F_{iJ} = \frac{\partial \varphi_i}{\partial X_J} = \begin{bmatrix} 1 + A X_2 & B + A X_1 \\ 0 & 1 \end{bmatrix} \quad (5.20)$$

consists of the deformation gradient \mathbf{F}^{hom} of the homogeneous deformation and the perturbation with a small parameter A :

$$F_{iJ} = F_{iJ}^{hom}(B) + A \begin{bmatrix} X_2 & X_1 \\ 0 & 0 \end{bmatrix} \quad (5.21)$$

Here, the 2nd-order deformation gradient is constant for the present case of the quadratic deformation field:

$$G_{iJ1} \equiv \frac{\partial F_{iJ}}{\partial X_1} = \begin{bmatrix} 0 & A \\ 0 & 0 \end{bmatrix} \quad G_{iJ2} \equiv \frac{\partial F_{iJ}}{\partial X_2} = \begin{bmatrix} A & 0 \\ 0 & 0 \end{bmatrix} \quad (5.22)$$

Interesting enough, the deformation (5.19) can be represented in a format, which is similar to the common simple shear deformation

$$\varphi = \mathbf{F}^{inhom} \cdot \mathbf{X} ; \quad \mathbf{F}_{iJ}^{inhom} = \begin{bmatrix} 1 & \gamma(\mathbf{X}) \\ 0 & 1 \end{bmatrix} \neq \mathbf{F}_{iJ} \quad (5.23)$$

Note however that the non-linear map \mathbf{F}^{inhom} differs from the deformation gradient \mathbf{F} . The shear number γ is no longer constant over \mathcal{B}_0 and depends on the component X_1 of the material position vector \mathbf{X} :

$$\gamma(\mathbf{X}) = B + A X_1 \quad (5.24)$$

Straight vertical lines in the material configuration thus transform to straight lines in the spatial configuration with a slope depending on the material coordinate X_1 , see fig. 5.4.

5.3.2 Detailed Investigations

To investigate the influence of the higher-order gradient, the chosen non-homogeneous deformation has been studied for various ratios A/B . To describe the interatomic interaction, the above mentioned Lennard-Jones pair potential (1.20) with material parameters fitted to aluminium, i.e. $\sigma = 0.2575 \text{ nm}$ and $\varepsilon = 0.1699 \text{ nN nm}$, is used as a prototype model. These parameters are obtained by a fitting procedure under the constraint of a stress free material configuration and equality of the atomic energy in the material configuration to the sublimation energy of aluminium, i.e. $E^{sub} = 3.58 \text{ eV} = 0.574 \text{ nN nm}$. Thereby, the cut-off radius r_c is equal to five atomic spacings $r_0 = 0.286 \text{ nm}$.

Fig. 5.5 depicts the material and spatial collection of atoms representing the crystal of interest for two ratios A/B , whereby $A/B = 0$ corresponds to the homogeneous deformation field (5.16). The circles in the spatial configuration contain the next neighbours of the atoms in their centers where the deformation field has its origin. The deformed ellipses correspond to these circles pulled back by the deformation to the material configuration⁴. It is easy to recognise that the consideration of the 2nd-order deformation leads to a change of the spatial configuration even for the small ratio $A/B = 0.1$. This could be better observed in fig. 5.6 where the next neighbours distributions for three different ratios $A/B > 0$ are compared with such distribution for $A/B = 0$ corresponding to the homogeneous deformation. On the right-hand side, the regions in which the circles and triangles overlap denote regions of a homogeneous deformation state. The homogeneous and non-homogeneous deformation fields lead roughly to the same displacement in these regions. With increasing A/B , these regions tend to become smaller. Fig. 5.7 represents this observation even better. Here, each figure except for the first one, is an overlay of two spatial configurations. One of them is deformed homogeneously ($A/B = 0$) and the other one non-homogeneously with the corresponding ratio A/B varying from

⁴To obtain a deformed ellipse depicting the boundary of the next neighbours of the atom i in the material configuration, the circle in the spatial configuration must be pulled back to the material configuration. In general, this is connected with the solution of the non-linear system of algebraic equations (5.19) with respect to X_1 and X_2 . In the special case chosen here $X_2 = \varphi_2$ remains constant and this renders X_1 simply by substituting X_2 in the 1st row of (5.19).

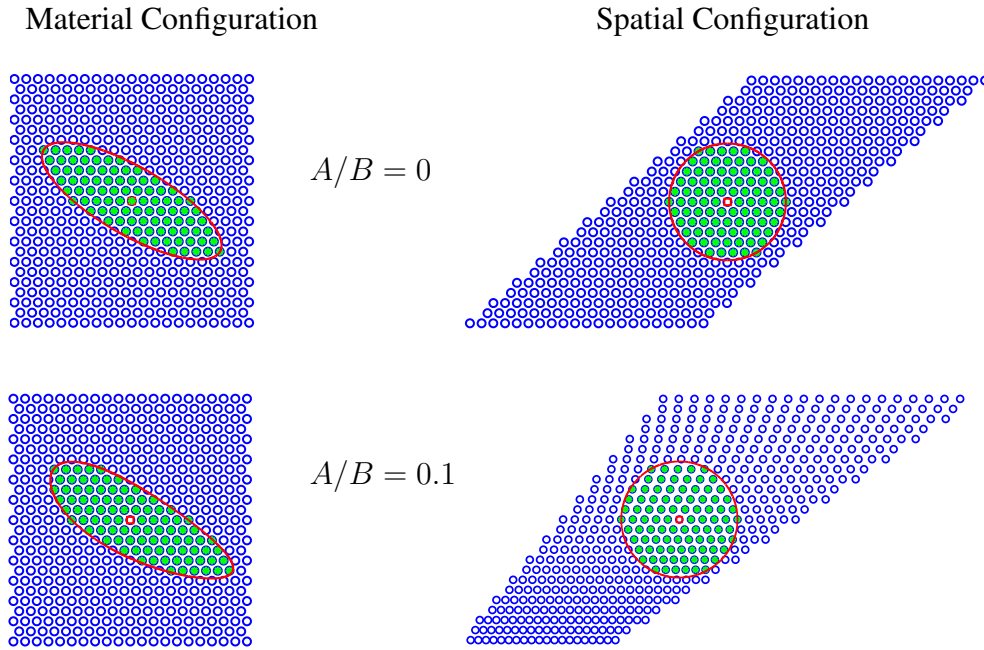


Figure 5.5: The material (on the left-hand side) and spatial configuration according to (5.19). Prototype model configuration for $A/B = 0$ (homogeneous deformation) and $A/B = 0.1$ (inhomogeneous deformation). The right-hand side corresponds to $B = 1.16$

0.01 to 0.25. It is plausible that the decision whether the deformation is homogeneous enough such that the standard Cauchy-Born rule applies or it should be treated as a non-homogeneous deformation depends on the length of the cut-off radius r_c . For instance, the deformation in the case $A/B = 0.02$ can not be considered as homogeneous if $r_c \gtrsim 2r_0$, whereby r_0 denotes the lattice constant, i.e the atomic spacing.

The energy of the central atom for various ratios A/B has been chosen as further qualitative criterion of inhomogeneity. Thereby, B increases from 0 to 3.48 continuously. Fig. 5.8 shows the corresponding energy curves together with the snap-shots of the atom distribution within the cut-off circle for special values of B . The first curve is strongly periodic since the reference crystal structure repeats itself periodically during the homogeneous simple shear deformation. The energy becomes particularly minimal for the shear numbers $B = 1.16, 2.32$ and so on for the chosen structure. All the snap-shots correspond to the repeating reference crystal structure and the first three minima of the energy curve for homogeneous deformation. The energy curves differ more and more from this curve with increasing ratio A/B . It can nevertheless be observed that the energy change for the given parameter set is non-essential within the first period. This can be attributed especially to the short-range interaction of the used pair potential. In conclusion, a simple quantitative inhomogeneity criterion should be elaborated.

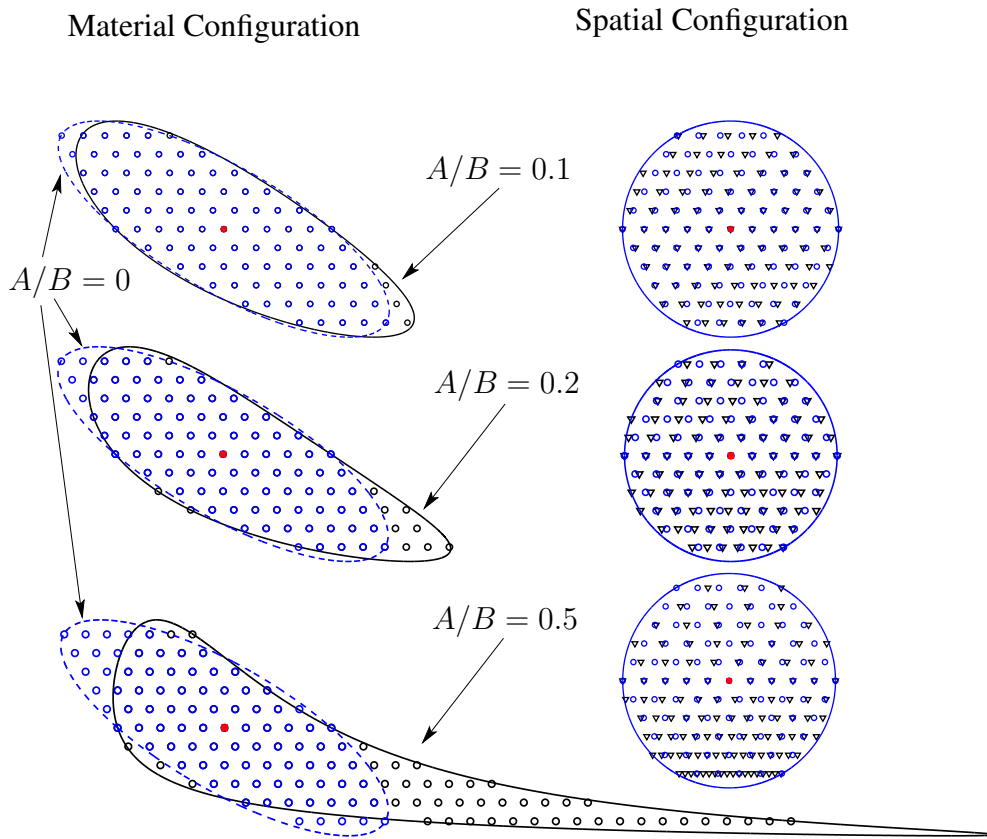


Figure 5.6: The next neighbours of the central atom in the material and spatial configurations for different ratios A/B (solid lines on the left-hand side) compared with the next neighbours distribution in the case of the homogeneous deformation $A/B = 0$ (dashed line on the left-hand side). The atoms in the case of the non-homogeneous deformation are represented as triangles on the right-hand side. The circles correspond to a homogeneous deformation. Both cases coincide in the material configuration. The right-hand side corresponds to $B = 1.16$.

5.3.3 Simple Deformation Inhomogeneity Measure

The essential information about the deformation field inhomogeneity is contained in the 2^{nd} -order deformation gradient \mathbf{G} , which is needed within the gradient extended framework. For the planar case, \mathbf{G} consists of the four vectors:

$$[\mathbf{G}] \doteq \left[\frac{\partial \mathbf{F}}{\partial \mathbf{X}} \right] = \begin{bmatrix} \frac{\partial F_{11}}{\partial \mathbf{X}} & \frac{\partial F_{12}}{\partial \mathbf{X}} \\ \frac{\partial F_{21}}{\partial \mathbf{X}} & \frac{\partial F_{22}}{\partial \mathbf{X}} \end{bmatrix} \quad (5.25)$$

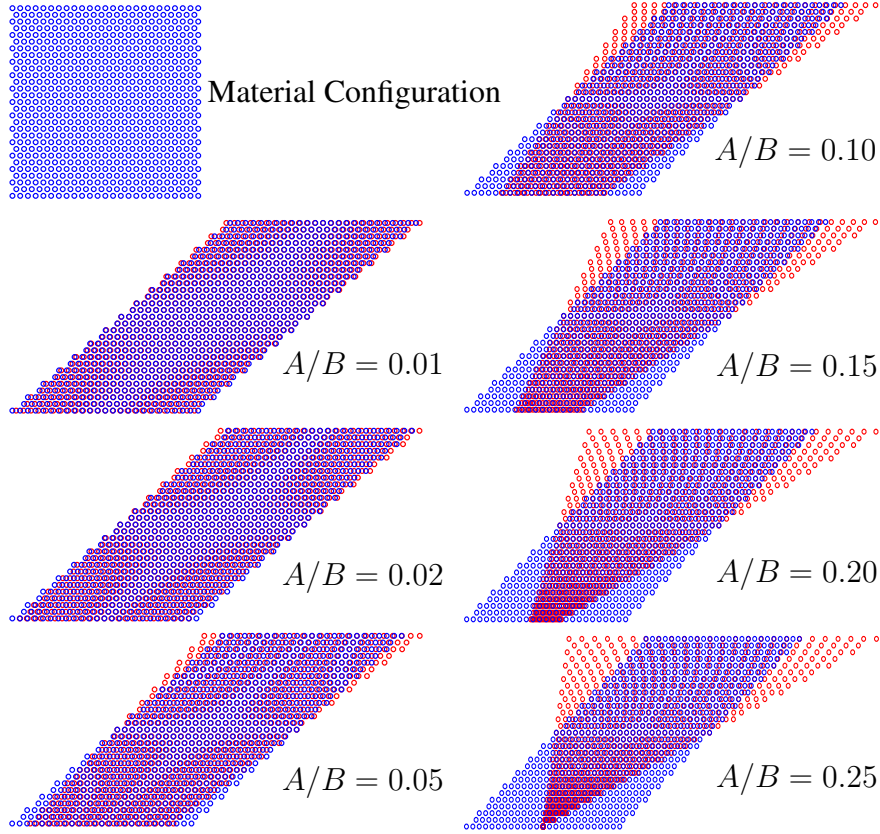


Figure 5.7: The overlapping of two spatial configurations of a homogeneously and a non-homogeneously deformed material area with various ratios A/B . The deformed state corresponds to $B = 1.16$.

Next, the matrix $\mathbf{D}(\mathbf{X})$ consisting of norms of the corresponding components of \mathbf{G} has been introduced :

$$[\mathbf{D}(\mathbf{X})] \doteq \begin{bmatrix} \left\| \frac{\partial F_{11}}{\partial \mathbf{X}} \right\| & \left\| \frac{\partial F_{12}}{\partial \mathbf{X}} \right\| \\ \left\| \frac{\partial F_{21}}{\partial \mathbf{X}} \right\| & \left\| \frac{\partial F_{22}}{\partial \mathbf{X}} \right\| \end{bmatrix} \equiv \begin{bmatrix} D_{11}(\mathbf{X}) & D_{12}(\mathbf{X}) \\ D_{21}(\mathbf{X}) & D_{22}(\mathbf{X}) \end{bmatrix} \quad (5.26)$$

Each component must be evaluated at the site of each atom from the next neighbours list in the cut-off circle and the maximum value must be found :

$$D^{max} \doteq \max_{i,J} \left\{ \max_{\mathbf{X}} \{D_{iJ}(\mathbf{X})\} \right\} \quad (5.27)$$

D^{max} has dimension of an inverse length and the inhomogeneity length can thus be introduced as the inverse value of D^{max} :

$$L \doteq \frac{1}{D^{max}} \quad (5.28)$$

Now, the deformation inhomogeneity measure can be defined as the ratio of the cut-off radius and the inhomogeneity length:

$$\varepsilon \doteq \frac{r_c}{L} = \max_{i,j} \left\{ \max_{\mathbf{X}} \{D_{ij}(\mathbf{X})\} \right\} r_c \quad (5.29)$$

This measure characterises how rapidly the deformation field changes within the cut-off circle. For a homogeneous deformation, L tends to infinite and thus ε tends to zero. The question, which ε should be chosen as a critical value indicating that a sufficiently non-homogeneous deformation occurs depends on the problem and must be further studied.

In the example considered above, the 1st and the 2nd deformation gradients are given by (5.20) and (5.22). Then the matrix \mathbf{D} is constant and can be represented as follows:

$$[\mathbf{D}(\mathbf{X})] = \begin{bmatrix} \sqrt{[0^2 + A^2]} & \sqrt{[A^2 + 0^2]} \\ 0 & 0 \end{bmatrix} = \begin{bmatrix} A & A \\ 0 & 0 \end{bmatrix} \quad (5.30)$$

Consequently, the following expressions can be obtained for L and ε under consideration of (5.28)-(5.30):

$$L = \frac{1}{A} \quad \varepsilon = A r_c \quad (5.31)$$

To determine the correspondence between the introduced measure ε and the inhomogeneity, the energy level curves shown in fig. 5.8 have been computed for each atom within the cut-off circle for various A/B ratios. These data have been then represented in the form of energy isolines as shown in fig. 5.9. The isolines are numbered according to tab. 5.3.3. The minimum energy level corresponds to the energy of an atom in the reference lattice. The first nine levels are equidistant with the interval of length 0.5. Because of the behaviour of the used pair potential given in fig. 1.10, the energy under compression tends to reach enormously positive values due to the reduction of the distances between the atoms in such areas. Thus, the levels 10 to 16 correspond to such positive energy values. In fig. 5.9, the areas occupied by the next neighbours of the central atom are shown within the cut-off circle together with the energy distribution in these areas. The corresponding ε computed according to (5.29) are depicted additionally. As expected, ε vanishes for the homogeneously distributed energy (1st column and 1st row). With increasing A/B and B the energy distribution becomes more and more inhomogeneous and ε increases simultaneously. Apparently, as already mentioned above, the theory-based critical value of ε corresponding to a still sufficiently homogeneous deformation field depends on the problem and the cut-off radius. In our particular case only the energy distribution in the 2nd column and in the 1st two upper figures of the 3rd column can be considered as homogeneous enough in the vicinity of the center atom. In this case $\varepsilon^{max} \approx 0.066$.

Table 5.1: The enumeration of the energy levels as shown in fig. 5.9

		Energy levels								
Number		1	2	3	4	5	6	7	8	9
Value [$\times 10^{-18}$ J]		-4.0	-3.5	-3.0	-2.5	-2.0	-1.5	-1.0	-0.5	0.0
Number		10	11	12	13	14	15	16		
Value [$\times 10^{-18}$ J]		1	10	10^2	10^3	10^4	10^5	10^6		

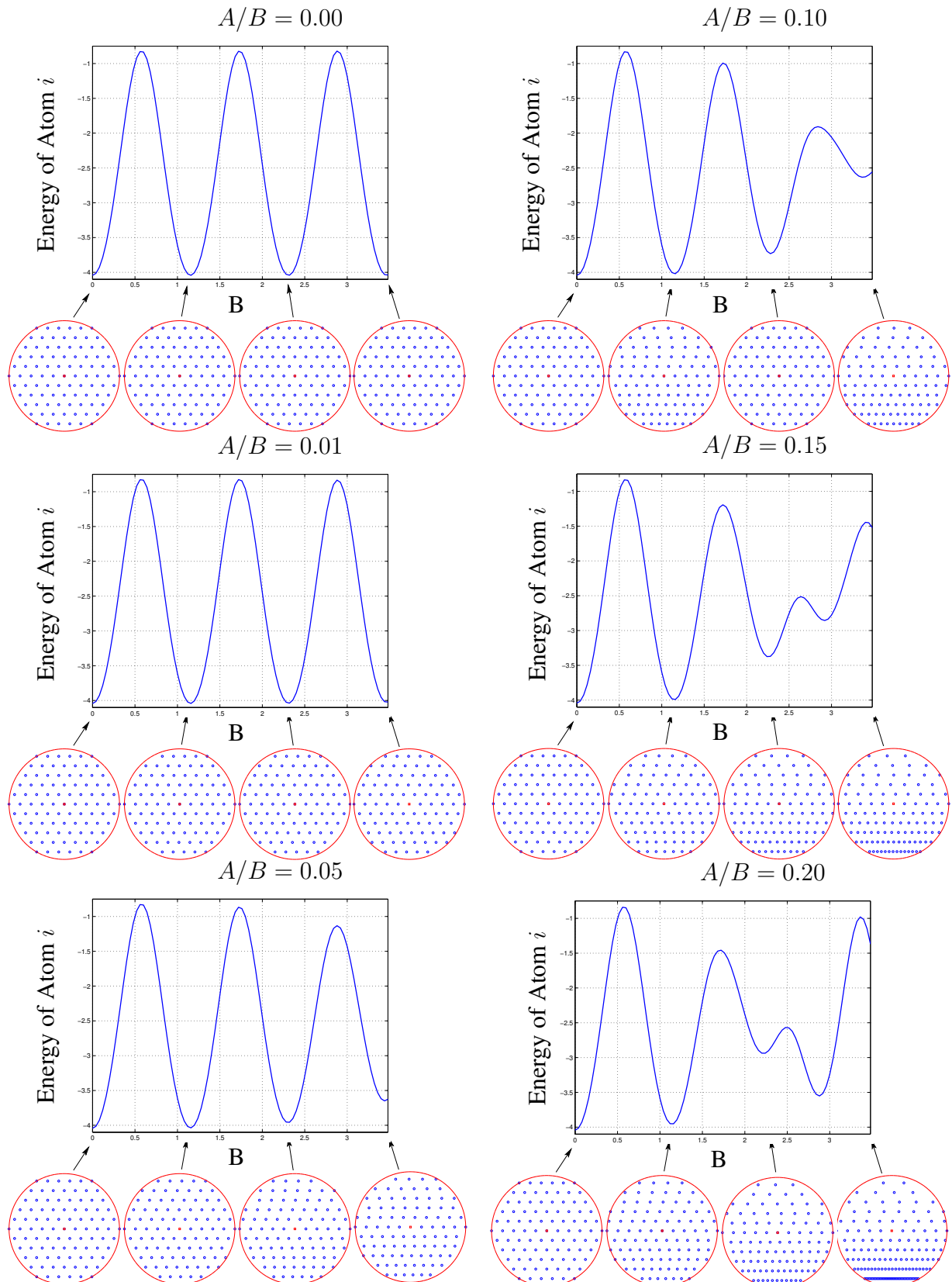


Figure 5.8: The energy of the atom in the center of the cut-off circle for various ratios A/B , whereby B continuously increases from 0 to 3.48. The snap-shots of the atomic distribution within the cut-off circle correspond to the minima of the energy curve for the case of homogeneous deformation ($A/B = 0$).

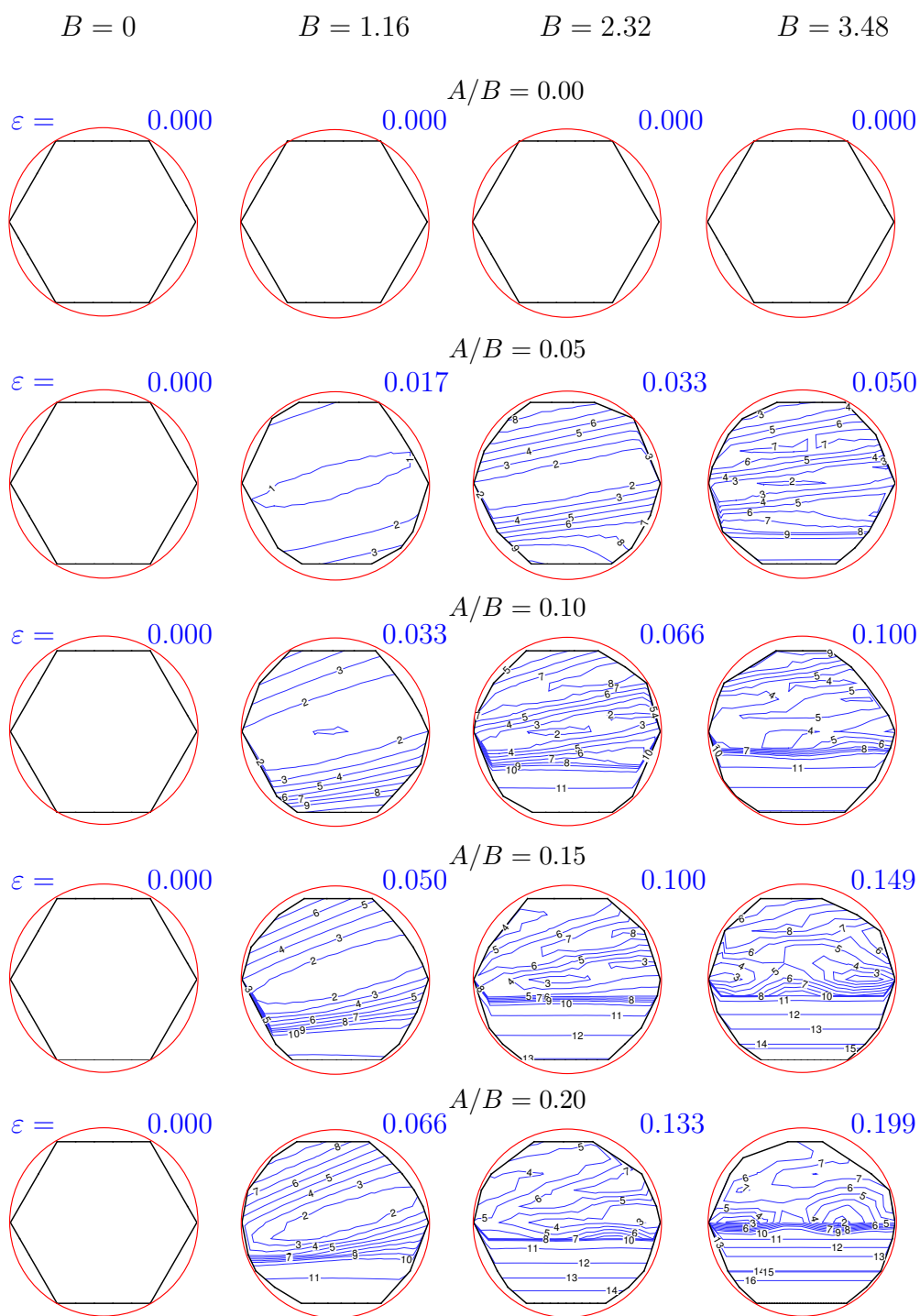


Figure 5.9: The energy distribution within the cut-off circle for various ratios A/B and B increasing from 0 to 3.48. The corresponding values of ε computed according to (5.29) are given additionally. The correspondence between the energy levels numbering and the energy values is given in tab. 5.3.3.

Chapter 6

Discussion

The work is complete, and now it is the time to declare, which results have been newly obtained and which of them seem to be important (of course, in my opinion). I would also like to represent my vision of further development of the method described here.

What is New?

The new aspects of this contribution are

- a compact tensor format for all derivations and results;
- a description of the transition from a discrete atomic lattice to a continuous body as continuation and homogenisation; in particular a derivation of the Cauchy-Born rule from the main principle of homogenization, i.e. from the equivalence of the virtual macro and micro powers;
- an introduction of a cellwise Cauchy-Born rule;
- a consideration of a discrete homogenisation, which requires among others, a discrete analog of the Gauss theorem;
- an explicit format of the 1st Piola-Kirchhoff stress tensor and the corresponding 4th-order tangent operator for both the Lennard-Jones pair potential and the EAM potential;
- an overview of the problems arising during an application of continuum convexity notions to a discrete lattice system;
- an application of the continuum formulation of strain localisation within the frame of continuum-atomistics;
- a computation of the yield condition based on the continuum-atomistic model; this condition can simultaneously be viewed as a condition of first dislocation nucleation;
- a presentation of the method developed for a consideration of periodical boundary conditions;
- a representation of the microstructures computed by relaxation;
- an application of the path-change procedure for a computation of an energetically favourable configuration of a discrete lattice structure;

- a presentation of the newly proposed method for the determination of scaling factors required in the path-change procedure;
- an application of the continuum-atomistic principles within the 2^{nd} -order theory;
- a derivation of explicit expressions for the higher-order stress, its push-forward and its linearisation for the 2^{nd} -order continuum-atomistic formulation;
- a study of the relevance of the 2^{nd} -order theory for non-homogeneous deformations on the basis of a simple example;
- an introduction of the deformation inhomogeneity measure to characterise the change of the deformation field within the interaction circle.

What is Important?

The main contribution of the present work is an investigation and a mathematical formulation of failure of the continuum-atomistic approach at the elastic limit as well as the computation of a failure surface based on the detection of the loss of infinitesimal rank-one convexity for various stress states.

Thereby, most results are in a good agreement with theoretical expectations. For instance, the appearance of localisation effects depends heavily on the orientation and thus on the anisotropy of the representative crystallite. In particular, a part of the obtained failure directions coincide with the expected slip directions of *fcc*-type lattice. However, the deviation of other failure directions from theoretical expectations should be studied additionally.

Furthermore, it also seems to be important that the work contains a detailed overview of various atomistic energy functions including an explicit format of the (M)EAM potential, which has been scheduled from different publications.

A step-by-step review of continuum-atomistic principles supported by the continuum mechanics as well as atomistics gives rise to better an understanding of the problem and systemises the already existing results.

A representation of the main settings of the non-linear finite element method allows this work to be read without a necessity to consult a wide range of corresponding literature. The given explicit format of the element stiffness matrices can be directly used for an implementation into a finite-element code.

Homogenised field variables such as 1^{st} Piola Kirchhoff stress tensor, 2^{nd} -order stress, tangent operators in both 1^{st} - and 2^{nd} -order theories are derived independently of any specification of an energy function. Only a general dependence on the interatomic separation is taken into account. It means that these expressions are valid for any energy function depending on the interatomic separation as

$$E^{int} = \sum_i E_i(r_{i1}, r_{i2} \dots) \quad \text{or at least as} \quad E^{int} = \frac{1}{2} \sum_i \sum_j \Phi(r_{ij}) \quad \text{as in chapter 5.}$$

What is Left?

Firstly, the robustness of relaxation should be completed. To improve the convergence, the damped Newton method should be probably used instead of the classical Newton-Raphson approach. Thereby,

a development of rank-one laminates can be considered as a simplified particular problem. This would allow to implement the transition to plasticity in a finite element code.

A more correct plasticity model being able to capture the dislocations should be considered. The conception of a geometrically necessary dislocations (GND), see [67], could represent an example for such a model. Note that the simple shear deformation proposed in chapter 5 by (5.19) can describe a region containing one or several dislocations, cf. fig. 5.4. Thereby, the difference between the slopes α_l and α_r of the left and right edges of the deformed area is connected with the Burgers vector \mathbf{b} and the number n of dislocations stored in the area by, see fig. 6.1,

$$n\mathbf{b} = h [\tan \alpha_r - \tan \alpha_l] \mathbf{e}_1 \equiv h [\gamma(\mathbf{X}^{max}) - \gamma(\mathbf{X}^{min})] \mathbf{e}_1$$

in terms of the position-dependent shear number $\gamma(\mathbf{X})$ introduced in (5.24). Here, h denotes the

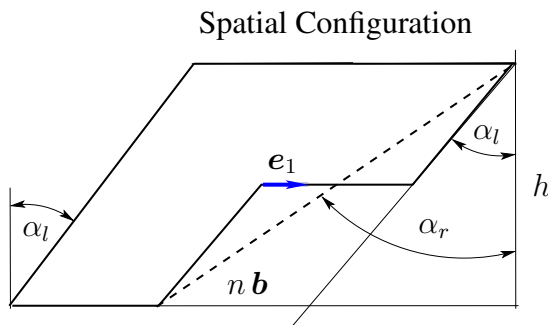


Figure 6.1: The non-homogeneous simple-shear-like deformation capturing n edge dislocations; cf. fig. 5.4

height of the cell, b is here identical with the atomic separation r_0 in the slip direction and \mathbf{e}_1 is the cartesian basis vector pointing into the slip direction.

Then, an extension of the simulation code into the 3^{rd} dimension together with the usage of realistic energy functions such as the EAM potential would provide a possibility to simulate a behavior of realistic systems, e.g. various microstructured materials.

I am also sure that a completion of the discrete homogenisation framework can be an interesting challenge for a mathematician.

The aim of further studies related to the higher-order gradients is to discretise and to implement the equilibrium conditions and to solve boundary value problem based on the gradient-extended theory similar to the case of small deformations investigated by Shu et al. [79].

Besides the boundary value problem, an elaboration of a failure condition based on the gradient-extended formulation similar to the investigations on the basis of the 1^{st} -order theory is intended.

It is shown that the newly introduced deformation inhomogeneity measure ε indirectly characterises the change of deformation field within the interaction circle. The applicability and universality as well as the physical meaning of this measure deserve a detailed study.

Clearly, the achieved results shall not be seen yet as a completed framework, but rather as an academic example, which points at the direction and potential of further research needed to decide whether the proposed framework becomes accepted or is a dead-end brunch and should be forgotten. However, I hope that this work contributes in any case to a better understanding of the problems arising during the multiscale modelling linking continuous and discrete systems.

Appendix A

Investigation of $\sum_{j \neq i} \mathbf{R}_{ij} \otimes \mathbf{R}_{ij}$

It is to be proven in this appendix that $\sum_{j \neq i} \mathbf{R}_{ij} \otimes \mathbf{R}_{ij}$ is proportional to the identity matrix for a sufficiently symmetrical planar lattice like the (111)–plane of a fcc crystal.

The sum over all atoms can be rewritten as a sum over the contributions of the atoms lying at the

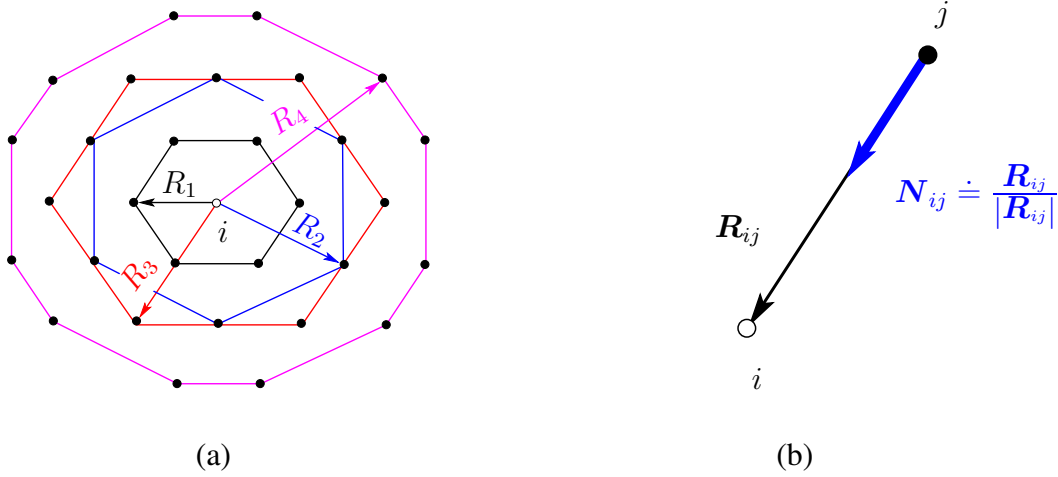


Figure A.1: (a) The 1st four next-neighbours atomic shells of an atom i in the (111)–plane of a fcc-type lattice. R_α is the atomic separation between the atom i and the atoms in the α –th shell. (b) The definition of the unit vector N in the direction of \mathbf{R}_{ij} .

same separation from the atom i :

$$\begin{aligned}
 \sum_{j \neq i} \mathbf{R}_{ij} \otimes \mathbf{R}_{ij} &= \sum_{j=1}^{m_1} \mathbf{R}_{ij} \otimes \mathbf{R}_{ij} + \sum_{j=1}^{m_2} \mathbf{R}_{ij} \otimes \mathbf{R}_{ij} + \dots \\
 &= R_1^2 \sum_{j=1}^{m_1} \mathbf{N}_{ij} \otimes \mathbf{N}_{ij} + R_2^2 \sum_{j=1}^{m_2} \mathbf{N}_{ij} \otimes \mathbf{N}_{ij} + \dots
 \end{aligned} \tag{A.1}$$

- m_α is the number of atoms in α –th neighbour's shell of the atom i ; e.g. $m_1 = m_2 = m_3 = 6$; $m_4 = 12$, see fig. A.1 (a);

- R_α is the length of the distance vector \mathbf{R}_{ij} for atom j from the α -th neighbour's shell of the atom i ; e.g. $R_1 = r_0$; $R_2 = r_0 \sqrt{3}$; $R_3 = 2r_0$; $R_4 = r_0 \sqrt{7}$;
- $\mathbf{N}_{ij} \doteq \mathbf{R}_{ij}/|\mathbf{R}_{ij}|$ is a unit vector in the direction of \mathbf{R}_{ij} , see fig. A.1 (b).

Thus, the investigation of the initial sum is reduced to the investigation of $\sum_{j=1}^{m_\alpha} \mathbf{N}_{ij} \otimes \mathbf{N}_{ij}$. Firstly, the non-diagonal components of this matrix should be discussed. The following is valid for these components:

Lemma A.1. *The non-diagonal components of $\sum_{j=1}^{m_\alpha} \mathbf{N}_{ij} \otimes \mathbf{N}_{ij}$ vanish if the atomic arrangement is sufficiently symmetric, i.e.*

$$\forall \mathbf{N}_{ij} \exists \tilde{\mathbf{N}}_{ij} \text{ or } -\tilde{\mathbf{N}}_{ij} : (\mathbf{N}_{ij})_1 = (\tilde{\mathbf{N}}_{ij})_1 \text{ and } (\mathbf{N}_{ij})_2 = -(\tilde{\mathbf{N}}_{ij})_2$$

Here, $(\mathbf{N}_{ij})_\alpha$ denotes the α -th component of the vector \mathbf{N}_{ij} (and the same for $(\tilde{\mathbf{N}}_{ij})_\alpha$).

Proof The proof is straightforward. Consider a symmetrical atomic arrangement, which fulfils the requirement of the proposition. Such arrangement is shown in fig. A.2.

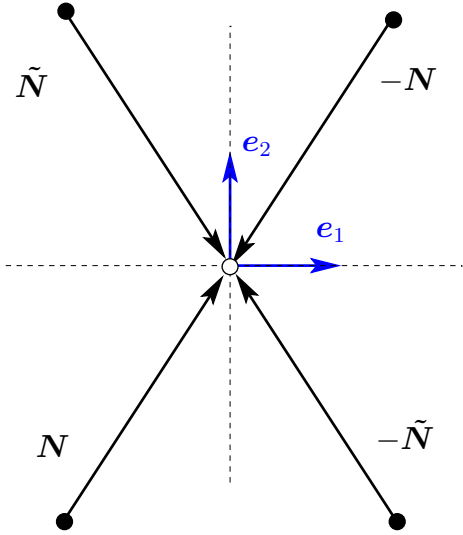


Figure A.2: A symmetrical atomic arrangement where for each \mathbf{N}_{ij} there exists $\tilde{\mathbf{N}}_{ij}$ or $-\tilde{\mathbf{N}}_{ij} : (\mathbf{N}_{ij})_1 = (\tilde{\mathbf{N}}_{ij})_1$ and $(\mathbf{N}_{ij})_2 = -(\tilde{\mathbf{N}}_{ij})_2$

According to this figure, two vectors \mathbf{N} and $\tilde{\mathbf{N}}$ can be represented in an orthonormal basis $\{\mathbf{e}_1, \mathbf{e}_2\}$ as

$$\begin{aligned} \mathbf{N} &= N_1 \mathbf{e}_1 + N_2 \mathbf{e}_2 \\ \tilde{\mathbf{N}} &= N_1 \mathbf{e}_1 - N_2 \mathbf{e}_2 \end{aligned}$$

The indices ij are omitted here to simplify the expressions. According to this, the matrices of the corresponding dyadic products are given by

$$\begin{aligned} [\mathbf{N} \otimes \mathbf{N}]_{\alpha\beta} &= \begin{pmatrix} N_1^2 & N_1 N_2 \\ N_1 N_2 & N_2^2 \end{pmatrix} \\ [\tilde{\mathbf{N}} \otimes \tilde{\mathbf{N}}]_{\alpha\beta} &= \begin{pmatrix} N_1^2 & -N_1 N_2 \\ -N_1 N_2 & N_2^2 \end{pmatrix} \end{aligned}$$

Now, the sum of these two matrices yield a diagonal matrix:

$$[\mathbf{N} \otimes \mathbf{N}]_{\alpha\beta} + [\tilde{\mathbf{N}} \otimes \tilde{\mathbf{N}}]_{\alpha\beta} = 2 \begin{pmatrix} N_1^2 & 0 \\ 0 & N_2^2 \end{pmatrix} \quad (\text{A.2})$$

An analogous result can be obtained for the other two vectors $-\mathbf{N}$ and $-\tilde{\mathbf{N}}$:

$$[-\mathbf{N} \otimes -\mathbf{N}]_{\alpha\beta} + [-\tilde{\mathbf{N}} \otimes -\tilde{\mathbf{N}}]_{\alpha\beta} = 2 \begin{pmatrix} N_1^2 & 0 \\ 0 & N_2^2 \end{pmatrix} \quad (\text{A.3})$$

It is straightforward that this result is true for each pair \mathbf{N} - $\tilde{\mathbf{N}}$ or \mathbf{N} - $-\tilde{\mathbf{N}}$ in the shell so that the matrix $\sum_{j=1}^{m_\alpha} \mathbf{N}_{ij} \otimes \mathbf{N}_{ij}$ is diagonal and the lemma (A.1) is proven. \square

To prove the main proposition of this appendix, a 2nd lemma is needed:

Lemma A.2. Consider a sufficiently symmetric atomic arrangement as in the lemma (A.1). The following is then valid for the components $(\mathbf{N}_{ij})_1$ and $(\mathbf{N}_{ij})_2$ of a vector \mathbf{N}_{ij} and at least for the 1st six next-neighbours shells¹:

$$\sum_{j=1}^{m_\alpha} (\mathbf{N}_{ij})_1^2 = \sum_{j=1}^{m_\alpha} (\mathbf{N}_{ij})_2^2$$

Proof The components of the unit vector \mathbf{N}_{ij} are given by

$$\begin{aligned} (\mathbf{N}_{ij})_1 &= \cos \varphi_{ij} \\ (\mathbf{N}_{ij})_2 &= \sin \varphi_{ij} \end{aligned}$$

with the angle φ_{ij} between the basis vector e_1 and the vector \mathbf{N}_{ij} , see fig. A.3. The proposition of this lemma can then be rewritten as

$$\begin{aligned} \sum_{j=1}^{m_\alpha} [(\mathbf{N}_{ij})_1^2 - (\mathbf{N}_{ij})_2^2] &= \sum_{j=1}^{m_\alpha} [\cos^2 \varphi_{ij} - \sin^2 \varphi_{ij}] \\ &= \sum_{j=1}^{m_\alpha} \cos 2 \varphi_{ij} = 0 \end{aligned}$$

(A.4)

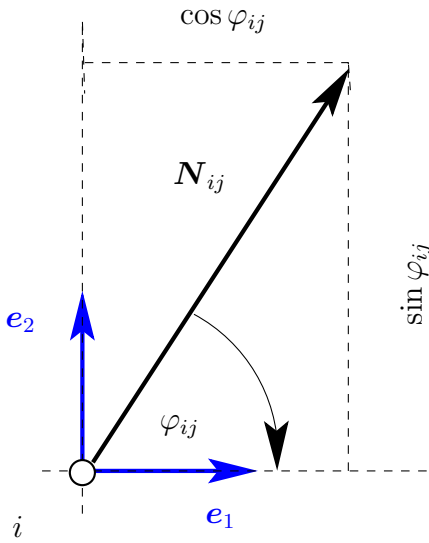


Figure A.3: The components of the vector \mathbf{N}_{ij}

The validity of this last equation has been checked directly for the 1st six next-neighbours shells. \square

In other words, the lemma states that the sum of the length of the projection of all the \mathbf{N}_{ij} on the e_1 -axis and e_2 -axis are equal. It is not proven in the general case but seems to be true for the symmetric arrangement considered here.

Now, in view of lemmas A.1 and A.2, the following proposition can be suggested:

Proposition A.3. For the sufficiently symmetric atomic arrangement described above, $\sum_{j=1}^{m_\alpha} \mathbf{N}_{ij} \otimes \mathbf{N}_{ij}$ is proportional to the identity matrix with the scaling factor n_α^2 , which depends on the number and positions of the atoms in the α -th next-neighbours shell of the atom i :

$$\sum_{j=1}^{m_\alpha} \mathbf{N}_{ij} \otimes \mathbf{N}_{ij} = n_\alpha^2 \mathbf{I}$$

¹ $R_6 = 3.464 r_0$

Proof The proposition follows immediately from both lemmas. Indeed, according to these lemmas

$$\begin{aligned} \left[\sum_{j=1}^{m_\alpha} \mathbf{N}_{ij} \otimes \mathbf{N}_{ij} \right]_{\alpha\beta} &= \sum_{j=1}^{m_\alpha} \begin{pmatrix} (\mathbf{N}_{ij})_1^2 & 0 \\ 0 & (\mathbf{N}_{ij})_2^2 \end{pmatrix} = \begin{pmatrix} \sum_{j=1}^{m_\alpha} (\mathbf{N}_{ij})_1^2 & 0 \\ 0 & \sum_{j=1}^{m_\alpha} (\mathbf{N}_{ij})_2^2 \end{pmatrix} \\ &= \left[\sum_{j=1}^{m_\alpha} (\mathbf{N}_{ij})_1^2 \right] \begin{pmatrix} 1 & 0 \\ 0 & 1 \end{pmatrix} \equiv n_\alpha^2 \mathbf{I} \end{aligned} \quad (\text{A.5})$$

The scaling factor $n_\alpha^2 \doteq \sum_{j=1}^{m_\alpha} (\mathbf{N}_{ij})_1^2$ depends on the number and arrangement of the atoms in the corresponding next-neighbours shell, e.g. $n_1^2 = n_2^2 = n_3^2 = 3$, $n_4^2 = 6$ etc. \square

In view of the proposition (A.3), the decomposition (A.1) can be represented as

$$\sum_{j \neq i} \mathbf{R}_{ij} \otimes \mathbf{R}_{ij} = \left(\sum_{\alpha} n_\alpha^2 R_\alpha^2 \right) \mathbf{I} \equiv \rho^2 \mathbf{I} \quad (\text{A.6})$$

and the main proposition of this appendix is proven.

Appendix B

On the Discrete Homogenisation

Theorem B.1. (*discrete Gauss theorem*) Consider a body $\mathcal{B}_0 \in \mathbb{R}^3$ with the volume V_0 consisting of N cells, whereby the volume of the α -th cell is V_α and $\sum_\alpha V_\alpha = V_0$.

Let $\mathbf{H}_\alpha : \mathbb{R}^3 \rightarrow \mathcal{B}_0 \subset \mathbb{R}^3$ be a discrete vector-valued function with the components $[P(X_\alpha, Y_\alpha, Z_\alpha) \ Q(X_\alpha, Y_\alpha, Z_\alpha) \ R(X_\alpha, Y_\alpha, Z_\alpha)]$ where $\mathbf{R}_\alpha \doteq [X_\alpha, Y_\alpha, Z_\alpha]$ is a chosen point within the cell α . Thereby, each cell contains only one such point, see fig. B.1 (a).

The following sum over all cells can then be transformed into a sum over the values of the function \mathbf{H}_β for the cells β at the boundary of the body \mathcal{B}_0 :

$$\begin{aligned} & \sum_{\alpha=1}^N \left[\frac{\Delta(\mathbf{H}_\alpha)_X}{\Delta X} + \frac{\Delta(\mathbf{H}_\alpha)_Y}{\Delta Y} + \frac{\Delta(\mathbf{H}_\alpha)_Z}{\Delta Z} \right] V_\alpha \\ &= \sum_{i=1}^{K_X} A_i^X [(\mathbf{H}_i)_X^H - (\mathbf{H}_i)_X^L] + \sum_{j=1}^{K_Y} A_j^Y [(\mathbf{H}_j)_Y^H - (\mathbf{H}_j)_Y^L] + \sum_{k=1}^{K_Z} A_k^Z [(\mathbf{H}_k)_Z^H - (\mathbf{H}_k)_Z^L] \end{aligned} \quad (\text{B.1})$$

The following notions are introduced here:

- $\frac{\Delta(\mathbf{H}_\alpha)_X}{\Delta X} \doteq \frac{P(X_\alpha + \Delta X, Y_\alpha, Z_\alpha) - P(X_\alpha, Y_\alpha, Z_\alpha)}{\Delta X}$ denotes the increment in the X -component of \mathbf{H}_α between two neighbour cells related to the increment in X between the discrete points within these two cells; analogous for $\frac{\Delta(\mathbf{H}_\alpha)_Y}{\Delta Y}$ and $\frac{\Delta(\mathbf{H}_\alpha)_Z}{\Delta Z}$;
- A_i^X is the area of the projection of a cell on the coordinate plane YZ ; analogous for A_j^Y and A_k^Z ;
- $(\mathbf{H}_i)_X^H \doteq P(X_i^H, Y_i, Z_i)$ and $(\mathbf{H}_i)_X^L \doteq P(X_i^L, Y_i, Z_i)$, whereby $\mathbf{R}_i^H \doteq [X_i^H, Y_i, Z_i]$ and $\mathbf{R}_i^L \doteq [X_i^L, Y_i, Z_i]$ lie within two outer cells and $\mathbf{R}_i^H - \mathbf{R}_i^L$ is parallel to the X axis; analogous for $(\mathbf{H}_j)_Y^H$ and $(\mathbf{H}_j)_Y^L$ as well as for $(\mathbf{H}_k)_Z^H$ and $(\mathbf{H}_k)_Z^L$;
- K_X , K_Y and K_Z are in general different integers.

Proof The proof of this theorem is analogous to the proof of the Gauss theorem. Consider a collection of parallelepiped-shaped cells forming a body \mathcal{B}_0 . Thereby, the cell α has the volume V_α and contains a point with the site vector \mathbf{R}_α , whereby the collection of these points form a discrete configuration

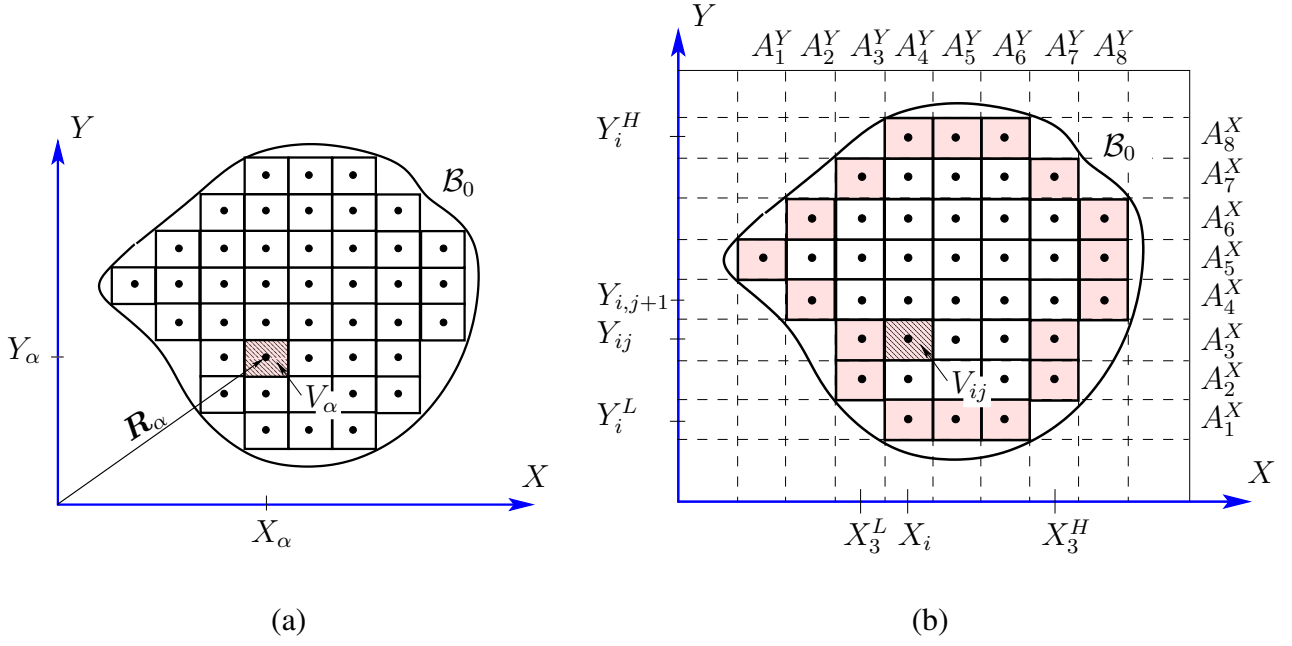


Figure B.1: Explanation to the discrete Gauss theorem.

$\mathcal{C}_0 \subset \mathcal{B}_0$. Such a structure is displayed in fig. B.1 (a) for a planar case with the objective of clarity. Consider a sum over all cells from the increment $\Delta Q_\alpha / \Delta Y$ only in the Y -component of \mathbf{H}_α related to the increment ΔY in Y_α . This sum replaces the body integral from the partial derivative $\partial Q / \partial Y$, i.e. $\iiint_{\mathcal{B}_0} (\partial Q / \partial Y) dX dY dZ$ in the discrete case:

$$\sum_{\alpha=1}^N \frac{\Delta Q_\alpha}{\Delta Y} V_\alpha \doteq \sum_{\alpha=1}^N \frac{Q(X_\alpha, Y_\alpha + \Delta Y, Z_\alpha) - Q(X_\alpha, Y_\alpha, Z_\alpha)}{\Delta Y} V_\alpha \quad (\text{B.2})$$

Here, ΔY is equal to the separation in the Y -direction between two next points of \mathcal{C}_0 and is specified below. To transform this sum, consider the body \mathcal{B}_0 consisting of, say, K_Y columns. Thereby, the column i contains m_i cells. Now, the α -th cell in fig. B.1 (a) obtains the indices ij declaring that this cell is from the i -th column and has the number j from m_i in this column, see fig. B.1 (b), where $i = 4$ (from the left) and $j = 3$ (from the bottom). According to such description, the components of \mathbf{R}_α obtain the following new notations: $X_\alpha \equiv X_i$, $Y_\alpha \equiv Y_{ij}$ and the increment ΔY can be defined as $Y_{i,j+1} - Y_{ij}$.

The volume V_0 can be represented on the one hand as a sum over all cell contributions V_α as mentioned above or, on the other hand, as the double sum over all columns and over the contributions of each cell in the column:

$$V_0 = \sum_{\alpha=1}^N = \sum_{i=1}^{K_Y} \sum_{j=1}^{m_i} V_{ij}$$

Under the assumption that the cell edges cut the lines connecting two next-neighbour points of \mathcal{C}_0 into two equivalent parts (i.e. the cells are the Voronoi polyhedrons or polygons in the planar case), the volume V_{ij} can be represented as

$$V_{ij} = A_i [Y_{i,j+1} - Y_{ij}] ,$$

where A_i is the area of the projection of the i -th column on the XZ coordinate plane. In fig. B.1 (b), these projections are represented by lines of the length A_i^Y , $i = \overline{1, 8}$. Now, the initial sum can be rewritten as

$$\begin{aligned}
\sum_{\alpha=1}^N \frac{Q(X_\alpha, Y_\alpha + \Delta Y, Z_\alpha) - Q(X_\alpha, Y_\alpha, Z_\alpha)}{\Delta Y} V_\alpha &= \sum_{i=1}^{K_Y} \sum_{j=1}^{m_i} \frac{Q(X_i, Y_{i,j+1}, Z_i) - Q(X_i, Y_{ij}, Z_i)}{Y_{i,j+1} - Y_{ij}} V_{ij} \\
&= \sum_{i=1}^{K_Y} \sum_{j=1}^{m_i} [Q(X_i, Y_{i,j+1}, Z_i) - Q(X_i, Y_{ij}, Z_i)] A_i \\
&= \sum_{i=1}^{K_Y} A_i [Q(X_i, Y_{i2}, Z_i) - Q(X_i, Y_{i1}, Z_i) + Q(X_i, Y_{i3}, Z_i) - Q(X_i, Y_{i2}, Z_i) + \dots] \\
&= \sum_{i=1}^{K_Y} A_i [Q(X_i, Y_{i,m_i}, Z_i) - Q(X_i, Y_{i1}, Z_i)] \equiv \sum_{i=1}^{K_Y} A_i [Q(X_i, Y_i^H, Z_i) - Q(X_i, Y_i^L, Z_i)]
\end{aligned} \tag{B.3}$$

Here, Y_i^L and Y_i^H are the minimum and the maximum values of the Y -coordinates in the i -th column, i.e. the Y -coordinates of the boundary points from \mathcal{C}_0 in this column. Thus, the sum over all cell contributions is reduced to the sum over the contributions from those cells, which correspond to the boundary points of \mathcal{C}_0 . This transformation represents a basic transformation for further formulas containing a vector- or tensor-valued functions. A continuous analog for (B.3) is

$$\iiint_{\mathcal{B}_0} \frac{\partial Q}{\partial Y} dX dY dZ = \iint_{\partial \mathcal{B}_0} Q dX dZ$$

Analogously to (B.3), a similar transformation for another two components of \mathbf{H}_α can be obtained:

$$\begin{aligned}
\sum_{\alpha=1}^N \frac{P(X_\alpha + \Delta X, Y_\alpha, Z_\alpha) - P(X_\alpha, Y_\alpha, Z_\alpha)}{\Delta X} V_\alpha &= \sum_{i=1}^{K_X} A_i [P(X_i^H, Y_i, Z_i) - P(X_i^L, Y_i, Z_i)] \\
\sum_{\alpha=1}^N \frac{R(X_\alpha, Y_\alpha, Z_\alpha + \Delta Z) - R(X_\alpha, Y_\alpha, Z_\alpha)}{\Delta Z} V_\alpha &= \sum_{i=1}^{K_Z} A_i [R(X_i, Y_i, Z_i^H) - R(X_i, Y_i, Z_i^L)]
\end{aligned} \tag{B.4}$$

After the summation of (B.3) and (B.4), a transformation for \mathbf{H}_α can be obtained in the following format:

$$\sum_{\alpha=1}^N \left[\frac{\Delta P_\alpha}{\Delta X} + \frac{\Delta Q_\alpha}{\Delta Y} + \frac{\Delta R_\alpha}{\Delta Z} \right] V_\alpha = \sum_{i=1}^{K_X} A_i^X [P_i^H - P_i^L] + \sum_{i=1}^{K_Y} A_i^Y [Q_i^H - Q_i^L] + \sum_{i=1}^{K_Z} A_i^Z [R_i^H - R_i^L] \tag{B.5}$$

Note that (B.5) corresponds to

$$\iiint_{\mathcal{B}_0} \left[\frac{\partial P}{\partial X} + \frac{\partial Q}{\partial Y} + \frac{\partial R}{\partial Z} \right] dX dY dZ = \iint_{\partial \mathcal{B}_0} [P dY dZ + Q dX dZ + R dX dY]$$

To complete the transformation, a discrete analog of the transition

$$\iint_{\partial \mathcal{B}_0} [P dY dZ + Q dX dZ + R dX dY] = \iint_{\partial \mathcal{B}_0} [P \cos \lambda + Q \cos \mu + R \cos \nu] dS \equiv \iint_{\partial \mathcal{B}_0} \mathbf{H} \cdot \mathbf{N} dS \quad (\text{B.6})$$

should be considered. Here, $\mathbf{N} \doteq [\cos \lambda \cos \mu \cos \nu]$ is the normal vector to the surface element dS , which is a part of $\partial \mathcal{B}_0$. In other words, a transition from the projections of such a surface element on the coordinate plane to the surface element should be found. A sufficient difference between the continuous case and the discrete case considered here is that in the continuous case, the fragmentation of $\partial \mathcal{B}_0$ is arbitrary since the function \mathbf{H} is continuous while in the discrete case, the fragmentation is caused by the prescribed positions of the discrete lattice \mathcal{C}_0 . For this reason, the numbers K_X , K_Y and K_Z are in generally different, and a transition similar to (B.6) is not possible apart from particular cases. Furthermore, for our application, it is reasonable to assume that $\partial \mathcal{B}_0$ coincides with the surface formed by surfaces of the outer cells so that the projection of the surface element on the coordinate planes is equal either to the surface element or to zero. Thus, (B.5) corresponds to the continuous Gauss theorem (B.6) in the case of the discrete lattice structure. \square

Unfortunately, the theorem in such a formulation cannot be directly applied to the derivation of the Cauchy-Born boundary conditions. The reason is that a discrete analog of Div applied on a 2^{nd} -order tensor appears in the derivation so that a discrete analog for

$$\iiint_{\mathcal{B}_0} \text{Div} \boldsymbol{\sigma} dV = \iint_{\partial \mathcal{B}_0} \boldsymbol{\sigma} \cdot \mathbf{N} dA$$

is needed, whereby $\boldsymbol{\sigma}$ denotes a 2^{nd} -order tensor in $\mathbb{R}^{2 \times 2}$ or $\mathbb{R}^{3 \times 3}$. To solve this problem, the question ‘‘how the Div operation can be understood in the discrete case?’’ should be discussed. In particular, a local equilibrium condition should be derived at the continuous micro scale for \mathbf{P}_i instead of (2.21).

The derivation is given here for the planar case. Consider a cell structure displayed in fig. B.2 and representing the continuous micro scale configuration. Cut a square area out with the edges parallel to the x and y axes, so that each edge lies within a cell ¹. The equilibrium at this area can be expressed as

$$[(\mathbf{P}_j)_{XX} - (\mathbf{P}_l)_{XX}] \Delta Y + [(\mathbf{P}_i)_{YX} - (\mathbf{P}_k)_{YX}] \Delta X = 0 \quad (\text{B.7})$$

$$[(\mathbf{P}_i)_{YY} - (\mathbf{P}_k)_{YY}] \Delta Y + [(\mathbf{P}_j)_{XY} - (\mathbf{P}_l)_{XY}] \Delta X = 0 \quad (\text{B.8})$$

Under consideration of simple transformations

$$(\mathbf{P}_l)_{XX} = (\mathbf{P}_j)_{XX} + [(\mathbf{P}_l)_{XX} - (\mathbf{P}_j)_{XX}] = (\mathbf{P}_j)_{XX} + \frac{(\mathbf{P}_l)_{XX} - (\mathbf{P}_j)_{XX}}{\Delta X} \Delta X$$

$$(\mathbf{P}_l)_{XY} = (\mathbf{P}_j)_{XY} + [(\mathbf{P}_l)_{XY} - (\mathbf{P}_j)_{XY}] = (\mathbf{P}_j)_{XY} + \frac{(\mathbf{P}_l)_{XY} - (\mathbf{P}_j)_{XY}}{\Delta X} \Delta X$$

$$(\mathbf{P}_k)_{YY} = (\mathbf{P}_i)_{YY} + [(\mathbf{P}_k)_{YY} - (\mathbf{P}_i)_{YY}] = (\mathbf{P}_i)_{YY} + \frac{(\mathbf{P}_k)_{YY} - (\mathbf{P}_i)_{YY}}{\Delta Y} \Delta Y$$

$$(\mathbf{P}_k)_{YX} = (\mathbf{P}_i)_{YX} + [(\mathbf{P}_k)_{YX} - (\mathbf{P}_i)_{YX}] = (\mathbf{P}_i)_{YX} + \frac{(\mathbf{P}_k)_{YX} - (\mathbf{P}_i)_{YX}}{\Delta Y} \Delta Y$$

¹The four neighbour cells are needed for the reason that \mathbf{P}_i is constant within the corresponding i^{th} Voronoi cell.

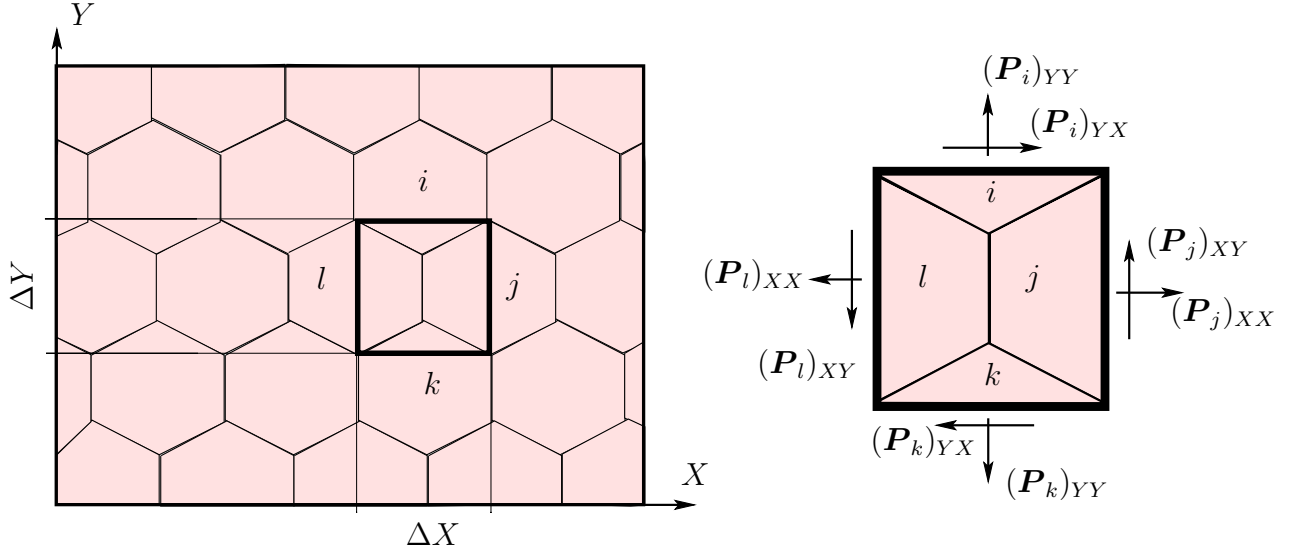


Figure B.2: The cell structure corresponding to the continuous micro scale configuration. The 1st Piola-Kirchhoff stress tensor \mathbf{P}_i is constant within a cell i . The square area lying within four neighbour cells denoted as i , j , k and l must be in equilibrium. This cut-out area with the components of the internal stress acting on the edges of the area is shown on the right-hand side.

(B.7) and (B.8) results in the desired local equilibrium conditions

$$\frac{(\mathbf{P}_j)_{XX} - (\mathbf{P}_l)_{XX}}{\Delta X} + \frac{(\mathbf{P}_i)_{YX} - (\mathbf{P}_k)_{YX}}{\Delta Y} = 0 \quad (\text{B.9})$$

$$\frac{(\mathbf{P}_j)_{XY} - (\mathbf{P}_l)_{XY}}{\Delta X} + \frac{(\mathbf{P}_i)_{YY} - (\mathbf{P}_k)_{YY}}{\Delta Y} = 0, \quad (\text{B.10})$$

which are analogous to the continuous case (2.21):

$$\begin{aligned} \frac{\partial(\mathbf{P})_{XX}}{\partial X} + \frac{\partial(\mathbf{P})_{YX}}{\partial Y} &= 0 \\ \frac{\partial(\mathbf{P})_{XY}}{\partial X} + \frac{\partial(\mathbf{P})_{YY}}{\partial Y} &= 0 \end{aligned}$$

Moreover, after the summation of the equilibrium conditions (B.9) and (B.10) stated for each four elements, only a sum over the cells at the boundary remains, see fig. B.3. This sum states the equilibrium of the whole continuous RVE and is given in (B.11) for the case shown in fig. B.3.

$$\begin{aligned} & \left[\frac{(\mathbf{P}_g)_{XX} - (\mathbf{P}_d)_{XX}}{\Delta X} + \frac{(\mathbf{P}_o)_{XX} - (\mathbf{P}_k)_{XX}}{\Delta X} + \frac{(\mathbf{P}_v)_{XX} - (\mathbf{P}_s)_{XX}}{\Delta X} \right] \\ & + \left[\frac{(\mathbf{P}_a)_{YX} - (\mathbf{P}_w)_{YX}}{\Delta Y} + \frac{(\mathbf{P}_b)_{YX} - (\mathbf{P}_x)_{YX}}{\Delta Y} + \frac{(\mathbf{P}_c)_{YX} - (\mathbf{P}_y)_{YX}}{\Delta Y} \right] = 0 \end{aligned} \quad (\text{B.11})$$

$$\begin{aligned} & \left[\frac{(\mathbf{P}_g)_{XY} - (\mathbf{P}_d)_{XY}}{\Delta X} + \frac{(\mathbf{P}_o)_{XY} - (\mathbf{P}_k)_{XY}}{\Delta X} + \frac{(\mathbf{P}_v)_{XY} - (\mathbf{P}_s)_{XY}}{\Delta X} \right] \\ & + \left[\frac{(\mathbf{P}_a)_{YY} - (\mathbf{P}_w)_{YY}}{\Delta Y} + \frac{(\mathbf{P}_b)_{YY} - (\mathbf{P}_x)_{YY}}{\Delta Y} + \frac{(\mathbf{P}_c)_{YY} - (\mathbf{P}_y)_{YY}}{\Delta Y} \right] = 0 \end{aligned}$$

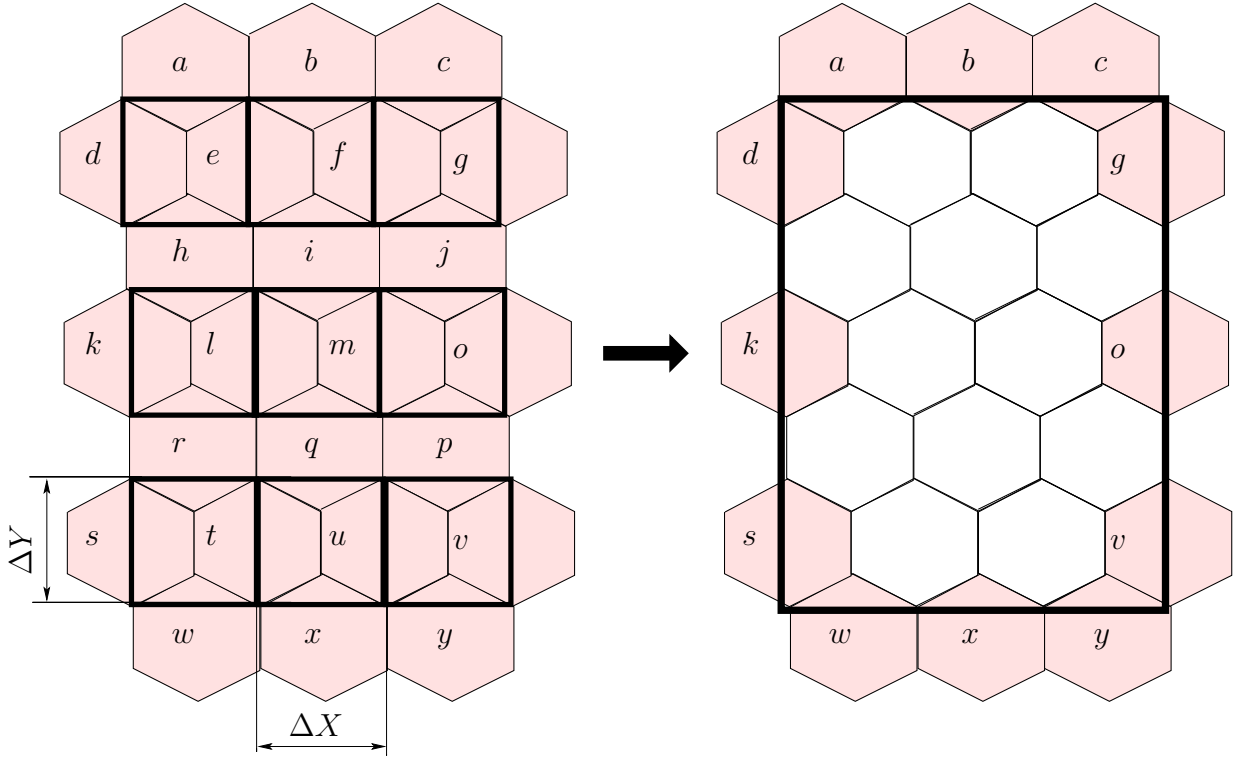


Figure B.3: A sum of the equilibrium conditions (B.9) and (B.10) stated for each of the 9 depicted square areas (on the left) can be transformed into a sum over the boundary cells of the continuous micro scale configuration (on the right).

Now, the power requirement (2.67) can be rewritten as

$$\bar{\mathbf{P}} : \dot{\bar{\mathbf{F}}} = \frac{1}{V_0} \sum_i \mathbf{P}_i : \dot{\mathbf{F}}_i V_i = \frac{1}{\rho V_0} \sum_i \sum_{j \neq i} \mathbf{P}_i : [\dot{\mathbf{r}}_{ij} \otimes \mathbf{R}_{ij}] \quad (\text{B.12})$$

under consideration of the cellwise Cauchy-Born rule (2.62). The right-hand side of (B.12) is thereby equivalent to $\frac{1}{V_0} \int_{B_0} \mathbf{P} : \text{Grad} \dot{\varphi} dV$ from (2.50). For further transformations, a discrete analog of (2.49) is needed in which the equilibrium conditions appear local in the format (B.9)-(B.10) or global as in (B.12). Then the discrete Gauss theorem can be used to obtain the sum running only over the boundary cells and, possibly, the desired result i.e. the Cauchy-Born boundary conditions for the continuous micro scale configuration. Because of the large scale of the needed operations, the proof of this proposition remains open.

Appendix C

The Non-Linear Finite Element Method

The FEM and in particular, non-linear FEM, is a well-known numerical minimisation method for a variational problem like (2.19) for an arbitrary body. This method is widely presented in a large number of books such as Zienkiewicz [97] or Wriggers [95].

General Assumptions

Within the general FEM concept, the body of interest \mathcal{B} is approximated by n_e bodies of a simple geometry, the finite elements Ω_e :

$$\mathcal{B} \approx \mathcal{B}^h = \bigcup_{e=1}^{n_e} \Omega_e \quad (\text{C.1})$$

Further approximations needed within the FEM relate to the field values such as displacements and stresses as well as to the computation of some integrals appearing during the discretisation of (2.20). Exact field values within an element are approximated by a polynomial function:

$$\mathbf{u}(\mathbf{X}) \approx \mathbf{u}^h(\mathbf{X}) = \sum_{I=1}^n N_I(\mathbf{X}) \mathbf{u}_I \quad (\text{C.2})$$

with the shape functions $N_I(\mathbf{X})$ and the unknown nodal values \mathbf{u}_I ; n denotes the number of nodes in the element. The isoparametric concept used in this work states that either the geometry or the field values are approximated by the same shape functions within an element. It is concerns, in particular, the geometry of the material and the spatial configuration of the element Ω_e :

$$\mathbf{X}_e = \sum_{I=1}^n N_I(\boldsymbol{\xi}) \mathbf{X}_I \quad (\text{C.3})$$

$$\mathbf{x}_e = \sum_{I=1}^n N_I(\boldsymbol{\xi}) \mathbf{x}_I. \quad (\text{C.4})$$

Thereby, the shape functions $N_I(\boldsymbol{\xi})$ are defined in the reference element Ω^{ref} with the unit edge length and the coordinates $\boldsymbol{\xi}$. Thus, (C.3) and (C.4) describe a unique transformation from the global to the local coordinates $\boldsymbol{\xi}$ for each element. Note that \mathbf{X}_I resp. \mathbf{x}_I are the global nodal coordinates in the material resp. spatial configuration. This isoparametric mapping for a triangular element used in

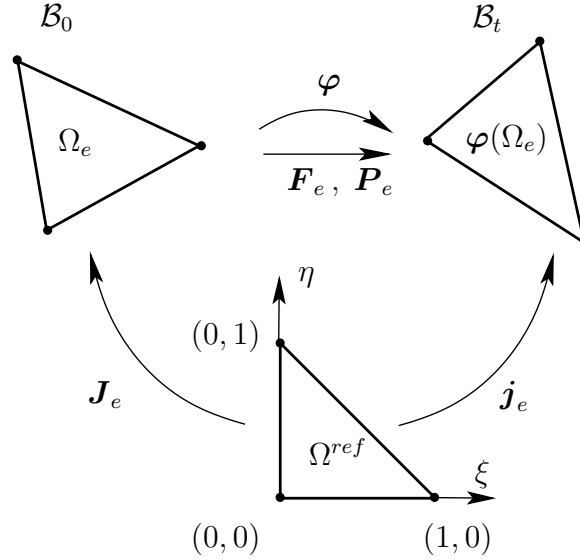


Figure C.1: The isoparametrical deformation mapping of a triangular element.

the present work is displayed in fig. C.1. \mathbf{J}_e and \mathbf{j}_e denote the Jacobi matrices of the transformations from the local to the global material and global spatial coordinates:

$$\mathbf{J}_e \doteq \nabla_{\xi} \mathbf{X}_e = \sum_{I=1}^n \mathbf{X}_I \otimes \nabla_{\xi} N_I(\boldsymbol{\xi}) \quad (\text{C.5})$$

$$\mathbf{j}_e \doteq \nabla_{\xi} \mathbf{x}_e = \sum_{I=1}^n \mathbf{x}_I \otimes \nabla_{\xi} N_I(\boldsymbol{\xi}). \quad (\text{C.6})$$

Among different possibilities, the Lagrange polynomials are often used as shape functions. Such polynomial of the order $(n - 1)$ is given in the one-dimensional case by the following expression:

$$N_I(\xi) \doteq \prod_{J \neq I} \frac{(\xi_J - \xi)}{(\xi_J - \xi_I)} \quad (\text{C.7})$$

The shape functions for a higher-order ansatz result from the product of the one-dimensional shape functions (C.7):

$$N_J(\xi, \eta) = N_I(\xi) N_K(\eta) \quad (\text{C.8})$$

Discretisation of the Weak Form of Equilibrium

The approximation of the integrals appearing in the weak formulation (2.20) can schematically be represented as

$$\int_{\mathcal{B}} (\dots) dV \approx \int_{\mathcal{B}^h} (\dots) dV^h = \bigcup_{e=1}^{n_e} \int_{\Omega_e} (\dots) d\Omega = \bigcup_{e=1}^{n_e} \int_{\Omega^{ref}} (\dots) d\Omega^{ref} \quad (\text{C.9})$$

Here, $\bigcup_{e=1}^{n_e}$ is an assembly operator, which replaces the summation over all elements. In such a representation, (2.20) can be rewritten as

$$\delta E^{int} = \bigcup_{e=1}^{n_e} \int_{\Omega_e} \mathbf{P}_e : \nabla_{X_e} \delta \boldsymbol{\varphi}_e dV = \bigcup_{e=1}^{n_e} \int_{\Omega_e} \mathbf{b}_{0e} \cdot \delta \boldsymbol{\varphi}_e dV + \bigcup_{e=1}^{n_e} \int_{\partial \Omega_e} \mathbf{t}_{0e}^P \cdot \delta \boldsymbol{\varphi}_e dA = \delta E^{ext} \quad (\text{C.10})$$

All values in this equation are defined within the element e ; $\mathbf{P}_e \doteq \partial W_{0e} / \partial \mathbf{F}_e$ denotes the 1st Piola-Kirchhoff stress tensor in the element e . To represent (C.10) in a discretised form, a discretisation of the virtual spatial placement $\delta \boldsymbol{\varphi}_e$ and of the virtual deformation gradient $\delta \mathbf{F}_e \doteq \nabla_{X_e} \delta \boldsymbol{\varphi}_e$ are needed. The virtual spatial placement can be expressed in terms of the virtual displacement $\mathbf{u}_e(\boldsymbol{\xi}) \doteq \mathbf{x}_e(\boldsymbol{\xi}) - \mathbf{X}_e(\boldsymbol{\xi})$:

$$\mathbf{x}_e(\boldsymbol{\xi}) = \sum_{I=1}^n N_I(\boldsymbol{\xi}) \mathbf{X}_I + \sum_{I=1}^n N_I(\boldsymbol{\xi}) \mathbf{u}_I \quad (\text{C.11})$$

Then

$$\delta \boldsymbol{\varphi}_e \equiv \delta \mathbf{x}_e(\boldsymbol{\xi}) = \sum_{I=1}^n N_I(\boldsymbol{\xi}) \delta \mathbf{X}_I + \sum_{I=1}^n N_I(\boldsymbol{\xi}) \delta \mathbf{u}_I = \sum_{I=1}^n N_I(\boldsymbol{\xi}) \delta \mathbf{u}_I \quad (\text{C.12})$$

since \mathbf{X}_I are the prescribed nodal positions in the material configuration and their variation cannot differ from zero. The discretised deformation gradient results from its definition (2.12) under consideration of (C.4)-(C.6):

$$\mathbf{F}_e = \nabla_{X_e} \boldsymbol{\varphi}_e = \sum_{I=1}^n \mathbf{x}_I \otimes \nabla_{X_e} N_I = \left[\sum_{I=1}^n \mathbf{x}_I \otimes \nabla_{\xi} N_I \right] \cdot \mathbf{J}_e^{-1} = \mathbf{j}_e \cdot \mathbf{J}_e^{-1} \quad (\text{C.13})$$

The variation of (C.13) immediately yields for $\delta \mathbf{F}_e$:

$$\delta \mathbf{F}_e = \nabla_{X_e} \delta \boldsymbol{\varphi}_e = \left[\sum_{I=1}^n \delta \mathbf{x}_I \otimes \nabla_{\xi} N_I \right] \cdot \mathbf{J}_e^{-1} = \left[\sum_{I=1}^n \delta \mathbf{u}_I \otimes \nabla_{\xi} N_I \right] \cdot \mathbf{J}_e^{-1} \quad (\text{C.14})$$

After substituting (C.12) and (C.14) into the left part of (C.10), the variation of the internal energy can be rewritten as

$$\begin{aligned} \delta E^{int} &= \bigcup_{e=1}^{n_e} \int_{\Omega_e} \mathbf{P}_e : \delta \mathbf{F}_e dV = \bigcup_{e=1}^{n_e} \int_{\Omega_e} \mathbf{P}_e : \left[\sum_{I=1}^n \delta \mathbf{u}_I \otimes \nabla_{X_e} N_I \right] dV \\ &= \bigcup_{e=1}^{n_e} \sum_{I=1}^n \left[\delta \mathbf{u}_I \cdot \int_{\Omega_e} \mathbf{P}_e \cdot \nabla_{X_e} N_I dV \right] \equiv \bigcup_{e=1}^{n_e} \sum_{I=1}^n [\delta \mathbf{u}_I \cdot \mathbf{F}_I^{int}] = \bigcup_{e=1}^{n_e} \delta \mathbf{u}_e \cdot \mathbf{F}_e^{int} \end{aligned} \quad (\text{C.15})$$

with the following notations:

$$\delta \mathbf{u}_e \doteq [\delta \mathbf{u}_1, \delta \mathbf{u}_2, \dots, \delta \mathbf{u}_n], \quad \mathbf{F}_e^{int} \doteq [\mathbf{F}_1^{int}, \mathbf{F}_2^{int}, \dots, \mathbf{F}_n^{int}]. \quad (\text{C.16})$$

Thereby, the internal force vector \mathbf{F}_I^{int} at the node I of the element e is given by

$$\mathbf{F}_I^{int} \doteq \int_{\Omega_e} \mathbf{P}_e \cdot \nabla_{X_e} N_I(\mathbf{X}_e) dV = \int_{\Omega^{ref}} \mathbf{P}_e \cdot [\nabla_{\xi} N_I(\boldsymbol{\xi}) \cdot \mathbf{J}_e^{-1}] \det \mathbf{J}_e d\boldsymbol{\xi} \quad (\text{C.17})$$

Note that this vector consists of two or three components for a planar or 3-dimensional case respectively.

The right part of (C.10) can be now analogously transformed to a desired format like (C.15):

$$\begin{aligned}
\delta E^{ext} &= \bigcup_{e=1}^{n_e} \int_{\Omega_e} \mathbf{b}_{0e} \cdot \delta \boldsymbol{\varphi}_e dV + \bigcup_{e=1}^{n_e} \int_{\partial\Omega_e} \mathbf{t}_{0e}^P \cdot \delta \boldsymbol{\varphi}_e dA \\
&= \bigcup_{e=1}^{n_e} \int_{\Omega_e} \mathbf{b}_{0e} \cdot \left[\sum_{I=1}^n N_I \delta \mathbf{u}_I \right] dV + \bigcup_{e=1}^{n_e} \int_{\partial\Omega_e} \mathbf{t}_{0e}^P \cdot \left[\sum_{I=1}^n N_I \delta \mathbf{u}_I \right] dA \\
&= \bigcup_{e=1}^{n_e} \sum_{I=1}^n \left[\delta \mathbf{u}_I \cdot \int_{\Omega_e} \mathbf{b}_{0e} N_I dV \right] + \bigcup_{e=1}^{n_e} \sum_{I=1}^n \left[\delta \mathbf{u}_I \cdot \int_{\partial\Omega_e} \mathbf{t}_{0e}^P N_I dA \right] \\
&\equiv \bigcup_{e=1}^{n_e} \sum_{I=1}^n [\delta \mathbf{u}_I \cdot {}^{vol} \mathbf{F}_I^{ext}] + \bigcup_{e=1}^{n_e} \sum_{I=1}^n [\delta \mathbf{u}_I \cdot {}^{surf} \mathbf{F}_I^{ext}] = \bigcup_{e=1}^{n_e} \delta \mathbf{u}_e \cdot \mathbf{F}_e^{ext}
\end{aligned} \tag{C.18}$$

with the notations similar to (C.16). The internal force vector \mathbf{F}_I^{ext} at the node I of the element e consists of the contributions of the volume forces and the surface forces acting on the part of the element surface and corresponding to the boundary conditions (2.22):

$$\mathbf{F}_I^{ext} \doteq {}^{vol} \mathbf{F}_I^{ext} + {}^{surf} \mathbf{F}_I^{ext}$$

An expression for the contribution of volume forces has a format similar to (C.17):

$${}^{vol} \mathbf{F}_I^{ext} \doteq \int_{\Omega_e} \mathbf{b}_{0e} N_I(\mathbf{X}_e) dV = \int_{\Omega_{ref}} \mathbf{b}_{0e} N_I(\boldsymbol{\xi}) \det \mathbf{J}_e d\boldsymbol{\xi} \tag{C.19}$$

Contrariwise, the contribution of the surface forces ${}^{surf} \mathbf{F}_I^{ext}$ is a surface or a curve integral for a three-dimensional or a planar case respectively:

$${}^{surf} \mathbf{F}_I^{ext} \doteq \int_{\partial\Omega_e} \mathbf{t}_{0e}^P N_I(\mathbf{X}_e) dA \tag{C.20}$$

Note that the shape functions in (C.20) are those for an element of one dimension less than the problem of interest. A transition from the global to the local element coordinates in the surface or curve integral is thereby straightforward and can be carried out by applying the corresponding Jacobi determinant. For the I th node of the element e , the ${}^{surf} \mathbf{F}_I^{ext}$ consists of a number of components equal to the dimension of the problem. But in general, a part of these components or even all of them can be zero if the corresponding degree of freedom is unloaded.

A combination of (C.15) and (C.18) yields now an expression for the discretised weak form of the equilibrium:

$$\bigcup_{e=1}^{n_e} \delta \mathbf{u}_e \cdot [\mathbf{F}_e^{int} - \mathbf{F}_e^{ext}] = 0 \tag{C.21}$$

Under application of the so-called Boole's or incidence matrices \mathbf{a}_e , a connection between the element test functions $\delta \mathbf{u}_e$ and the global test function $\delta \mathbf{u}$ with the length equal to the total number of degrees of freedom can be established:

$$\delta \mathbf{u}_e = \mathbf{a}_e \cdot \delta \mathbf{u}$$

Using this ansatz, (C.21) obtains the format:

$$\delta \mathbf{u} \cdot \left[\sum_{e=1}^{n_e} \mathbf{a}_e \cdot [\mathbf{F}_e^{int} - \mathbf{F}_e^{ext}] \right] = 0 \quad \Leftrightarrow \quad \delta \mathbf{u} \cdot [\mathbf{F}^{int} - \mathbf{F}^{ext}] = 0 \quad (\text{C.22})$$

with the global internal \mathbf{F}^{int} and external \mathbf{F}^{ext} force vectors. Under consideration that this equation must be fulfilled for an arbitrary $\delta \mathbf{u}$, a desired system of the non-linear algebraic equations can be obtained from (C.22):

$$\mathbf{R}(\mathbf{x}) \doteq \mathbf{F}^{int}(\mathbf{x}) - \mathbf{F}^{ext} = \mathbf{0}, \quad \mathbf{x} = \mathbf{X} + \mathbf{u} \quad (\text{C.23})$$

The solution of this system yields the unknown vector \mathbf{u} of the nodal displacements occurring under the action of the external load \mathbf{F}^{ext} .

Numerical Solution of a Non-Linear Systems of Equations

Among a number of different approximative solution strategies of a non-linear algebraic equation systems like (C.23), only two iterative implicit methods should be viewed in this section: the Newton-Raphson (NR) and the damped Newton methods. Whereas the first method have been used in the present work, the second one can be recommended for further development of the path-change procedure instead of the Newton-Raphson method. For a detailed discussion of another methods see e.g. Wriggers [95].

The NR method is based on the Taylor series expansion of (C.23) in the vicinity of a known state \mathbf{x}_k :

$$\mathbf{0} = \mathbf{R}(\mathbf{x}_k + \Delta \mathbf{x}) \approx \mathbf{R}(\mathbf{x}_k) + \mathbf{K}_T(\mathbf{x}_k) \cdot \Delta \mathbf{x} \quad \Rightarrow \quad \Delta \mathbf{x} = -\mathbf{K}_T^{-1}(\mathbf{x}_k) \cdot \mathbf{R}(\mathbf{x}_k) \quad (\text{C.24})$$

with the tangential stiffness matrix \mathbf{K}_T defined by

$$\mathbf{K}_T(\mathbf{x}_k) \doteq \left. \frac{\partial \mathbf{R}}{\partial \mathbf{x}} \right|_{\mathbf{x}=\mathbf{x}_k} \quad (\text{C.25})$$

Now, an algorithm for the solution of (C.23) shown in the fig. C.2 results from (C.24) An explanation of the NR method is shown in the fig. C.3 (a).

A drawback of the NR method is its local convergence. In the case depicted in fig. C.3 (b), the only starting values like x_k^1 lying within the highlighted area lead to the solution point P . The choice of another starting value such as x_k^2 would lead to another solution point or even to a divergence of the solution procedure. To overcome this problem, a damping factor $\alpha_k \in [0, 1]$ should be introduced into the expression for the new placement:

$$\mathbf{x}_{k+1} = \mathbf{x}_k + \alpha_k \Delta \mathbf{x}_{k+1} = \mathbf{x}_k - \alpha_k \mathbf{K}_T^{-1}(\mathbf{x}_k) \cdot \mathbf{R}(\mathbf{x}_k) \quad (\text{C.26})$$

To find α_k , a function

$$f(\mathbf{x}) \doteq \mathbf{R}(\mathbf{x}) \cdot \mathbf{R}(\mathbf{x})$$

should be minimised with respect to α_k . Such minimisation results in a non-linear equation

$$g(\alpha_k) \doteq \mathbf{R}(\mathbf{x}_k + \alpha_k \Delta \mathbf{x}_{k+1}) \cdot \mathbf{R}(\mathbf{x}_k + \alpha_k \Delta \mathbf{x}_{k+1}) = 0 \quad (\text{C.27})$$

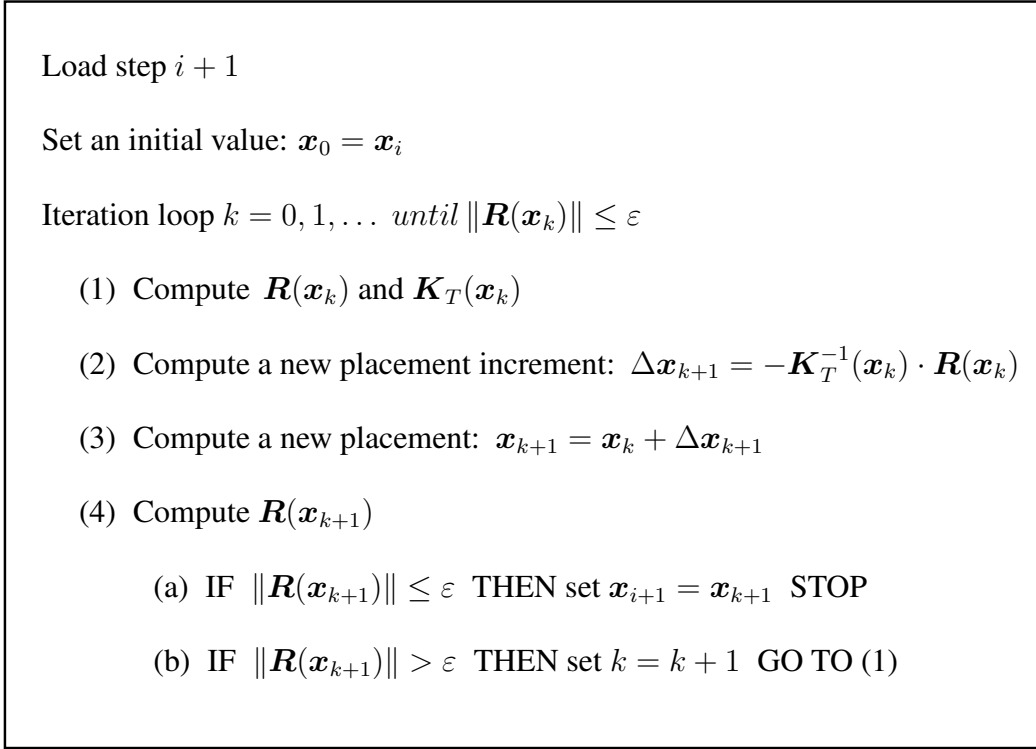


Figure C.2: The algorithm for the Newton-Raphson method.

which can be solved e.g. with the line search method, see Wriggers [95]:

$$\alpha_k^{i+1} = \alpha_k^i - g(\alpha_k^i) \left[\frac{\alpha_k^i - \alpha_k^{i-1}}{g(\alpha_k^i) - g(\alpha_k^{i-1})} \right] \quad (\text{C.28})$$

with the additional constraint

$$g(0)g(1) < 0$$

corresponding to the requirement that α_k lies between zero and one. It is thereby not necessary to find an exact solution of (C.27); the iterations (C.28) can be terminated as soon as the condition

$$|g(\alpha_k^{i+1})| \leq 0.8|g(0)| \quad (\text{C.29})$$

is fulfilled.

linearisation at the Element Level

The tangential stiffness matrix defined in (C.25) is the directional derivative of the residual force $\mathbf{R}(\mathbf{x})$ so that

$$D\mathbf{R} \doteq \frac{d}{d\varepsilon} \mathbf{R}(\mathbf{x} + \varepsilon\Delta\mathbf{x})|_{\varepsilon=0} = \mathbf{K}_T \cdot \Delta\mathbf{x} = D\mathbf{F}^{int} \quad (\text{C.30})$$

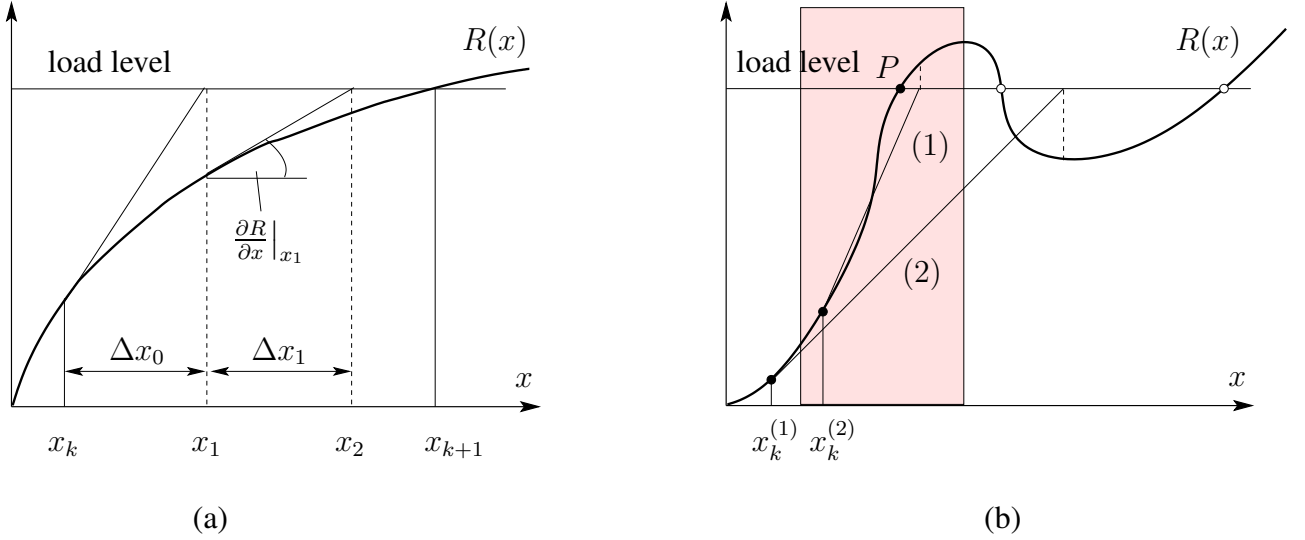


Figure C.3: (Wriggers [95]) (a) An explanation of the one-dimensional Newton-Raphson method; (b) the region of the convergence of the Newton-Raphson method.

if the external force \mathbf{F}^{ext} is independent of the deformation. On the other hand, $D\mathbf{F}^{int}$ can be represented in terms of the element stiffness matrices defined below. Indeed, under consideration of (C.16) and (C.22), the directional derivative of the internal force vector takes the format:

$$D\mathbf{F}^{int} = \sum_{e=1}^{n_e} \mathbf{a}_e \cdot D\mathbf{F}_e^{int} = \sum_{e=1}^{n_e} \mathbf{a}_e \cdot [D\mathbf{F}_1^{int} \quad D\mathbf{F}_2^{int} \quad \dots \quad D\mathbf{F}_n^{int}] \quad (\text{C.31})$$

Thus, the global linearisation (C.24) is now expressed in terms of the linearisation of \mathbf{F}_I^{int} at the element level. To obtain $D\mathbf{F}_I^{int}$, the definition (C.17) of the nodal internal force should be used:

$$D\mathbf{F}_I^{int} = \int_{\Omega_e} D\mathbf{P}_e \cdot \nabla_{X_e} N_I(\mathbf{X}_e) dV = \int_{\Omega_e} [\mathbb{L}_e : D\mathbf{F}_e] \cdot \nabla_{X_e} N_I(\mathbf{X}_e) dV \quad (\text{C.32})$$

with the 4th-order tangent operator $\mathbb{L}_e \doteq \frac{\partial \mathbf{P}_e}{\partial \mathbf{F}_e}$ introduced in (2.23). For the *Gâteaux* derivative $D\mathbf{F}_e$ of the discretised deformation gradient \mathbf{F}_e it follows from (C.13) that

$$D\mathbf{F}_e \doteq \sum_{J=1}^n \frac{d}{d\varepsilon} [\mathbf{x}_J + \varepsilon \Delta \mathbf{x}_J]_{\varepsilon=0} \otimes \nabla_{X_e} N_I = \sum_{J=1}^n \Delta \mathbf{x}_J \otimes \nabla_{X_e} N_J \quad (\text{C.33})$$

After application of this ansatz, (C.32) can be rewritten as

$$\begin{aligned} D\mathbf{F}_I^{int} &= \int_{\Omega_e} \left[\mathbb{L}_e : \left[\sum_{J=1}^n \Delta \mathbf{x}_J \otimes \nabla_{X_e} N_J \right] \right] \cdot \nabla_{X_e} N_I dV \\ &= \sum_{J=1}^n \int_{\Omega_e} [\mathbb{L}_e : [\Delta \mathbf{x}_J \otimes \nabla_{X_e} N_J]] \cdot \nabla_{X_e} N_I dV \\ &= \sum_{J=1}^n \left[\int_{\Omega_e} \mathbb{L}_e \cdot [\nabla_{X_e} N_I \otimes \nabla_{X_e} N_J] dV \right] \cdot \Delta \mathbf{x}_J \equiv \sum_{J=1}^n \mathbf{K}_{TIJ}^e \cdot \Delta \mathbf{x}_J \end{aligned} \quad (\text{C.34})$$

with the contribution of the nodes I and J to the tangential stiffness matrix ¹:

$$\mathbf{K}_{TIJ}^e \doteq \int_{\Omega_e} \mathbb{L}_e \overline{\cdot} [\nabla_{X_e} N_I \otimes \nabla_{X_e} N_J] dV = \int_{\Omega^{ref}} \mathbb{L}_e \overline{\cdot} [\nabla_{\xi} N_I \otimes \nabla_{\xi} N_J] \overline{\cdot} [\mathbf{J}_e^{-1} \otimes \mathbf{J}_e^{-1}] \det \mathbf{J}_e d\xi \quad (\text{C.35})$$

The transformation (C.31) can now be continued under consideration of (C.34):

$$\begin{aligned} D\mathbf{F}^{int} &= \sum_{e=1}^{n_e} \mathbf{a}_e \cdot \left[\sum_{J=1}^n \mathbf{K}_{T1J}^e \cdot \Delta \mathbf{x}_J \quad \sum_{J=1}^n \mathbf{K}_{T2J}^e \cdot \Delta \mathbf{x}_J \quad \dots \quad \sum_{J=1}^n \mathbf{K}_{TnJ}^e \cdot \Delta \mathbf{x}_J \right] \\ &= \sum_{e=1}^{n_e} \mathbf{a}_e \cdot \mathbf{K}_T^e \cdot \Delta \mathbf{x}_e = \left[\sum_{e=1}^{n_e} \mathbf{a}_e \cdot \mathbf{K}_T^e \cdot \mathbf{a}_e \right] \cdot \Delta \mathbf{x} = \mathbf{K}_T \cdot \Delta \mathbf{x} \end{aligned} \quad (\text{C.36})$$

Here, the following representation has been used:

$$\Delta \mathbf{x}_e = \mathbf{a}_e \cdot \Delta \mathbf{x}.$$

A comparison of (C.36) with (C.30) yields an expression for the tangential stiffness matrix \mathbf{K}_T :

$$\mathbf{K}_T = \sum_{e=1}^{n_e} \mathbf{a}_e \cdot \mathbf{K}_T^e \cdot \mathbf{a}_e. \quad (\text{C.37})$$

The element stiffness matrix \mathbf{K}_T^e consists thereby of the nodal contributions \mathbf{K}_{TIJ}^e :

$$\mathbf{K}_T^e \doteq \begin{bmatrix} \mathbf{K}_{T11}^e & \mathbf{K}_{T12}^e & \dots & \mathbf{K}_{T1n}^e \\ \mathbf{K}_{T21}^e & \mathbf{K}_{T22}^e & \dots & \mathbf{K}_{T2n}^e \\ \vdots & \vdots & & \vdots \\ \mathbf{K}_{Tn1}^e & \mathbf{K}_{Tn2}^e & \dots & \mathbf{K}_{Tnn}^e \end{bmatrix} \quad (\text{C.38})$$

Note that the format (C.35) is related to the mixed representation when the two-point tensors \mathbf{P} and \mathbb{L} are used. \mathbf{S} and \mathbb{C} or $\boldsymbol{\tau}$ and \mathbb{E}_2 , which are defined in section 2.2 should be used instead of \mathbf{P} and \mathbb{L} in the case of a material or a spatial representation respectively. It can be shown (see e.g. Miehe [57]) that the element stiffness matrix in the material representation takes the format

$$\begin{aligned} {}^{mat} \mathbf{K}_{TIJ}^e &\doteq \int_{\Omega_e} [[\nabla_{X_e} N_I \cdot \mathbf{S} \cdot \nabla_{X_e} N_J] \mathbf{I} + [\mathbf{F} \otimes \nabla_{X_e} N_I] : \mathbb{C} : [\nabla_{X_e} N_J \otimes \mathbf{F}^t]] dV \\ &= \int_{\Omega^{ref}} [[\nabla_{\xi} N_I \cdot [\mathbf{J}^{-1} \cdot \mathbf{S} \cdot \mathbf{J}^{-t}] \cdot \nabla_{\xi} N_J] \mathbf{I} \\ &\quad + [\mathbf{F} \otimes \nabla_{\xi} N_I] : [[\mathbf{I} \overline{\otimes} \mathbf{J}^{-1}] : \mathbb{C} : [\mathbf{J}^{-t} \overline{\otimes} \mathbf{I}]] : [\nabla_{\xi} N_J \otimes \mathbf{F}^t]] \det \mathbf{J} d\xi \end{aligned} \quad (\text{C.39})$$

To obtain the spatial element stiffness matrix, the push-forward operation with respect to ${}^{mat} \mathbf{K}_{TIJ}^e$ should be carried out. This could be done by using of the transformation (2.29) and the representation

$$\mathbf{S} = \mathbf{F}^{-1} \cdot \boldsymbol{\tau} \mathbf{F}^{-t}.$$

¹The non-standard double contraction $\overline{\cdot}$ emerging in (C.34) is introduced in chapter 4

An application of this transformation leads to the following format of ${}^{sp}\mathbf{K}_{TIJ}^e$:

$$\begin{aligned}
{}^{sp}\mathbf{K}_{TIJ}^e &= p.f. \left({}^{mat}\mathbf{K}_{TIJ}^e \right) \doteq \int_{\varphi(\Omega_e)} \left[[\nabla_{x_e} N_I \cdot \boldsymbol{\tau} \cdot \nabla_{x_e} N_J] \mathbf{I} + [\mathbf{I} \otimes \nabla_{x_e} N_I] : \mathbb{E}_2 : [\nabla_{x_e} N_J \otimes \mathbf{I}] \right] dv \\
&= \int_{\Omega^{ref}} \left[[\nabla_{\xi} N_I \cdot [\mathbf{j}^{-1} \cdot \boldsymbol{\tau} \cdot \mathbf{j}^{-t}] \cdot \nabla_{\xi} N_J] \mathbf{I} \right. \\
&\quad \left. + [\mathbf{I} \otimes \nabla_{\xi} N_I] : [[\mathbf{I} \overline{\otimes} \mathbf{j}^{-1}] : \mathbb{E}_2 : [\mathbf{j}^{-t} \overline{\otimes} \mathbf{I}]] : [\nabla_{\xi} N_J \otimes \mathbf{I}] \right] \det \mathbf{j} d\xi
\end{aligned} \tag{C.40}$$

Depending on the representation (material, mixed or spatial), the corresponding tangent operator and the element stiffness matrix should be used.

Numerical Integration (Gauss Quadrature)

There is often no possibility to obtain the integrals in (C.17), (C.19), (C.20) and (C.35) in an analytical form. Due to this, a numerical integration becomes essential in the FEM. In this work, the Gauss quadrature has been used. According to this method, an integral of a function $P(\xi)$ is replaced by a sum of the weighting factors w_i multiplied by the function evaluated at a set of extra chosen sampling points ξ_i . For a one-dimensional case, the Gauss quadrature is given by

$$\int_{-1}^{+1} P(\xi) d\xi = \sum_{i=1}^n w_i P(\xi_i). \tag{C.41}$$

The weighting factors and the sampling points result from the requirement that a polynomial expression of degree $(2n-1)$ should be exactly integrated by (C.41). This requirement leads to the following system of $2n$ equations with $2n$ unknowns w_i and ξ_i :

$$\begin{cases} \sum_{i=1}^n w_i \xi_i^\alpha = \frac{2}{\alpha+1} & \text{for } \alpha = 0, 2, 4, \dots, 2n-2 \\ \sum_{i=1}^n w_i \xi_i^\alpha = 0 & \text{for } \alpha = 1, 3, 5, \dots, 2n-1 \end{cases} \tag{C.42}$$

An Isoparametric Triangular Element

A description of a simple isoparametric two-dimensional triangular element with three nodes used in present work should be given here. Such an element in the local coordinates $\boldsymbol{\xi}$ and the global coordinates \mathbf{X} is shown in fig. C.4. For a linear approximation ansatz, the shape functions are given by

$$\begin{aligned}
N_1(\xi, \eta) &= 1 - \xi - \eta \\
N_2(\xi, \eta) &= \xi \\
N_3(\xi, \eta) &= \eta
\end{aligned} \tag{C.43}$$

Thereby, a numbering of nodes must be taken into account; otherwise the Jacobi determinant $\det \mathbf{J}_e$ becomes negative. The coordinate transformation (C.3) thereby obtains the format

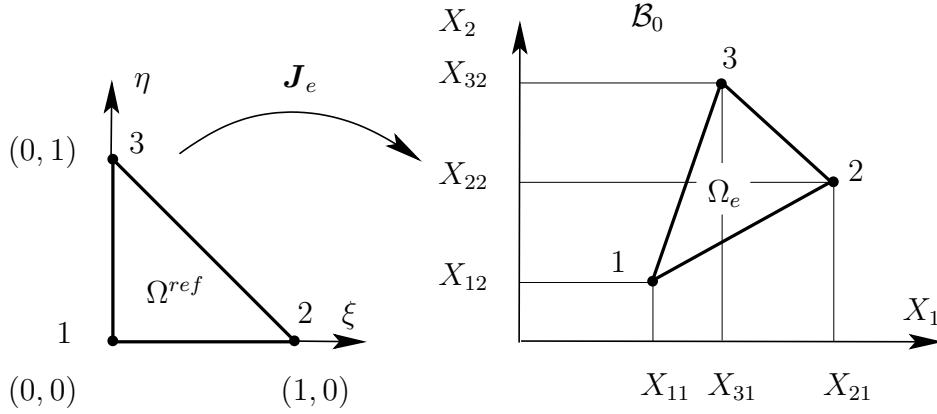


Figure C.4: Triangular three-nodes element.

$$\mathbf{X}_e(\boldsymbol{\xi}) = \mathbf{N}(\boldsymbol{\xi}) \mathbf{X}_e^{node} \quad (\text{C.44})$$

with the matrix

$$\mathbf{N} \doteq \begin{pmatrix} 1 - \xi - \eta & 0 & \xi & 0 & \eta & 0 \\ 0 & 1 - \xi - \eta & 0 & \xi & 0 & \eta \end{pmatrix}$$

and the vector \mathbf{X}_e^{node} of the nodal coordinates:

$$(\mathbf{X}_e^{node})^t \doteq (X_{11} \ X_{12} \ X_{21} \ X_{22} \ X_{31} \ X_{32}) .$$

All derivatives of the shape functions (C.43) are constant within an element and consequently, the deformation gradient \mathbf{F}_e given by (C.13) is also constant within an element since the Jacobi matrix C.5) remains constant:

$$\mathbf{J}_e = \begin{pmatrix} X_{21} - X_{11} & X_{31} - X_{11} \\ X_{22} - X_{12} & X_{32} - X_{12} \end{pmatrix} \quad (\text{C.45})$$

This immediately leads to the constant Jacobi determinant

$$\det \mathbf{J}_e = (X_{21} - X_{11})(X_{32} - X_{12}) - (X_{31} - X_{11})(X_{22} - X_{12}) = 2 A_e \quad (\text{C.46})$$

with the area A_e of the element.

The Gauss quadrature for a general triangular element has the following format:

$$\begin{aligned} \int_{\Omega_e} \mathbf{P}(\mathbf{X}) dV &= \int_{\Omega^{ref}} \mathbf{P}(\boldsymbol{\xi}) \det \mathbf{J}_e d\boldsymbol{\xi} = \int_0^1 \int_0^{1-\xi} \mathbf{P}(\xi, \eta) \det \mathbf{J}_e d\xi d\eta \\ &\approx \sum_{i=1}^n \mathbf{P}(\xi_i, \eta_i) \det \mathbf{J}_e(\xi_i, \eta_i) w_i \end{aligned} \quad (\text{C.47})$$

For the element considered here, the number n of the quadrature points per element is equal to one. Thereby, the sampling point $\xi_1 = (\xi_1 \ \eta_1)$ as well as the weighting factor w_1 are

$$\xi_1 = \eta_1 = 1/3, \quad w_1 = 1/2$$

Thus, the Gauss quadrature get a simple format for the three-nodes triangle element:

$$\int_{\Omega_e} \mathbf{P}(\mathbf{X}) dV = \int_{\Omega^{ref}} \mathbf{P}(\boldsymbol{\xi}) \det \mathbf{J}_e d\boldsymbol{\xi} \approx \frac{1}{2} \mathbf{P}(1/3, 1/3) \det \mathbf{J}_e \quad (\text{C.48})$$

Appendix D

The Frame Indifference of $W(\mathbf{F})$

In this section, the derivation of (3.10) is reviewed. This derivation is based on the properties (3.8) and (3.9) as well as on the well-known property of the matrix:

$$(\mathbf{A} \cdot \mathbf{B})^t = \mathbf{B}^t \cdot \mathbf{A}^t \quad (\text{D.1})$$

for $\mathbf{A}, \mathbf{B} \in \mathbb{R}^{n \times n}$. According to (3.9)

$$W(\mathbf{Q} \cdot \mathbf{F} \cdot \mathbf{H}) = \Phi(\mathbf{A}^t \cdot [\mathbf{Q} \cdot \mathbf{F} \cdot \mathbf{H}]^t \cdot [\mathbf{Q} \cdot \mathbf{F} \cdot \mathbf{H}] \cdot \mathbf{A}) \quad (\text{D.2})$$

Using (D.1) and the orthogonality of $\mathbf{Q} : \mathbf{Q}^t \cdot \mathbf{Q} = \mathbf{I}$, we obtain:

$$\begin{aligned} \Phi(\mathbf{A}^t \cdot [\mathbf{Q} \cdot \mathbf{F} \cdot \mathbf{H}]^t \cdot [\mathbf{Q} \cdot \mathbf{F} \cdot \mathbf{H}] \cdot \mathbf{A}) &= \Phi(\mathbf{A}^t \cdot \mathbf{H}^t \cdot \mathbf{F}^t \cdot [\mathbf{Q}^t \cdot \mathbf{Q}] \cdot \mathbf{F} \cdot \mathbf{H} \cdot \mathbf{A}) \\ &= \Phi(\mathbf{A}^t \cdot \mathbf{H}^t \cdot \mathbf{F}^t \cdot \mathbf{F} \cdot \mathbf{H} \cdot \mathbf{A}) \end{aligned} \quad (\text{D.3})$$

Recall that $\mathbf{H} \in \mathbf{A} \cdot [GL(\mathbb{Z}^3)] \cdot \mathbf{A}^{-1}$ and can be represented as $\mathbf{A} \cdot \mathbf{M} \cdot \mathbf{A}^{-1}$ with $\mathbf{M} \in GL(\mathbb{Z}^3)$. Then (D.3) leads to the desired result by using (D.1), (3.8), (3.9) and the ansatz for \mathbf{H} :

$$\begin{aligned} \Phi(\mathbf{A}^t \cdot \mathbf{H}^t \cdot \mathbf{F}^t \cdot \mathbf{F} \cdot \mathbf{H} \cdot \mathbf{A}) &= \Phi([\mathbf{A}^t \cdot \mathbf{A}^{-t}] \cdot \mathbf{M}^t \cdot \mathbf{A}^t \cdot \mathbf{F}^t \cdot \mathbf{F} \cdot \mathbf{A} \cdot \mathbf{M} \cdot [\mathbf{A}^{-1} \cdot \mathbf{A}]) \\ &= \Phi(\mathbf{M}^t \cdot \mathbf{A}^t \cdot \mathbf{F}^t \cdot \mathbf{F} \cdot \mathbf{A} \cdot \mathbf{M}) = \Phi(\mathbf{A}^t \cdot \mathbf{F}^t \cdot \mathbf{F} \cdot \mathbf{A}) = W(\mathbf{F}) \end{aligned} \quad (\text{D.4})$$

So that $W(\mathbf{Q} \cdot \mathbf{F} \cdot \mathbf{H}) = W(\mathbf{F})$ as stated in (3.10)

Appendix E

Derivation of the Higher-Order Equilibrium and Boundary Conditions

Now we provide the main steps of the derivation of the higher-order equilibrium and boundary conditions (5.5)-(5.7). Firstly, eq. (5.2) is partially integrated (the 2nd term two times):

$$\begin{aligned}
 \delta E^{int} &= \int_{\mathcal{B}_0} \mathbf{P} : \delta \mathbf{F} + \mathbf{Q} : \delta \mathbf{G} \, dV \\
 &= \int_{\mathcal{B}_0} \text{Div}(\delta \boldsymbol{\varphi} \cdot \mathbf{P}) \, dV - \int_{\mathcal{B}_0} \delta \boldsymbol{\varphi} \cdot \text{Div} \mathbf{P} \, dV \\
 &+ \int_{\mathcal{B}_0} \text{Div}(\delta \mathbf{F} : \mathbf{Q}) \, dV - \int_{\mathcal{B}_0} \delta \mathbf{F} : \text{Div} \mathbf{Q} \, dV \\
 &= \int_{\mathcal{B}_0} \text{Div}(\delta \boldsymbol{\varphi} \cdot \mathbf{P}) \, dV - \int_{\mathcal{B}_0} \delta \boldsymbol{\varphi} \cdot \text{Div} \mathbf{P} \, dV \\
 &+ \int_{\mathcal{B}_0} \text{Div}(\delta \mathbf{F} : \mathbf{Q}) \, dV - \int_{\mathcal{B}_0} \text{Div}(\delta \boldsymbol{\varphi} \cdot \text{Div} \mathbf{Q}) \, dV + \int_{\mathcal{B}_0} \delta \boldsymbol{\varphi} \cdot \text{Div}(\text{Div} \mathbf{Q}) \, dV
 \end{aligned} \tag{E.1}$$

After application of the Gauss theorem on the 1st, 3rd and 4th terms of the last expression and grouping of corresponding terms, we obtain:

$$\begin{aligned}
 \delta E^{int} &= \int_{\mathcal{B}_0} \delta \boldsymbol{\varphi} \cdot \text{Div}[\text{Div} \mathbf{Q} - \mathbf{P}] \, dV + \int_{\partial \mathcal{B}_0} \delta \boldsymbol{\varphi} \cdot [\mathbf{P} - \text{Div} \mathbf{Q}] \cdot \mathbf{N} \, dA \\
 &+ \int_{\partial \mathcal{B}_0} \delta \mathbf{F} : [\mathbf{Q} \cdot \mathbf{N}] \, dA
 \end{aligned} \tag{E.2}$$

The 1st and 2nd terms of (E.2) contribute to (5.6) and (5.5) respectively. The variation of $\mathbf{F} = \nabla_X \boldsymbol{\varphi}$ in the 3rd term is not independent of the variation of $\boldsymbol{\varphi}$ on $\partial \mathcal{B}_0$ because if $\delta \boldsymbol{\varphi}$ is known on $\partial \mathcal{B}_0$, so is the surface gradient of $\delta \boldsymbol{\varphi}$, see Mindlin [60]. Therefore, this term cannot directly contribute to the boundary conditions and should be further transformed.

Here, the above mentioned material gradient decomposition into normal and tangential parts is used

and we obtain:

$$\begin{aligned} & \int_{\partial\mathcal{B}_0} \nabla_X \delta\varphi : [\mathbf{Q} \cdot \mathbf{N}] dA \\ &= \int_{\partial\mathcal{B}_0} \nabla_N \delta\varphi \cdot [\mathbf{Q} : [\mathbf{N} \otimes \mathbf{N}]] dA + \int_{\partial\mathcal{B}_0} \nabla_X^T \delta\varphi : [\mathbf{Q} \cdot \mathbf{N}] dA \end{aligned} \quad (\text{E.3})$$

The 1st term contains independent variations $\nabla_N \delta\varphi$ and results in (5.7). The 2nd term should be partially integrated:

$$\begin{aligned} & \int_{\partial\mathcal{B}_0} \nabla_X^T \delta\varphi : [\mathbf{Q} \cdot \mathbf{N}] dA \equiv \int_{\partial\mathcal{B}_0} [\nabla_X \delta\varphi \cdot \mathbf{T}] : [\mathbf{Q} \cdot \mathbf{N}] dA \\ &= \int_{\partial\mathcal{B}_0} \nabla_X (\delta\varphi \cdot [\mathbf{Q} \cdot \mathbf{N}]) : \mathbf{T} dA - \int_{\partial\mathcal{B}_0} \delta\varphi \cdot \nabla_X (\mathbf{Q} \cdot \mathbf{N}) : \mathbf{T} dA \end{aligned} \quad (\text{E.4})$$

with $\mathbf{T} \doteq [\mathbf{I} - \mathbf{N} \otimes \mathbf{N}]$. Now, the 1st term of the last expression of (E.4) can be transformed according to the so-called surface divergence theorem stemming essentially from the well-known Stokes theorem for the closed surface $\partial\mathcal{B}_0$, see Brand [15]:

$$\int_{\partial\mathcal{B}_0} (\nabla_X \mathbf{v} : \mathbf{T} + K \mathbf{v} \cdot \mathbf{N}) dA = 0, \quad (\text{E.5})$$

whereby $K \doteq -\nabla_X \mathbf{N} : \mathbf{T} = -\nabla_X^T \mathbf{N} : \mathbf{I}$ is the mean curvature of the surface $\partial\mathcal{B}_0$ and \mathbf{v} is a vector. Application of this transformation leads to the final format of the 2nd integral in (E.3):

$$\begin{aligned} & \int_{\partial\mathcal{B}_0} \nabla_X^T \delta\varphi : [\mathbf{Q} \cdot \mathbf{N}] dA \\ &= - \int_{\partial\mathcal{B}_0} K [\delta\varphi \cdot [\mathbf{Q} \cdot \mathbf{N}]] \cdot \mathbf{N} dA - \int_{\partial\mathcal{B}_0} \delta\varphi \cdot \nabla_X (\mathbf{Q} \cdot \mathbf{N}) : \mathbf{T} dA \\ &= - \int_{\partial\mathcal{B}_0} \delta\varphi \cdot [K \mathbf{Q} : [\mathbf{N} \otimes \mathbf{N}] + \nabla_X^T (\mathbf{Q} \cdot \mathbf{N}) : \mathbf{I}] dA \\ &\equiv \int_{\partial\mathcal{B}_0} \delta\varphi \cdot \mathfrak{L}(\mathbf{Q} \cdot \mathbf{N}) dA \end{aligned} \quad (\text{E.6})$$

Here, the differential operator \mathfrak{L} is defined as

$$\mathfrak{L}(\bullet) \doteq -K(\bullet) \cdot \mathbf{N} - \nabla_X^T(\bullet) : \mathbf{I} \quad (\text{E.7})$$

With the ansatz (E.6) and considering (E.3), the variation of the total energy (E.2) results in

$$\begin{aligned} \delta E^{tot} &= \int_{\mathcal{B}_0} \delta\varphi \cdot \text{Div} [\text{Div} \mathbf{Q} - \mathbf{P}] dV \\ &+ \int_{\partial\mathcal{B}_0} \delta\varphi \cdot [[\mathbf{P} - \text{Div} \mathbf{Q}] \cdot \mathbf{N} + \mathfrak{L}(\mathbf{Q} \cdot \mathbf{N})] dA \\ &+ \int_{\partial\mathcal{B}_0} \nabla_N \delta\varphi \cdot [\mathbf{Q} : [\mathbf{N} \otimes \mathbf{N}]] dA + \delta E^{ext} = 0 \end{aligned} \quad (\text{E.8})$$

Each integrand in this expression contains only independent variations so that the equilibrium and boundary conditions can therefore be written in the format (5.5)-(5.7).

Bibliography

- [1] M. P. Allen and D. J. Tildesley. *Computer Simulation of Liquids*. Oxford University Press, 1987.
- [2] M. Arroyo and T. Belytschko. An atomistic-based finite deformation membrane for single crystalline films. *Journal of the Mechanics and Physics of Solids*, 50:1941–1977, 2002.
- [3] J. M. Ball. Convexity conditions and existence theorems in nonlinear elasticity. *Arch. Ration. Mech. Anal.*, 63:337–403, 1977.
- [4] M. I. Baskes. Application of the embedded-atom method to covalent materials: a semiempirical potential for silicon. *Physical Review*, B29:6443, 1984.
- [5] M. I. Baskes. Modified embedded-atom potentials for cubic materials and impurities. *Physical Review*, B46:2727, 1992.
- [6] M. I. Baskes. Determination of modified embedded-atom method parameters for nickel. *Materials Chemistry and Physics*, 50:152–158, 1997.
- [7] M. I. Baskes and M. S. Daw. Semiempirical, quantum mechanical calculation of hydrogen embrittlement in metals. *Phys. Rev. Lett.*, 50:1285, 1983.
- [8] M. I. Baskes and M. S. Daw. Embedded atom method: derivation and application to impurities, surfaces and other defects in metals. *Phys. Rev.*, B29:6443, 1984.
- [9] M. I. Baskes and R. A. Jonson. Modified embedded-atom method for hcp metals. *Modelling Simul. Mater. Sci. Eng.*, 2:505–518, 1994.
- [10] M. I. Baskes, J. S. Nelson, and A. F. Wright. Semiempirical modified embedded-atom potentials for silicon and germanium. *Physical Review*, B40:6085, 1989.
- [11] F. Bloch. über die quantenmechanik der elektronen in kristallgittern. *Zeitschrift für Physik*, 52:555–600, 1929.
- [12] D. I. Blochinzew. *Grundlagen der Quantenmechanik*. Harri Deutsch, 1988.
- [13] M. Born. *Dynamik der Kristallgitter*. Teubner, 1915.
- [14] M. Born and K. Huang. *Dynamical theory of crystal lattices*. Oxford, Clarendon Press, 1954.
- [15] L. Brand. *Vector and Tensor Anylysis*. New York, Wiley, 1957.

- [16] A. L. Cauchy. De la pression ou tension dans un système de points matériels. *Exercices De Mathematiques*, 1828. Available in Cauchy, Augustin Louis Oeuvres Complètes, Tome 20, 253-277.
- [17] A. L. Cauchy. Sur l'équilibre et le mouvement d'un système de points matériels sollicités par des forces d'attraction ou de répulsion ou de répulsion mutuelle. *Exercices De Mathematiques*, 1828. Available in Cauchy, Augustin Louis Oeuvres Complètes, Tome 20, 227-252.
- [18] A. L. Cauchy. Sur l'équilibre et le mouvement intérieur des corps considérés comme des masses continues. *Exercices De Mathematiques*, 1829. Available in Cauchy, Augustin Louis Oeuvres Complètes, Tome 21, 162-173.
- [19] A. L. Cauchy. Sur les équations différentielles d'équilibre ou de mouvement pour un système de points matériels sollicités par de forces d'attraction ou de répulsion mutuelle. *Exercices De Mathematiques*, 1829. Available in Cauchy, Augustin Louis Oeuvres Complètes, Tome 21, 162-173.
- [20] M. Chipot and D. Kinderlehrer. Equilibrium configurations in crystals. *Arch. Ration. Mech. Anal.*, 103:237–277, 1988.
- [21] B. Dacorogna. *Weak Continuity and Weak Lower Semicontinuity of Non-Linear Functionals*. Springer Verlag, 1982.
- [22] B. Dacorogna. *Direct Methods in the Calculus of Variations*. Springer Verlag, 1989.
- [23] B. Dacorogna. *Implicit partial differential equations*. Boston: Birkhaeuser, 1999.
- [24] P. Ehrenfest. *Zeitschrift für Physik*, 45:455, 1927.
- [25] F. Ercolessi, M. Parrinello, and E. Tosatti. *Philos. Mag. A*, 58:213, 1988.
- [26] J. L. Ericksen. Some phase transitions in crystals. *Arch. Ration. Mech. Anal.*, 73:99–124, 1980.
- [27] J. L. Ericksen. *Phase Transformations and Material Instabilities in Solids*. Academic Press, 1984.
- [28] J. L. Ericksen. *Twinning of crystals*. Springer, 1987.
- [29] M. W. Finnis and J. E. Sinclair. *Philos. Mag. A*, 50:45, 1984.
- [30] N. A. Fleck and J. W. Hutchinson. Strain gradient plasticity. *Advances in Applied Mechanics*, 33, 1996.
- [31] S. M. Foiles, M. I. Baskes, and M. S. Daw. Embedded-atom-method functions for the fcc metals cu, ag, au, ni, pd, pt, and their alloys. *Phys. Rev. B*, 33:7983–7991, 1986.
- [32] I. Fonseca. Variational methods for elastic crystals. *Arch. Ration. Mech. Appl.*, 97:175–195, 1987.
- [33] G. Friesecke and F. Theil. Convexity conditions and existence theorems in nonlinear elasticity. *J. Nonlinear Sci.*, 12:445–478, 2002.

- [34] H. Gao, Y. Huang, and F. F. Abraham. Continuum and atomistic studies of intersonic crack propagation. *Journal of the Mechanics and Physics of Solids*, 49:2113–2132, 2001.
- [35] M. G. D. Geers, V. Kouznetsova, and W. A. M. Brekelmans. Gradient-enhanced computational homogenization for the micro-macro scale transition. *Journal de Physique IV*, 11:145–152, 2001.
- [36] W. Heitler and F. London. Wechselwirkung neutraler atome und homöopolare bindung nach der quantenmechanik. *Zeitschrift für Physik*, 44:455–472, 1927.
- [37] F. Herman and S. Skillman. *Atomic Structure Calculations*. Prentice-Hall, Inc., Englewood Cliffs, New Jersey, 1963.
- [38] R. Hill. A general theory of uniqueness and stability in elastic-plastic solids. *J. Mech. Phys. Solids*, 6:236–249, 1958.
- [39] P. Hohenberg and W. Kohn. Inhomogeneous electron gas. *Physical Review 3B*, 136:864–871, 1964.
- [40] N. Huber. *Zur Bestimmung von mechanischen Eigenschaften mit dem Eindruckversuch*. PhD thesis, Forschungszentrum Karlsruhe GmbH, 1996.
- [41] J. N. Israelachvili. *Intermolecular and Surface Forces*. Academic Press, 1995.
- [42] K. W. Jacobsen, J. K. Nørskov, and M. J. Puska. *Phys. Rev. B*, 35:7423, 1987.
- [43] P. Klein, J. W. Foulk, E. P. Chen, S. A. Wimmer, and H. Gao. Physics-based modeling of brittle fracture: cohesive formulation and the application of meshfree methods. *Theoretical and Applied Fracture Mechanics*, 37:99–166, 2001.
- [44] P. Klein and H. Gao. Crack nucleation and growth as strain localization in a virtual bond continuum. *Engineering Fracture Mechanics*, 61:21–48, 1998.
- [45] S. Kohlhoff, P. Gumbsch, and H. F. Fischmeister. Crack propagation in b.c.c. crystals studied with a combined finite-element and atomistic model. *Philosophical Magazine A*, 64:851–878, 1991.
- [46] V. Kouznetsova, M. G. D. Geers, and W. A. M. Brekelmans. Multi-scale constitutive modelling of heterogeneous materials with a gradient-enhanced computational homogenization scheme. *Int. J. Numer. Meth. Engng.*, 54(8):1235–1260, 2002.
- [47] M. Lambrecht. *Theorie und Numerik von Materialinstabilitäten elastoplastischer Festkörper auf der Grundlage inkrementeller Variationsformulierungen*. PhD thesis, University of Stuttgart, 2002.
- [48] M. J. Leamy, P. W. Chung, and R. Namburu. On an exact mapping and a higher-order born rule for use in analyzing graphene carbon nanotubes. In *Proceedings of the 11th Annual ARL-USMA Technical Symposium*, 2003.

- [49] B.-J. Lee and M. I. Baskes. Second nearest neighbor modified embedded-atom method potential. *Physical Review B*, 62:8564–8567, 2000.
- [50] B.-J. Lee, M. I. Baskes, H. Kim, and Y. K. Cho. Second nearest-neighbor modified embedded-atom method potentials for bcc transition metals. *Physical Review B*, 64:184102–1 – 184102–11, 2001.
- [51] J. E. Lennard-Jones. *Proc. R. Soc. London A*, 106:463, 1924.
- [52] F. London. The general theory of molecular forces. *Trans. Faraday Soc.*, 33:8–26, 1937.
- [53] J. W. Martin. Many-body forces in metals and the Brugger elastic constants. *J Phys. C: Solid State Phys.*, 8:2837–2857, 1975.
- [54] J. W. Martin. Many-body forces in metals and the Brugger elastic constants ii: Inner elastic constants. *J Phys. C: Solid State Phys.*, 8:2858–2868, 1975.
- [55] J. W. Martin. Many-body forces in solids: Elastic constants in diamond-type crystals. *J Phys. C: Solid State Phys.*, 8:2869–2888, 1975.
- [56] J. C. Maxwell. *Treatise of Electricity and Magnetism*. Oxford, Clarendon, 1873.
- [57] C. Miehe. Numerical computation of algorithmic (consistent) tangent moduli in large-strain computational inelasticity. *Comput. Methods Appl. Mech. Engrg.*, 134:223–240, 1995.
- [58] F. Milstein. *Mechanics of solids*. Oxford, Pergamon Press, 1982.
- [59] R. D. Mindlin. Micro-structure in linear elasticity. *Archive rational Mechanics Analysis*, 16:51–78, 1964.
- [60] R. D. Mindlin. Second gradient in strain and surface tension in linear elasticity. *Int. J. Solids Structures*, 1:417–438, 1965.
- [61] C. B. Morrey. Quasiconvexity and the semicontinuity of multiple integrals. *Pacific J. Math.*, 2:23–53, 1952.
- [62] P. M. Morse. *Phys. Rev.*, 34:57, 1929.
- [63] S. Müller. Variational models for microstructure and phase transitions, 1996. CIME Lecture Notes.
- [64] M. Nakane, K. Shizava, and K. Takahashi. Macroscopic discussions of macroscopic balance equations for solids based on atomistic configurations. *Archive App. Mech.*, 70:533–549, 2000.
- [65] NavalResearchLaboratory. Materials science and technology division. <http://cst-www.nrl.navy.mil/>.
- [66] Q. S. Nguen. *Stability and Nonlinear Solid Mechanics*. New York, Wiley, 2000.
- [67] W. D. Nix and H. Gao. Indentation size effects in crystalline materials: a law for strain gradient plasticity. *J. Mech. Phys. Solids*, 46(3):411–425, 1998.

- [68] R. W. Ogden. *Non-Linear Elastic Deformations*. Wiley, 1984.
- [69] M. Ortiz and R. Phillips. Quasicontinuum analysis of defects in solids. *Philosophical Magazine A*, 73:1529–1563, 1996.
- [70] M. Ortiz and R. Phillips. Nanomechanics of defects in solids. *Adv. Appl. Mech.*, 36:1–71, 1999.
- [71] ParticleDataGroup. <http://durpdg.dur.ac.uk/lbl>.
- [72] L. Pauling. *The Nature of the Chemical Bond*. Cornell University Press, 1960.
- [73] R. Phillips. *Crystals, Defects and Microstructures*. Cambridge University Press, 2001.
- [74] L. Prandtl. *Goettinger Nachr, Math. Phys. Kl.*, 5(2):74–85, 1920.
- [75] M. J. Puska, R. M. Nieminen, and M. Manninen. Atoms embedded in an electron gas: Immersion energies. *Physical Review B*, 24:3037, 1981.
- [76] D. Raabe. *Computational Materials Science*. Wiley-vch, 1998.
- [77] J. R. Rice. The localization of plastic deformation. In W. T. Koiter, editor, *Theoretical and Applied Mechanics*, pages 207–220, 1976.
- [78] V. B. Shenoy, R. Miller, E. B. Tadmor, D. Rodney, R. Phillips, and M. Ortiz. An adaptive finite element approach to atomic-scale mechanics - the quasicontinuum method. *Journal of the Mechanics and Physics of Solids*, 47:611–642, 1999.
- [79] J. Y. Shu, W. E. King, and N. A. Fleck. Finite elements for materials with strain gradient effects. *Int. J. Numer. Meth. Engng.*, 44:373–391, 1999.
- [80] J. C. Slater. *Quantum Theory of Molecules and Solids, Vol. 1: Electronic structure of molecules*. New York: McGraw-Hill, 1963-74.
- [81] P. Steinmann. Modellierung und numerik uktiler kristalliner werkstoffe, 1997. Habil. Thesis, University of Hannover.
- [82] P. Steinmann, R. Larsson, and K. Runesson. On the localization properties of multiplicative hyperelasto-plastic continua with strong discontinuities. *Int. J. Solid Structures*, 34:969–990, 1997.
- [83] F. Stillinger and T. A. Weber. *Phys. Rev. B*, 31:5262, 1985.
- [84] M. J. Stott and E. Zaremba. Quasiatoms: An approach to atoms in nonuniform electronic systems. *Physical Review 4B*, 22:1564–1583, 1980.
- [85] R. Sunyk and P. Steinmann. Localization analysis of mixed continuum-atomistic models. *J. Phys. IV France*, 11:251–258, 2001.
- [86] R. Sunyk and P. Steinmann. Mixed continuum-atomistic analysis of single crystals. In S. Diebels, editor, *Zur Beschreibung komplexen Materialverhaltens*, pages 175–188. University of Stuttgart, 2001.

- [87] R. Sunyk and P. Steinmann. On higher gradients in continuum-atomistic modelling. *Int. J. Solids Structures*, 40:6877–6896, 2003.
- [88] E. B. Tadmor. *The Quasicontinuum Method*. PhD thesis, Brown University, 1996.
- [89] E. B. Tadmor, G. S. Smith, N. Bernstein, and E. Kaxiras. Mixed finite element and atomistic formulation for complex crystals. *Physical Review B*, 59:235–245, 1999.
- [90] J. Tersoff. *Phys. Rev. B*, 37:6991, 1988.
- [91] R. A. Toupin. Elastic materials with couple stresses. *Archive rational Mechanics Analysis*, 11:385–414, 1962.
- [92] C. Truesdell and R. Toupin. The classical field theories. In S. Flügge, editor, *Encyclopedia of physics*, volume III/1, pages 491–498. Springer Verlag, 1960.
- [93] W. Wagner. Zur behandlung von stabilitätsproblemen der elastostatik mit der methode der finiten elemente, 1991. Habil. Thesis, University of Hannover.
- [94] W. Wagner and P. Wriggers. A simple method for the calculation of postcritical branches. *Engineering Computations*, 5(2):103–109, 1988.
- [95] P. Wriggers. *Nichtlineare Finite-Element-Methoden*. Springer, 2001.
- [96] G. Zanzotto. The cauchy-born hypothesis, nonlinear elasticity and mechanical twinning in crystals. *Act. Cryst.*, A52:839–849, 1996.
- [97] O. C. Zienkiewicz. *The Finite Element Method*. McGRAW-HILL, 1982.

Curriculum Vitae

Name: Rudolf Sunyk
Adress: Dr.-Gustav-Knodel-Str. 8, D-76344 Eggenstein
Date and place of birth: 03.12.68, Kiev (Ukraine)
Marital status: married since 01.11.1991

Schools and Universities:

1975 - 1985 General-education school in Kiev
1985 - 1987 University of Technology of Leningrad
1987-1989 military service
1989 - 1993 University of Technology of St. Peterburg
(Diploma in Physics)
1996 - 1998 University of Kassel
(“Hauptstudium” of Physics)

Professional experience:

2/1999 - 5/2003 research associate at University of Kaiserslautern
since 5/2003 research associate at Research Centre Karlsruhe